Acoustic studies for the non-destructive testing of wood

Michael J. Frampton

A thesis presented for the degree of
Doctor of Philosophy
in
Electrical and Computer Engineering
at the
University of Canterbury,
Christchurch, New Zealand.

25 March 2019

ABSTRACT

Acoustic technologies are an established means of measuring wood stiffness. Acoustic tools are useful because they are non-destructive, relatively cheap, and quick and easy to use. These tools have been used in tree breeding programs, silvicultural applications, and log grading systems.

Acoustic tools work by measuring the speed of sound in wood, which is related to two key wood quality parameters: stiffness and density. However, several factors make this measurement difficult. Wood structure is complex, being both anisotropic (directionally variable) and inhomogeneous (spatially variable). Additionally, wood is highly attenuating to acoustic waves, which means it is also dispersive.

In this thesis, several aspects of acoustic testing of wood are explored. A review is provided of existing findings in the field, and an overview of the requisite wave mechanics is provided. Following this, a series of original studies on the topic are described.

Several models are proposed for the effect of the wood-loading on a spike-shaped acoustic transducer. It is demonstrated that these models, known as radiation impedance models, determine the low-frequency performance of the transducer.

A methodology is proposed for determining the frequency-dependent transfer-function of an acoustic wave propagating in wood. Several transmission-line models are proposed for the observed behaviour of green wood. Of the proposed models, the Zener model with spherical spreading is shown to match the measured data most closely.

A new time of flight (ToF) measurement system, Wireless Treetap, is presented. The hardware, software, and testing of this system is described. A field test of the system is described. The findings of this test demonstrate that the system is feasible, however some problems regarding its robustness remain unresolved.

A new method is proposed for measuring the acoustic velocity variation along the length of a harvested tree stem. An array of transducers is used to measure a series of waveforms in two *Pinus radiata* stems. It is shown that two of the proposed processing methods: time of flight and reflected-wave cancellation, are insufficient for determining the velocity variation. However, it is shown that the position of the resonant nodes gives an indication of the variation in acoustic velocities between each half of the stem.

Deputy Vice-Chancellor's Office
Postgraduate Office

UNIVERSITY OF CANTERBURY
Te Whare Wānanga o Waitaha
CHRISTCHURCH NEW ZEALAND

Co-Authorship Form

This form is to accompany the submission of any thesis that contains research reported in co-authored work that has been published, accepted for publication, or submitted for publication. A copy of this form should be included for each co-authored work that is included in the thesis. Completed forms should be included at the front (after the thesis abstract) of each copy of the thesis submitted for examination and library deposit.

Publication 1: Frampton, M.J. and Hayes, M.P. (2014), 'Electromechanical modelling of a time-of-flight transducer for wood applications', In *Electronics New Zealand Conference (ENZCon)*, University of Waikato, Hamilton, pp. 51–56.

Parts of Section 3.3, Section 3.6, and Appendix C present material from this publication.

Publication 2: Frampton, M.J. and Hayes, M.P. (2016), 'Wireless Treetap: a new electronic device for time-of-flight tree-stiffness measurement', In *Electronics New Zealand Conference (ENZCon)*, University of Victoria, Wellington, pp. 32–37

Parts of Chapter 5, particularly sections 5.2, 5.3, and 5.5, present material from this publication.

Publication 3: Frampton, M.J. and Hayes, M.P. (2016), 'A system for non-destructively determining variation in acoustic velocity within a harvested tree stem.', In *Electronics New Zealand Conference (ENZCon)*, University of Victoria, Wellington, pp. 152–157

Parts of Chapter 6, particularly sections 6.2-6.5, present material from this publication.

Publication 4: Frampton, M.J. and Hayes, M.P. (2017), 'Estimating the Frequency Response of Green Wood Using Time of Flight Measurements', In *Electronics New Zealand Conference (ENZCon)*, University of Canterbury, Christchurch

Parts of Chapter 4, particularly sections 4.2 and 4.4, present material from this publication.

Please detail the nature and extent (%) of contribution by the candidate:

Publication 1: Methodology developed through discussions between candidate and M. P. Hayes. Data collected by candididate. Software, results, figures, and written

content produced by candidate. Both authors provided comments and review. 80% of the research, and 95% of the writing was contributed by the candidate.

Publication 2: Methodology proposed by M. P. Hayes. Experimental data captured by both authors. Software written by both authors. Results, figures, and written content produced by candidate. Both authors provided comments and review. 70% of the research, and 95% of the writing was contributed by the candidate.

Publication 3: Methodology developed through discussions between candidate and M. P. Hayes. Software written by both authors. Results, figures, and written content produced by candidate. Both authors provided comments and review. 80% of the research, and 95% of the writing was contributed by the candidate.

Publication 4: Methodology developed through discussions between candidate and M. P. Hayes. Software written initially by M. P. Hayes, and then developed further by candidate. Results, figures, and written content produced by candidate. Both authors provided comments and review. 80% of the research, and 95% of writing was contributed by candidate.

Certification by co-authors

If there is more than one co-author then a single co-author can sign on behalf of all. The undersigned certifies that:

- The above statement correctly reflects the nature and extent of the PhD candidate's contribution to this co-authored work
- In cases where the candidate was the lead author of the co-authored work, he or she wrote the text.

Name: *Dr Michael P. Hayes* Signature: MPH Date: *25 March 2019*

CONTENTS

ACKNOWLEDGEMENTS

Firstly I would like to acknowledge my primary supervisor Associate Professor Michael Hayes. Michael is an extraordinary researcher, an excellent teacher, and a good friend. He always goes the extra mile for his students, whether it's summarising a topic in notes, writing some code, or even just popping in daily to see how things are going. His contributions are often above and beyond the call of duty, and I hope he knows that they are appreciated. So thank you Michael for your continual support, I cannot imagine that I could have got this far without you.

Secondly I would like to thank my co-supervisor Associate Professor Clemens Altaner from the NZ School of Forestry (SoF). While Clemens has played a lesser role in my thesis overall, his provision of feedback and critique of my work has been invaluable. I'd also like to thank Professor (now emeritus) John Walker from the SoF. John helped me to obtain a UC Doctoral scholarship through the SoF. Without this support my thesis would not have been possible.

I'd like to give my thanks to all the technical staff in the Electrical and Computer Engineering (ECE) department. The technicians are the backbone of the department. They've put up with a lot over the last few years, with the earthquake and subsequent rebuilding of the department. Particular thanks go to Mike Cusdin (now retired) for his work on Treetap. I also need to give a huge thanks to Nigel Pink and Lachlan Kirk in the SoF (both have now left the department). Their technical and practical forestry experience was very helpful throughout my degree. Also, a special thanks to Jodie, Ruth and Marco from the Radiata Pine Breeding company for your support on the Wireless Treetap trial. I'd also like to extend my thanks to the other academic staff in the ECE department. They all work incredibly hard, and it really shows, as the department is a great place to work and study. A big thanks also must go to the excellent administrative staff: Deborah and Catherine in the ECE department, and Jeanette in the SoF.

A big thanks to the other postgrad students in the ECE department who make the day-to-day bearable (and fun). Napasool (A-man!), Alana, Laura, Yanni, Nurzhan, Sudhanshu, Louise, Azy, Lance, Matthew, Ben, and anyone else that's given me support, or even just shared a laugh. Special thanks have to go to Blair Bonnett, you have been a mentor to me over the years, and I wish you all the best, wherever you end up (you'll

be back!?).

I'd also like to thank Dr Stan Floyd and Dr Tim Molteno for examining this work, and Professor Rick Millane for acting as the examination chair. I appreciate that it must've been difficult reading the work over the Christmas break, and then performing the actual examination right at the start of term. Thank you all for your contributions.

I must give my thanks to the School of Forestry for funding this research, which was provided through a UC doctoral scholarship. I'm really grateful that this support was given to me.

Finally I'd like to thank my family and friends, particularly those that have lived with me over the last few years. I'm really lucky to be surrounded by so many excellent people, without you guys I couldn't have done it.

PREFACE

In this age where advanced materials are commonplace, wood remains one of humanity's most important resources. Consequently, to remain competitive it is crucial that the wood material we produce is of a high standard. An inherent difficulty in wood production is that its mechanical composition is highly variable, both within a single tree and between trees. In the past skilled tradesmen would have developed a keen eye for recognising the traits of good quality wood. Now we seek to develop automated tools which will perform this classification for us.

The ability of wood material to propagate sound waves has been known, at least intuitively, since ancient times, through the crafting of musical instruments. The mathematical theory of wave behaviour is comparatively a recent development–occurring in the mid 1700s [Wheeler and Crummett 1987]. Although wooden musical instruments are still of great importance, in recent times there has been renewed interest in sound wave propagation through wood. This is because acoustic waves can be used to characterise wood properties through non-destructive testing techniques. Acoustic testing techniques like the time of flight (ToF) method and the resonance method allow the velocity of sound waves in wood to be measured. The wave velocity is related to the stiffness and density of the wood–both key indicators of wood quality.

The work described in this thesis began as a desire to produce improved non-destructive testing tools for forestry applications. This follows over 15 years of research and development on wood quality measurement devices at the University of Canterbury. This development was conducted as a collaboration between the School of Forestry and the Department of Electrical and Computer Engineering, and was led primarily by Dr Michael Hayes, and Prof. John Walker (now Professor Emeritus). The result of this work was a series of electronic systems including several *Treetap* ToF acoustic measurement devices, *Treetwist*–a system for measuring the acoustic velocity of an extracted increment core, and *Treedisk*–a system for measuring acoustic velocity in a crosscut disk from a tree stem.

I soon learned that the techniques of acoustic testing of wood are, in many cases, based on oversimplifications of the underlying physical theory. For instance, the commonly cited relationship between acoustic velocity, c, stiffness, E, and density, ρ, is $E = c^2\rho$. This equation assumes that the medium is one-dimensional, lossless, isotropic,

and homogeneous–all of which are demonstrably wrong for the case of wood material. The work described in this thesis grew out of a desire to produce a theory of wood acoustics rooted in substantive physical models. I proposed that this approach would enable me to develop improved testing tools. An example of such tool would be a ToF device capable of producing an accurate measurement of a standing tree's static stiffness. I soon learned that this goal was a difficult one. I hope that I have conveyed in this document that the development of a physical theory of wood acoustics is a difficult business.

This thesis is arranged into seven chapters. Chapter 1 provides an overview of existing work on the measurement of wood quality using acoustic techniques. It is written with an emphasis on plantation forestry applications. It does not include a rigorous treatment of the foundational acoustic physics.

Chapter 2 provides an overview of the physics of wave behaviour in solids. The intention of this chapter is to develop an understanding of wave behaviour in wood, though much of the theory is applicable to other types of media.

Chapter 3 is a description of the development of a mathematical model for an acoustic transducer, the Fakopp SD-02. This device is a spike-shaped accelerometer, designed specifically for use in forestry applications. The transducer is used in measurements conducted throughout the remainder of the thesis, therefore, this work is included as the first non-background chapter.

Chapter 4 describes a method for measuring the viscoelastic dispersion of acoustic waves in a standing tree. The findings of this chapter suggest that the well known overestimation of the ToF method is, in part, due to viscoelastic effects.

Chapter 5 describes the design and construction of a new ToF measurement system, Wireless Treetap (WTT). This chapter includes a description of the hardware, software, and algorithms which constitute this system. The results of a field trial of the system are also documented.

Chapter 6 describes an attempt to develop a new acoustic measurement procedure for harvested tree stems. The goal of this project was to measure the longitudinal variation in acoustic velocity along the length of a tree stem. The purpose of this work was to develop a system which would allow a stem to be measured for stiffness prior to sawing, allowing different segments to be assigned to different end-products.

The thesis concludes in Chapter 7 with a summary of the main results and a list of recommendations for future work.

The first two chapters of the thesis contain introductory material. The remaining five chapter are, by and large, original material.

The following people have made significant contributions to the work documented in this thesis. Michael Hayes wrote the Lcapy python program, which was used for calculating the response of the SD-02 circuit model, described in Chapter 3. He also

assisted in conducting the probe-mass experiment described at the end of that chapter. Michael also assisted in writing the program for calculating the viscoelastic model parameters, described in Chapter 4.

The development of the WTT system began as a final-year engineering project by Tom Harrison, Daniel Lower, and Thomas Potter [Harrison et al. 2014]. They performed some useful background work, which enabled several inappropriate clock-synchronisation methods to be eliminated. The system's electronics were designed by myself, Matthew Edwards, and Michael Hayes. Matthew Edwards also assisted in the development of some python scripts for measuring the device's frontend performance. Mike Cusdin and Scott Lloyd assisted in construction of the PCBs. Nigel Pink designed and built the probe housings. The firmware for WTT was written by Michael Hayes and myself. The field test of the device was conducted with assistance by the Radiata Pine Breeding Company (RPBC), through the contractors Marco Lausberg and Jodie Wharekura.

The stem experiment also started as a final-year engineering project by Hugo Saathof, Matthew Curnow, and Tony Chen. This work was funded by the (now discontinued) research organisation Solid Wood Innovation (SWI). The experiment described in Chapter 6 was conducted by myself and Michael Hayes, with chainsaw assistance from Lachlan Kirk and Nigel Pink.

PUBLICATIONS

The following papers were published during the course of this thesis.

Frampton, M.J. and Hayes, M.P. (2014), 'Electromechanical modelling of a time-of-flight transducer for wood applications', In *Electronics New Zealand Conference (ENZCon)*, University of Waikato, Hamilton, pp. 51–56

Frampton, M.J. and Hayes, M.P. (2016), 'Wireless Treetap: a new electronic device for time-of-flight tree-stiffness measurement', In *Electronics New Zealand Conference (ENZCon)*, University of Victoria, Wellington, pp. 32–37

Frampton, M.J. and Hayes, M.P. (2016), 'A system for non-destructively determining variation in acoustic velocity within a harvested tree stem.', In *Electronics New Zealand Conference (ENZCon)*, University of Victoria, Wellington, pp. 152–157

Frampton, M.J. and Hayes, M.P. (2017), 'Estimating the Frequency Response of Green Wood Using Time of Flight Measurements', In *Electronics New Zealand Conference (ENZCon)*, University of Canterbury, Christchurch

LIST OF SYMBOLS AND ABBREVIATIONS

A	Voltage gain
c	Phase speed
c_{tof}	Time of flight speed
c_{res}	Resonance speed
c_g	Group speed
C	Stiffness tensor component
$\boldsymbol{C}$	Stiffness tensor
$\hat{\boldsymbol{e}}_{\boldsymbol{x}}$	x-direction unit vector
$\hat{\boldsymbol{e}}_{\boldsymbol{y}}$	y-direction unit vector
$\hat{\boldsymbol{e}}_{\boldsymbol{z}}$	z-direction unit vector
E	Young's modulus
f	Force (instantaneous)
F	Force (complex amplitude)
f_{res}	Resonant frequency
f_{s}	Sampling frequency
k_{r}	Ratio between ToF and resonance velocities
k	Wave number
m	Mass
n	Resonance harmonic number
$\dot{n}$	Component of propagation-direction vector
$\hat{\boldsymbol{n}}$	Propagation-direction vector
r	Radius
s	Compliance tensor component
$\boldsymbol{S}$	Compliance tensor
S	Treetap threshold sensitivity
T	Threshold level
u	Particle displacement magnitude
$\boldsymbol{u}$	Particle displacement vector
v	Voltage (instantaneous)
V	Voltage (complex amplitude)
x	Equilibrium position magnitude

$\mathbf{x}$	Equilibrium position vector
z_0	Probe-spike separation
Δz	Probe-probe separation
Z_0	Characteristic acoustic impedance
Z_m	Mechanical rectilinear impedance
α	Attenuation coefficient
$\alpha_\mathrm{dB/cm}$	Attenuation coefficient in decibels per centimetre
γ	Propagation coefficient
$\dot{\gamma}$	Christoffel matrix component
Γ	Reflection coefficient
$\boldsymbol{\Gamma}$	Christoffel matrix
ϵ	Strain tensor component
$\boldsymbol{\epsilon}$	Strain tensor
η	Damping coefficient
$\boldsymbol{\eta}$	Damping tensor
λ	Wavelength
λ_1	Lamé's first parameter
μ_1	Lamé's second parameter
ν	Poisson's ratio
ρ	Density
σ	Stress tensor component
$\boldsymbol{\sigma}$	Stress tensor
σ_u	Strength (modulus of rupture)
τ	Propagation time
$\dot{\tau}$	Traction vector component
$\dot{\boldsymbol{\tau}}$	Traction vector
ξ	Particle displaced magnitude
$\boldsymbol{\xi}$	Particle displaced vector

AWGN Additive white gaussian noise

CRLB Cramér-Rao lower bound

DBH Diameter at breast height

FFT Fast Fourier Transform

FTSP Flooding time synchronisation protocol

LiPo Lithium polymer

LTI Linear, time-invariant

LVL Laminated veneer lumber

MC Moisture content

MFA Microfibril angle

MoE Modulus of elasticity

MoR Modulus of rupture

MSG Machine stress-graded

PDF Probability density function

PCB Printed circuit board

PGA Programmable gain amplifier

PSD Power spectral density

RMS Root mean square

SLS Standard linear solid

STP Standard pressure and temperature

TCXO Temperature-controlled crystal oscillator

ToF Time of flight

WTT Wireless Treetap

Chapter 1

MEASURING WOOD QUALITY USING ACOUSTICS

A general definition of *wood quality* is: wood material which closely matches the desired specifications of a particular market. There are many different markets for wood products, each with its own set of specifications. Manufacturers of structural timber seek to maximise stiffness and stability, while manufacturers of pulp are more concerned with fibre and chemical features. Often, authors using the term wood quality are specifically referring to the desires of the market for high quality structural wood applications. This market desires a product with high stiffness, high dimensional stability, uniformity of grain, with minimal amount of knots and other imperfections. Finished products in this market are amongst the higher value wood products available.

Foresters must balance the desire for a high quality product against other constraining requirements. For example, in order to maximise profitability, rotation times are kept as short as possible, effectively reducing the volume of high-stiffness wood produced. Foresters have many parameters to adjust, including: seedling selection, stocking density, site selection, thinning, branch pruning, and rotation length. In order to assess the effect of these parameters across a wide range of environmental conditions, effective tools for analysing the properties of their stock is required.

Acoustic tools offer the potential for rapid assessment of wood quality. For several decades research has been conducted on the use of acoustics for measuring wood properties. This chapter will summarise the findings of this research. In Section 1.1, an overview of the structural composition of softwoods is given, and an introduction to the concepts of wood stiffness and wood density. In Section 1.2, several acoustic techniques of measuring wood stiffness are described, and the known problems with these methods are discussed. Finally, in Section 1.3, an overview of some of the wood features which affect stiffness are discussed.

1.1 WOOD PROPERTIES AND THEIR EFFECT ON QUALITY

Wood is one of the most successful engineering materials in existence, having seen ongoing use for thousands of years. However, the structure of wood makes it particu-

larly challenging to use effectively. Within a tree, wood properties vary directionally (*anisotropy*), and spatially (*inhomogeneity*). Wood properties also vary considerably between trees, even in the same stand. Acoustic[1] waves propagating within wood are also affected by the wood's structure. The speed of the wave is strongly influenced by the stiffness and density of the medium (this is demonstrated in Section 1.2). To develop an understanding of how the mechanical properties vary within a tree, an overview of wood structure is discussed in Section 1.1.1. Next, in Section 1.1.2, an overview of stiffness is provided, including known trends in stiffness variation. Next, in Section 1.1.3, an overview of wood density and its variation is discussed.

1.1.1 The structural composition of softwood

Wood is a general term used to refer to a variety of hard plant tissues. A specific definition is: "the hard, fibrous tissue that comprises the major part of stems, branches, and roots of trees, belonging to the plant groups known as the gymnosperms and the dicotyledonous angiosperms [Schniewind 1989]." Wood structure can be classified as a hierarchy, beginning with the macroscopic, or visible scale; then progressing down to the microscopic, or cellular scale; and then down to the sub-microscopic, or molecular composition of wood cells. In this section, an emphasis is placed on the elements which comprise the tree's stem, as these are the primary concern for plantation forestry applications. For a more detailed analysis of the composition of wood, a number of references are available, including Stamm [1964], Kollmann and Côté [1968], Jane et al. [1970], Butterfield and Meylan [1980], Fengel and Wegener [1983], Ping [2000], Harrington [2002], and Walker [2006b].

At the macroscopic scale, several characteristic growth patterns are observed. Consider a cross section of a cut tree stem. At the centre is a region known as the *pith*. In a mature tree, the pith is a small, spongy area of wood which forms a nexus where radially oriented cells coincide. Another growth pattern is that of *annual growth rings*, which are prominent in trees growing in temperate climates. Growth rings occur because new cell growth tends to be of lower density early in the season. This growth is called *earlywood*. This growth is contrasted against *latewood*, which is of higher density, and usually has a darker colour. At some point in a tree's life, *heartwood* begins to form in a region around the pith. For example, in *Pinus radiata* this occurs after approximately 15 years [Walker 2006a]. The heartwood is a region of lower moisture content, it is often easily identifiable as a region of darker colour, caused by the presence of chemicals in the wood called *extractives*. Heartwood forms a cone within the stem which spreads upwards and outwards with age. The heartwood extractives can play

[1]Some authors specifically use *acoustics* or *acoustic wave* to refer to sound waves propagating in air. The terms *stress wave* and *elastic wave* are typically used to describe acoustic waves propagating in solid elastic media. In the field of acoustic non-destructive testing of wood, the three terms are used interchangeably, as they are in this thesis.

an important role in reducing decay due to fungi and insects. In some applications heartwood is desirable because its colouration can be used to create attractive finished products. Outside of the heartwood is a region known as the *sapwood*. Sapwood is higher in moisture content than heartwood and is active in water transport and other physiological processes [Walker 2006b].

At the microscopic level are the cells which constitute the woody tissue. At functional maturity, the majority of cells in both the heartwood and sapwood are effectively dead and do not reproduce. Outside of the sapwood is a region called the *vascular cambium*. This consists of a thin layer of *meristematic* (undifferentiated) cells located near the outside of the stem, just beneath the bark. These cells divide to form *secondary vascular tissues*, which consist of the *xylem* and *phloem* cells. The phloem forms the inner layer of bark. This layer is responsible for carbohydrate conduction and forming a protective layer in the juvenile tree [Butterfield 2006]. Outside of this is the outer bark, which consists of effectively dead cells, functioning as protection for the stem [Butterfield 2006]. The other secondary growth type is that of *xylem*. In softwoods[2], up to 95% of the xylem growth by volume is *tracheid* cells [Kollmann and Côté 1968]. These cells function as the primary support structure of the tree, thus contribute significantly to the elasticity of the wood. Tracheids are approximately axially aligned with the tree, with lengths ranging from 2 to 5 mm. These cells are about 100 times longer than they are wide [Butterfield 2006]. The elongated structure of the tracheid cells helps to give softwoods their high elasticity along the grain. The inner cavity, or *lumen*, of the tracheid facilitates water conduction up the stem. The majority of mature tracheid cells lose their protoplasm (nucleus and surrounding material) in the year that they formed, preventing further biological processes including reproduction [Kollmann and Côté 1968]. A cross-section of tracheid cells in a growth ring of *Thuja plicata* is shown in Figure 1.1a.

Another less common type of xylem cell found in softwoods are *parenchyma*. These cells have a functional protoplasm, which allows them to remain alive for a longer period than tracheid cells [Kollmann and Côté 1968]. Parenchyma cells main functions are to repair the plant and provide food storage. In softwoods, the majority of parenchyma cells are radial, though sometimes a small minority are axially oriented. Many softwoods also contain a dark sticky substance known as *resin*. Resin usually occurs in specialised canals lodged between the tracheids. When the tree is wounded the resin seeps from the canals, which acts to protect the tree from invading insects and pathogens. Softwoods also contain several types of cells oriented radially outwards from the pith. These are collectively known as *rays*. These cells have a range of functions including food storage, wound healing, and the transport of water, minerals, and other organic substances in

[2]It should be noted that *softwood* is a misnomer. Softwood refers to coniferous (cone producing) plants, which form part of the *gymnosperms*. Hardwood refers to flowering plants, known as *angiosperms*. Softwoods are not always softer than hardwoods.

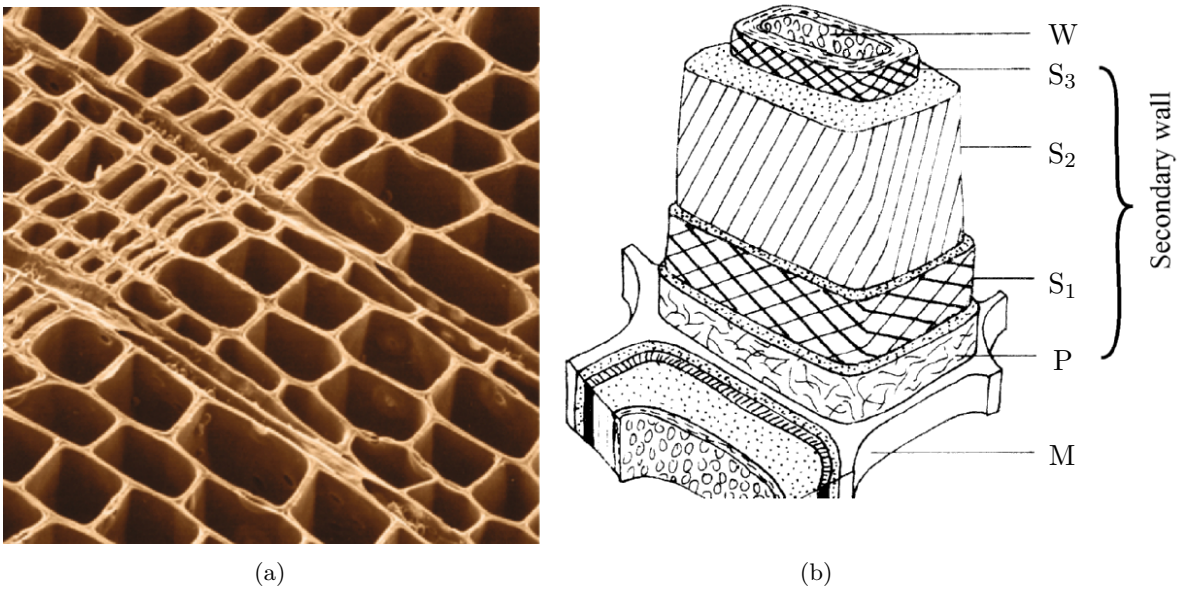

(a) (b)

Figure 1.1 The cellular structure of softwood. (a) Tracheid cells from *Thuja plicata*. A growth ring is visible, with thicker walled latewood in the upper left, and thinner walled earlywood in the lower right (taken from [Butterfield 2006]). (b) The structure of the tracheid cell wall; labelled from top: Warty later, S_3 layer, S_2 layer, S_1 layer, Primary wall, Middle lamella (taken from [Cote 1967]).

the radial direction.

At the sub-microscopic level are the molecules which constitute the parts of the cell. Fengel and Wegener [1983] explain that the molecular constituents of the cell wall are cellulose, hemicellulose, lignin, and extractives. The exact proportions of these constituents varies between and within species. Tracheid cell walls consist of chains of cellulose polymers wound around the cell, termed *microfibrils*. These microfibrils form various matrix-like macrostructures, termed *lamellae*. Bucur [2006] explains that these lamellae can be classified into various layers of the cell wall, for which there is a generally accepted denomination. Working inwards from the outside of the cellular wall: the M layer is the middle lamella, P is the primary wall of adjoining cells, and the S layer is the secondary cell wall. The S layer is further dissected into three distinct layers: S_1, S_2, and S_3. S_1 is the outer later of the secondary wall ($\approx 1\,\mu$m thick in latewood). The S_2 layer is the thickest and dominant component ($\approx 10\,\mu$m thick in latewood). S_3 is the inner layer of the secondary wall ($\approx 1\,\mu$m thick in latewood). W is the warty membrane that lines the cell lumen. S_2 layer microfibrils are densely packed and inclined at an angle of 10° to 30° with respect to the cell axis. The average value of the inclination is known as the microfibril angle (MFA). The MFA has been shown to have a strong impact on the wood's stiffness [Cave 1968, 1969, Cave and Walker 1994]. When the MFA is low, the microfibrils are closely aligned with the cellular axis, resulting in a high longitudinal stiffness. When the MFA is high, the longitudinal stiffness is decreased and the across-grain stiffness is relatively higher. A diagram of the various components of

the cellular wall is shown in Figure 1.1b.

Trees have evolved to cope with a large variety of environments. In order to survive and reproduce they must endure a wide range of weather, soil conditions, predators, and competition from other species. The biological nature of wood, and its adaptability to conditions leads to inhomogeneities in wood structure [Bodig and Jayne 1982]. One consequence of complex and variable environmental conditions is a high degree of variability in wood quality. For example, Bodig and Jayne [1982] explain that the density of wood is known to vary by up to six times within a species, and by more than three times within a growth ring. This high variability in wood structure and quality can be a frustration for wood processors and manufacturers of products. These effects make wood unique as an engineering material, because its quality is dependent on many genetic and environmental factors, as well as care and management by the various parties of interest.

1.1.2 Wood stiffness

The term *stiffness* refers to the elasticity of the wood material in a tree, stem, or piece of timber. It is usually defined as the ratio of *stress* σ, to *strain* ϵ,

$$E = \frac{\sigma}{\epsilon}. \tag{1.1}$$

Stress is the applied pressure, measured in pascals, and strain is the resultant (dimensionless) fractional deformation along the axis at which the pressure was applied. (1.1) is known as *Hooke's law*. Wood is typically considered an elastic material, i.e., over some applied stress range the strain is proportional to the stress. For structural purposes, engineers prefer materials with a high stiffness because they reduce the distortion under load [Pellerin and Ross 2002]. Additionally, engineers seek materials which have a high *strength*, which is defined as the stress at which a material suffers permanent deformation [Bodig and Jayne 1982]. Strength cannot be directly measured for each individual piece of wood, as this would require its destruction. Fortunately, stiffness and strength are correlated, thus stiffness is useful as a proxy indicator of strength [Wang et al. 2000].

The term stiffness is often used synonymously with modulus of elasticity (MoE). In much of the forestry literature these terms are vaguely defined. The term MoE actually refers to a number of different elastic moduli[3] [Beer et al. 2006]. Where the abbreviation MoE is used in this thesis, the reader can assume that Young's modulus in the longitudinal direction is meant.

Many factors contribute to a tree's stiffness, therefore, it is not surprising that stiffness is highly variable. Species, environmental conditions, and silvicultural methods all play a role in determining a tree's stiffness [Chauhan et al. 2006b]. Across all

[3]For further definitions of elastic moduli, see Chapter 2.

species, stiffness values range between approximately 0.5–20 GPa [Chauhan et al. 2006b]. Stiffness variation within a tree tends to follow a predictable pattern. A tree stem may be grouped into two regions. *Corewood* is usually defined as the central column of a tree's material, inside which, wood properties are changing with cambial age, with stiffness increasing outwards. *Outerwood* is the region surrounding the corewood, where wood properties are relatively stable in the radial direction, and stiffness is maximal [Chauhan et al. 2006a, Cown 1992]. Researchers have studied and quantified this within-tree variation in stiffness. Studies by Xu and Walker [2004], Tsehaye et al. [2000b], and Grabianowski et al. [2006] used harvested stems of *Pinus radiata* cut into boards and then measured the stiffness of each board to determine the stiffness variation within the stems. These studies show that the stiffest part of a tree is the outerwood, and at the opposite extreme, the corewood is generally of low stiffness. There is a gradient of stiffness between these two extremities. This trend tends to be exaggerated at the lowest parts of the stem, i.e., the newest growth (mature) outerwood is much stiffer than oldest growth (juvenile) corewood.

Stiffness also varies considerably between trees of the same species growing in close proximity [Dyck 2003, Grabianowski et al. 2006]. This variation is large enough that the corewood of one tree can be stiffer than the outerwood of a nearby tree [Chauhan et al. 2006a]. This high variability suggests that large stiffness improvements are possible through better seedling selection [Apiolaza 2009].

Wood stiffness also varies with respect to direction. A property's dependency on direction is referred to as *anisotropy*. Wood's stiffness is usually considered to present *orthotropic symmetry* [Bodig and Jayne 1982, Bucur 2006]. This means that there are three orthogonal planes of symmetry, with each plane presenting a different set of stiffness values along its constituent axes[4]. Direction in wood is typically defined using three orthogonal axes: longitudinal, or along the grain (L), radially outwards from the pith (R), and tangential to the growth rings (T) [Bodig and Jayne 1982]. The stiffness is greatest in the longitudinal direction; and the radial and tangential stiffness values are approximately 1/10th as large. For example, the mean stiffness values for Loblolly pine at 12% moisture content are: $E_{\mathrm{L}} = 12.3\,\mathrm{GPa}$, $E_{\mathrm{R}} = 1.39\,\mathrm{GPa}$, and $E_{\mathrm{T}} = 0.96\,\mathrm{GPa}$ [Kretschmann 2010]. The discrepancy between stiffness values of these axes is explained by the characteristic growth patterns in these directions, i.e., tracheid cells are aligned approximately in the longitudinal direction, ray cells are oriented in the radial direction, and growth rings have their perimeter in the tangential direction.

As previously stated, a useful feature of wood stiffness is its ability to predict yield strength. The limits of a material's stiffness are its *tensile* and *compressive*, and *shear* strengths; these are the stresses at which permanent deformation will occur. The stress at which deformation occurs is known as the modulus of rupture (MoR), and

[4]For further discussion on orthotropic symmetry, see Section 2.4.2.

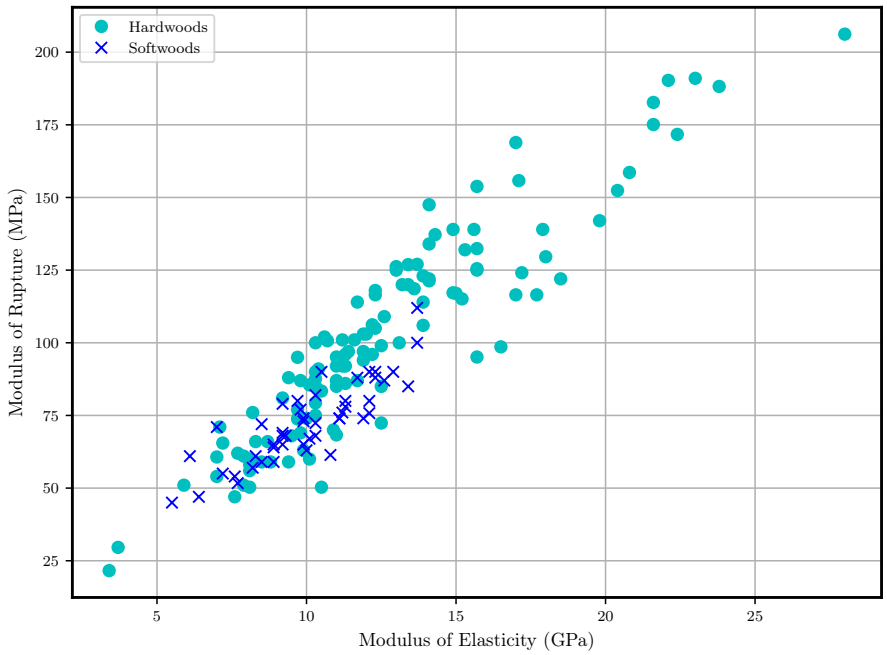

Figure 1.2 Correlation between stiffness and strength for several species. Reproduced from data published by Kretschmann [2010].

is measured in pascals. Wood is significantly stronger in tension than in compression [Kretschmann and Hernandez 2006]. Kretschmann and Hernandez [2006] described a study of 1348 pieces of *Picea sitchensis* (Sitka spruce) timber, where the MoE and MoR were measured using a static bending test. The coefficient of determination between the MoE and MoR was $r^2 = 0.49$, indicating a reasonably strong relationship between the two variables. Salmi et al. [2013] estimated the stiffness using an ultrasonic acoustic technique of 102 *Picea abies* samples, and then measured the strength of each sample. They measured r^2 values between the ultrasonic stiffness and MoR ranging from 0.3 to 0.53, depending on the ultrasonic frequency employed. A similar study was performed by Yang and Fortin [2001] on *Pinus radiata*, they found an r^2 of 0.56 between the ultrasonic stiffness and the MoR. The correlation between strength and stiffness over a wide range of species has also been studied. Figure 1.2 plots the average MoE versus the average MoR for a large number of softwood and hardwood species. These results suggest that stiffness is useful as a proxy indicator of strength.

Wood strength, like stiffness, is also strongly dependent on direction. Hankinson's formula is an empirically derived equation for calculating the strength at an arbitrary angle to the grain,

$$\sigma_{\mathrm{u}}(\phi) = \frac{\sigma_{\mathrm{u}\parallel}\sigma_{\mathrm{u}\perp}}{\sigma_{\mathrm{u}\parallel}\sin^n\phi + \sigma_{\mathrm{u}\perp}\cos^n\phi}, \tag{1.2}$$

where σ_{u} is the ultimate strength in the direction ϕ from the grain, $\sigma_{\mathrm{u}\parallel}$ is the strength parallel to the grain, $\sigma_{\mathrm{u}\perp}$ is the strength perpendicular to the grain, and n is a value derived from experimental data [Hankinson 1921]. However, Radcliffe [1965] noted that

n should be equal to 2 in order to agree with the equations of orthotropic symmetry.

1.1.3 Density

The *density* of a material is its mass per unit volume, and has the SI unit of kg/m^3. The density of dry cell wall of all woody plants is approximately 1500 kg/m^3 [Walker 2006c]. It follows that the density of wood is primarily a measure of the amount of fibrous cellular tissue present, and also the amount of moisture contained within.

The density of wood varies considerably depending on moisture content (MC). As moisture is reduced, the wood's mass reduces, and the wood also tends to shrink, changing its effective volume. The MC of wood is typically expressed as a percentage,

$$\mathrm{MC} = \frac{m_{\mathrm{water}}}{m_{\mathrm{wood}}} \cdot 100\%, \tag{1.3}$$

where m_{water} is the mass of the water in the sample, and m_{wood} is the mass of the dry woody material. The moisture content of green wood can range from less than 30% to more than 200% [Glass and Zelinka 2010].

Walker [2006c] explains that the density of wood is quantified with an associated MC, specified as a percentage,

$$\rho_{\%} = \frac{\text{mass of wood at } x\% \text{ MC}}{\text{volume of wood at } x\% \text{ MC}}. \tag{1.4}$$

Special cases of (1.4) are commonly in use. The *green density* is when the wood is freshly harvested, thus close in MC to that of growing conditions. The *oven-dry density* is when the wood has been dried in an oven, removing all moisture. The *air-dry density* is when the harvested wood is in equilibrium with the surrounding atmospheric conditions [Walker 2006c]. In all three cases, to determine the density, the mass and volume of a sample of wood is measured under the same conditions. Air-dry density is often assumed in the literature to occur at 12% MC. The air-dry MC of wood depends on both the temperature and the relative humidity. Glass and Zelinka [2010] show that a relative humidity of 65% and an ambient temperature of 25 °C corresponds to a MC of approximately 12%.

Basic density is the ratio between the oven dry mass of a sample, and its green volume,

$$\rho_{\mathrm{basic}} = \frac{\text{mass of wood oven-dry}}{\text{volume of wood green}}. \tag{1.5}$$

Basic density is a measure of the density of wood fibre in a green tree. A benefit of basic density is that both oven-dry and green conditions are easily reproducible, unlike the air-dry condition which is dependent on environment.

Walker [2006c] explains that in wood tissue, water is stored in two distinct regions. *Free water* is stored in the cell lumens (e.g. the interior of tracheid cells) and inter-

cellular cavities. *Bound water* is stored within the cell walls. As wood is dried, the free water is removed first. The point where all free water has been removed is known as the *fibre saturation point*, and is typically specified as a percentage MC, which is around 30% MC for most species [Glass and Zelinka 2010]. Further drying past the saturation point results in removal of the bound water. Bodig and Jayne [1982] explain that this concept is important because the removal of the free water has little or no impact on the mechanical properties of the wood, while the removal of bound water tends to increase stiffness and strength.

A common method of measuring density is Archimedes' principle [Grundelius 1990]. In this method, a volume of water is placed on a scale. The scale is then tared so that it reads zero. A green wood sample is then completely submersed in the water. Since the majority of woods are less dense than water when green, a downwards force must be applied. With the sample stationary and submerged, the scale reads the mass of the water's displacement. The volume of displaced water is equal to the wood's volume. The density of water at standard pressure and temperature (STP)[5] is approximately 1000 kg/m^3 [Riddick et al. 1986], therefore, the scale's reading in kilograms is equal to the wood's volume in litres. If measuring the basic density of the wood, the samples are then dried and weighed.

There are several other methods of measuring wood density. One such method is termed the *maximum moisture content* method [Smith et al. 1954]. In this method, the difference in mass between oven dry wood, and wood completely saturated in water is measured. This enables the wood's specific gravity to be determined. Another method of determining wood density is via X-ray densitometry [Evans et al. 2000b, Polge 1978]. An X-ray source is used to expose a CCD detector (or in older devices, a film), with a wood sample of known size obstructing the CCD from the source. This produces a negative on the CCD, with an exposure intensity inversely related to the density. A relatively new technique of measuring density, based on measurement of the electrical permittivity, was proposed by Schinker et al. [2003]. This work led to the development of a commercial microwave densitometry device named *lignostation*. A difficulty of this method is that the electrical permittivity is strongly dependent on the moisture content [Glass and Zelinka 2010]. Thus, it is important that the samples used in the permittivity technique have a known and well-controlled moisture content.

Density within a stem follows a similar pattern of variation to that of stiffness. Basic density tends to increase radially outwards from the pith [Chauhan et al. 2006a, Donaldson et al. 1995, Grabianowski et al. 2006, Legg and Bradley 2016, Tsehaye et al. 2000a]. The corewood region around the pith is of low basic density, as a consequence of thin cellular walls and relatively little latewood. In the outerwood, basic density is greater than in the corewood, and is relatively constant with radius. [Legg and

[5]Defined as a temperature of 273 K (0 °C) and a pressure of 1 atm [McNaught and Wilkinson 1997].

Bradley 2016] noted that the low basic density near the pith is offset to some degree by an increase in MC. This effect produces a more uniform green density from pith to sapwood.

Basic density values for New Zealand grown *Pinus radiata* range between 350-550 kg/m^3 [RPBC 2003]. Typical average values are between 400-420 kg/m^3. The basic density varies considerably with latitude. Wood grown at 35° S is generally greater than 475 kg/m^3, while wood produced at 45° S is generally less than 450 kg/m^3. Walker [2006c] explains that the green density of a living tree is not constant. The green density varies across the volume, varying largely between heartwood and sapwood.

Density has long been considered a key determinant of wood quality [Apiolaza 2009, Apiolaza et al. 2013, Chauhan et al. 2006a]. This is likely because density correlates strongly with stiffness. Gibson [2005] explains that the honeycomb-like structure of wood means that as density increases, cell-wall thickness increases. The result of this is that longitudinal stiffness increases linearly with density. For wood used in structural applications, high density does not offer an intrinsic advantage, as it must also support its own weight in addition to any external loads. For this reason, the ratio of stiffness-to-density, known as the *specific modulus*, is possibly a better measure of wood quality than density.

1.2 MEASURING WOOD STIFFNESS

A commonly used metric for wood quality is the MoE or *stiffness*. Several methods are available for determining wood stiffness in a standing tree or harvested stem. Static bending tests are typically used on cut timber. Acoustic resonance testing is typically used on harvested stems. It is desirable in some cases to measure stiffness while the tree is still standing. The time of flight (ToF) method can be used to measure the transit time of an acoustic wave on a standing tree.

The theory of acoustic stiffness tools is well established [Legg and Bradley 2016]. Under certain conditions[6], the relationship between the stiffness, stress-wave speed, and density is given by

$$E = c^2 \rho, \tag{1.6}$$

where E is the MoE (stiffness), c is the acoustic wave speed[7], and ρ is the density of the medium. Thus, if the density of the wood is known (or approximated), the wave-speed can be measured, and thus the stiffness calculated.

[6] That the wood is isotropic and lossless. This is a demonstrably false assumption, but is typically ignored for the purpose of simplification. This limits the effectiveness of the technique in determining the *absolute* stiffness. However, it is still useful for determining *relative* stiffness.

[7] At this point the stress wave speed is not well defined. The differences between various wave speeds are described in more detail in Chapter 2.

Several authors have provided reviews on acoustic measurement of wood stiffness [Beall 2002, Beall et al. 2013, Bucur 2006, Divos et al. 2005, Falk et al. 1990, Kawamoto and Williams 2002, Legg and Bradley 2016, Ouis 1999, Ross 1992, Ross and Pellerin 1994, Walker and Nakada 1999, Wessels et al. 2011]. These reviews focus on two non-destructive acoustic techniques which are commonly in use: the *resonance method*, and the *time of flight* method. These reviews show that static bending tests and resonance tests consistently yield similar stiffness values. They also report that the ToF method consistently measures a higher acoustic velocity than the resonance method, and thus a higher stiffness. The remainder of this section is an overview of these acoustic techniques and the systemic discrepancies between them. In order to measure the effectiveness of acoustic testing, static testing techniques are discussed in Section 1.2.1. The resonance method is then discussed in Section 1.2.2. The time of flight method is discussed in Section 1.2.3. Observations regarding the discrepancy between the ToF method and other methods are discussed in Section 1.2.4. Finally, approaches to resolving the discrepancy between these methods are explored in Section 1.2.5.

1.2.1 Static testing

Static testing is a class of techniques for directly measuring the stiffness and strength properties of wood specimens. It is conducted by applying a mechanical load to a specimen and recording the amount of deflection, or the deflection at which rupture occurs. This allows the MoE or the MoR of a harvested log, piece of timber, or clearwood specimen to be determined. This type of analysis is conducted for research purposes as well as wood grading.

In New Zealand, structural timber is commonly graded using one of two systems [Buchanan 2007]. *Visual grading* uses the size of knots (branches) and other features to sort timber into several strength grades [BSI 2017]. This method relies on a correlation between the wood's visual properties and its strength and stiffness. The labour intensive nature and tendency for operators to overestimate the quality means that visual grading is generally less favourable than mechanical methods [Kretschmann and Hernandez 2006, Wang et al. 2007a]. *Machine grading* directly measures the stiffness of timber by applying a load to it and measuring the timber's deflection. In New Zealand and Australia, machine graded timber is called machine stress-graded (MSG). MSG timber is sorted using a combination of mechanical and visual testing [Kretschmann and Hernandez 2006]. The mechanical testing is typically conducted using a three point bending test.

Bodig and Jayne [1982] explain how beam theory is applied to static bending of timber. In a three point bending-test, the ends of the piece of timber are fixed and a load is placed at the centre. Classical beam theory predicts that the MoE of a beam

under this type of load is equal to

$$E_f = \frac{fL^3}{4\Delta bh^3}, \tag{1.7}$$

where E_f is the beam's *flexural* MoE, f is the force of the applied load, L is the distance between the beam's supports, Δ is the vertical deflection under load, b is the breadth of the beam, and h is the height of the beam. E_f is sometimes called the *apparent modulus of elasticity* because the deflection is resisted by shear forces as well as the bending moment, though the effect of shear is not incorporated in (1.7) [Bodig and Jayne 1982]. Ideally, the flexural MoE would be identical to Young's modulus, however, in practice the two values can differ significantly, due to the addition of shear forces. For example, Hearmon [1948] found that for a series of Pine and Beech samples, the longitudinal modulus exceeded the flexural modulus by 5% to 8%. When performing flexural tests in practice, the load is sometimes applied at two separate locations on the beam [BSI 2011]. By altering the span of the applied load, the amount of shear versus tension and compression force can controlled. Without this feature, it may be unclear whether a piece of timber ruptured due to shear or longitudinal forces [Bodig and Jayne 1982].

Static testing can also be conducted by directly applying a longitudinal load in either compression or tension. Kretschmann and Hernandez [2006] explain that in general, longitudinal static tests are difficult to perform because wood has low shear strength in the direction of the grain; if the harness performing a strength test is not well aligned, a shear stress will result, which will likely yield before the longitudinal strength does. Bodig and Jayne [1982] explain that direct mechanical techniques are often used for research purposes, for example, to determine the average mechanical properties of a particular species. Of particular interest for structural applications is the stiffness and strength of a clearwood sample in tension along the grain. ASTM D143 describes a method for performing this type of test [ASTM 2014]. In this method, a sample is cut so that it may be placed between two clamps, with a *necked-down* critical section of wood in between. The critical section experiences the greatest strain when loaded, thus deflects the greatest amount, and is most often the location of rupture.

1.2.2 The resonance method

Stiffness can be determined acoustically by measuring the resonant frequency of an oscillating wood member. There are two types of resonance tests: *transverse resonance*, and *longitudinal resonance*. Transverse resonant vibrations have long been used for gauging wood stiffness of logs and timber [Jayne 1959, Marra et al. 1966, Pellerin 1965]. In this method, a wooden member is suspended at specific locations, known as *nodes*. A transverse vibration is excited in the member by striking it at an *antinode*, usually the middle of the member. A measurement device is used to record the frequency

at which an antinodal location oscillates vertically. Haines et al. [1996] explains that the frequency of oscillation can be modelled using the Timoshenko beam theory. The resulting MoE is given by

$$E = \frac{0.946\rho {f_{\text{res}}}^2 L^4}{D^2}, \tag{1.8}$$

where ρ is the wood's density, f_{res} is the induced resonant frequency, L is the length of the specimen, and D is the diameter of the specimen. A derivation of (1.8) is found in Timoshenko [1955]. The transverse resonance method is not as widely used as the longitudinal method, this is possibly due to the difficulty of suspending the sample when conducting a measurement.

It has been known since the 1950s that longitudinal resonance vibrations could be used to measure the MoE of wood [Bell et al. 1954, Bodig and Jayne 1982, Galligan and Courteau 1965, Pellerin and Galligan 1973, Porter et al. 1972]. The longitudinal resonance method is usually referred to simply as the *resonance method*. Though it was used in laboratories for some time, the method was first used for log grading applications by Japanese researchers [Aratake et al. 1992, Arima et al. 1990, Fujisawa et al. 1994]. The resonance method is a technique used for measuring the stiffness of harvested logs (and sometimes cut timber). The method uses a specialised device called a *resonance tester*. This device contains a single transducer, which is placed against one end of a log. The operator strikes the end of the log with a hammer, causing a stress wave to propagate longitudinally. The wave is reflected by the end faces of the log, causing a *standing wave* oscillation. The stress wave predominates at frequencies given by

$$f_{\text{res}} = \frac{n c_{\text{res}}}{2L}, \tag{1.9}$$

where n is a positive integer, called the *harmonic* number; c_{res} is the resonant wave's velocity in the log; and L is the length of the log. Each harmonic number corresponds to a *resonant frequency* of the system. Each harmonic is separated in frequency by an integer multiple of the fundamental. The device records the signal at the transducer and then performs a fast Fourier Transform (FFT) analysis to find the resonant harmonics. (1.9) can then be used to determine the longitudinal acoustic velocity of the nth harmonic. The velocity can then be used to estimate the MoE using (1.6), the result of combining these equations is

$$E = 4\rho \left(\frac{f_{\text{res}} L}{n} \right)^2. \tag{1.10}$$

An illustration of how the measurement is conducted, and a plot of the variation in magnitude along the length of the log for the first three harmonics, is shown in Figure 1.3. Note that the amplitude is zero at the nodes, such as in the middle of the member; and maximal at the antinodes, such as at the member's ends.

Lindström et al. [2002] explained that using a hammer hit for excitation generates

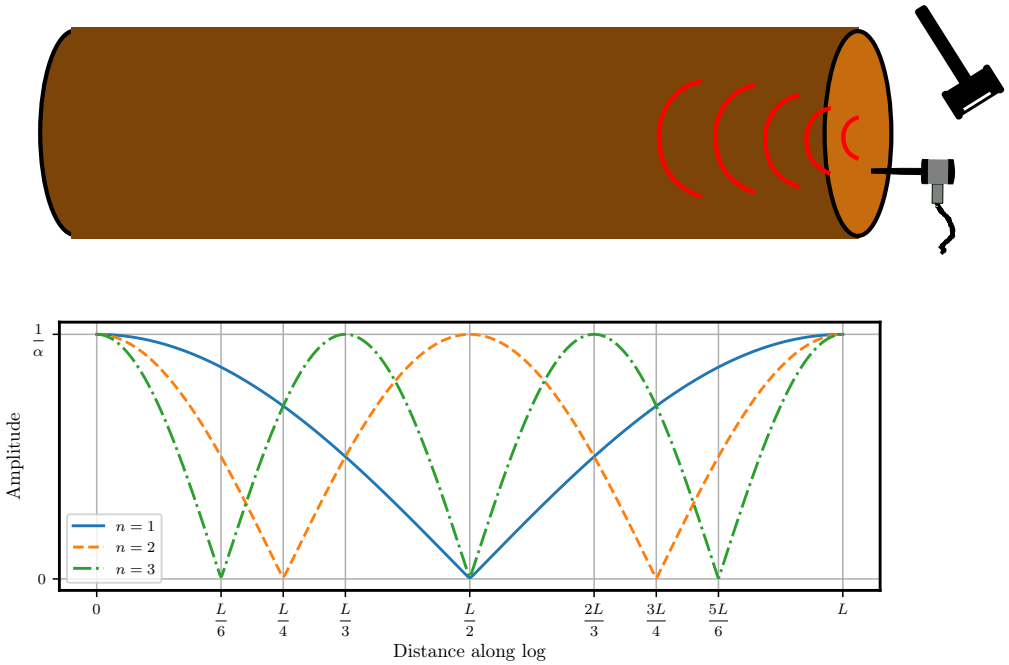

Figure 1.3 In the resonance method, striking the end of the log induces a standing wave. A receiving transducer is held in contact with one end of the log. The magnitude of the stress wave varies along the length of the log.

frequencies in the low kHz range. They claimed that this is only suitable for samples longer than about 200 mm. For this reason, to test small samples they employed a *swept resonance* excitation technique. This technique uses an amplified loudspeaker on one end of the sample, and a receiving transducer on the other end. The frequency of the loudspeaker is swept over a range of frequencies (typically 10 harmonics), and the spectrum of the received signal is analysed to find the resonant harmonics. Harris et al. [2002] described the WoodSpec system, which uses the swept resonance technique for measuring the velocity of small samples. They explain that the sample is stimulated using "a predefined band of frequencies in a continuous or semi-continuous fashion over an excitation period."

Few papers have focused specifically on the implementation of the resonance method, though details may be gleaned from papers which performed experiments using the method. Harris and Andrews [1999] noted that implementations of the method generally use the second harmonic to determine the MoE, though the reason for this choice is unclear. Carter et al. [2007] stated that the Director HM200 also uses the second harmonic. Several authors have noted that the resonance peaks may not be integer-multiple harmonics of each other [Andrews 2000]. Chauhan and Walker [2006] observed that the first and second harmonics can differ in speed by as much as 11%. It is unclear which harmonic gives the closest estimate of the static stiffness. Harris et al.

[2002] showed using a time-frequency analysis that the initial portion of the recorded waveform contains comparatively more high-frequency content. This was explained as a result of the "hit function" of the hammer excitation, which decays away after some time. This effect tends to bias the lower harmonics to slightly higher frequencies. They showed that by dividing the waveform into time windows, a more consistent frequency reading is obtained by discarding the first window and keeping subsequent windows. The WoodSpec system, described by Harris et al. [2002], circumvents this problem by continuously or semi-continuously exciting the sample. Ross et al. [1997] used a variant of the resonance method. Instead of performing an FFT analysis, they measured the time between peaks in the time-domain. This method was first described by Ross et al. [1994], and was also used by Wang et al. [2004b]. This method is likely less exact, as higher frequency harmonics can overlay the fundamental, which makes it more difficult to identify the exact location of the fundamental.

Several studies have compared the MoE, as calculated using (1.10), to that measured by static methods. Wang et al. [2001a] conducted resonance and static bending tests on a total of 159 *Pinus resinosa* (red pine) and *Pinus banksiana* (jack pine) logs. They found that both methods determined similar values of MoE for both species, with r^2 values 0.95 and 0.85 for red pine and jack pine, respectively. Harris et al. [2002] measured resonance velocity on 44 small internodal bolts cut from clonal stems aged 2 years. They found a close match between the static MoE of the samples and the resonance-estimated MoE ($E_{\text{static}} = 1.02\ E_{\text{res}}$), with $r^2 = 0.93$. Lindström et al. [2002] conducted resonance and static bending tests on seven *Pinus radiata* clones of age four years. Regressions calculated between the methods showed a close correspondence using both a microphone based resonance ($E_{\text{static}} = 1.04\ E_{\text{res}}$), and a swept-resonance based approach ($E_{\text{static}} = 1.07\ E_{\text{res}}$). Evans and Kibblewhite [2002] measured the resonance velocity on 50 small *Pinus radiata* samples of age 25 years. These were compared against an X-ray based estimate of the static stiffness (for details on this method, see Evans et al. [2000a] and Evans and Ilic [2001]). They found that the two methods reported similar values for the MoE of the samples, with $r^2 = 0.88$. Lindström et al. [2004] conducted resonance and static compression tests on 22 *Pinus radiata* clones of age three years. Measuring at 12% MC, they found a close relationship between the two methods ($E_{\text{static}} = 1.02\ E_{\text{res}}$), with $r^2 = 0.93$. Ilic [2001] measured the resonance velocity of 104 *Eucalyptus delegatensis* samples, and then compared the resonance MoE to that determined using a static technique. A strong correlation between the two methods was found ($r^2 = 0.95$). Hodousek et al. [2017] conducted resonance and static tests on a total of 110 samples of *Cupressus lusitanica* and *Populus canadensis*. They found strong correlations, with values of $r^2 = 0.87$, and $r^2 = 0.81$, respectively.

Several authors have suggested that the resonance method's close match with static tests is due to the method providing a weighted average of the log's cross sectional stiffness [Carter et al. 2007, Chauhan et al. 2005, Grabianowski et al. 2006, Harris

et al. 2002]. Chauhan et al. [2005] measured the MoE of layered plywood which was constructed using several different layering configurations. They predicted the overall MoE of each type of plywood using an area-weighted sum of each layer's effective MoE. They found that for most plywood configurations the difference between the resonance-predicted MoE and the weighted-average predicted MoE was significantly less than 5%. Carter et al. [2007] measured the resonance velocity in six *Pinus radiata* logs aged 24 years, followed by the resonance velocity in boards sawn from the logs. They found that while there was significant variation amongst the board velocity, the average of all boards in a log was similar to the log's overall velocity. These studies appear to confirm the hypothesis that the resonance method provides an area-weighted average measurement of a log's MoE.

1.2.3 Time of flight acoustics

The *time of flight* method (ToF), also known as the *stress wave method* [Kang and Booker 2002], can also be used to acoustically estimate the stiffness of a standing tree. In this method, the time is measured for a stress-wave to propagate a fixed distance, Δz, along a tree or cut piece of wood. Typically, two transducers are attached to the tree, separated by Δz in the tree's longitudinal direction. A stress wave is generated by striking the lower transducer. This method is described by [Wang et al. 2000]. By measuring the ToF, τ, taken for the wave to propagate to the upper transducer, the wave's speed can be calculated as

$$c = \frac{\Delta z}{\tau}. \tag{1.11}$$

The wood's stiffness can then be estimated using (1.6) [Bucur 2006]. The density, ρ, is usually not known, but in practice the density of green radiata pine wood is close to that of water, 1000 kg/m^3 [Chauhan et al. 2006a].

There are two variations of the ToF method with respect to transducer placement. The first uses two transducers oriented with the tips inward, facing each other. The lower transducer is struck with a hammer, initiating the measurement. The upper transducer is sampled until a signal is received. The time taken for propagation between the two devices is then calculated. This method is described in the patents by Huang [2005] and Wang et al. [2008]. The second variant uses two receiving transducers, with the wave being excited by striking a metal spike some distance below the transducers [Toulmin and Raymond 2007, Woods 2006]. This variant is depicted in in Figure 1.4. Both transducers are concurrently sampled; the propagation time is the difference between the stress-wave arrival times of the two transducers. An advantage of this method is that both transducers are receiving the same wave but at separate locations in space, this allows the wood's effect on the wave to be studied. In addition, by not striking the transducer directly, a high voltage spike is not generated, which can saturate the receiving electronics. In either variant, a downside of using a hammer to generate

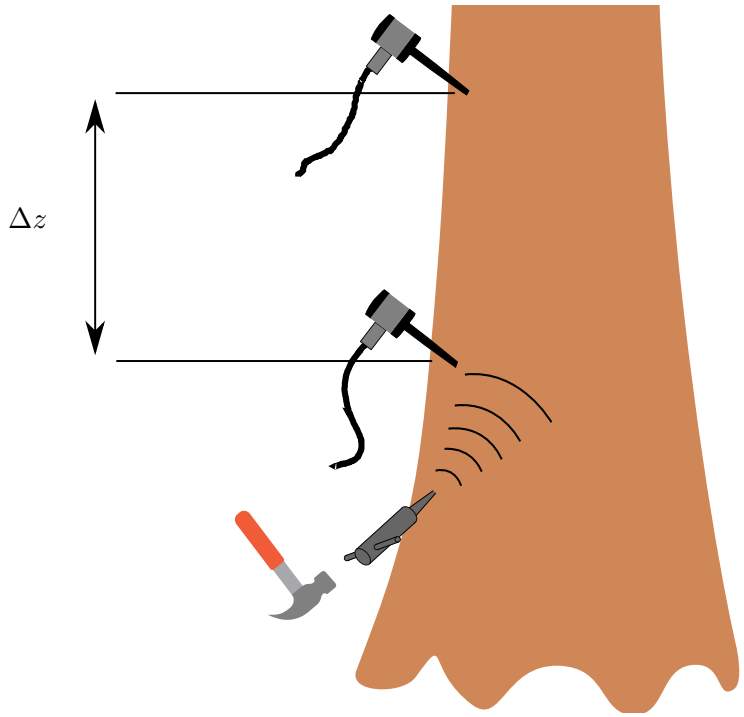

Figure 1.4 A time of flight system measures the stress-wave speed by measuring the propagation time of a wave between two transducers. In this variant, the stress-wave is excited by striking a metal spike inserted in the tree slightly below the transducers.

the excitation is that the signal amplitude is not consistent between hits [Harris and Andrews 1999].

The transducers used for conducting stress-wave measurements are usually spike-shaped to facilitate insertion in the tree. The devices are generally most responsive along the axis of the spike, as is the case for the Fakopp SD-02 transducer [Fakopp Bt 2000]. The angle of insertion in the tree is usually about 45° [Legg and Bradley 2016, Wang et al. 2000]. It was explained by Huang [2005] that this angle is required to ensure that the probe is inserted past the bark and cambium into the xylem wood. The non-zero angle between the tree's axis and the transducer reduces the amplitude of the received signal. A model for the total received amplitude is,

$$A = A_L \cos\theta + A_R \sin\theta, \tag{1.12}$$

where A is the total received signal's amplitude, A_L is the amplitude of the longitudinal component of the wave, A_R is the amplitude of the radial component of the wave, and θ is the probe's angle relative to the tree. The longitudinal wave is the fastest and most dominant component, due to high along-grain stiffness. Therefore, increasing the probe angle tends to decrease the received signal's amplitude.

Instead of using a hammer to excite the stress wave, an electrically pulsed transducer may be used [Hayes and Pink 2012, Hayes and Chen 2003, Sandoz and Benoit

2007, Sandoz et al. 2000, Sandoz 1991]. This has the advantage that each wave is relatively consistent in amplitude. However, it is difficult to produce a large signal, as the attenuation in green wood is high [Bucur 2006]. Electrically pulsed transducers allows measurements to be conducted in the ultrasonic frequency range. These measurements are usually conducted on small, dry, clearwood samples, as this avoids the high attenuation caused by greenwood [Bucur and Feeney 1992, Salmi et al. 2013].

ToF measurements have been used to measure the directional variation in wood stiffness. Vázquez et al. [2015] cut *Castanea sativa* wood into a sample shaped as a 26-sided polyhedron. The ToF was measured between adjacent faces using an Olympus NDT device. These measurements were then used to construct an orthotropic stiffness matrix (see Chapter 2 for the definition of the stiffness matrix) for the wood being tested. Similar methods have also been used by Bucur [1983], Ozyhar et al. [2013], and Yaitskova and van de Kuilen [2014].

ToF techniques have also been applied to seedlings [Divos 2010, Emms et al. 2012, 2013]. A hammer-hit cannot be used on such a small wood sample, so the wave must be excited electrically or mechanically using a very small striker. Emms et al. [2012] employed a plastic pinhead as a striker, and two miniaturised transducers attached to the seedling. Emms et al. [2013] used the same technique to show that the ToF velocity measured in a control group of *Pinus radiata* seedlings was significantly higher than in a group of artificially stressed seedlings.

The ToF technique has also been applied to grade engineered products such as laminated veneer lumber (LVL) and wood panels [Han et al. 2006, Pellerin and Ross 1991, Ross 1984]. These techniques are fundamentally the same as those applied to raw wood.

1.2.4 Overestimation of stiffness by the time of flight method

It has been reported that the stiffness calculated using the ToF method using (1.6) is an overestimation compared to other methods. A number of studies have compared ToF measurements taken on standing trees to resonance measurements taken once the trees were felled [Chauhan and Walker 2006, Chiu et al. 2013, Gonçalves et al. 2011, Grabianowski et al. 2006, Hsu 2003, Lasserre et al. 2007, Llana et al. 2016, Mora et al. 2009, Ross and Wang 2005, Wang 2013, Yin et al. 2010]. These studies consistently find that ToF measurements on standing trees measure a higher velocity than resonance measurements on the felled logs. Hsu [2003] performed ToF measurements on 120 *Pinus radiata* clones at age 6 years and found that ToF on the standing trees was faster than resonance on the logs by 15% on average. Lasserre et al. [2007] found ToF velocity measured on standing *Pinus radiata* trees to be faster than resonance measured on the felled logs by 22% on average (with a range of 16-31%). Mora et al. [2009] found ToF velocity from standing *Pinus taeda* trees to be 32% greater on average than

resonance velocity on the felled stems. Yin et al. [2010] found ToF velocity from standing *Cunninghamia lanceolata* (Chinese fir) trees were 18.4% greater than resonance. They also found that ToF using an ultrasonic technique was 26.7% greater than resonance on average. Lindström et al. [2009] measured the ToF velocity on 192 *Pinus sylvestris* trees of age 90–150 years, followed by resonance velocity on the cut logs. They found that the ToF method predicted a MoE which was on average 41% greater than that predicted by the resonance method. Salmi et al. [2013] found that ultrasonic ToF measurements on specimens cut from 102 *Picea abies* trees estimated a MoE which was greater than statically measured MoE by 29% at 500 kHz, 60% at 4 MHz, and 50% at 8 MHz.

The overestimation has been reported to occur even when the ToF measurement was conducted from end to end of the felled log [Dickson et al. 2004, Hsu 2003]. Grabianowski et al. [2006] measured the ToF and resonance velocity on *Pinus radiata* logs of ages 8, 16, and 26. They found that ToF measured an 11% greater velocity on average than resonance. Chiu et al. [2013] performed a similar study, where they measured the ToF on a 32 year old *Calocedrus formosana* (Taiwan incense cedar) tree, and then performed ToF and resonance measurements on the sawn timber. They concluded that the lower outerwood on the tree, with a higher Diameter at breast height (DBH), has greater resonance velocity. These experiments were performed to determine whether the discrepancy between the methods was due to some effect which only occurs in a standing tree, such as extra internal stresses. These results suggest that this is not the case.

A number of studies have compared the ToF MoE determined using (1.6), taken on a standing tree to static tests performed on the green harvested wood. Wang et al. [2000] and Wang et al. [2001b] measured the ToF velocity on 168 trees of species *Picea sitchensis* (Sitka spruce) and *Tsuga heterophylla* (western hemlock), followed by static MoE analysis on the clear wood specimens cut from the trees. They found that the MoE predicted by the ToF method was significantly higher than that directly measured on the samples. Other authors have performed similar studies, consistently finding that the MoE predicted by the ToF method is higher than the directly measured static MoE. Even though the methods are not directly comparable, the authors have investigated the statistical relationship between ToF and static testing. Varying coefficients of determination between the two methods have been reported: $r^2 = 0.73$ [Halabe et al. 1997], $r^2 = 0.79$ [Wang and Ko 1998], $r^2 = 0.66$ [Wang et al. 2000], $r^2 = 0.46$ [Tsehaye et al. 2000a]. These numbers suggest that there is a reasonable correlation between the ToF MoE and the static MoE. This correlation has allowed the ToF method to successfully rank the wood harvested from a stand from highest to lowest in stiffness [Huang 2000, Tsehaye et al. 2000a, Wang et al. 2000].

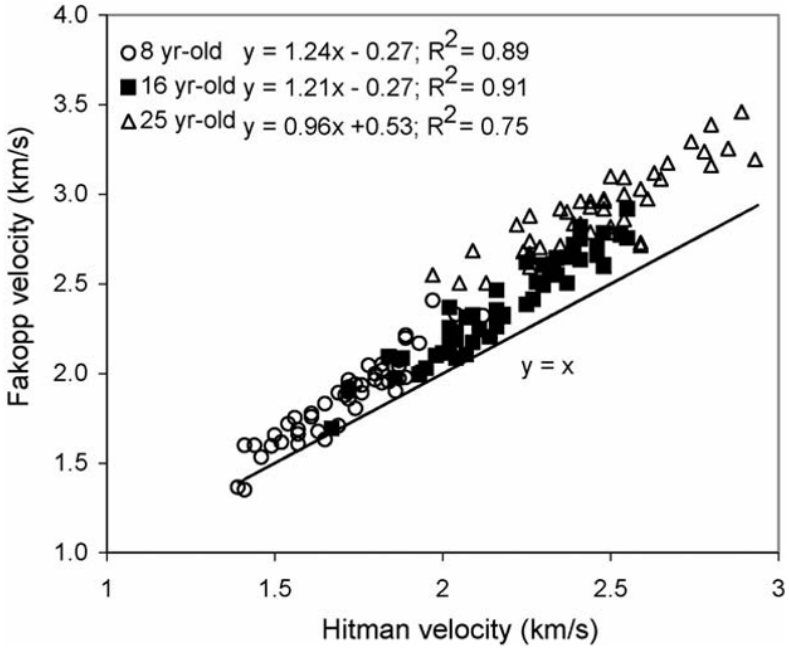

Figure 1.5 Comparison between ToF (Fakopp) and resonance (Hitman) velocities for stands of *Pinus radiata* trees aged 8, 16, and 25 years [Chauhan and Walker 2006].

1.2.5 Approaches to resolving errors in the time of flight method

The ToF method is currently the only method for rapidly obtaining a measure of a standing tree's stiffness. This makes it a valuable tool for breeding programs. For example, early selection of the best wood based on stiffness has been suggested [Apiolaza 2009, Huang et al. 2003, Matheson et al. 2008]. However, a problem with the ToF method is that it consistently overestimates the MoE, as shown in Section 1.2.4. This overestimation is demonstrated in Figure 1.5, which shows the result of one study which compared ToF and resonance measurements [Chauhan and Walker 2006].

Some authors have modelled the discrepancy between the two methods as a ratio, known as the *velocity ratio*,

$$k_{\mathrm{r}} = \frac{\widehat{c_{\mathrm{tof}}}}{\widehat{c_{\mathrm{res}}}}, \tag{1.13}$$

where $\widehat{c_{\mathrm{tof}}}$ is the mean ToF velocity for a particular experiment and $\widehat{c_{\mathrm{res}}}$ is the mean resonance velocity measured on the same wood samples. Wang [2013] provided a review of studies which quantified the velocity ratio for several species. The studies that were cited found k_{r} values ranging from 1.09 to 1.36. A number of authors have attempted to resolve the discrepancy between methods using linear regression models. Wang et al. [2007a] provided an overview of this type of model, as applied to non-destructive testing in forestry applications. The basic form of the model, with two parameters, is

$$c_{\mathrm{tof}} = Ac_{\mathrm{res}} + B, \tag{1.14}$$

where A and B are the regression parameters, which are fitted to the data using a numerical method such as least-squares. Ross and Wang [2005] applied this model to a number of different species and provided values for A, B, and the resultant coefficient of determination, r^2. Baar et al. [2012] applied this model to the heartwood of 5 different tropical hardwoods, and found a strong correlation ($r^2 = 0.81$) for this type of model.

Other authors have attempted to incorporate the dimensions of the tree and stem into the regression model. Wang et al. [2004a] developed an empirical model with a dependency on stem diameter. Their model is given by

$$E' = A \left({c_{\text{tof}}}^2 \rho \right)^B D^C, \tag{1.15}$$

where E' is the adjusted MoE, for comparison to the resonance velocity; c_{tof} is the ToF velocity; D is the log diameter; and A, B, and C, are the fitted model parameters, which are determined numerically. They found that (1.15) produced a closer fit to the resonance method's estimate of the MoE, when compared to the simpler model of (1.14). This model was also applied to data presented by Wang et al. [2007b].

Researchers have suggested several explanations why the ToF method overestimates the stiffness when compared to other methods. It is understood that wood stiffness increases radially outwards from pith to bark[8] [Chauhan et al. 2006a]. Authors hypothesise that static and resonance methods provide an average measurement of the stiffness throughout the sample [Carter et al. 2007]. In contrast, the ToF method may only measure a wave in the high-stiffness outerwood. Chauhan and Walker [2006], and Lasserre et al. [2007] suggested that the discrepancy between methods is due to the ToF stress wave "flight path" transiting the outerwood.

Studies have quantified the discrepancy between corewood and outerwood stiffness by measuring both ToF and resonance on stems, and also boards cut from the stems [Baar et al. 2012, Grabianowski et al. 2006]. This type of experiment seeks to homogenise the quality of the wood on which an experiment is performed by cutting boards at fixed radial distances from the pith. Grabianowski et al. [2006] hypothesised that the over estimation of the ToF was due to the waves propagating through the stiffer outerwood, while the resonance method measures a weighted cross section throughout the log. To test this, they measured the ToF and resonance of several *Pinus radiata* logs of ages 8, 16, and 26, and then sawed them into boards, which were also tested for ToF and resonance. Some of the results of this study are shown in Table 1.1. The results show that the mean ToF velocity of the outerwood boards was close to the ToF of the log, while the ToF of the corewood was significantly lower. They also show that the ToF method measured a significantly greater velocity than the resonance method on the complete logs. These finding support the idea that the ToF method predominantly measures the propagation through the outerwood.

[8] See Section 1.3 for a discussion of the factors which influence stiffness.

Table 1.1 Average velocity of 43 stems, using both the time-of-flight and resonance methods. The stems were cut into outerwood and corewood boards, from which the velocity was measured [Grabianowski et al. 2006]. ToF was measured using Fakopp 2D [Fakopp Bt 2001]; resonance was measured using WoodSpec [Harris et al. 2002].

	ToF (m/s)		Resonance (m/s)	
	Mean	Range	Mean	Range
Logs	2,466	1,739–2,929	2,202	1,655–2,603
Green outerwood boards	2,505	1,852–2,966	2,099	1,665–2,600
Green corewood boards	2,223	1,598–2,685	1,931	1,445–2,360

However, the results shown in Table 1.1 also leave some questions unanswered. The mean ToF velocity in the outerwood boards (2505 m/s) is significantly greater than the resonance velocity on the same boards (2099 m/s). A similar discrepancy was also observed in the corewood boards. It is possible that there is some additional effect in either of the methods causing this discrepancy, which appears to be present even when the wood samples have been homogenised.

Andrews [2002] suggested that the discrepancy between the methods is related to stem diameter. This type of wave phenomenon was referred to by Kolsky [1963] as *bar waves*. The theory predicts that a cylindrical bar, such as a tree stem, acts like a waveguide, causing the majority of energy to propagate at the speed given by (1.6), provided that the wavelength is significantly longer than the diameter of the log. Andrews [2002] supposed that measurements made using the resonance method propagate at this bar speed, provided that the wavelength is sufficiently long. Kolsky [1963] suggested that a small portion of energy propagates at the *dilatational* speed, given by $c = \sqrt{C_{11}/\rho}$ (see Section 2.7.1 for the definition of the dilatational speed). This speed is always greater than the bar wave speed. Andrews [2002] suggested that the ToF method measures the dilatational speed. This would explain the consistently greater speed which is measured. An overview of this theory, as applied to wood testing is described by Wang et al. [2005] and Wang et al. [2007b] (see Appendix B for a description of the theory). Mora et al. [2009] used the bar wave theory to estimate Poisson's ratio in *Pinus radiata* trees. They found that the bar wave theory produced an effective correction factor for the discrepancy between ToF and resonance methods. The correction factor reduced the mean discrepancy from 32% to 0.02%, with $r^2 = 0.98$. Though it is unclear whether this model is generalisable to other species or environmental conditions.

Several authors have evaluated the effect of log diameter on wave speed. Wang et al. [2004a] measured the MoE both statically and using the ToF method for 201 small logs from four different species. They found that for larger diameter samples, the discrepancy between static and ToF methods tends to increase. Other authors have also evaluated the effect of diameter on resonance. Chauhan and Walker [2006] noted that

the difference between ToF and resonance was greatest in older, larger diameter trees. Andrews [2002] measured the ToF and resonance on a number of logs and cylindrical metal samples. He argued that the speed discrepancy between methods was dependent on the ratio of length to diameter of the sample. However, some studies have not found any systemic difference between ToF and resonance with respect to diameter [Lasserre et al. 2007, Mora et al. 2009]. Gonçalves et al. [2011] found that the dependence of velocity on diameter was only observed in some species. Zhang [1995] observed that within a stand the bigger trees generally produce a wood of lower density and stiffness. Lasserre et al. [2005] observed the same trend by influencing the DBH by controlling planting density. This effect is likely due to a reduction in density as the DBH is increased, i.e., the tree contains the same volume of cell wall material, but cell walls are thinner and cell lumens are larger, resulting in a larger stem diameter.

Some authors have observed that the presence of bark on a tree can cause the resonance velocity to be significantly lower than the same tree when de-barked, [Chauhan and Walker 2006, Grabianowski et al. 2006, Lasserre et al. 2007]. Lasserre et al. [2007] found that removing bark from *Pinus radiata* caused the resonance velocity to increase by 8.3% on average. The increase was consistently observed amongst sampled stems. Hsu [2003] sampled bolts cut from different heights up a *Pinus radiata* tree and found that the debarked velocity on the bottom bolt was 7.2% higher. The debarked velocity at the top of the tree increased by 22.6%. These are surprising results because bark's low density and stiffness would be expected to prevent a large amount of acoustic energy from being coupled into it. These results seem to support the idea that the resonance method provides an average of the cross-sectional stiffness throughout the stem. The effect of bark on ToF measurements has also been examined. Grabianowski et al. [2006] found that debarking *Pinus radiata* did not have a significant effect on the ToF measurements. They note that this finding supports the hypothesis that the ToF stress wave propagates primarily through the outerwood. Their finding suggests that the ToF velocity is not an average of the stem's cross-sectional stiffness.

Some authors have found that the presence of both branches and knots reduces the measured velocity. Lasserre et al. [2007] found that branch removal increased resonance velocity by 5.4% on average and up to 24% in low MoE samples, but this increase did not always occur. This finding is consistent with the cross-sectional average theory of the resonance method, as the branches increase the overall cross-section, but do not contribute significantly to the stiffness. Hsu [2003] measured the ToF velocity between clearwood sections (internodes) and compared that to ToF measurements taken across an entire stem. It was found that an area containing knots decreases the acoustic velocity by approximately 5%. These findings are to be expected, as the direct path through a knot takes the stress wave across the grain.

Attempts have been made to correct for the discrepancy between ToF and resonance by placing the two probes on opposite sides of the tree, thus measuring across the

grain [Dickson et al. 2003, 2004, Mahon 2007, Mahon et al. 2009, Matheson et al. 2002]. These studies measured a slower speed for the across-grain velocity than the direct-path ToF velocity. A problem with this approach is that it underestimates the MoE. This is likely because the authors did not incorporate the lower across-grain stiffness and lower heartwood stiffness into their analyses.

Some authors have observed that the frequency of ToF stimulation has an effect on the measured velocity. Haines et al. [1996] observed that dynamic bending tests overestimate the MoE of boards compared to static bending. They hypothesised that this was because the wood was acting *viscoelastically*. This causes the effective stiffness to increase with the frequency of stimulation. Ouis [2002] explained that the viscoelasticity of wood leads to an acoustic wave speed which is frequency dependent. This is known as *dispersion*. O'Donnell et al. [1980] explained that a Kramers-Kronig relationship may be used to show that a medium which exhibits attenuation is also dispersive. The dispersive and attenuative qualities of generalised solids are explored in more detail by Kolsky [1963]. Divos et al. [2005] analysed the speeds of resonant modes in a spruce specimen. They found that the speed of the modes tends to increase with frequency. Bucur and Feeney [1992] measured the attenuation and stress wave velocity in horse chestnut wood using a continuous transmission technique. They found that the longitudinal velocity increased significantly with frequency. Salmi et al. [2013] measured the dynamic MoE in Norway spruce samples at several ultrasonic frequencies. They found a general trend of increasing MoE as frequency increases. Chiu et al. [2013] measured acousic velocity in Taiwan incense cedar using both ultrasonic ToF and hammer-excited ToF methods. They found that in general the ultrasonic velocity was greater than the lower-frequency hammer-hit excited velocity. These results are consistent with the behaviour of viscoelastic models of solids, which predict that MoE and acoustic velocity increase as frequency increases.

1.3 FACTORS WHICH AFFECT STIFFNESS

Gibson [2005] explains that the structure of wood may be modelled, to a first approximation, as a honeycomb. Wood, like a honeycomb, is stiffest in the direction of the alignment of the cells. The honeycomb model suggests that the longitudinal stiffness varies linearly with density. While the stiffness across the grain varies with the cube of the density. It should be noted that the density of dry cell-wall material is approximately 1500 kg/m^3 across all species [Gibson 2005, Walker 2006c]. The MoE and MoR of cell-wall material in the direction of the microfibrils is approximately 35 GPa and 350 MPa, respectively [Cave 1968, 1969]. The density and stiffness of the material which constitutes the cell wall is relatively uniform. The density and stiffness of the resultant honeycomb structure, however, is largely determined by the cell wall thickness and the alignment of the cell wall fibres with the cell's axis (MFA).

Silvicultural practices are known to affect the stiffness of wood. The initial spacing of seedlings appears to influence stiffness. Lasserre et al. [2009] found that close planting of *Pinus radiata* seedlings (2500 stems/ha vs. 833 stems/ha) led to an increase in the resonance MoE of 81 %. Lasserre et al. [2004] found that the effect of seedling planting density (at the same stocking levels as above) was significantly greater than the effect due to clonal variations. Lasserre et al. [2008] compared the effect of seedling spacing across two different sites. They found that the effect of stocking density on MoE was significantly greater than the effect of site variation between clones. Carson et al. [2014] assessed the mid-rotation performance of *Pinus radiata* trees subjected to variation in stocking density and pruning in several sites across New Zealand. They found that: "increasing stand density is consistently associated with stiffer and denser outerwood." Lasserre et al. [2009] found that increasing the planting density of seedlings had other effects in addition to the expected increase in MoE. They observed a significantly reduced MFA, an increase in tracheid length, increase in latewood percentage and cell wall thickness, a decrease in growth-ring width and overall diameter. Density and fibre width were not significantly affected.

Other authors provided dissenting opinions on the effect of stocking density. Grabianowski et al. [2004] evaluated the effect of the variation in acoustic velocity of two stands of different stocking density (625 stems/ha vs. 100 stems/ha) of 27 year-old *Pinus radiata*. They found no significant difference between the two. They also assessed two narrow contiguous strips planted perpendicular to the prevailing NW wind, with one strip upwind, and one downwind of a larger stand of trees providing shelter. They found that the downwind (sheltered) trees had a significantly higher mean stiffness.

1.3.1 Microfibril angle

One of the strongest determinants of wood stiffness is the microfibril angle [Barnett and Bonham 2004, Chauhan et al. 2006a, Evans and Ilic 2001]. The MFA is the mean angle between the tracheid cell axis and the orientation of the cellulose microfibrils in the S_2 layer of the cell wall. Cave [1968] showed that the cellulose microfibrils in the cell wall are highly anisotropic. This result suggests that the MFA is the predominant factor in the anisotropic stiffness of the cell wall. His work showed that the longitudinal and transverse Young's moduli of the cell wall are approximately 35 and 10 GPa, respectively. Reiterer et al. [1999] strengthened this result by showing that the relationship between stiffness and MFA also applies to larger groups of fibres. It has also been observed [Cave 1969] that in order to maximise wood stiffness in the longitudinal direction, the MFA should be minimised.

Barnett and Bonham [2004] explained that the MFA enables a tree to alter its effective stiffness. The large MFA in juvenile wood allows a young tree to flex when required, i.e., allows a larger strain before failing. This is necessary, for example, to

prevent the tree breaking in a strong wind. Mature softwood trees also have the ability to produce higher MFA regions known as *compression wood*. These regions allow a tree to exhibit tension or compression on one side, which allows the stem to bend if required.

MFA is typically measured using X-ray diffractometry [Cave 1997, Chauhan et al. 2006a, Stuart and Evans 1995]. Originally this was conducted using photographic film, which was very slow to process. More recently, CCD-devices have rapidly sped up the process. Hayes and Pink [2012] demonstrated the feasibility of measuring the MFA of wood samples acoustically. They built a machine for measuring the ToF velocity of increment cores in a range of orientations. By applying a mechanical model of plant cell walls [Cave 1968] to measurements from the machine, the MFA of the core sample was estimated. Mason et al. [2017] measured the ToF velocity of *Pinus radiata* discs using a robotic scanning device. The MFA of the discs were then tested using X-ray diffractometry. The found a strong negative correlation between MFA and ToF velocity ($r < -0.84$).

1.3.2 Spiral grain

The tracheid cells which form the majority of xylem tissue in softwoods are, in most wood, not aligned with the axis of the tree stem. The angle formed between the tracheids and the stem is termed the *grain angle*. Due to the interlocking structure of tracheid cells, nearby tracheids have approximately constant GA, which forms a visible spiral in the grain around the stem. For this reason, this effect is often referred to as *spiral grain*. Spiral grain can be observed visually as a twisting in the grain of the tissue up the stem. This reduces the stiffness of the resulting timber and can lead to warping as the timber dries [Buchanan 2007]. Spiral grain can be visually inspected in timber but is more difficult to see in live trees because the grain angle typically changes as the tree grows outwards.

1.3.3 Reaction wood

Compression wood occurs in regions where a softwood stem experiences an excess of compressional force. It typically occurs on the lower side of a leaning stem, but can also be a result of asymmetrical branch growth or environmental stress such as wind. In a cut stem, compression wood is identified as a dull-coloured region of growth, where growth rings are accentuated, and there is less contrast between earlywood and latewood [Kollmann and Côté 1968]. In regions of compression wood the length of tracheid cells expand longitudinally, and cell walls thicken. This acts to correct stem lean [Chauhan et al. 2006b]. Compression wood is undesirable in timber as it has a high MFA, increased density, and lower stiffness and strength, when compared to normal wood [Butterfield 2006]. It also exhibits larger longitudinal shrinkage than regular wood when dried.

A different type of growth, known as *tension wood*, occurs in hardwoods. This eccentric growth occurs on the upper side of a leaning stem, where the hardwood fibres contract longitudinally to correct the lean. Tension wood typically has a higher stiffness and strength than normal wood, with a lower MFA and greater cellulose content [Butterfield 2006]. Collectively, compression and tension wood are known as *reaction wood*.

1.3.4 Moisture content

As described in Section 1.1.3, water is absorbed in wood in both the cell wall and the cell lumen. The MC at which the cell wall becomes saturated is known as the fibre saturation point. Mechanical properties tend to decline as water is absorbed up until fibre saturation [Bodig and Jayne 1982, Kretschmann 2010]. At MC above fibre saturation, water is absorbed into the cell lumen, and the mechanical properties are relatively constant.

Bodig and Jayne [1982] suggest that for MC values below fibre saturation, wood strength decreases exponentially as MC increases,

$$\sigma_{\mathrm{u}} = Ae^{-BM}, \tag{1.16}$$

where σ_{u} is the wood strength, M is the moisture content, and A, B are constants fitted to the model. Bodig and Jayne [1982] also suggest that this model will apply to other mechanical properties (such as stiffness).

Kretschmann [2010] suggested a slightly different model

$$P = P_{12\%}\left(\frac{P_{12\%}}{P_{\mathrm{green}}}\right)^{\left(\frac{12-M}{M_{\mathrm{p}}-12}\right)}, \tag{1.17}$$

where P is an arbitrary mechanical property, $P_{12\%}$ is the value of the property at 12% MC, P_{green} is the value of the property when the wood is green, M is the moisture content, and M_{p} is the intersection moisure content[9]. Kretschmann [2010] states that M_{p} is slightly less than the fibre saturation point; he provides values of M_{p} for several species. Kretschmann [2010] provides data suggesting that (1.17) is an appropriate model for strength and stiffness properties in tension, compression, and bending; both parallel and perpendicular to the grain.

Reducing MC tends to increase stiffness and decrease density. Therefore, according to (1.6), as wood is dried, acoustic velocity should undergo a significant increase. Several authors have found that MC correlates negatively with ToF velocity [Hasegawa et al. 2011, Llana et al. 2018, Mishiro 1995, Sakai et al. 1990, Sandoz 1993]. Carter et al.

[9]Defined by Kretschmann [2010] as the point at which mechanical properties begin to increase when wood is dried from green.

[2007] found that air dry *Pinus radiata* wood had a 6% higher dynamic MoE than green wood. Based on these studies, it is not clear whether the observed increase in acoustic velocity with MC is reflective of the models described by (1.16) and (1.17).

1.3.5 Temperature

Kretschmann [2010] explains that mechanical properties of wood tend to decrease linearly with increasing temperature, provided that the temperature does not exceed approximately 150 °C. He describes this effect as a *reversible* temperature effect, i.e., if the temperature is returned to its previous value, the mechanical properties will also return. Kretschmann [2010] suggests that the relationship between temperature and mechanical properties are modelled by

$$\Delta P\% = \left(\frac{P - P_{21}}{P_{21}}\right) \times 100 = A + BT + CT^2, \tag{1.18}$$

where $\Delta P\%$ is the percentage change in the mechanical property; P_{21} is the value of the property at 21 °C; A, B, and C, are constants for the model; and T is temperature in degrees Celsius. Kretschmann [2010] provides values for the model constants when the wood property being determined are MoE or MoR. If C is non-zero, the model includes a second-order term, though Kretschmann [2010] shows that in most cases C is zero or very small.

In addition to reversible temperature effects, Kretschmann [2010] shows that sustained exposure to high temperature can induce a permanent degradation in mechanical properties. Typically this will occur if the wood has been heated to a high temperature (exceeding 100 °C) for a number of hours. Kretschmann [2010] explains that this effect is dependent on a number of factors including: moisture content, heating medium, temperature, period of exposure, and species of wood.

Chapter 2

ELASTIC WAVES IN WOOD

Most solids behave *elastically* when subjected to external forces. That is, an applied force produces a proportional mechanical deformation. Additionally, each particle element in a solid has non-zero mass. This means that it behaves inertially; an applied force accelerates the particle according to Newton's second law. The interplay between the elastic and inertial forces in a solid produces the elastic wave phenomenon. A deformation at one location triggers the elastic restoring forces of the adjacent particles. These restoring forces then cause further particles to accelerate and deform. This propagating deformation is known as an *elastic wave*, and propagates through space at the *wave speed*.

It should be noted that the terms elastic wave, *stress wave*, and *acoustic wave* are used interchangeably in the literature. Some authors use acoustic wave to specifically refer to sound waves in air. In this thesis, the term stress wave is preferred because it is more common in literature pertaining to non-destructive testing of wood.

In this chapter, the fundamental physical models which describe stress wave behaviour in wood are documented. This includes the wave equation and its solutions. In order to derive the wave equation, the appropriate kinematic and kinetic models for an elastic solid must be first established. This thesis makes use of wave models both in one-dimension and three dimensions. The approach in the following sections is to establish each concept first in the one-dimensional case and then generalise to three dimensions.

2.1 NOTATION

The remainder of this chapter describes the behaviour of elastic waves in one-dimensional and three-dimensional media. This description requires the use of scalar, vector, and tensor quantities. The following notational conventions are followed.

Lower-case letters are used to indicate scalar quantities, including scalar fields. Lower-case boldface letters are used to indicate vector quantities. A non-bold version of

a vector quantity indicates the vector's magnitude. For example, $\boldsymbol{\xi}$ indicates the vector displacement field and ξ its associated magnitude.

Upper-case boldface letters are used to indicate matrix or tensor quantities. The matrix symbol's equivalent lower-case letter with index subscripts is used to indicate the terms of the matrix. For example, $\boldsymbol{\epsilon}$ is the Cauchy strain tensor, and ϵ_{11} is a single component of the tensor.

Some exceptions are made to these rules in order to comply with commonly-used conventions. Each symbol is defined when it is first used; the reader should refer to the list of symbols if they are unsure about any definition.

2.2 CONTINUOUS MEDIA

Elastic wave theory assumes that the wave's propagation medium is a *continuum*, rather than formed of individual lumped elements. This is technically untrue, as all materials fundamentally consist of atoms. However, it is assumed that on the macroscopic scale at which wave behaviour occurs, many nearby atoms move in unison. Collectively these atoms form *particles*, which are small regions in space, within which the mechanical properties can be considered constant.

In this section, two quantities for describing continuous media are described: *stress* and *strain*. Each of these quantities is defined for both a lumped one-dimensional object, and then generalised to continuous three-dimensional media.

2.2.1 Strain

Strain is a quantity used to describe a material's deformation. Suppose a solid object, such as a small wooden block, is compressed along one axis. The object, which has an undeformed length of L, experiences a change in length of ΔL. The strain on the object is the fractional deformation, given by

$$\epsilon = \frac{\Delta L}{L}. \tag{2.1}$$

Strain is not limited to describing the deformation of a macroscopic object, and can be extended to continuous media. In a continuous, three dimensional medium, each particle has a rest position given by the vector $\mathbf{x}$. When subjected to a external forces, the constituent particles are displaced relative to their original positions. The *particle displacement field* is defined as the particle's movement from its equilibrium position

$$\boldsymbol{u}(\mathbf{x}) = \boldsymbol{\xi}(\mathbf{x}) - \mathbf{x}, \tag{2.2}$$

where $\mathbf{x}$ is the particle's resting position, and $\boldsymbol{\xi}$ is the particle's deformed position [Auld

1973]. Strain is then defined in a continuum as

$$\epsilon_{ij}(\mathbf{x}) = \frac{1}{2}\left(\frac{\partial u_i}{\partial \mathrm{x}_j} + \frac{\partial u_j}{\partial \mathrm{x}_i}\right) \tag{2.3}$$

[Auld 1973], where u_i is the displacement along the ith axis, and x_j is the particle's rest position on the jth axis. This is known as the *Cauchy strain tensor*, and is a second-order tensor which can be equivalently written as

$$\boldsymbol{\epsilon} = \left[\epsilon_{ij}(\mathbf{x})\right] \tag{2.4}$$

$$= \begin{bmatrix} \epsilon_{xx} & \epsilon_{xy} & \epsilon_{xz} \\ \epsilon_{yx} & \epsilon_{yy} & \epsilon_{yz} \\ \epsilon_{zx} & \epsilon_{zy} & \epsilon_{zz} \end{bmatrix}. \tag{2.5}$$

As in the one-dimensional case, ϵ_{ij} is a unitless quantity (units of length / length). The strain tensor is symmetric, therefore, is completely defined by 6 independent components. A more compact form of $\boldsymbol{\epsilon}$, known as Voigt notation, makes use of this symmetry. This notation is defined in Appendix A.1.

2.2.2 Stress

Stress is a quantity which describes the internal forces in a deformed material. Consider again a solid object, such as a small wooden block. Suppose a force, f, is applied to two opposite faces of the block. Each face has a cross-sectional area, A. The magnitude of the block's internal stress is then given by

$$\sigma = \frac{f}{A}. \tag{2.6}$$

Tensional stresses are, by convention, positive in sign, while compressional stresses are negative in sign. Stress has units of Pascals.

This concept can also be applied to a continuum. When a body is subjected to an external force, the constituent particles transfer the force throughout the body via elastic coupling forces. Each particle within an object may be considered a bounded volume with three sets of orthogonal, parallel faces. Each pair of faces may have a force acting upon it, known as a *traction vector*, or *stress vector* $\dot{\boldsymbol{\tau}}$. Each tractional force can be expressed in Cartesian coordinates as

$$\begin{aligned} \dot{\boldsymbol{\tau}}_x &= \sigma_{xx}\hat{\boldsymbol{e}}_{\boldsymbol{x}} + \sigma_{yx}\hat{\boldsymbol{e}}_{\boldsymbol{y}} + \sigma_{zx}\hat{\boldsymbol{e}}_{\boldsymbol{z}}, \\ \dot{\boldsymbol{\tau}}_y &= \sigma_{xy}\hat{\boldsymbol{e}}_{\boldsymbol{x}} + \sigma_{yy}\hat{\boldsymbol{e}}_{\boldsymbol{y}} + \sigma_{zy}\hat{\boldsymbol{e}}_{\boldsymbol{z}}, \\ \dot{\boldsymbol{\tau}}_z &= \sigma_{xz}\hat{\boldsymbol{e}}_{\boldsymbol{x}} + \sigma_{yz}\hat{\boldsymbol{e}}_{\boldsymbol{y}} + \sigma_{zz}\hat{\boldsymbol{e}}_{\boldsymbol{z}}, \end{aligned} \tag{2.7}$$

which have units of Pascals. The vector $\dot{\boldsymbol{\tau}}_x$ acts on the face normal to the x direction

of the volume. The vectors $\hat{\boldsymbol{e}}_{\boldsymbol{x}}$, $\hat{\boldsymbol{e}}_{\boldsymbol{y}}$, and $\hat{\boldsymbol{e}}_{\boldsymbol{z}}$ are unit vectors in the x, y, and z directions, respectively. Due to Newton's third law, the force acting on each parallel opposing face is equal in magnitude and opposite in direction [Boresi et al. 1993]. The traction vectors of (2.7) are more conveniently represented as a second-order tensor,

$$\boldsymbol{\sigma} = \begin{bmatrix} \sigma_{xx} & \sigma_{xy} & \sigma_{xz} \\ \sigma_{yx} & \sigma_{yy} & \sigma_{yz} \\ \sigma_{zx} & \sigma_{zy} & \sigma_{zz} \end{bmatrix}, \tag{2.8}$$

which is known as the *Cauchy stress tensor*. Like strain, the stress tensor is commonly represented in a reduced form, which is described in Appendix A.1.

2.3 HOOKE'S LAW

Hooke's law is the principle which states that the stress applied to a material is proportional to the resultant strain, i.e., that the material behaves elastically. A material's *stiffness*, C, is the ratio of stress to strain along a particular axis. For the case of a one-dimensional solid object, Hooke's law[1] is given by

$$\sigma = C\epsilon. \tag{2.9}$$

Strain is a unitless quantity, therefore, stiffness has units of Pascals. Wood material is known to behave *elastically*, i.e., according to (2.9). It is explained in Section 2.5 that this leads directly to the phenomenon of acoustic waves.

This concept can be extended to continuous, anisotropic media. Generalised Hooke's law expresses each stress component as a linear sum of each strain component. For example, the first term of the stress tensor is given by

$$\begin{aligned} \sigma_{xx} = {} & C_{xxxx}\epsilon_{xx} + C_{xxxy}\epsilon_{xy} + C_{xxxz}\epsilon_{xz} \\ & + C_{xxyx}\epsilon_{yx} + C_{xxyy}\epsilon_{yy} + C_{xxyz}\epsilon_{yz} \\ & + C_{xxzx}\epsilon_{zx} + C_{xxzy}\epsilon_{zy} + C_{xxzz}\epsilon_{zz}, \end{aligned} \tag{2.10}$$

where C_{ijkl} are the *elastic stiffness constants*. Therefore, the stiffness relationship is given by

$$\sigma_{ij} = C_{ijkl}\epsilon_{kl}, \tag{2.11}$$

expressed in component form using Einstein notation[2]. This relationship can be

[1] Sometimes Hooke's law is expressed using a negative sign because it is described in terms of the restoring forces. It has been defined here in terms of the applied forces.

[2] This means that the repeated subscripts which do not appear in the result indicate a summation over those indices [Weisstein 2002].

expressed more simply in tensor notation as

$$\boldsymbol{\sigma} = \boldsymbol{C} : \boldsymbol{\epsilon}, \tag{2.12}$$

where $\boldsymbol{C}$ is known as the *stiffness tensor*. The *double dot* ($:$) product indicates the product of a fourth-order and a second-order tensor, as demonstrated in the calculation of the first component in (2.10).

The entire stiffness tensor consists of 81 stiffness constants. However, they are not all independent. Symmetry in the stiffness tensor reduces the number of independent constants to 21 for any homogeneous medium [Auld 1973]. In practice, though, many materials exhibit symmetries which reduce the number of constants. Some of these symmetries are documented in Section 2.4. A reduced-notation form of $\boldsymbol{C}$, which takes advantage of this symmetry, is described in Appendix A.1.

Hooke's law can also be expressed in terms of the *compliance tensor*, $\boldsymbol{S}$,

$$\boldsymbol{\epsilon} = \boldsymbol{S} : \boldsymbol{\sigma}. \tag{2.13}$$

The compliance tensor is the inverse of the fourth-order stiffness tensor $\boldsymbol{S} = \boldsymbol{C}^{-1}$ [Chapman 2004]. The Voigt notation form of the compliance tensor is defined in Appendix A.1.

2.3.1 Damping

An medium which behaves according to Hooke's law is *purely elastic*. In a purely elastic medium there are no energy losses as it is stressed. As such, a purely elastic medium is described as *lossless*. Such media do not exist in nature. In a real medium, internal friction results in energy losses; the amount of loss is referred to as *damping* [Mason 1958]. A damped-elastic medium is sometimes referred to as *viscoelastic* [Kolsky 1963]. Auld [1973] explains that for most purposes, viscoelasticity can be adequately modelled by adding a damping term to (2.9). Hooke's law then becomes,

$$\sigma = C\epsilon + \eta\frac{\partial \epsilon}{\partial t}, \tag{2.14}$$

where η is called the *damping coefficient*, or the *viscosity coefficient*. Wood material is known to behave viscoelastically, this is known to result in significant attenuation of acoustic waves [Bucur 2006].

The equivalent form of Hooke's law for a three-dimensional continuous viscoelastic medium is given by

$$\boldsymbol{\sigma} = \boldsymbol{C} : \boldsymbol{\epsilon} + \boldsymbol{\eta} : \frac{\partial \boldsymbol{\epsilon}}{\partial t}, \tag{2.15}$$

where $\boldsymbol{\eta}$ is the fourth-order *damping tensor*, which has the same dimensions as the

stiffness tensor.

2.4 SOLID SYMMETRIES

A medium is described as *isotropic* if its mechanical properties are identical in all directions. In contrast, an *anisotropic* medium's properties are directionally dependent. A medium is *homogeneous* or *uniform* if its mechanical properties do not change spatially, i.e., under translation. Uniformity and isotropy are easily mixed-up, but are independent. A solid may possess one or more *plane of symmetry*, i.e., a plane or axis, a reflection about which leaves the stiffness tensor unchanged [Landau and Lifshitz 1970]. The planes of symmetry define the form of the stiffness tensor. A material's anisotropy is defined by the internal structure of the material. For example, in softwood there are three orthogonal growth features which strongly influence the wood's stiffness: tracheid cells, growth rings, and ray cells. Wood is a complicated solid to model effectively, as it is both inhomogeneous and anisotropic. Researchers have applied isotropic, transverse isotropic, and orthotropic models to describe wood's behaviour, though orthotropic is probably most commonly employed [Bodig and Jayne 1982, Bucur 2006, Subhani et al. 2013].

In this section, two different types of solid symmetries are defined: the isotropic solid, and the orthotropic solid. The stiffness tensor is defined for each solid symmetry.

2.4.1 Isotropic solids

The stiffness tensor for an isotropic solid is unchanged under rotational transformation. It can be shown that only two independent parameters are necessary to fully define the stiffness (or compliance) tensor of an isotropic material [Riley et al. 2007]. In this section, one method of defining the tensor, in terms of Young's modulus and Poisson's ratio, is explained.

Consider a sample of an isotropic material with a tensional stress applied to one pair of faces. The stress-strain relationship in that direction is given by

$$\epsilon_1 = \frac{1}{E}\sigma_1 \tag{2.16}$$

[Bauchau and Craig 2009], in Voigt notation, where E is *Young's modulus* (defined in Appendix A.3). The sample also contracts transversely, with the relationship

$$\epsilon_2 = -\frac{\nu}{E}\sigma_1, \quad \epsilon_3 = -\frac{\nu}{E}\sigma_1, \tag{2.17}$$

where ν is *Poisson's ratio* (defined in Appendix A.3). (2.16) and (2.17) may also be defined for stressed applied in the 2, 3 directions. The theory of *linear elasticity* implies that the resulting strain will be the sum of the strains produced by each individual

applied stress. Bauchau and Craig [2009] also show that the relationship between shear stress and strain components is given by

$$\epsilon_4 = \frac{2\,(1+\nu)}{E}\sigma_4. \tag{2.18}$$

The isotropy of the material means that the other shear components, ϵ_5 and ϵ_6, are identical to (2.18), with the appropriate subscript modifications. Bauchau and Craig [2009] explain that in an isotropic material, there is no coupling between axial and shear strains, therefore, the upper-right and lower-left quadrants of the compliance tensor are zero. The possible combinations of (2.16), (2.17) and (2.18) may be combined to construct the compliance tensor as

$$\boldsymbol{S} = \frac{1}{E}\begin{bmatrix} 1 & -\nu & -\nu & 0 & 0 & 0 \\ -\nu & 1 & -\nu & 0 & 0 & 0 \\ -\nu & -\nu & 1 & 0 & 0 & 0 \\ 0 & 0 & 0 & 2\,(1+\nu) & 0 & 0 \\ 0 & 0 & 0 & 0 & 2\,(1+\nu) & 0 \\ 0 & 0 & 0 & 0 & 0 & 2\,(1+\nu) \end{bmatrix}. \tag{2.19}$$

The stiffness tensor for an isotropic solid is then given by calculating the inverse of (2.19),

$$\boldsymbol{C} = \frac{E}{(1+\nu)\,(1-2\nu)}\begin{bmatrix} 1-\nu & \nu & \nu & 0 & 0 & 0 \\ \nu & 1-\nu & \nu & 0 & 0 & 0 \\ \nu & \nu & 1-\nu & 0 & 0 & 0 \\ 0 & 0 & 0 & \frac{1-2\nu}{2} & 0 & 0 \\ 0 & 0 & 0 & 0 & \frac{1-2\nu}{2} & 0 \\ 0 & 0 & 0 & 0 & 0 & \frac{1-2\nu}{2} \end{bmatrix}. \tag{2.20}$$

2.4.2 Orthotropic solids

An *orthotropic* or *orthorhombic* material has three orthogonal planes of symmetry [Boresi et al. 1993]. Boresi et al. [1993] shows that the compliance tensor for an orthotropic material is

$$\boldsymbol{S} = \begin{bmatrix} \frac{1}{E_x} & -\frac{\nu_{yx}}{E_y} & -\frac{\nu_{zx}}{E_z} & 0 & 0 & 0 \\ -\frac{\nu_{xy}}{E_x} & \frac{1}{E_y} & -\frac{\nu_{zy}}{E_z} & 0 & 0 & 0 \\ -\frac{\nu_{xz}}{E_x} & -\frac{\nu_{yz}}{E_y} & \frac{1}{E_z} & 0 & 0 & 0 \\ 0 & 0 & 0 & \frac{1}{\mu_{yz}} & 0 & 0 \\ 0 & 0 & 0 & 0 & \frac{1}{\mu_{zx}} & 0 \\ 0 & 0 & 0 & 0 & 0 & \frac{1}{\mu_{xy}} \end{bmatrix}, \tag{2.21}$$

where E_x is the value of Young's modulus in the x direction, and ν_{xy} is the value of Poisson's ratio which defines the strain in the x direction from a stress applied in the y direction. The axes defined here are arbitrary, in the wood science literature the axes are typically labelled L, R, and T for longitudinal, radial, and transverse, respectively. Boresi et al. [1993] noted that the compliance tensor is symmetric, therefore,

$$\begin{aligned}\frac{\nu_{xy}}{E_x} &= \frac{\nu_{yx}}{E_y},\\ \frac{\nu_{xz}}{E_x} &= \frac{\nu_{zx}}{E_z},\\ \frac{\nu_{yz}}{E_y} &= \frac{\nu_{zy}}{E_z}.\end{aligned}$$

This means that the orthotropic stiffness tensor is completely defined by 9 parameters: three Young's moduli, three Poisson's ratios, and three shear moduli.

Auld [1973] demonstrated that the stiffness tensor of an orthotropic solid has the form

$$\boldsymbol{C} = \begin{bmatrix} C_{11} & C_{12} & C_{13} & 0 & 0 & 0 \\ C_{12} & C_{22} & C_{23} & 0 & 0 & 0 \\ C_{13} & C_{23} & C_{33} & 0 & 0 & 0 \\ 0 & 0 & 0 & C_{44} & 0 & 0 \\ 0 & 0 & 0 & 0 & C_{55} & 0 \\ 0 & 0 & 0 & 0 & 0 & C_{66} \end{bmatrix}. \tag{2.22}$$

The values of the stiffness tensor have not been provided, but they are easily calculated by evaluating the inverse of the compliance tensor, $\boldsymbol{C} = \boldsymbol{S}^{-1}$.

2.5 THE WAVE EQUATION

A *wave equation* is a second-order differential equation which describes the propagation of waves. A wave equation expresses a relationship between a *wave variable* (such as stress or strain), a time variable, and a spatial variable. Wave equations are found in a number of different disciplines including acoustics, electromagnetism, and fluid dynamics. A *particular solution* is the solution of the wave equation once initial conditions and boundary conditions are specified. A particular solution can be considered a description of an actual wave.

It was previously noted that the isotropic solid model is insufficient to describe wood material's three-dimensional elasticity. The orthotropic model is typically more appropriate. However, it is shown in the following sections that the wave equation, and its solutions, can quickly become very complicated for any geometry more complex than the one-dimensional case. For this reason, researchers often apply the one-dimensional

model to wood quality studies, even though it is known to be a simplification. In order to remain as general as possible, this section will define the one-dimensional model, and then generalise it to the more complex three-dimensional case in an anisotropic solid.

As explained at the beginning of this chapter, two elements are necessary to produce an elastic wave: elastic restoring forces, and inertia due to particle mass. Elastic restoring forces can be described using Hooke's law, which was defined in Section 2.3. The second component, inertia, is modelled using Newton's second law. Newton's second law can be written in terms of stress, σ, and particle displacement, u, as

$$\frac{\partial \sigma}{\partial x} = -\rho \frac{\partial^2 u}{\partial t^2}, \tag{2.23}$$

[Love 1927], where ρ is the mass density of the medium. This is called the *equation of motion*. (2.23) is expressed in terms of particle displacement, while Hook's law, (2.9), is in terms of strain. These two quantities are related using the *strain-displacement relation*, which, in one-dimension is given by

$$\epsilon = \frac{\partial u}{\partial x}, \tag{2.24}$$

Kelly [2015]. This is the one-dimensional equivalent of (2.3).

To derive the wave equation, (2.24) is substituted into (2.9) to eliminate ϵ. The result is then differentiated with respect to x, and substituted into (2.23) to give

$$\frac{\partial^2 u}{\partial t^2} = c^2 \frac{\partial^2 u}{\partial x^2}, \tag{2.25}$$

where

$$c = \sqrt{\frac{C}{\rho}}. \tag{2.26}$$

(2.25) is the one dimensional wave equation in terms of the particle displacement, and c is the wave's *phase speed*. Sometimes Young's modulus, E is substituted in place of the stiffness term of (2.26). In a one-dimensional medium with no transverse expansion (i.e. Poisson's ratio equal to zero), these two moduli of elasticity are equivalent. (2.26) only applies when the medium is lossless. In a viscoelastic medium the phase speed will be frequency-dependent. The frequency-dependence of the speed is known as *dispersion* [Kolsky 1963].

The same approach can be applied to determine the wave equation for a plane wave in a three-dimensional anisotropic medium. Itskov [2007] demonstrates that the three-dimensional equivalent of the equation of motion is obtained by taking the divergence of the stress field,

$$\nabla \cdot \boldsymbol{\sigma} = \rho \frac{\partial^2 \boldsymbol{u}}{\partial t^2}, \tag{2.27}$$

where $\nabla \cdot \boldsymbol{\sigma}$ is the divergence of the stress field[3], ρ is the density. The strain-displacement relation in three-dimensions is given by (2.3). This can be expressed in tensor notation as

$$\boldsymbol{\epsilon} = \frac{1}{2}\left(\nabla \boldsymbol{u} + \nabla \boldsymbol{u}^{\mathbf{T}}\right), \tag{2.28}$$

[Auld 1973] where $\nabla \boldsymbol{u}$ is the gradient of the vector field[4] $\boldsymbol{u}$, and $\nabla \boldsymbol{u}^{\mathbf{T}}$ indicates that the transpose of the tensor was taken. $\nabla \boldsymbol{u}$ is known as the *particle displacement gradient*, which is a second-order tensor. The right-hand side of (2.28) is the *symmetric part* of the displacement gradient, $\nabla \boldsymbol{u}$. This is more compactly represented by the notation

$$\boldsymbol{\epsilon} = \nabla_{\mathrm{s}} \boldsymbol{u}, \tag{2.29}$$

where ∇_{s} is the *symmetric matrix* operator, defined by (2.28). As in the one-dimensional case, to derive the wave equation, (2.29) is substituted into (2.12) to eliminate $\boldsymbol{\epsilon}$. The result is then substituted into (2.27) to give

$$\nabla \cdot (\boldsymbol{C} : \nabla_{\mathrm{s}} \boldsymbol{u}) = \rho \frac{\partial^2 \boldsymbol{u}}{\partial t^2}, \tag{2.30}$$

which is the three dimensional equivalent of the wave equation. For the three dimensional case, the phase speed is not immediately apparent. It is shown in Section 2.6 that the three dimensional wave equation gives rise to different wave *modes*, which travel at different speeds. Additionally, in general, the phase speed is dependent on the direction, or polarisation, of the wave mode. Auld [1973] demonstrates that the three-dimensional wave equation can also be expressed in component form

$$\nabla_{iJ} C_{JK} \nabla_{Kl} u_l = \rho \frac{\partial^2 u_i}{\partial t^2}, \tag{2.31}$$

where ∇_{iJ} is the divergence operator expressed in component form[5], and ∇_{Kl} is the symmetric operator in componentised form[6]. Note that upper-case indices are used here to indicate that Voigt reduced-notation has been used for the tensor components, as defined in Appendix A.1.

[3] See Itskov [2007] for a definition of the divergence of a second-order tensor.

[4] The gradient of an n dimensional vector is an $n \times n$ tensor. This operation is defined by Kelly [2015].

[5] See Appendix A for a definition of the divergence operator.

[6] See Appendix A for a definition of the symmetric operator.

2.6 SOLUTIONS TO THE ONE-DIMENSIONAL WAVE EQUATION

It can be shown using the technique of separation of variables that the general solution to the one-dimensional wave equation, (2.25), has the form

$$u(x,t) = f(x - ct) + g(x + ct), \tag{2.32}$$

[Graff 1991], where f and g are arbitrary functions defined by the initial conditions. f and g represent the positive and negative-travelling parts of the wave, respectively. Another possible solution is the complex exponential,

$$u(x,t) = Ae^{j(\omega t - kx)} + Be^{j(\omega t + kx)}, \tag{2.33}$$

where ω is the angular frequency, and k is the *wavenumber*, which is the spatial frequency of the wave, in radians per metre, given by

$$k = \frac{2\pi}{\lambda} = \frac{\omega}{c}. \tag{2.34}$$

The wave equation is linear, therefore, a sum of complex exponentials are also a solution to the wave equation. The Fourier transform is a decomposition of an arbitrary signal into a sum of complex exponentials, therefore, this suggests that the two solutions are related by the Fourier transform [Bose 1995].

If the medium is viscoelastic, then there is a loss component as the wave propagates through space. In this case, the complex exponential solution to the wave equation may be written

$$u(x,t) = Ae^{\gamma x}e^{-j\omega t} + Be^{-\gamma x}e^{-j\omega t}, \tag{2.35}$$

where γ is the *propagation coefficient*. The propagation coefficient is a complex quantity,

$$\gamma = \alpha + jk, \tag{2.36}$$

its real part, α, is called the *attenuation coefficient*, and the imaginary part, k, is equal to the wavenumber [Kolsky 1963].

2.6.1 Phase speed and group speed

A medium which has a frequency-dependent phase speed is referred to as *dispersive*. Kolsky [1963] explains that rate at which the energy in a pulse-like vibration propagates is not defined by the phase speed, but by the *group speed*. This is the speed at which a packet of waves propagates. Whereas the phase speed is the speed of a single frequency.

The group velocity is given by

$$c_g = \frac{\partial \omega}{\partial k}, \tag{2.37}$$

[Crawford 1968]. Kim [1994] explains that the speed measured depends on the character of the propagating wave. Continuous waves can be used to measure the stiffness parameters along an axes. For example, C_{11} can be determined by measuring the phase speed along axis 1, for example, using a continuous-wave technique. Many acoustic sources, however, are transient in nature, including impulsive sources and acoustic emission phenomena.

2.7 SOLUTIONS TO THE THREE-DIMENSIONAL WAVE EQUATION

The wave equation for a general three-dimensional solid is given by (2.30). This equation was provided in vector form, and thus, a scalar value for the phase speed was not obtained immediately from the equation (as it was for the one-dimensional case). In this section, the phase speeds and propagation modes are defined for several cases of plane waves in solids. First, in Section 2.7.1, a plane wave propagating in an isotropic solid in the direction of one of the constituent axes, is examined. Second, in Section 2.7.2, the Christoffel equation is defined. It is explained that this equation allows the wave speed to be calculated in an arbitrary direction in an anisotropic solid. Finally, in Section 2.7.3, the modes and speeds for another special case are defined, that of a plane wave propagating in an orthotropic solid.

2.7.1 Plane waves in an isotropic solid

Consider the three-dimensional wave equation, (2.30). This equation is a vector quantity, which can represent any arbitrary propagation-direction and polarisation. As a special case, suppose a plane wave is excited along the x axis. This means that the wave's amplitude is equal throughout the entire y-z plane. Therefore, the only spatial derivatives which are non-zero are those which contain $\frac{\partial}{\partial x}$ terms. Auld [1973] explains that the first non-zero term is

$$C_{11}\frac{\partial^2 u_x}{\partial x^2} = \rho \frac{\partial^2 u_x}{\partial t^2}. \tag{2.38}$$

This is the case of a longitudinal (compressional) plane wave. This mode has also been referred to (in Section 1.2.5 and Appendix B) as a *dilatational* wave. The dilatational

wave propagates at a phase speed given by

$$c_x = \sqrt{\frac{C_{11}}{\rho}} \tag{2.39}$$

$$= \sqrt{\frac{E}{\rho}\frac{(1-\nu)}{(1+\nu)(1-2\nu)}}. \tag{2.40}$$

The other non-zero terms of the wave equation are

$$C_{66}\frac{\partial^2 u_y}{\partial x^2} = \rho\frac{\partial^2 u_y}{\partial t^2}, \tag{2.41}$$

$$C_{44}\frac{\partial^2 u_z}{\partial x^2} = \rho\frac{\partial^2 u_z}{\partial t^2}. \tag{2.42}$$

These are the y and z polarised *shear waves*, i.e., the polarisation direction is perpendicular to the wave's propagation direction. The phase speed of the shear waves is given by

$$c_y = c_z = \sqrt{\frac{C_{66}}{\rho}} = \sqrt{\frac{1}{s_{66}\rho}} \tag{2.43}$$

$$= \sqrt{\frac{E}{2\rho(1+\nu)}}. \tag{2.44}$$

The cross-axis terms (C_{12} etc) also generate a compressional wave travelling perpendicular to the x travelling wave. However, in the unconstrained plane wave case, the wavefront extends over the whole y-z plane so there would be nowhere for the wave to propagate, thus it is not considered further.

2.7.2 The Christoffel equation

The isotropic stiffness matrix, (2.20), is, by definition, identical under any rotational transformation. Therefore, the direction of a propagating wave will not have any bearing on the resulting speed in an isotropic material. However, if the medium is not isotropic, the resulting wave propagation will depend on both the mode of propagation (longitudinal, shear), and the direction.

Auld [1973] explains that a plane wave solution to the three dimensional wave equation is of the form

$$\boldsymbol{u}(\mathbf{x}, t) = \hat{\boldsymbol{u}} e^{j(\omega t - k\hat{\boldsymbol{n}}\cdot\mathbf{x})}, \tag{2.45}$$

where $\hat{\boldsymbol{n}}$ is the *propagation vector*, which is a unit-vector indicating the orientation of the plane-wave solution, and $\hat{\boldsymbol{u}}$ is the wave's *polarisation vector*. Both of these quantities depend on the initial conditions.

Auld [1973] explains that if (2.45) is substituted into the wave equation, it becomes

$$\rho\omega^2 u_i = k^2(\dot{n}_{iJ}C_{JL}\dot{n}^{\mathbf{T}}_{Lj})u_j \tag{2.46}$$

$$= k^2\dot{\gamma}_{ij}u_j, \tag{2.47}$$

where

$$\dot{n}_{iJ} = \dot{n}_{Lj} = \begin{bmatrix} \dot{n}_x & 0 & 0 & 0 & \dot{n}_z & \dot{n}_y \\ 0 & \dot{n}_y & 0 & \dot{n}_z & 0 & \dot{n}_x \\ 0 & 0 & \dot{n}_z & \dot{n}_y & \dot{n}_x & 0 \end{bmatrix}, \tag{2.48}$$

and $\dot{n}^{\mathbf{T}}_{Lj}$ is the transpose of $\dot{n}_{iJ}$. $\dot{\gamma}_{ij} = \dot{n}_{iJ}C_{JL}\dot{n}^{\mathbf{T}}_{Lj}$ is the *Christoffel matrix*, in component form. The Christoffel matrix is only a function of the stiffness matrix and the propagation vector. (2.46) can be expressed in vector notation as

$$\rho c^2\hat{\boldsymbol{u}} = \boldsymbol{\Gamma}\hat{\boldsymbol{u}}, \tag{2.49}$$

where $\boldsymbol{\Gamma}$ is the Christoffel matrix. (2.49) is known as the *Christoffel* equation.

(2.49) is an eigenvalue problem, where the eigenvector is the polarisation vector, and the eigenvalue is ρc^2. The eigenvalue-eigenvector pairs determine the characteristic polarisation modes, and the associated phase speeds, for a given propagation direction [Dellinger 1991]. As is typical for an eigenvalue problem, the solutions are obtained by setting the characteristic determinant to zero and solving the characteristic equation [Strang 1993]. In general, a plane wave can propagate in any arbitrary direction, $\hat{\boldsymbol{n}}$, in a solid. Furthermore, the particle motion can be polarised in any direction $\hat{\boldsymbol{u}}$. An arbitrary wave can, therefore, be decomposed into a sum of the characteristic modes, defined by (2.49).

2.7.3 Plane waves in an orthotropic solid

In Section 2.7.2, it was explained that the Christoffel equation can be used to determine the polarisation modes, and associated phase speeds, for a given propagation direction. In this section, the Christoffel equation is expanded for a special case, that of an orthortopic solid. The Christoffel matrix can be evaluated with the orthotropic stiffness tensor, (2.22), which gives

$$\boldsymbol{\Gamma} = \begin{bmatrix} C_{11}\dot{n}_x^2 + C_{66}\dot{n}_y^2 + C_{55}\dot{n}_z^2 & (C_{12}+C_{66})\dot{n}_x\dot{n}_y & (C_{13}+C_{55})\dot{n}_z\dot{n}_x \\ (C_{12}+C_{66})\dot{n}_x\dot{n}_y & C_{66}\dot{n}_x^2 + C_{22}\dot{n}_y^2 + C_{44}\dot{n}_z^2 & (C_{23}+C_{44})\dot{n}_y\dot{n}_z \\ (C_{13}+C_{55})\dot{n}_z\dot{n}_x & (C_{23}+C_{44})\dot{n}_y\dot{n}_z & C_{55}\dot{n}_x^2 + C_{44}\dot{n}_y^2 + C_{33}\dot{n}_z^2 \end{bmatrix}. \tag{2.50}$$

It can be shown that when the propagation vector is directed purely along the x axis, the characteristic solutions to (2.49) are

$$c = \sqrt{\frac{C_{11}}{\rho}}, \qquad \hat{\boldsymbol{u}} = \begin{bmatrix} 1 \\ 0 \\ 0 \end{bmatrix} \qquad \text{(longitudinal)}, \tag{2.51}$$

$$c = \sqrt{\frac{C_{66}}{\rho}}, \qquad \hat{\boldsymbol{u}} = \begin{bmatrix} 0 \\ 1 \\ 0 \end{bmatrix} \qquad (y \text{ polarised shear}), \tag{2.52}$$

$$c = \sqrt{\frac{C_{55}}{\rho}}, \qquad \hat{\boldsymbol{u}} = \begin{bmatrix} 0 \\ 0 \\ 1 \end{bmatrix} \qquad (z \text{ polarised shear}). \tag{2.53}$$

These solutions can easily be extended for the y and z propagating waves.

Solutions of the Christoffel equation for an arbitrary propagation direction are typically obtained using numerical methods. However, Auld [1973] shows that by considering propagation along any direction in a plane bound by two axes, closed form solutions for each mode's phase speeds can be derived. Consider a plane-wave propagating at some direction in the x-y plane. When the direction is purely in the x or y direction, the solutions reduce to the aforementioned speeds and modes. If the propagation direction is not directly along an axis, the solution is, in general, not a pure longitudinal or shear wave [Auld 1973]. In this case, phase speeds are given by

$$c = \left(\frac{C_{44} \cos^2 \phi + C_{55} \sin^2 \phi}{\rho} \right)^{1/2}, \tag{2.54}$$

$$c = \left(\frac{C_{66} + C_{11} \cos^2 \phi + C_{22} \sin^2 \phi - \sqrt{\left(C_{66} + C_{11} \cos^2 \phi + C_{22} \sin^2 \phi \right)^2 - 4\bar{C}}}{\rho} \right)^{1/2}, \tag{2.55}$$

$$c = \left(\frac{C_{66} + C_{11} \cos^2 \phi + C_{22} \sin^2 \phi + \sqrt{\left(C_{66} + C_{11} \cos^2 \phi + C_{22} \sin^2 \phi \right)^2 - 4\bar{C}}}{\rho} \right)^{1/2}, \tag{2.56}$$

where ϕ is the propagation angle in the plane relative to the x axis and,

$$\bar{C} = \left(C_{11} \cos^2 \phi + C_{66} \sin^2 \phi \right) \left(C_{66} \cos^2 \phi + C_{22} \sin^2 \phi \right). \tag{2.57}$$

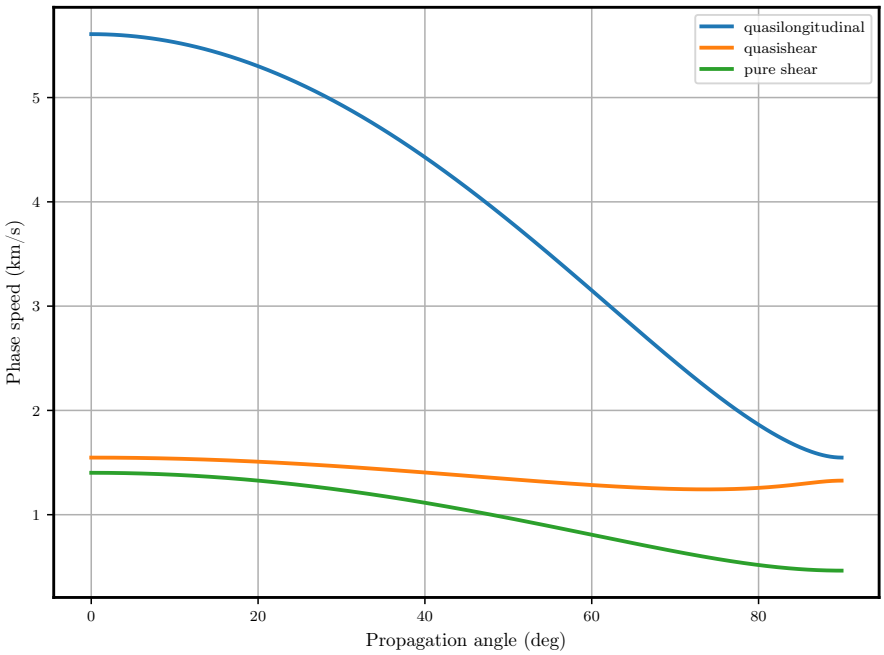

Figure 2.1 The phase speed in an orthotropic solid, provided for the quasilongitudinal, quasishear, and pure shear modes. Speeds were calculated using Douglas-fir stiffness values, obtained from Kretschmann [2010].

(2.54) is the *pure shear* solution; the polarisation is directed along the z axis. (2.55) is the *quasishear* solution–the polarisation is predominantly shear but has a component in the direction of propagation. (2.56) is the *quasilongitudinal* solution; the polarisation is predominantly longitudinal but has a shear component.

Speeds have been calculated for the quasilongitudinal, quasishear, and pure shear modes. These speeds, shown in Figure 2.1, use average stiffness-tensor values for the species Douglas-fir, using data reported by Kretschmann [2010].

Chapter 3

ELECTRO-MECHANICAL MODELLING OF AN ACOUSTIC TRANSDUCER IN WOOD

The Treetap ToF system developed at the University of Canterbury uses the Fakopp SD-02 transducer [Fakopp Bt 2000] for measuring stress waves in standing trees. This transducer is also used in the new Wireless Treetap system (discussed in Chapter 5). The Fakopp SD-02 transducer acts as an accelerometer. For an ideal accelerometer, the output signal is proportional to the applied acceleration. For a real device, however, it is only proportional over a finite range of frequencies, termed the device's *bandwidth*. In this chapter, several mathematical models are presented for describing the SD-02 transducer's frequency response.

This work is important because all of the other acoustic measurements described in this thesis were performed using the SD-02 transducer. In general the response of the transducer depends on both its own construction, and the mechanical parameters of the wood it interfaces with. This suggests that the response of the transducer could, in principle, be used to infer some useful information about the wood properties.

The work documented in this chapter builds upon a model developed by Woods [2006]. First, an overview of generic electro-mechanical transducer models is discussed in Section 3.1. Next, Woods [2006] lumped-element model of the SD-02 is described in Section 3.2. Following this, several different models for the loading effect of the wood upon the transducer, known as the *radiation impedance* models, are considered in Section 3.3. These models are then briefly compared in Section 3.4. Following this, in Section 3.5, Woods [2006] transducer model is loaded with each of the radiation impedances to produce an estimate of the device's complete frequency response in wood. Next, in Section 3.6, an experiment is described where a series of signals were captured in a standing tree. Finally, a summary and discussion of the findings of this work is provided in Section 3.7.

3.1 ELECTRO-MECHANICAL TRANSDUCER MODELS

An accelerometer is an example of an electro-mechanical system. A model for an accelerometer typically includes two ports [Busch-Vishniac 2012]. A mechanical port, to which a velocity or acceleration signal is applied, and an electrical port, where the output voltage or current is produced. The internal behaviour of the accelerometer may be described using *lumped element* components[1]. The components may be combined to form electrical and mechanical equivalent circuits. In this section, the concepts of electrical and mechanical impedances are introduced, and a generic circuit for an acoustic transducer is presented.

3.1.1 Electrical and mechanical impedance

In electrical systems the concept of impedance is commonly applied to quantify the relationship between current and voltage for a circuit or component [Hayt et al. 2002]. The electrical impedance is given by $Z_{\mathrm{e}}(f) = V(f)/I(f)$, where V is the complex voltage, and I is the complex current[2]. The concept of impedance can be extended to acoustic or mechanical systems [Firestone 1933]. In mechanical systems the impedance is given by $Z_{\mathrm{m}}(f) = F(f)/U(f)$, where F is force, and U is velocity. In acoustic systems the *specific acoustic impedance* is given by $Z_{\mathrm{sp}}(f) = P(f)/U(f)$, where P is pressure and U is the particle velocity [Kinsler et al. 2000, Olson 1957].

These analogies between electrical, mechanical, and acoustical systems allow an *equivalent circuit* representation to be created for certain mechanical or acoustical systems. In an equivalent circuit, the mechanical and acoustical components are converted into equivalent electrical components, and a circuit can be drawn. This circuit can then be analysed using circuit analysis techniques and simulation tools. An overview of the electro-mechanical analogies used in this chapter is given in Appendix C.

3.1.2 Generic model of a transducer

Figure 3.1 shows a high level lumped-element model of an electro-acoustical transducer. This type of system may be decomposed into three sections. The electrical components serve to convert electrical energy into mechanical energy and vice versa. The impedance of the electrical components are represented by a lumped element Z_{e}. The electrical circuit is coupled to the mechanical components through a gyrator[3] with a current-to-force conversion factor of α. The mechanical components are modelled as a lumped

[1] Lumped element parameters are not appropriate at all frequencies, for more information see Appendix C

[2] The ambiguous terms *complex voltage* and *complex current* are used here to indicate that quantities are in frequency domain. They may be phasor quantities, or variables in the Fourier or Laplace domains.

[3] A gyrator is used in this model instead of a transformer because of this model's use in moving-coil loudspeaker systems. The force on a moving coil is proportional to the current through the coil [Skilling 1948].

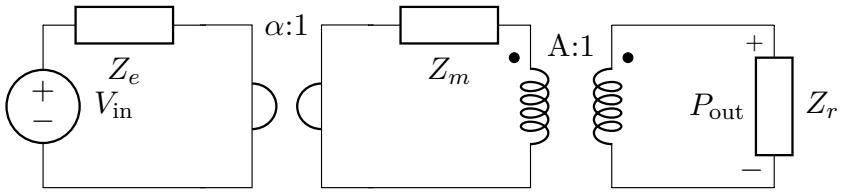

Figure 3.1 A general model of an electro-acoustic transducer [Lemaitre et al. 2008]. The impedances Z_{e}, Z_{m}, and Z_{r} represent the circuit's electrical, mechanical, and acoustic (radiation impedance) loads, respectively. In this case, the circuit is a model for a driver, e.g., a loudspeaker, as the input is on the electrical side.

mechanical-impedance Z_{m}. The mechanical components are coupled to the acoustical circuit through an ideal transformer. The turns ratio of the transformer is equal to A:1, where A is the effective radiator area of the transducer. The acoustical impedance Z_{r} is the specific acoustic impedance presented by the medium the device is driving into. This impedance is called the *radiation impedance* [Kinsler et al. 2000, Lemaitre et al. 2008]. It is the impedance at the radiating source's boundary, thus it is the load "seen" by the source "looking" into the medium.

3.2 LUMPED-ELEMENT MODEL OF THE FAKOPP SD-02 TRANSDUCER

Woods [2006] disassembled an SD-02 transducer [Fakopp Bt 2000] and documented its construction. The major components of the transducer are shown in Figure 3.2. The body of the transducer is constructed of stainless steel. The device uses a piezoelectric ceramic crystal to convert the received stress wave into a voltage; the voltage across a piezoelectric crystal is proportional to the applied force [Arnau 2008, Bonnett 2010]. Fixed to the crystal is a small brass mass. The crystal and brass mass are pressed together in the body of the transducer by a rubber mat.

Woods explained that the stiffness of both the crystal and brass mass are much larger than that of the rubber mat. He assumed that the piezoelectric crystal behaves like a spring, with an output voltage proportional to the strain across it. Therefore, the operating components can be approximately modelled as the crystal's compliance, s_{p}, connected to both the brass mass, m_1, and the transducer's body, m_2.

Woods used mechanical-electrical reciprocity to convert the spring-mass system into an equivalent electrical circuit. In his chosen circuit analogy, force replaces voltage as the across-component variable and velocity replaces current as the through-component variable (this circuit analogy is described in Appendix C). In this circuit analogy, masses convert into inductances and springs convert into capacitances. A damping element was added to the crystal compliance, which converts to a capacitor and resistor in series. He explained that the force-voltage relationship of the crystal may be described using an ideal transformer. The turns-ratio of the transformer is equal to the piezoelectric

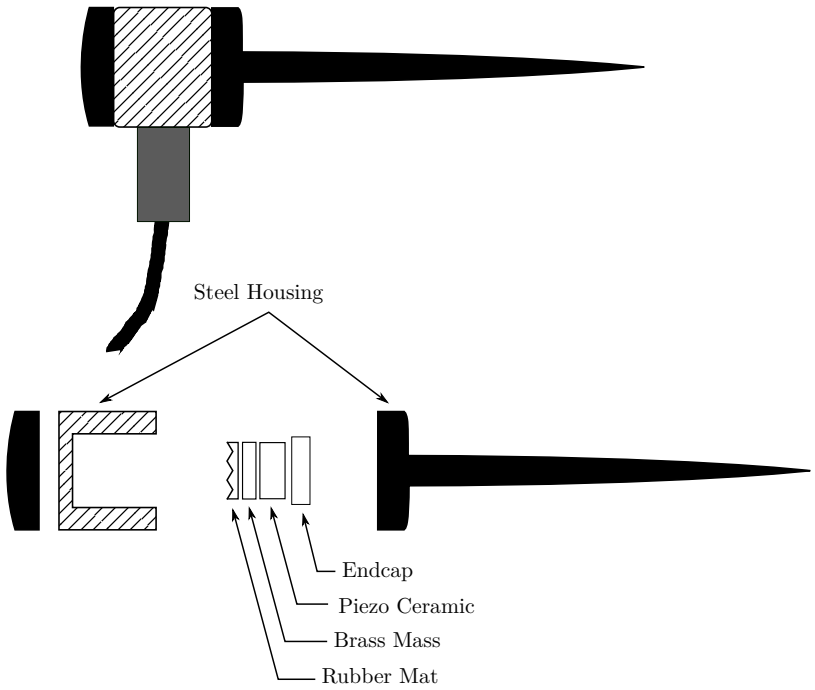

Figure 3.2 Internal construction of the Fakopp SD-02 transducer.

coupling factor, α [Richter et al. 2009].

Woods incorporated the mass of the crystal by distributing it between the small brass mass and the body mass,

$$m_1' = m_1 + \frac{m_c}{2} \tag{3.1}$$

$$m_2' = m_2 + \frac{m_c}{2}. \tag{3.2}$$

The electrical model of the crystal was approximated as a capacitor, ignoring higher resonances of the crystal [Richter et al. 2009]. The value of this capacitance was obtained from the transducer's datasheet [Fakopp Bt 2000]. Woods measured the complex admittance of the transducer over its predicted bandwidth using a signal generator and oscilloscope. Using the admittance data, he was able to determine the effective compliance, s_p, using the transducer's measured resonant frequency. By measuring the real value of the admittance at resonance, and the bandwidth of the resonant peak he was able to determine values for α and η_p. The values of the parameters determined by Woods are shown in Table 3.1. Woods' complete mechanical-electrical model is shown in Figure 3.3.

There are several different versions of the Fakopp SD-02 available. These versions differ slightly in the resonant frequency of the transducer. The device datasheet notes that the typical resonance of the transducer is 23 kHz [Fakopp Bt 2001]. Woods [2006] explained that the resonant frequency of the transducer is due to the small mass and

Table 3.1 Electrical and mechanical parameters for the model shown in Figure 3.3.

Component	Value
Small brass mass m_1	3.3 g
Transducer body mass m_2	50 g
Piezoelectric capacitance C_p	670 pF
Piezoelectric compliance s_p	$8.5 \times 10^{-9}\,\mathrm{s}^2/\mathrm{kg}$
Force-Voltage coupling factor α	0.02
Mechanical resistance (damping factor) η_p	123 Ns/m

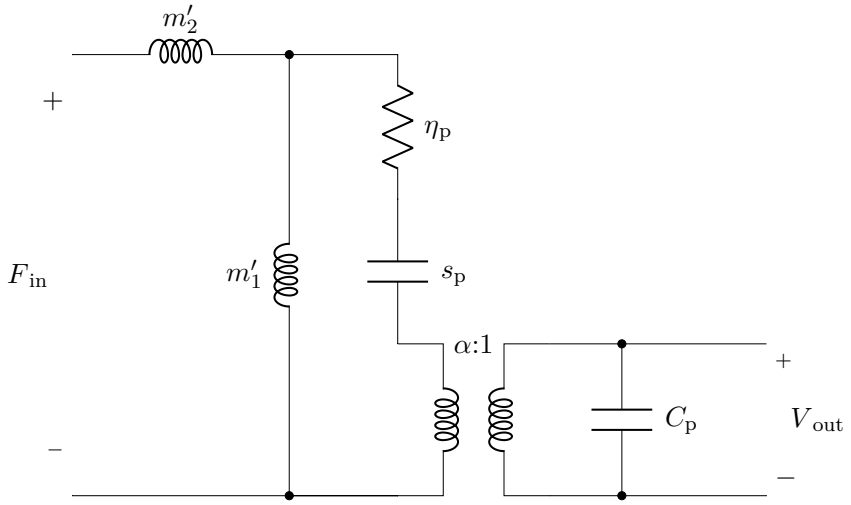

Figure 3.3 Electrical-mechanical model of the Fakopp SD-02.

the crystal compliance oscillating. This resonance is approximately equal to

$$f = \frac{1}{2\pi\sqrt{s_\mathrm{p} m_1'}}. \tag{3.3}$$

The transducer Woods deconstructed and characterised has a resonant frequency of 30 kHz. This frequency was used to determine the value of the crystal compliance, s_p, shown in Table 3.1. It is unknown whether the variation in resonant frequency is due to a variation in the small mass, crystal compliance, or both. The body mass and overall construction is approximately the same for each of the devices, regardless of resonant frequency.

3.2.1 Measurement of the transducer's response in wood

An experiment was performed to measure the frequency response of an SD-02 transducer in a piece of timber. A transducer was inserted in one end of a piece of dry *Pinus radiata* timber. The transducer was connected to an Agilent DS06034A digital storage oscilloscope. The oscilloscope was configured to capture 1000 samples at a sampling frequency of 200 kHz. The experimental setup is shown in Figure 3.4.

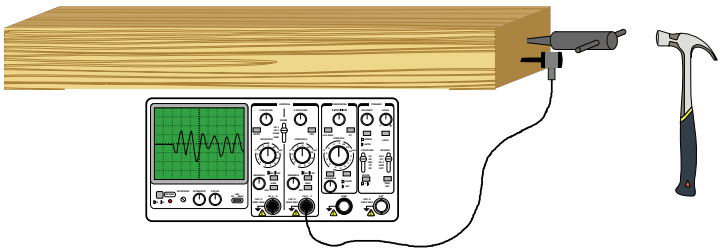

Figure 3.4 Experimental setup for evaluating the SD-02 transducer's impulse response in wood.

The transducer was excited by gently tapping a steel spike inserted in the timber near the transducer. This excitation is an approximation to an impulse excitation. Although a true impulse is not physically possible, the excitation is impulse-like in the sense that it contains a wider bandwidth than the transducer itself. The broad-bandwidth nature of the excitation was expected to excite any resonances in the wood-transducer system, allowing frequency domain analysis to be performed.

3.2.2 The transducer's impulse response in timber

The signal recorded by the transducer is shown in Figure 3.5(a). The signal displays a high-frequency transient at the beginning, this decays away after approximately 1500 μs. After this time the signal oscillates at a lower frequency. This low-frequency oscillation takes much longer to decay, extending to the right of the figure.

The FFT magnitude of the signal is shown in Figure 3.5(b). The plot shows a large peak at approximately 30 kHz, this is the resonant frequency of the transducer, given by (3.3). The spectrum also shows another peak at approximately 50 kHz. The origin of this peak is unknown, though it may be due to an internal resonance of the crystal. Woods' model of the transducer considered the crystal's electrical port as a lumped capacitance (C_p in Figure 3.3). More complex models of piezoelectric crystals are available, which incorporate the crystal's internal resonances [Mason 1964], though these models have not been considered in this analysis.

The spectrum also contains a low-frequency peak at approximately 2.75 kHz. It was expected initially that this peak is due to the fundamental longitudinal resonance of the timber. However, this would correspond to a resonance velocity of 7370 ms^{-1}, which is unusually high for radiata pine. Subsequent measurements using the SD-02 in standing trees (see Section 4.4) have revealed that a dominant peak in the frequency response consistently occurs at approximately 3 kHz.

Woods' model does not include the loading effect of a radiation impedance. In the generic transducer circuit, shown in Figure 3.1, the radiation impedance is included

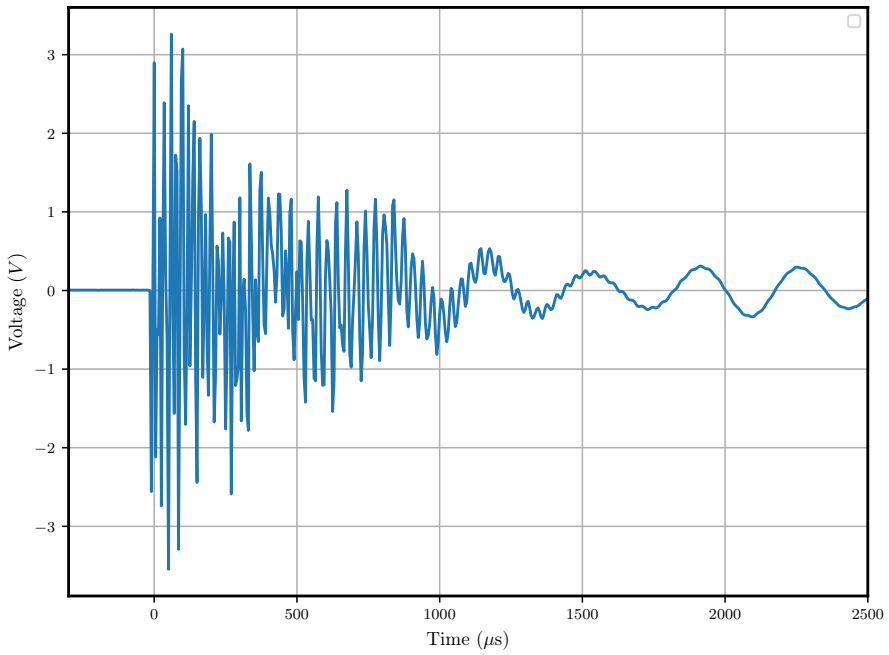

(a)

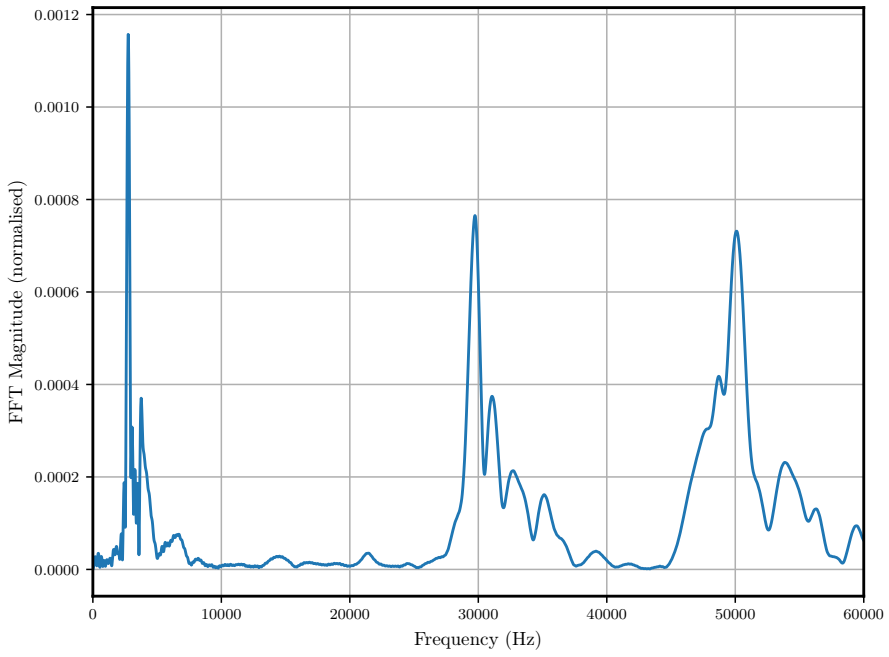

(b)

Figure 3.5 Response of the SD-02 transducer to an impulse-like excitation. The time-domain signal (a), and its FFT spectrum (b).

as an acoustic load, Z_r. The unknown peak at approximately 3 kHz might be caused by the radiation impedance load. If the radiation impedance acts like a compliance at 3 kHz, then it can form a harmonic oscillator with the transducer's mass, forming a resonance in the response. This phenomenon is known as *contact resonance* [Johnson 1985]. This interaction is interesting from a wood quality perspective because the radiation impedance is a function of the wood's mechanical properties. Thus, if the radiation impedance can be measured, it might be possible to infer something about the mechanical properties. To explore this effect, a physical model of the impedance of the wood (seen by the transducer) is required. In the following section, the concept of a radiation impedance model is introduced, and several potential models to describe the observed effect are proposed.

3.3 RADIATION IMPEDANCE MODELS

Radiation impedance is the specific acoustic impedance, $Z(f) = P(f)/U(f)$, taken at the interface between a radiator and the medium it is radiating-to or receiving-from [Bose 1995]. The radiation impedance is a complex quantity, which defines how energy is transferred between the transducer and the medium [Kinsler et al. 2000]. The radiation impedance is interesting for non-destructive testing applications because it is a function of the mechanical parameters of the medium, as well as the radiating device itself. The real component of the radiation impedance, R_r, defines the amount of real power radiated between the *far field* of the medium and the transducer. The imaginary component, X_r, defines the amount of energy which oscillates between the *near field* of the medium and the transducer. The total radiation impedance is given by

$$Z_\mathrm{r} = R_\mathrm{r} + jX_\mathrm{r}. \tag{3.4}$$

In the ideal case, the radiation impedance is purely real, and equal to the characteristic impedance of the medium, which is given by

$$Z_0 = \rho c \tag{3.5}$$

[Kinsler et al. 2000], which is also equal to the impedance of a plane wave.

The generalised transducer model (Figure 3.1) can be inverted so that it is operating as a receiver, which is the typical mode of operation for the SD-02. It is not immediately clear how the radiation impedance should be included in this new model, i.e., whether it should be placed in series or in parallel with the source. Tilmans [1996] showed that a lumped-element model of a transducer in receive mode is equivalent to that shown in Figure 3.6. In this circuit, the source is in series with the radiation impedance. This arrangement is used in subsequent transducer models incorporating the radiation impedance.

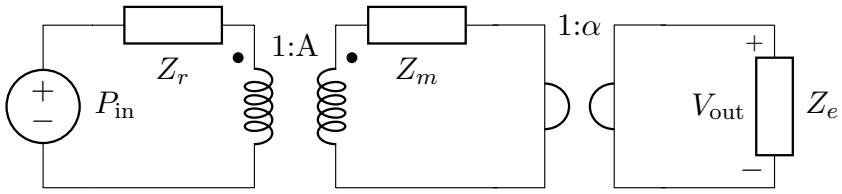

Figure 3.6 General model of an acoustic transducer operating as a receiver. This circuit is the reciprocal of that shown in Figure 3.1; the input signal is a pressure phasor and the output signal is a voltage. The radiation impedance Z_{r} is in series with the driving source.

3.3.1 Pulsating spherical source in a fluid

A spherical source is one of the simplest possible three-dimensional acoustical radiators. A pulsating spherical source, as the name suggests, is a sphere whose radius, r, is expanding and contracting at a prescribed frequency, with a prescribed velocity or pressure amplitude [Olson 1957]. It has no dependence on rotational angle, radiating equally in all directions.

The simplest type of radiation-impedance load is that of a pulsating sphere operating in a lossless fluid. In this chapter, this radiation-impedance model is referred to as the *fluid* model. The fluid model is presented because it is the most basic three-dimensional radiation impedance which can be calculated. The fluid model serves as a comparison for other, more complex models. It can be shown that the radiation impedance for the fluid model is given by

$$\begin{aligned} Z_{\text{r(fluid)}} &= \frac{F}{U} \\ &= AZ_0 \frac{(kr)^2 + jkr}{1 + (kr)^2}, \end{aligned} \tag{3.6}$$

[Kinsler et al. 2000, Mason 1948, Olson 1957]; where F, U, and $Z_{\text{r(fluid)}}$ are the complex amplitudes: force, velocity and mechanical impedance, respectively. A is the spherical radiator's surface area; k is the wavenumber, equal to $k = \omega/c$; r is the radius of the sphere; and Z_0 is the characteristic impedance of the medium. Note that the area, A, has been included because the radiation impedance has been translated into a mechanical impedance. In terms of the generalised transducer circuit of Figure 3.6, this means that the radiation impedance was moved to the mechanical side of the transformer.

This impedance is equivalent to a mass connected in series with a damper[4]. The magnitude of the damper is

$$\eta = AZ_0, \tag{3.7}$$

and the magnitude of the mass is

$$m = AZ_0 \frac{r}{c}. \tag{3.8}$$

[4]These components, and their equivalent-circuit elements, are defined in Appendix C

Using the analogies of Table C.1, this impedance corresponds to a resistor with value given by (3.7) in parallel with an inductor with value given by (3.8). The fluid model is explored more fully in Section 3.4, where it is compared to several other models.

3.3.2 Pulsating spherical source in an isotropic elastic medium

The next model considered was that of a spherical source operating in an isotropic elastic solid. Blake [1952] derived an expression for the radiation impedance of a spherical radiator in an isotropic solid. In this model, Blake considered a spherical source of radius r operating in an infinite, isotropic, homogeneous medium of density ρ, with Young's modulus E, and Poisson's ratio ν. Blake calculated the radiation impedance by substituting the spherical wave solution into the wave equation for an isotropic solid. Blake's radiation impedance, converted into a mechanical impedance, is given by

$$\begin{aligned} Z_{\mathrm{r(Blake)}} &= \frac{F}{U} \\ &= R_{\mathrm{r(Blake)}} + jX_{\mathrm{r(Blake)}}. \end{aligned} \tag{3.9}$$

$R_{\mathrm{r(Blake)}}$ is given by

$$R_{\mathrm{r(Blake)}} = AZ_0 \frac{(kr)^2}{1+(kr)^2}, \tag{3.10}$$

which is identical to the real part of (3.6). $X_{\mathrm{r(Blake)}}$ is given by

$$X_{\mathrm{r(Blake)}} = -AZ_0 \frac{1+(1-K)(kr)^2}{Kkr\left[1+(kr)^2\right]}, \tag{3.11}$$

where K is a constant, given by

$$K = \frac{1}{2}\frac{(1-\nu)}{(1-2\nu)}, \tag{3.12}$$

where ν is Poisson's ratio. Blake expressed (3.11) in terms of K instead of the Lamé parameters for brevity.

A fluid can be described as a material with a shear modulus equal to 0. This occurs when $\nu = 0.5$ [Boresi et al. 1993]. For Blake's model, when $\nu = 0.5$, K is infinite, and (3.11) is equal to the imaginary component of (3.6). Blake's model can therefore be considered a generalisation of the fluid model, as it incorporates both compressional and shear elastic forces. Blake's model is explored more fully in Section 3.4.

3.3.3 Oscillating spherical source in an isotropic viscoelastic medium

The next model considered was that of an *oscillating spherical source* in an isotropic viscoelastic medium. An oscillating spherical source is a rigid sphere which oscillates along one axis in translation with a prescribed pressure or velocity amplitude.

Oestreicher [1951] derived an expression for the radiation impedance of the oscillating sphere in a viscoelastic medium. The objective of Oestreicher's work was to determine the mechanical load on a radiator operating in human tissue, which is known to behave viscoelastically. Oestreicher explained that the oscillating sphere source was chosen because of its similarity to the piston radiator, which is commonly used in experiments, while also being significantly simpler than the piston to quantify mathematically. Oestreicher's model was considered for the SD-02 transducer's radiation impedance because wood is also known to behave viscoelastically [Bucur 2006]. Additionally, the spike-like shape of the SD-02 loosely resembles a piston when embedded in wood.

The impedance calculated by Oestreicher is given by

$$\begin{aligned} Z_{\text{oest}} &= \frac{F}{U} \\ &= AZ_0 \frac{jr}{3}\Psi, \end{aligned} \tag{3.13}$$

where

$$\Psi = \frac{\left(1 - \frac{3j}{rk_2} - \frac{3}{r^2k_2^2}\right) - 2\left(\frac{j}{rk_2} + \frac{1}{r^2k_2^2}\right)\left(3 - \frac{r^2k_1^2}{rk_1j+1}\right)}{\left(\frac{j}{rk_2} + \frac{1}{r^2k_2^2}\right)\frac{r^2k_1^2}{rk_1j+1} + \left(2 - \frac{r^2k_1^2}{rk_1j+1}\right)}, \tag{3.14}$$

r is the radius of the sphere, k_1, k_2 are the medium's compressional and shear wavenumbers, respectively, given by

$$k_1 = \sqrt{\frac{\rho\omega^2}{2\mu + \lambda}}, \tag{3.15}$$

$$k_2 = \sqrt{\frac{\rho\omega^2}{\mu}}, \tag{3.16}$$

where λ is Lamé's first (compressional) parameter, and μ is Lamé's second (shear) parameter, each of these parameters is composed of both elastic and viscous components,

$$\lambda = \lambda_1 + j\omega\lambda_2, \tag{3.17}$$

$$\mu = \mu_1 + j\omega\mu_2. \tag{3.18}$$

Oestreicher explains that the model can be used to describe several different types of materials, depending on the values chosen for λ and μ. For example, a frictionless fluid may be modelled by choosing $\mu_1 = \mu_2 = \lambda_2 = 0$. For the frictionless fluid case, (3.13) reduces to the impedance of the oscillating sphere in a fluid, derived by Olson [1957]. Oestreicher's impedance can also model a frictionless isotropic solid by setting the viscosity parameters, $\lambda_2 = \mu_2 = 0$.

Zhang et al. [2001] explains that the Oestreicher impedance can be modified to better approximate a piston oscillating in a half-space by dividing (3.13) by 2. This

follows logically from the fact that a piston in a half-space only has the elastic medium on one side, while the sphere is completely enclosed. von Gierke et al. [1952] found that Oestreicher's model predicted impedance values which overestimated the static stiffness of the tissue medium by a factor of 1.18.

The modified version of the Oestreicher impedance, as described by Zhang et al. [2001], is given by

$$Z_{\text{Zhang}} = \frac{Z_{\text{oest}}}{2 \cdot 1.18}. \tag{3.19}$$

This will be referred to as the *Zhang* impedance.

3.4 COMPARISON OF RADIATION IMPEDANCE MODELS

Each of the radiation impedance models discussed in Section 3.3 was evaluated for a range of frequencies. In order to evaluate the models, the model's parameters were estimated by approximating the transducer's effective-radius and the wood's effective mechanical properties. The SD-02's steel spike (Figure 3.2) has a cross-sectional diameter of approximately 5 mm when inserted at a depth of 2 cm. It is unclear how these dimensions would translate to an effective radius, as required by the proposed models. A radius of $r = 10\,\text{mm}$ was chosen for evaluating the models. The experiment to evaluate the transducer's response was performed in dry *Pinus radiata* timber, which has a density of approximately $500\,\text{kg/m}^3$. All of the models suggested in Section 3.3 assume an isotropic medium, which is obviously inappropriate for modelling wood (see Section 1.1.2). The experiment described in Section 3.2.1 placed the transducer in the direction of the wood's grain, therefore, it is assumed that the effective elastic parameters presented by the wood correspond to the along-grain stiffness. A Young's modulus value was assumed at 9 GPa.

To calculate the impedance of the fluid model, an effective value of the acoustic velocity, c, is required. This was calculated using the standard equation for a lossless isotropic medium (1.6).

In order to plot a reactance for Blake's model, an approximate value of Poisson's ratio in dry *pinus radiata* timber was selected. Wood is typically modelled as orthotropic. Therefore, rather than a single value for Poisson's ratio, there are three mutually exclusive values: ν_{LR}, ν_{LT}, and ν_{RT}. The first subscript indicates the direction of applied stress. For the experiment described in Section 3.2.1, the stress was applied longitudinally. Mean values of Poisson's ratio for a range of wood species are given by Kretschmann [2010]. The average values for the pine species listed by Kretschmann for ν_{LR} and ν_{LT} are 0.336 and 0.355, respectively. Kretschmann [2010] explains that these values vary considerably between and within species. A value of $\nu = 0.35$ was selected for plotting these models.

The real and imaginary components of the fluid impedance are plotted in Figure 3.7.

The impedance components were plotted for the approximate mechanical values of the SD-02 transducer in dry pine timber, as listed in the caption of Figure 3.7.

Oestreicher's model is slightly more complex due to the addition of the viscosity parameters, λ_2 and μ_2. It is not immediately clear how these parameters should be selected to approximate the viscosity of wood tissue. To observe the effect of these parameters on the Oestreicher model, the model has been plotted for two cases: with the viscosity parameters set to zero, and with the viscosity parameters set to small values ($1/1000^{\text{th}}$ of λ_1 and μ_1, respectively). These cases are referred to as the *Oestreicher-Elastic* and *Oestreicher-Viscoelastic* models.

The fluid model has both real (resistive) and imaginary (reactive) components. The fluid impedance is purely real when $\omega \gg c/r$, or equivalently when $r \gg L/2\pi$, where L is the wavelength. Distances greater than $L/2\pi$ correspond to the far field, where real power is radiated. When $r \ll L/2\pi$, the impedance is dominated by the imaginary component. At these frequencies, the impedance appears like a mass, this represents energy which oscillates only within the near field.

Blake's model also exhibits near and far field effects. The real component of Blake's impedance is identical to that of the fluid model, as displayed in Figure 3.7(a). The magnitude of the reactive component of Blake's model is plotted in Figure 3.7(b). In contrast to the fluid model, Blake's model does not have a positive imaginary component at all frequencies. Blake [1952] explained that when $K < 1$, i.e., when $\nu < \frac{1}{3}$, $X_{\text{r(Blake)}}$ is negative for all frequencies. In this case the reactance is spring-like at all frequencies. When $K > 1$, i.e., when $\nu > \frac{1}{3}$, there is a frequency at which $X_{\text{r(Blake)}}$ goes from negative, to positive, i.e., from spring-like to mass-like. This effect is not obvious in the plot shown in Figure 3.7(b), as the logarithmic plot does not show the sign of the impedance. In this particular plot, the transition from spring-like to mass-like occurs just below 300 kHz.

Figure 3.7(a) shows the real component of the Oestreicher model for both of these cases. The real component is approximately constant over the frequency range of interest, though the viscous case does trend upwards slightly with frequency. Figure 3.7(b) shows the imaginary part of the Oestreicher impedance for both cases. For the elastic case, the impedance is spring-like at all frequencies. For the viscous case, the impedance switches from spring-like to mass-like at approximately 9 kHz. The Zhang model has not been included in Figure 3.7 because it is simply a scaled version of the Oestreicher model.

Perhaps a better model for the transducer in a piece of wood is that of a piston oscillating in an elastic half-space. Miller and Pursey [1954] provided integral solutions for the field resulting from a vertical oscillation of a circular disk on the surface of an elastic half-space. They also calculated an average of the field equations across the surface of the piston to find a radiation impedance solution. Robertson [1966]

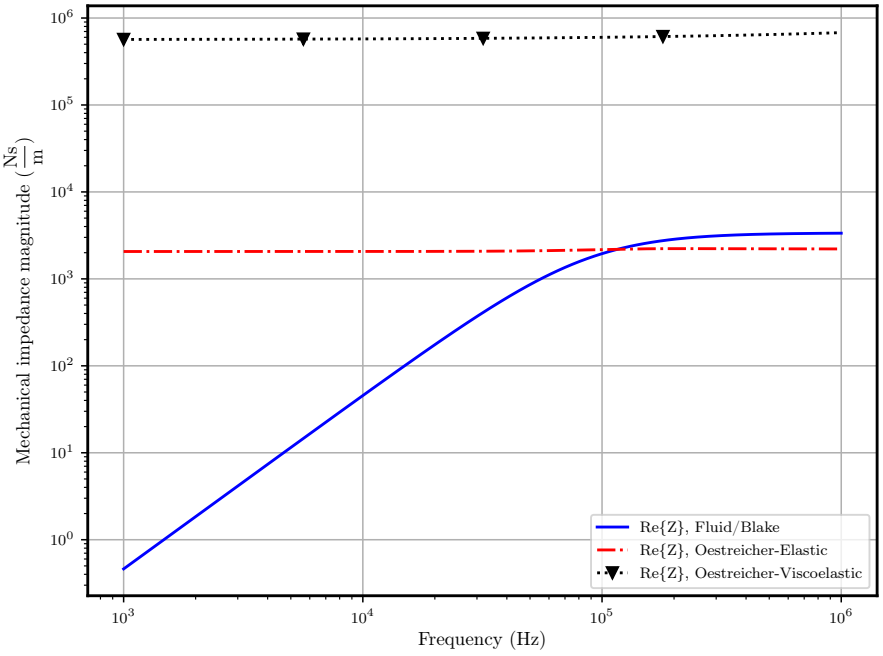

(a)

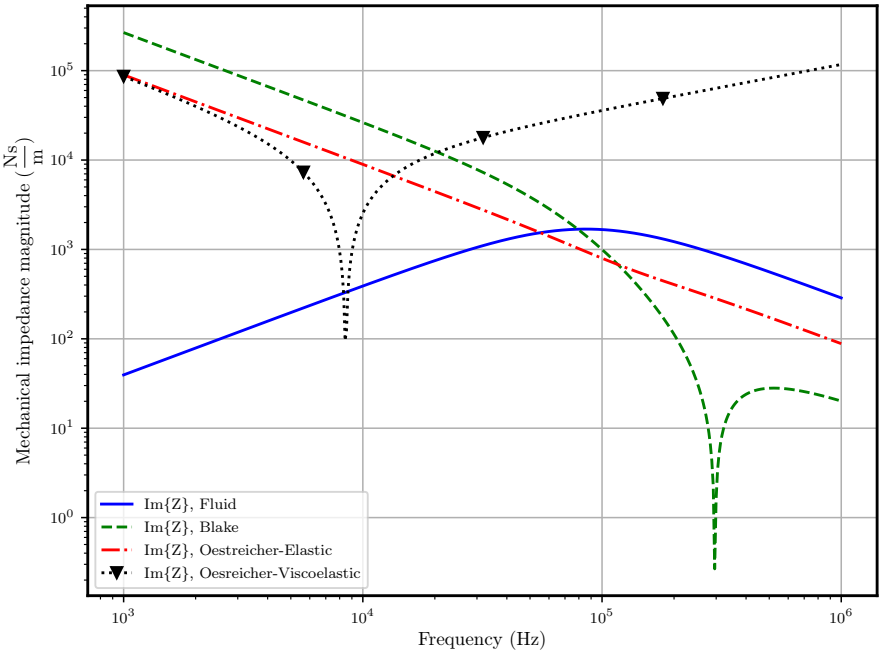

(b)

Figure 3.7 The real component (a), and the imaginary component (b), of the radiation impedance for the fluid model, Blake model, and Oestreicher model. All models were plotted with the parameters: $r = 0.01\,\text{m}$, $\rho = 500\,\text{kg/m}^3$, $E = 9\,\text{GPa}$. For the Blake and Oestreicher models, Poisson's ratio was set to $\nu = 0.35$. For the viscoelastic case of Oestreicher's model, the viscosity parameters λ_2, and μ_2 were set to $1/1000^{\text{th}}$ of the corresponding elastic parameter.

presented a solution to the oscillating piston in an elastic half-space as a Fredholm integral. Other work by Gladwell [1968] used the contact impedance concept for the design of an ultrasonic harness tester. These studies were not considered as possible candidates for the radiation impedance model, though they may be considered in future work.

3.5 RESPONSE OF THE TRANSDUCER MODEL WITH RADIATION IMPEDANCE LOADING

Woods [2006] calculated an expression for the frequency response of the SD-02 model, and plotted this expression as a Bode plot. In this section, the transducer model's frequency response is calculated again. In this case, the transducer is loaded with each of the radiation impedance models proposed in Section 3.3, and the effect of each of these models are explored.

To plot the transducer's response when loaded with an arbitrary impedance, an electronic-circuit simulation system is required. *Lcapy* is an open source software library for performing *linear circuit analysis in Python* [Hayes 2014]. Lcapy uses symbolic computation to analyse arbitrary electrical circuits[5]. Lcapy is capable of performing similar operations to a SPICE-based simulator. A useful feature of Lcapy, which is not generally found in SPICE simulators, is the ability to describe a component using an arbitrary frequency-domain impedance expression. This can be used to describe the radiation impedance as a lumped element.

A net list for the SD-02 transducer model shown in Figure 3.3 was created. Each of the proposed radiation impedance models was then defined symbolically as an expression in ω. Each impedance was then added in series with the device's mechanical port, as shown in Figure 3.6. The transfer function was found, using Lcapy to calculate the ratio between the input force and the output voltage, as a symbolic frequency domain expression,

$$H_{\text{loaded}} = \frac{V_{\text{out}}(j\omega)}{F_{\text{in}}(j\omega)}, \tag{3.20}$$

where V_{out} and F_{in} refer to the corresponding quantities in Figure 3.6 (P_{in} was shifted to the other side of the transformer to become a force input, F_{in}).

Figure 3.8 shows the resulting frequency domain expression as a Bode plot[6]. The unloaded response has a large resonant peak at 30 kHz, but does not excite a lower frequency resonance. For the selected parameters, the fluid impedance has a negligible effect on the transducer's response. The Blake, Oestreicher-Elastic, and Zhang models introduce a low-frequency resonance in the response. The Oestreicher-Viscoelastic

[5]See `http://lcapy.elec.canterbury.ac.nz` for more information about Lcapy.
[6]For an overview of Bode plots, see [Hayt et al. 2002].

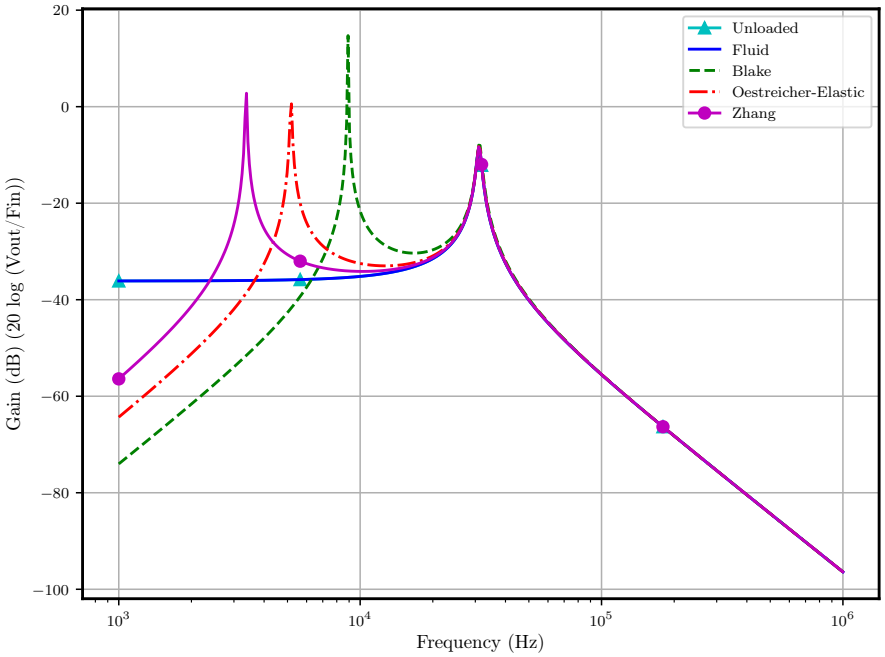

Figure 3.8 The frequency response of the SD-02 transducer model for various radiation impedance loads. The included loads are: no-load, fluid, Blake, Oestreicher-Elastic, Zhang models, and Oestreicher-Viscoelastic; plotted with parameters: $r = 1\,\text{mm}$, $\rho = 500\,\text{kg/m}^3$, $E = 9\,\text{GPa}$, $\nu = 0.35$. For the Oestreicher-Viscoelastic case, the viscosity parameters were set to $1/1000^{\text{th}}$ of the corresponding elastic parameters.

model was not included in this plot because Lcapy, unfortunately, is currently unable to symbolically solve the loaded transfer function using this model.

Resonance in a series electrical circuit occurs when the reactive component is at a minimum [Hayt et al. 2002]. The low frequency resonance peaks in Figure 3.8 occur at the frequencies at which $\text{Im}\{Z_{\text{in}}\} = -\,\text{Im}\{Z_{\text{r}}\}$, where Z_{in} is the mechanical impedance seen looking into the transducer's input port. To determine the frequency at which this occurs, the total impedance was calculated using Lcapy,

$$Z_{\text{total}} = Z_{\text{in}} + Z_{\text{r}}. \tag{3.21}$$

(3.21) was then solved numerically to find the first root of the imaginary component. The resonant frequency of the Blake, Oestreicher-Elastic, Zhang, and Oestreicher-Viscoelastic models were calculated for a range of radii, with the other parameters fixed. The results of this analysis are shown in Table 3.2. The resonant frequencies of the loaded models were then determined for a range of Young's modulus values, with the other parameters fixed. The results are shown in Table 3.3. The resonant frequencies of the loaded models were then determined for a range of Poisson's ratio values, with the other parameters fixed. The results are shown in Table 3.4. These analyses demonstrate that the selected models are all dependent on radius, Young's modulus, and Poisson's ratio.

Table 3.2 Resonant frequencies for the combined transducer-radiation impedance model, for various radii. (a) Blake model, (b) Oestreicher-Elastic model, (c) Zhang model, and (d) Oestreicher-Viscoelastic model. Calculated using parameters: $\rho = 500\,\mathrm{kg/m^3}$, $E = 9\,\mathrm{GPa}$, $\nu = 0.35$.

(a)

Radius (mm)	f Resonance (Hz)
0.1	2821.07
0.2	3988.42
0.5	6300.87
1.0	8896.61
2.0	12532.80

(b)

Radius (mm)	f Resonance (Hz)
0.1	1636.04
0.2	2313.51
0.5	3656.94
1.0	5169.25
2.0	7302.99

(c)

Radius (mm)	f Resonance (Hz)
0.1	1065.01
0.2	1506.11
0.5	2381.12
1.0	3366.71
2.0	4759.33

(d)

Radius (mm)	f Resonance (Hz)
0.1	1635.38
0.2	2310.27
0.5	3631.62
1.0	5050.24
2.0	6766.51

Table 3.3 Resonant frequencies for the combined transducer-radiation impedance model, for various values of Young's modulus. (a) Blake model, (b) Oestreicher-Elastic model, (c) Zhang model, and (d) Oestreicher-Viscoelastic model. Calculated using parameters: $\rho = 500\,\mathrm{kg/m^3}$, $\nu = 0.35$, $r = 1.0\,\mathrm{mm}$.

(a)

Young's mod (GPa)	f Resonance (Hz)
1.0	2973.40
2.0	4203.69
5.0	6640.18
10.0	9374.52
20.0	13204.68

(b)

Young's mod (GPa)	f Resonance (Hz)
1.0	1724.52
2.0	2438.55
5.0	3854.56
10.0	5448.21
20.0	7696.45

(c)

Young's mod (GPa)	f Resonance (Hz)
1.0	1122.63
2.0	1587.57
5.0	2509.83
10.0	3548.69
20.0	5016.38

(d)

Young's mod (GPa)	f Resonance (Hz)
1.0	1702.01
2.0	2400.33
5.0	3777.94
10.0	5319.46
20.0	7481.02

Table 3.4 Resonant frequencies for the combined transducer-radiation impedance model, for various values of Poisson's ratio. (a) Blake model, (b) Oestreicher-Elastic model, (c) Zhang model, and (d) Oestreicher-Viscoelastic model. Calculated using parameters: $\rho = 500\,\mathrm{kg/m^3}$, $E = 9\,\mathrm{GPa}$, $r = 1.0\,\mathrm{mm}$.

(a)

Poisson's (ν)	f Resonance (Hz)
0.00	10325.04
0.10	9848.58
0.20	9432.50
0.30	9064.94
0.40	8737.29

(b)

Poisson's (ν)	f Resonance (Hz)
0.00	5672.36
0.10	5469.95
0.20	5313.40
0.30	5203.95
0.40	5150.65

(c)

Poisson's (ν)	f Resonance (Hz)
0.00	3694.87
0.10	3562.85
0.20	3460.76
0.30	3389.33
0.40	3354.63

(d)

Poisson's (ν)	f Resonance (Hz)
0.00	5543.63
0.10	5346.94
0.20	5194.02
0.30	5085.70
0.40	5029.57

3.6 EFFECT OF ADDITIONAL MASS ON THE TRANSDUCER

The radiation impedance models predict that the transducer's total mass influences its low-frequency resonance. Specifically, as the mass increases, the low-frequency resonance should decrease in frequency. To illustrate this, the transducer model, loaded with the Blake impedance, is plotted in Figure 3.9. In this plot, the transducer's mass has been incrementally increased from its base mass of 50 g, up to a total mass of 100 g. The low-frequency resonance has significantly decreased as the mass was increased.

3.6.1 Added-mass experiment

An experiment was performed to measure the transducer's frequency response as mass is added to the transducer. Two SD-02 transducers were inserted in a standing Beech tree. A steel spike was inserted in the tree near the bottom of the stem, for exciting the stress wave. One transducer was placed 20 cm up the tree from the steel spike. The other transducer was placed 80 cm above the lower transducer. The lower transducer was designated the *reference channel*, no additional mass was added to this transducer. The upper transducer was designated the *mass* channel, Blu-Tack was added to this transducer in 5 g increments. For each mass, the spike was hit 10 times with a hammer. For each hit, the signal at each transducer was recorded using an oscilloscope.

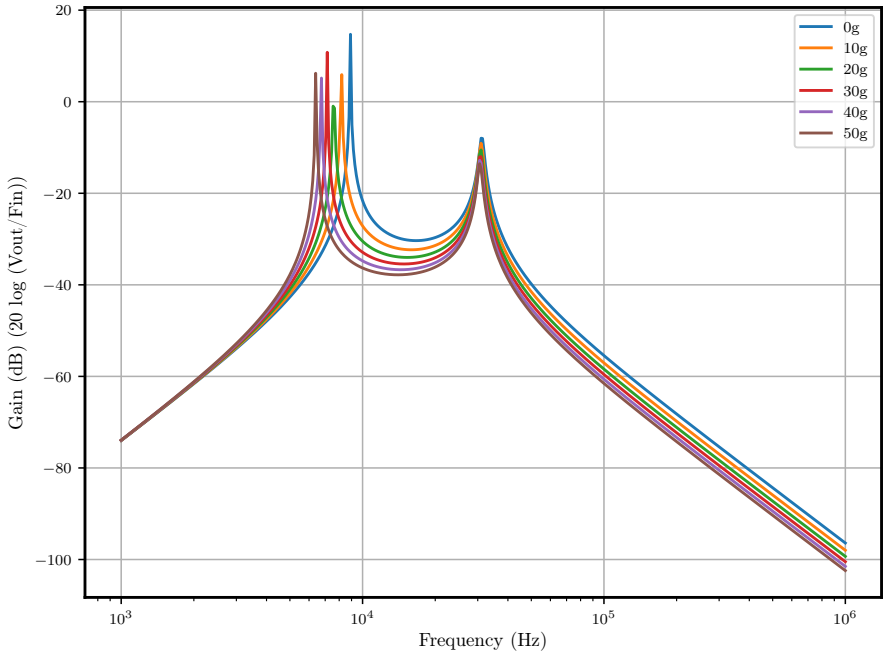

Figure 3.9 The effect of additional mass on the transducer's frequency response. The transducer was loaded with the Blake impedance with parameters: $r = 1\,\text{mm}$, $\rho = 500\,\text{kg/m}^3$, $E = 9\,\text{GPa}$, and $\nu = 0.35$.

3.6.2 Results

Figure 3.10 shows the spectrum of the mass channel for a single measurement. The signal was normalised by dividing it, in the time domain, by the reference channel's RMS value. The three most prominent peaks in the spectrum occur at approximately 1450 Hz, 1640 Hz, and 2300 Hz.

The frequency of each of these peaks is plotted against added mass in Figure 3.11. In this plot, the peak frequency has been subtracted from the zero-mass peak frequency. Thus, the plot shows the deviation of each peak. This plot demonstrates that none of the peaks have shifted significantly as mass was added. This finding is unexpected, as it was hypothesised that one of the peaks would decrease in frequency, as predicted by the Blake-loaded model (Figure 3.9).

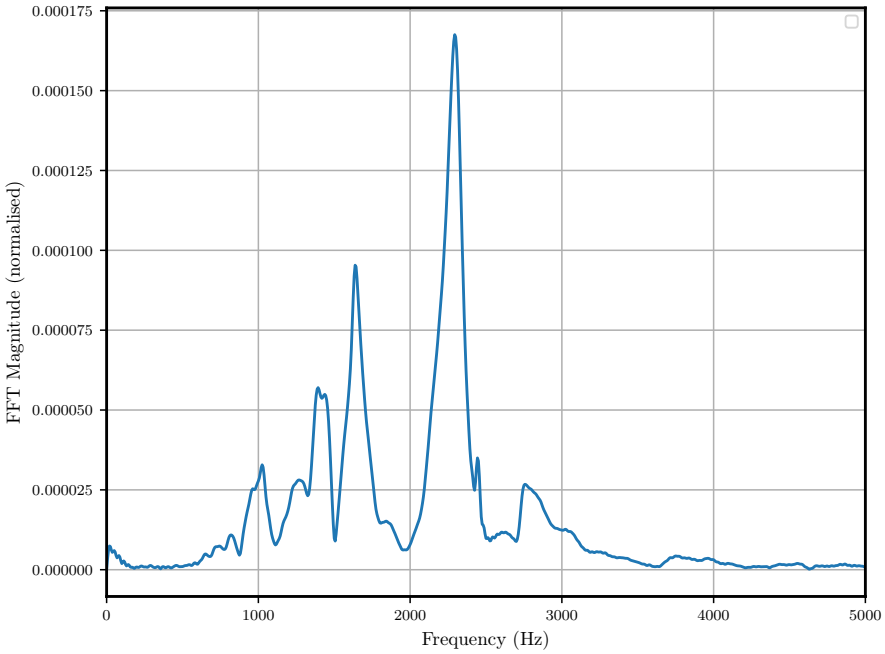

Figure 3.10 Spectrum of one signal captured during the added-mass experiment.

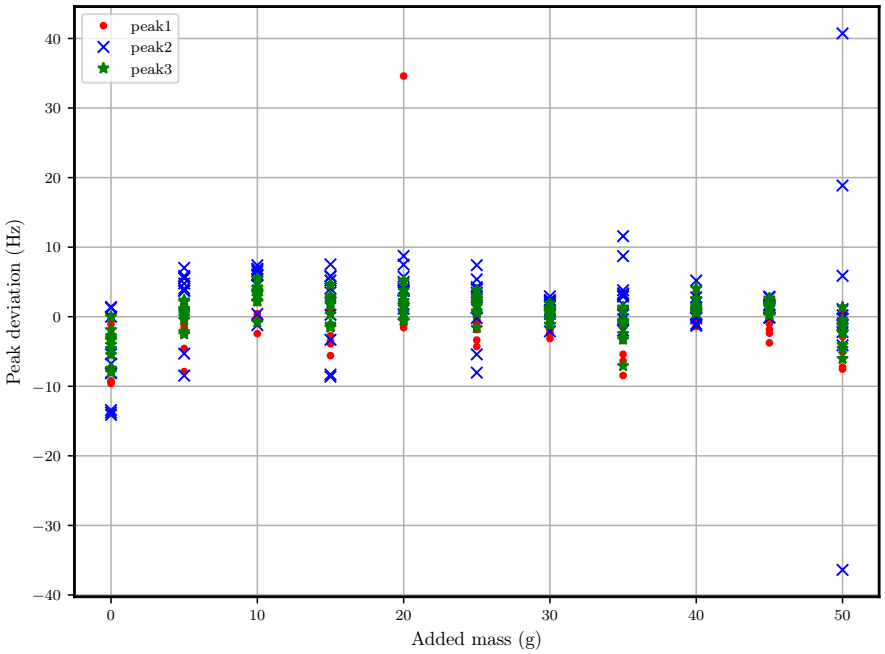

Figure 3.11 Peak-frequency deviation versus added mass. Deviation is plotted for the three most prominent peaks: peak 1 ~1430 Hz, peak 2 ~1640 Hz, and peak 3 ~2300 Hz.

3.7 DISCUSSION

In this chapter, the concept of radiation impedance was applied to a lumped-element model of the Fakopp SD-02 transducer. Three different model types were considered for this analysis, referred to as the Fluid model, the Blake model, and the Oestreicher model. Two variations on the Oestreicher model were also considered, referred to as the Oestreicher-Viscoelastic model and the Zhang model. It was hypothesised that the prominent peak in the transducer's frequency response, which is typically found in the 2-3 kHz range, is due to the radiation impedance resonating with the transducer's mass. This effect is sometimes referred to as *contact resonance* [Johnson 1985].

The models selected in this chapter simplify some aspects of the real wood-transducer system. For example, all of the proposed models assumed an isotropic medium. Wood, however, is known to be anisotropic (see Section 1.1.2). Additionally, the models all treated the radiator as either a pulsating or oscillating sphere. Perhaps a piston model would be a better description of the spike-shaped SD-02 transducer. The proposed models contain a number of parameters including stiffness, density, effective radius, Poisson's ratio, and viscosity. The approach taken in this chapter was to estimate each of these parameters, to see whether the resulting models would describe the behaviour of the transducer in a standing tree. A problem with this approach is that many of the model parameters interdependent. For instance, Tables 3.2, 3.3, and 3.4 show that the resonant frequency can be tuned by adjusting either radius, stiffness, or Poisson's ratio. Therefore, in order to use a radiation impedance model to predict a mechanical property, the other related properties would need to be measured, or accurately estimated, ahead of time.

It was shown in Section 3.6 that the transducer, loaded with the Blake model, predicts that the lower-frequency resonance of the transducer should decrease as the mass of the transducer is increased. The Blake model was used in this analysis, but similar behaviour is observed for any radiation impedance which presents a stiffness (rather than a mass) in the transducer's low frequency range. An experiment was performed to measure the effect of additional mass on the transducer. It was found that none of the peaks in the probe's response deviated significantly as mass was added. This suggests that the measured peaks are not due to the contact resonance of the radiation impedance with the probe's mass. The observed peaks may be due to an unforeseen resonant frequency, such as a radial or tangential mode through the stem, or possibly due to a mode within the spike itself.

Another possible explanation is that one (or more) of the peaks is due to the contact resonance of the steel spike. The spike used in the experiments is approximately 250 g, significantly heavier than the transducer. This decreases its contact resonance. However, the spike is also thicker than the transducer, thus has a larger effective radius. This increases the low frequency resonance (as shown in Table 3.2). Thus, it may be that

the spike produces a contact resonance in the same frequency range as the transducer.

It may be that a peak was not observed at the contact resonance frequency because the spike's excitation did not contain sufficient energy at that frequency. The loaded frequency response (Figure 3.9) also predicts that other parts of the transfer function are effected by the additional mass. For example, the loaded model predicts that the gain in the passband (between the two resonances) should be reduced as mass is added. This behaviour could be described by simplifying the loaded model to that of a linear time-invariant system, described in the Laplace domain as

$$Y(s) = H(s)X(s), \tag{3.22}$$

where $X(s)$ is the transform of the excitation signal, and $H(s)$ is the transform of the system's transfer function, which describes the response of the transducer, including the radiation impedance loading. The response of the transducer with additional mass added would be described by a modified transfer function $Y'(s) = H'(s)X(s)$. Y can be used to estimate Y', provided that the transfer functions are known,

$$Y'(s) = \frac{H'(s)}{H(s)}Y(s). \tag{3.23}$$

Or inversely, (3.23) can be used to estimate the transfer function, $H(s)$, if $Y'(s)$ and $Y(s)$ are measured. This would typically be performed using a numerical optimisation method. This analysis is left for future work.

Chapter 4

DISPERSION MODELS AND THEIR APPLICATION TO WOOD ACOUSTICS

The time of flight (ToF) method is a well established technique for evaluating wood quality in standing trees. However, the method is known to overestimate wood's stiffness when compared to other techniques, such as acoustic resonance or static bending tests. This is relevant because engineering applications are mostly interested in the static stiffness of wood. Acoustic tools, in contrast, measure the dynamic stiffness of wood. Similarly, wood quality researchers are interested in comparing data between these various methods of measuring wood stiffness. Therefore, it is important to understand the relationship between dynamic and static stiffness.

Some authors have suggested that the ToF method measures the stress-wave velocity through the high-stiffness outerwood, and thus provides an overestimation of the tree's overall longitudinal stiffness [Chauhan and Walker 2006][1]. In Section 1.2.5, a study by Grabianowski et al. [2006] was examined. The authors found that the ToF method tends to measure a greater velocity than the resonance method, even when measuring cut pieces of timber from a particular part of the tree. This finding suggests that the overestimation of the ToF method is not entirely due to propagation through the outerwood.

Another explanation for the overestimation of the ToF method is due to the phenomenon of acoustic dispersion. In this chapter, this hypothesis is explored through the application of lumped-element viscoelastic-solid models to a ToF system. In Section 4.1, the concepts of acoustic dispersion and attenuation are described. A summary of previous research is provided regarding the measurement of these quantities in wood. In Section 4.2, an overview is provided of viscoelastic transmission-line wave models. Two different viscoelastic models are described, which are then applied to the transmission-line. In Section 4.3, a simulation of a ToF system is described, where a strong dependence on the viscoelastic model parameters is demonstrated. In Section 4.4, an experiment is described, where a series of ToF measurements were performed on a

[1] An overview of studies which documented the overestimation of the ToF method was provided in Section 1.2.4.

standing Beech tree. The aforementioned viscoelastic models were then applied to the measurements to determine values for the model parameters. Finally, in Section 4.5, a discussion of the findings of this chapter is provided.

4.1 ACOUSTIC DISPERSION AND THE TIME OF FLIGHT METHOD

Dispersion is the phenomenon where a wave's phase velocity is a function of frequency [Kolsky 1963]. The dispersion of a material is quantified by the *dispersion relation*, which is typically expressed as

$$\omega(k) = c(k)k \tag{4.1}$$

[Crawford 1968], where k is the angular wavenumber, c is the phase velocity, and ω is the angular frequency. In general, c is a function of k. Or equivalently, c is a function of frequency. It was explained in Section 1.2.5 that wood is viscoelastic in nature, and thus exhibits acoustic attenuation [Bucur 2006]. It can be shown using a Kramers-Kronig relation that this implies wood is also dispersive [O'Donnell et al. 1980, Sachse and Pao 1978, Whitham 1974].

The viscoelastic behaviour of wood may be a significant contributor towards the discrepancy between the ToF and resonance methods. The two measurement techniques are known to produce waveforms with distinctive frequency content. The frequency response of the resonance method's signal contains peaks at the resonant harmonics, which are given by (1.9). The transient response of the ToF method's signal is typically a short burst, which usually means the frequency response is more broad-band. [Ouis 2002] explained that the viscoelastic nature of wood implies that wood's effective stiffness[2] increases with frequency. Therefore, if the ToF response contains energy at higher frequencies than that of the resonance response, a higher measurement of the wave velocity would be expected.

4.1.1 Measurement of attenuation in wood

As explained in Section 4.1, an acoustic medium which exhibits dispersion also exhibits attenuation. If the attenuation coefficient is known, then the dispersion relation can be derived [O'Donnell et al. 1980]. Experimental data on the dispersion of stress waves in wood is not widely available, however, several authors have studied acoustic attenuation in wood. In this section, an overview of these studies is provided, including the methods used to measure acoustic attenuation, and the value of the attenuation coefficient which was determined in each case.

[2]The term *effective stiffness*, also known as the dynamic stiffness, is used in this chapter to describe the wood's frequency dependent stiffness. Mathematically, it is the magnitude of the complex stiffness, which is described for the viscoelastic models provided in Section 4.2.2 and Section 4.2.3.

Bucur [2006] provided a thorough reference text on the use of acoustics for non-destructive testing of wood. She noted that measurements of acoustic dispersion and attenuation in wood are complicated by various factors. These include the physical properties of the substrate, i.e., the wood's elastic and viscous properties; the geometrical characteristics of the specimen under test, both macro-structural and micro-structural; the environmental conditions including temperature, moisture content, and mechanical loading; and the measurement conditions including the sensitivity and frequency response of the transducers, their size and location, the coupling medium, and the dynamic characteristics of the electronic equipment. Bucur and Feeney [1992] noted that the two principle causes of attenuation in wood are *scattering* and *absorption*. Scattering, they noted, is usually related to the size of the wavelength relative to the size of the wood fibres. They also explained that ultrasonic velocity and attenuation are best studied by choosing a source frequency such that the acoustic wavelength lies roughly in a range between the maximum dimension of the anatomical elements and the minimum specimen dimension.

The amount of attenuation in wood is typically expressed in units of dB/cm. The spatial gain of an acoustic wave can be expressed in decibels,

$$A_{\mathrm{dB}} = 20 \log_{10} \left(\exp \left(-z\alpha \right) \right) \tag{4.2}$$

$$= -8.686 z\alpha \tag{4.3}$$

where exp is the exponential function, and α is the attenuation coefficient, which is equal to $-\operatorname{Im}\{k\}$, where k is the wavenumber (see (2.36)), and has units of m^{-1}. The attenuation[3] in dB/cm is then given by

$$\alpha_{\mathrm{dB/cm}} = -\frac{8.686}{100}\alpha. \tag{4.4}$$

Bucur [2006] stated that the attenuation coefficient for compressional waves travelling along the grain is on the order of 2 dB/cm.

A common method of measuring acoustic attenuation in wood is via a *pulse transmission* technique [Bucur and Feeney 1992]. In this method, a transducer is attached to either side of a small wood sample. One of the transducers is driven using a pulse generator. The generator typically drives several cycles at an ultrasonic frequency (potentially ranging from about 100 kHz to several MHz). The attenuation coefficient is deduced by taking the ratio of the received-signal amplitude through the sample to the amplitude with no wood sample between the transducers. Either compressional or shear mode transducers can be used. The transducers can be placed across any of the sample's faces, depending on whether the operator wants to measure along the L, R, or

[3] $\alpha_{\mathrm{dB/cm}}$ is also referred to as the *attenuation coefficient*, or the *absorption coefficient*, though it is perhaps more accurately described as simply attenuation or gain.

T directions.

Okyere and Cousin [1980] used the pulse transmission technique to find the attenuation of longitudinal stress waves in small samples of four different species: White spruce, Red pine, American beech, and Red oak. Ultrasonic pulses were generated at frequencies of 250 kHz, 500 kHz, and 1.0 MHz. They found that each of the measured species displayed a trend of increasing attenuation with frequency. The range of the attenuation coefficients was between 0.5 dB/cm (Red oak at 250 kHz) to 5.0 dB/cm (White spruce at 1.0 MHz). Kamioka [1988] used pulse transmission to evaluate the longitudinal attenuation coefficient of Red lauan wood. Specifically, the effect on the response due to various different coupling substances was examined. Grease was determined to be the ideal coupling material, producing the largest response amplitude. The longitudinal attenuation coefficient of the wood sample due to an ultrasonic pulse of 1 MHz was found to be 1.62 dB/cm. Bucur and Feeney [1992] used pulse transmission to determine the ToF velocity and the acoustic attenuation of small samples of *Aesculus hypocastanum* (horse chestnut). The transducer was pulsed at ultrasonic frequencies ranging from 100 kHz to 1.5 MHz. This was conducted in each of the principle directions; L, R, and T; for both longitudinal and shear modes. They observed significant dispersion in the longitudinal direction between 100 kHz and 250 kHz, with the velocity increasing from approximately $3000\,\mathrm{ms}^{-1}$ to $4000\,\mathrm{ms}^{-1}$. The attenuation over this range was not quoted.

Another method of determining acoustic attenuation is by measuring the decay of reverberations within a sample. It was noted by Dunlop [1983] that the rate of decay is inversely proportional to the amount of absorption in the medium. Ouis [2000] used this technique to find the decay of an induced wave in a harvested log. He measured the decay due to an impulse-like signal in a log of *Picea Abies*, but did not provide a figure for the attenuation coefficient. This method requires that a fixed, known length wood-sample is used. It is therefore unsuitable for use on standing trees, where the ToF method is typically employed.

Studies performed using the pulse-transmission technique have noted that both acoustic velocity and attenuation tend to increase as the pulse frequency is increased [Bucur and Feeney 1992, Okyere and Cousin 1980]. Ouis [2002] provided a theoretical basis for this finding. He explained that the effective stiffness of wood (and most other solids) is expected to increase with frequency. Ouis explained that this follows from the fact that an acoustic medium is causal, i.e., no output response can precede its input. A consequence of this causality is that the real and imaginary parts of the frequency response are interrelated. Ouis [2000] explored a dispersive model of a viscoelastic medium, known as the *fractional Zener model* (defined by [Pritz 1996]) which could potentially be applied to wood studies. Ouis did not apply the viscoelastic model to experimental data, he only hypothesised on the form of the dispersion model for wood.

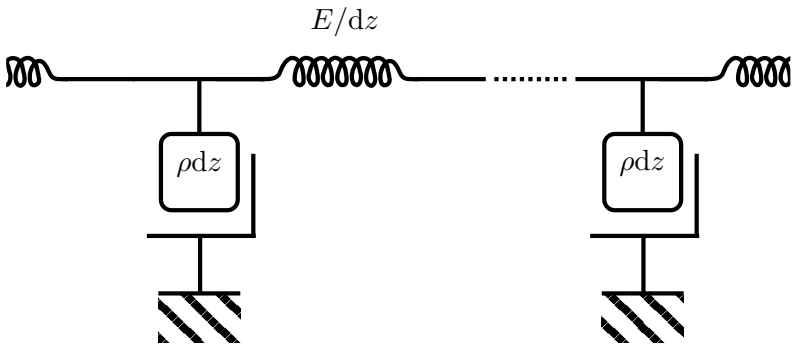

Figure 4.1 The one-dimensional lossless transmission-line model. The top elements are springs with stiffness per unit length $E/\mathrm{d}z$. The bottom elements are masses with values of $\rho\mathrm{d}z$.

4.2 VISCOELASTIC TRANSMISSION LINE MODELS

The wave equation for a stress-wave in a one-dimensional lossless solid is given by

$$\frac{\partial^2\sigma}{\partial t^2} = c^2\frac{\partial^2\sigma}{\partial z^2}, \tag{4.5}$$

where σ is the stress, z is the distance along the medium, and c is the wave's velocity [Feynman et al. 1963]. (4.5) can be derived from a one-dimensional lossless transmission-line model of the medium, such as shown in Figure 4.1. The general solution to (4.5) is given by

$$\sigma(t,z) = f(ct-z) + g(ct+z), \tag{4.6}$$

where f is the forward-travelling solution, and g is the backward-travelling solution. This analysis is a simplification, as real bulk-waves propagating in a material such as wood are three-dimensional, anisotropic, and spread spherically inside a volumetric space, or spread in plane when on the surface.

The one-dimensional solution, (4.6), can also be expressed as a Fourier-domain transfer function. It can be shown that a forcing function applied at the origin will result in a reproduction of that signal at distance z along the line, delayed in time by $\tau = z/c$. Thus, the transfer function in the Fourier domain is given by

$$H(j\omega, z) = \exp\left(jz\frac{\omega}{c}\right), \tag{4.7}$$

$$= \exp\left(jzk\right), \tag{4.8}$$

where k is the wavenumber, or angular spatial frequency, in radians per metre. In the lossless model, the wavenumber is real valued.

(4.7) is a pure phase delay with zero attenuation. To create a lossy model, the wavenumber is allowed to become complex,

$$H(j\omega, z) = \exp\left(-z \operatorname{Im}\{k\}\right) \exp\left(jz \operatorname{Re}\{k\}\right). \tag{4.9}$$

$\operatorname{Im}\{k\}$ is another way of expressing the attenuation coefficient[4], α. Alternatively, if the stiffness, E, is specified as the complex frequency-dependent quantity, (4.7) may be expressed as

$$H(j\omega, z) = \exp\left(j\omega z \sqrt{\frac{\rho}{E}}\right), \tag{4.10}$$

where (1.6) was substituted into (4.7). In sections 4.2.2 and 4.2.3, potential models for describing the complex stiffness, E, are proposed.

4.2.1 Transfer function for the time of flight method

Several variants of the ToF method were described in Section 1.2.3. In the present section, a transfer function is developed for the variant of the ToF method where a metal spike is used to excite the stress wave. This variant is depicted in Figure 1.4. Figure 4.2 shows a block diagram of a linear, time-invariant (LTI) system designed to model the ToF system. In the modelled ToF system, $x(t)$ represents the (unknown) input signal generated by the hammer striking the spike. The output signals $y_1(t)$ and $y_2(t)$ are received by the transducers, which are separated by a distance Δz. The spike and the lower transducer are separated by a distance z_0. The transfer function for wood, given by (4.9), is used to model the delay between the output signals. In the Fourier domain, the output signals are described by

$$Y_1(j\omega) = X(j\omega)H(j\omega, z_0)P(j\omega), \tag{4.11}$$

$$Y_2(j\omega) = X(j\omega)H(j\omega, z_0 + \Delta z)P(j\omega), \tag{4.12}$$

where $X(j\omega)$ is the input signal, and $P(j\omega)$ is the response of each transducer. This assumes that the two transducers are matched. These equations use convention of representing time-domain quantities with lower-case letters and frequency-domain quantities with the corresponding upper-case letters. By dividing (4.12) by (4.11), $H(j\omega, \Delta z)$ is obtained,

$$\frac{Y_2(j\omega)}{Y_1(j\omega)} = \frac{H(j\omega, z_0 + \Delta z)}{H(j\omega, z_0)} = \exp\left(jk\Delta z\right) = H(j\omega, \Delta z). \tag{4.13}$$

(4.13) shows that if $H(j\omega, \Delta z)$ is known, $Y_2(j\omega)$ may be obtained directly from

[4]More specifically, α should be referred to as the *absorption coefficient*, as it expresses the amount of energy lost in the medium due to frictional effects. In this chapter, the term absorption is preferred, but attenuation is used in some instances, as it is used more commonly in the literature.

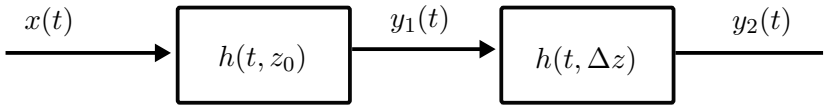

Figure 4.2 System diagram for the one-dimensional transmission-line model of the ToF method. In this diagram the input and output signals are described in the time domain. The wood is modelled as an impulse response, which is a function of time and distance.

$Y_1(j\omega)$, without knowledge of the input signal. In practice, $H(j\omega, \Delta z)$ is not known, and must be inferred from the measured signals $Y_1(j\omega)$ and $Y_2(j\omega)$. Rather than obtaining the wood's transfer function directly from (4.13), it is useful to first parametrise the wood's transfer function in terms of a lumped-element viscoelastic model. This approach allows various unknown quantities such as the static stiffness and the dispersion relation to be estimated.

4.2.2 The Voigt model

The *Voigt* model (also known as the Kelvin-Voigt model) is a lumped-parameter mechanical model of a viscoelastic material [Kolsky 1963]. The Voigt model describes a frequency dependent relationship for the material's effective stiffness. The model's stiffness can be substituted for the stiffness element of the lossless transmission line (Figure 4.1), allowing a frequency-dependent transfer function to be derived. The Voigt model is shown in Figure 4.3(a).

The Voigt model consists of two parameters, the spring element, E_0, representing the material's elasticity, and the damping element, η, representing the material's viscosity. Each of these parameters can be quantified in terms of its effective stiffness. The spring element's stiffness is a constant value, $E = \sigma/\epsilon$. The damper element exerts a stress proportional to the rate of change of its strain, $\sigma = \eta\frac{\mathrm{d}\epsilon}{\mathrm{d}t}$. In the Fourier domain, the damper's effective stiffness is $j\omega\eta$. The total effective stiffness of the Voigt model, in the Fourier domain, is

$$E(j\omega) = E_0 + j\omega\eta. \tag{4.14}$$

Kolsky [1963] suggested an alternative form of the Voigt model stiffness,

$$E(j\omega) = E_0\left(1 + j\omega\tau\right), \tag{4.15}$$

where τ is the *relaxation time*, in seconds, given by $\tau = \eta/E_0$. (4.15) shows that when the frequency, $f = \omega/2\pi$, is much smaller than $1/\tau$, the effective stiffness is approximately E_0. Therefore, E_0 is referred to as the *static stiffness*. When the frequency is much

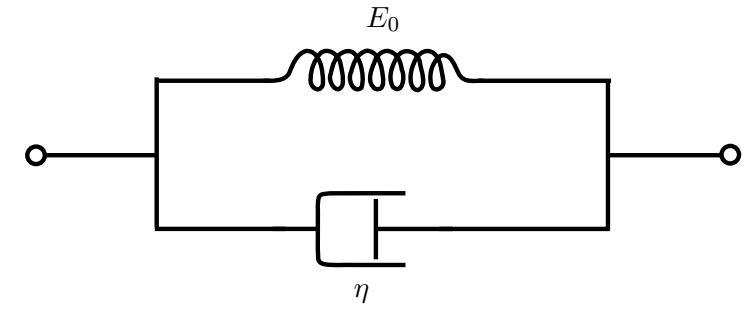

(a)

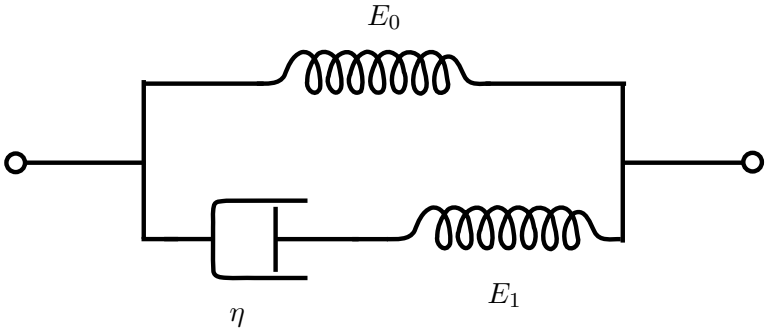

(b)

Figure 4.3 Viscoelastic solid models. (a) the Voigt model, (b) the Zener model.

greater than $1/\tau$, the total stiffness is dominated by the damping element, and thus increases linearly with frequency.

4.2.3 The Zener model

The *Zener* model (sometimes referred to as the standard linear solid (SLS) model) is another lumped-parameter viscoelastic model [Zener 1948]. The model is shown in Figure 4.3(b).

For the Zener model, the effective stiffness is given by

$$E(j\omega) = E_0 + \frac{E_1 j\omega\eta}{E_1 + j\omega\eta}. \tag{4.16}$$

(4.16) can be rewritten in the same form as (4.15),

$$E(j\omega) = \frac{E_0\,(1 + j\omega\tau_0)}{1 + j\omega\tau_1}, \tag{4.17}$$

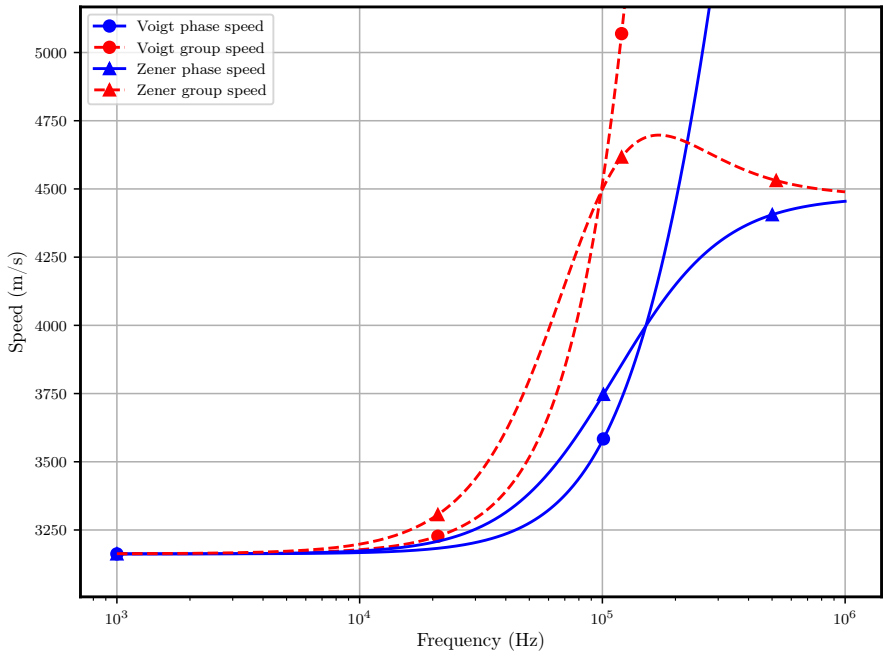

(a)

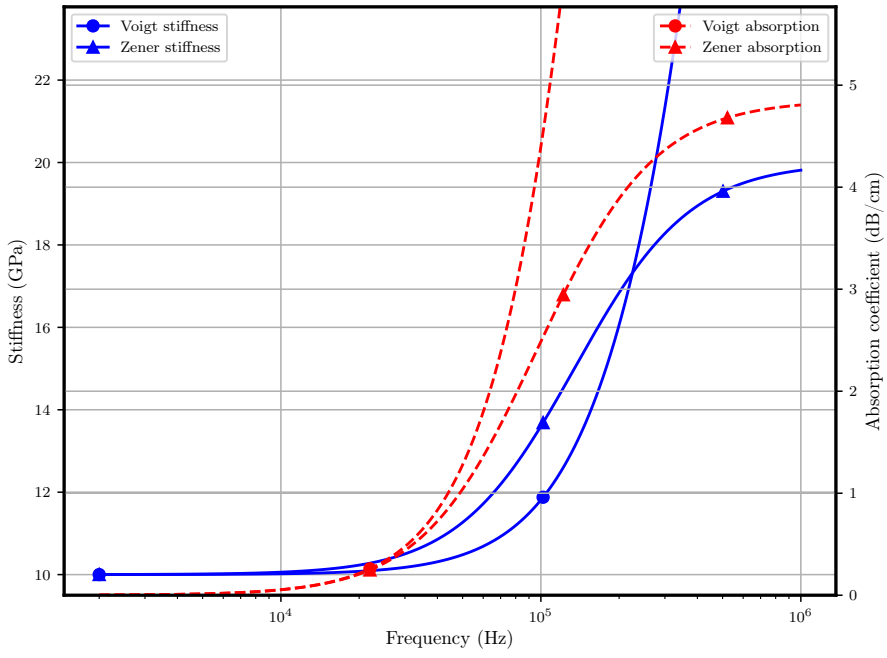

(b)

Figure 4.4 Viscoelastic model properties, plotted against frequency. (a) Phase velocity and group velocity. (b) Stiffness and absorption coefficient. Voigt model plotted with parameters: $E = 10\,\text{GPa}$, $\tau = 1\,\mu\text{s}$. Zener model plotted with parameters $E_0 = 10\,\text{GPa}$, $E_1 = 10\,\text{GPa}$, $\tau_1 = 1\,\mu\text{s}$.

where,

$$\tau_0 = \eta \left(\frac{1}{E_0} + \frac{1}{E_1} \right) \tag{4.18}$$

$$\tau_1 = \frac{\eta}{E_1}. \tag{4.19}$$

At frequencies much lower than $1/\tau_0$, the effective stiffness is approximately equal to E_0, the static stiffness. The numerator's relaxation frequency, $1/\tau_0$ is smaller than $1/\tau_1$, indicating that the stiffness increases linearly at frequencies greater than $1/\tau_0$. At frequencies much greater than $1/\tau_1$, the effective stiffness is approximately equal to $E_0 + E_1$. In subsequent sections, the Zener model is parametrised in terms of E_0, E_1, and τ_1, as τ_0 can be derived from the other parameters.

The phase velocity and group velocity of both models are plotted in Figure 4.4(a). The effective stiffness, in GPa, and the absorption coefficient, in dB/cm, are both plotted in Figure 4.4(b).

4.2.4 Spreading losses

A wave which obeys the one-dimensional wave equation, (4.5), and its associated general-solution, (4.6), does not suffer spreading losses, as all energy is contained in the plane perpendicular to the z direction. In reality, waves which are not constrained by fixed boundaries will spread in space. The wave energy can spread in various ways, depending on the geometry of the medium and the wave mode. Waves propagating on a surface spread in two dimensions; waves propagating through a volumetric space spread three dimensionally. It is currently unknown which of these modalities best describes the behaviour of a ToF wave. In this section, an analysis of each of these cases is performed. A gain value for each case is derived for the time of flight system.

Kolsky [1963] demonstrated that a wave which is spreading in three dimensions from a point is described by the wave equation

$$\frac{\partial^2 (r\epsilon)}{\partial r^2} = \frac{1}{c^2} \frac{\partial^2 (r\epsilon)}{\partial t^2}, \tag{4.20}$$

where r is the radial distance from the point source. The form of the general solution to (4.5) is

$$\epsilon(t, r) = \frac{1}{r} f(ct - r), \tag{4.21}$$

which is of the same form as (4.6), but decreases in amplitude with $1/r$.

Consider now the ToF system described in Section 4.2.1. Assuming that the input

signal spreads spherically from the input source[5], the two received signals are given by

$$y_1(t) = \frac{x(t)}{z_0}, \tag{4.22}$$

$$y_2(t) = \frac{x(t)}{z_0 + \Delta z}. \tag{4.23}$$

The unknown input signal, $x(t)$, is eliminated by taking the ratio between the two received signals, i.e., the gain between the transducers,

$$A_{\text{sphere}} = \frac{y_2(t)}{y_1(t)} = \frac{z_0}{z_0 + \Delta z}. \tag{4.24}$$

A similar analysis can also be applied to the case of surface spreading, which is known in the literature as *cylindrical* spreading [Kinsler et al. 2000]. Cremer et al. [2005] showed that the wave equation in cylindrical coordinates is given by

$$\frac{1}{r}\frac{\partial}{\partial r}\left(r\frac{\partial \epsilon}{\partial r}\right) = \frac{1}{c^2}\frac{\partial^2 \epsilon}{\partial t^2}. \tag{4.25}$$

The form of its corresponding general solution is

$$\epsilon(t, r) = \frac{1}{\sqrt{r}} f(ct - r). \tag{4.26}$$

Following the same approach as in the spherical case, the effective gain of the two signals for the case of spherical spreading is

$$A_{\text{cylinder}} = \frac{y_2(t)}{y_1(t)} = \sqrt{\frac{z_0}{z_0 + \Delta z}}. \tag{4.27}$$

The time of flight system's transfer function can now be appended to include the gain due to spreading,

$$H(j\omega, z_0, \Delta z) = A(z_0, \Delta z) \exp\left(j\omega \Delta z \sqrt{\frac{\rho}{E}}\right), \tag{4.28}$$

where A is the spreading gain, given by either (4.24) or (4.27), and E is the frequency-dependent effective-stiffness, given by either (4.15) or (4.17).

[5]It should be noted that spherical spreading does not mean that the wave's energy radiates equally in all directions. It means that the wave energy spreads in three dimensions. The directional distribution of energy in space is defined by the *directivity*. The transfer function described in Section 4.2.1 assumes that the source (the spike) is axially aligned with both transducers, so the directivity is assumed to be common to both transducers.

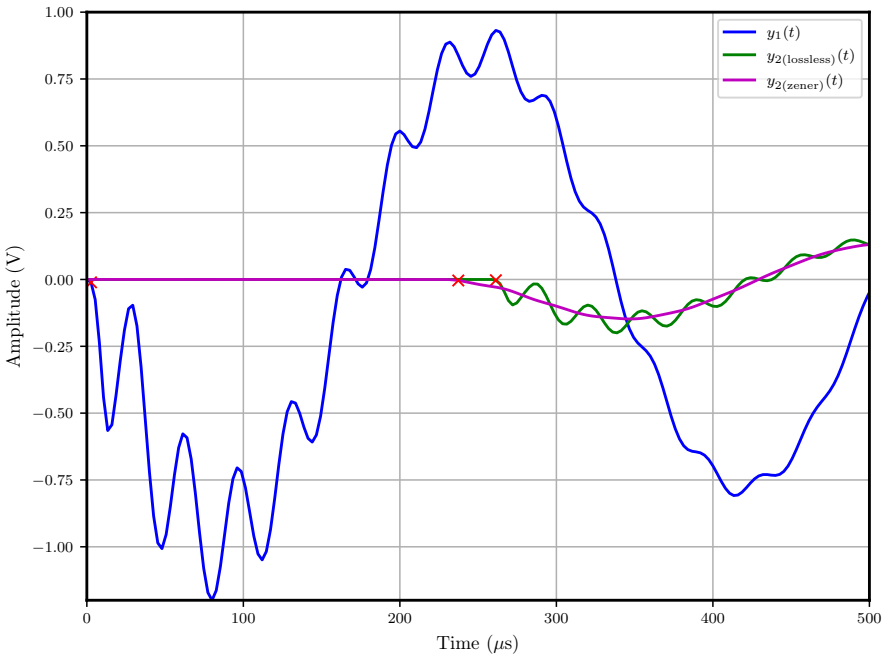

Figure 4.5 Signals generated in the ToF simulation. The threshold (arrival) time of each signal is marked with a red cross. The viscoelastic Zener model produces a smaller propagation time than the lossless model, and thus a greater measured velocity.

4.3 TIME OF FLIGHT SIMULATION

It was hypothesised in Section 4.1 that the high-frequency content would lead to a greater acoustic-velocity measurement, because the velocity in a viscoelastic material increases with frequency.

To test this effect, a simulation of a ToF system was created. In this simulation, a signal was synthesised to approximate that observed in a standing tree. The lower transducer's signal, $y_1(t)$, was formed by summing two exponentially-damped sinusoids at frequencies of 3 kHz and 30 kHz, respectively. The resulting signal was of length $N = 3750$ samples, at a sampling frequency of $f_\text{s} = 375\,\text{kHz}$ (the same frequency as that used in the experiment described in Section 4.4). The upper transducer's signal, $y_2(t)$, was created by filtering y_1 through the ToF system's transfer function. This was achieved using multiplication in the frequency domain. An FFT of the input signal, $y_1(t)$, was calculated, and then multiplied by the ToF system's transfer function, sampled at each of the FFT frequencies,

$$Y_2(j\omega) = H(j\omega, z_0, \Delta z) Y_1(j\omega) \tag{4.29}$$

$$= A(z_0, \Delta z) \exp\left(j\omega \Delta z \sqrt{\frac{\rho}{E}}\right) Y_1(j\omega). \tag{4.30}$$

An inverse FFT of the result was then calculated to produce $y_2(t)$. Spherical spreading was used for the spreading gain, $A(z_0, \Delta z)$.

Table 4.1 The ToF (propagation time), velocity, and estimated stiffness for the simulated ToF signals.

Model type	Time of flight (μs)	ToF velocity (m/s)	Estimated MoE (GPa)
Lossless	258.60	3866.92	14.95
Zener	232.11	4308.38	18.56

A threshold was applied to $y_1(t)$ and $y_2(t)$ to find each waveform's arrival time, and thus the ToF between the two signals. Two different models for the effective stiffness were applied to the simulation: the lossless model, and the Zener model. The lossless model has a real-valued, constant stiffness. It was evaluated with a stiffness value of $E = 15\,\text{GPa}$. The Zener model was evaluated using the parameters[6] $E_0 = 15\,\text{GPa}$, $E_1 = 5\,\text{GPa}$, $\tau = 5\,\mu\text{s}$. The models were calculated with density, spike-separation, and transducer-separation values of $\rho = 1000\,\text{kg/m}^3$, $z_0 = 0.2\,\text{m}$, and $\Delta z = 1.0\,\text{m}$, respectively.

The resulting simulated signals are shown in Figure 4.5. The Zener model has reduced the propagation time compared to that of the lossless model. The time of flight, velocity, and estimated stiffness (calculated using (1.6)) are shown in Table 4.1. The stiffness estimated using the lossless model is approximately the same as the static stiffness, the reason for the small discrepancy is unknown. The stiffness estimated using the Zener model is significantly greater than the static stiffness. This finding supports the hypothesis that the viscoelastic behaviour of a material causes a greater ToF velocity.

4.4 STANDING TREE EXPERIMENT

An experiment was performed to capture a series of ToF measurements in a standing *Fuscospora cliffortioides* (mountain beech) tree. The configuration of the experiment was similar to that depicted in Figure 1.4, i.e., a metal spike was struck to excite the stress wave. The spike was placed $z_0 = 0.2\,\text{m}$ below the lower transducer. The transducers were initially placed at the same distance from the spike, i.e., $\Delta z = 0$. At this separation, ten measurements were captured from each transducer. The upper transducer was then moved up the tree by 5 cm, where a further 10 waveforms were captured. This process was continued until the transducers were separated by $\Delta z = 0.5\,\text{m}$. The signals were captured using a Treetap 7c unit; each measurement is of length $N = 1200$ samples, at a sampling rate $f_\text{s} = 375\,\text{kHz}$. The experiment was conducted using Fakopp SD-02 transducers [Fakopp Bt 2000].

[6]These values were chosen because they are on the same order of magnitude as those found in the standing tree experiment results, Section 4.4.1.

4.4.1 Results

The complete data from one measurement, at a transducer separation of $\Delta z = 0.5\,\mathrm{m}$, is shown in Figure 4.6. The time-domain plot shows that the lower transducer's signal, y_1, has a large amount of high-frequency ringing for approximately the first $300\,\mu\mathrm{s}$. This high-frequency content is also present in the signal's spectrum, which contains more energy above 20 kHz than that of the upper transducer. Both signals have a dominant frequency component[7] at approximately 3 kHz.

An analysis was performed of the signal gain versus transducer separation. The received signal's amplitude is complicated by the wave reflecting internally within the tree. This means that the received signal does not obey the transfer function of (4.10), but rather a sum of transfer functions which are time-delayed according to the distance of each reflection. Rather than develop a model for the complicated nature of these internal reflections, the approach taken in this analysis was to only consider a subset of samples taken from the beginning of the waveform.

The beginning of the waveform was isolated by multiplying each signal by a window function, $w(t)$. The windows were centred on the initial edge of each waveform. The initial edge was determined using a threshold, set just above the noise floor. A Hann function of length 100 samples was used as the window function [Ambardar 1999]. This window length was selected because the envelope of the two signals were observed to diverge significantly after this period. The window function is shown in Figure 4.8.

The gain was calculated by finding the ratio of the root mean square (RMS) value of each signal, with the window applied. The resulting gain is plotted against transducer separation in Figure 4.7. Also shown on this plot are the gains due to spherical and cylindrical spreading, given by (4.24) and (4.27), respectively. The trend of the gain is mostly similar to that of spherical spreading, except at $\Delta z = 0.05\,\mathrm{m}$. At the other distances, the calculated gain is slightly lower than that predicted by spreading alone. It is hypothesised that the remaining attenuation, not accounted by the spreading gain, is due to viscoelastic absorption. In Section 4.4.2, this hypothesis is explored through the development of a method for fitting the viscoelastic model parameters to the data measured in the standing tree experiment.

4.4.2 Viscoelastic model fitting

In Section 4.3, a transfer function of the ToF system was used to calculate $y_2(t)$, given a simulated input signal, $y_1(t)$. In this section, it will be demonstrated that the transfer function can also be applied to measured signals in order to estimate the wood's viscoelastic parameters.

[7] See Chapter 3 for an analysis of the origin of this peak.

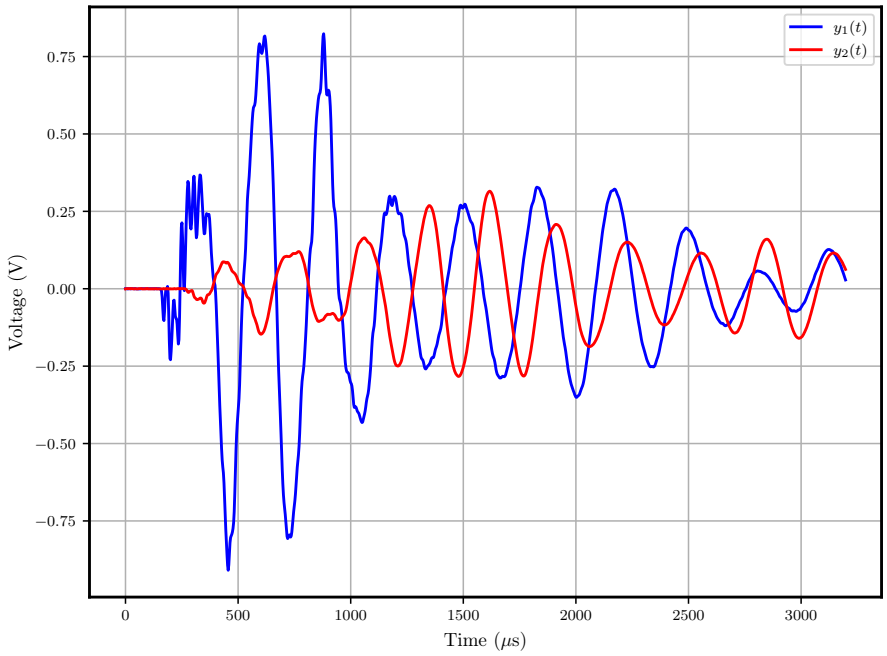

(a)

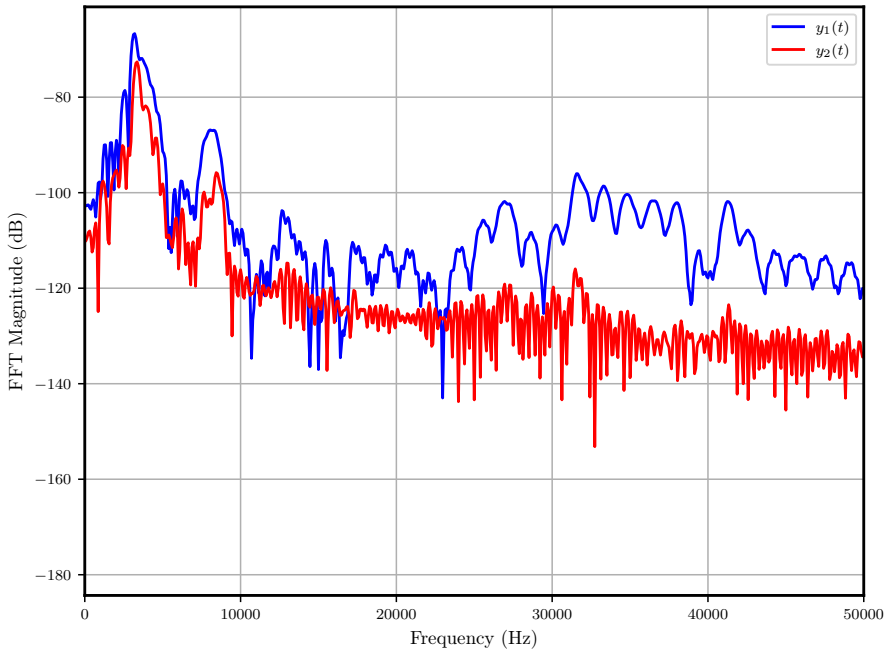

(b)

Figure 4.6 A single measurement of the standing tree experiment. Both channels are plotted for (a) the entire time-domain signal, and (b) the corresponding signal's spectra up to 50 kHz. Signals were captured at a transducer separation of $\Delta z = 0.5\,\mathrm{m}$.

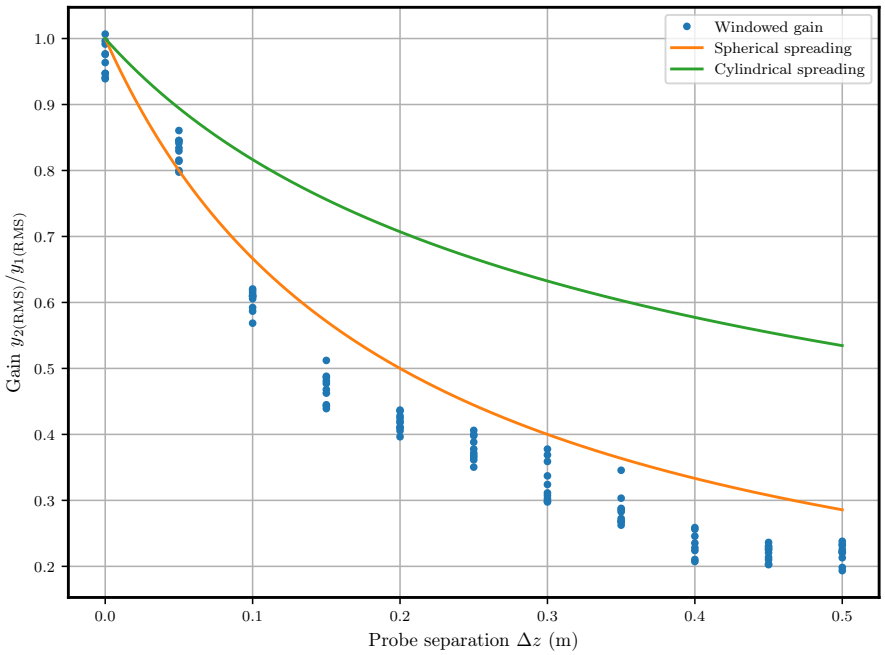

Figure 4.7 Signal gain is shown vs. probe separation, calculated as the ratio of RMS $\{y_2\}$ to RMS $\{y_1\}$, calculated with the window applied. Also shown are the expected gains due to spherical and cylindrical spreading.

An optimisation method was used to fit the parameters of each viscoelastic model to the measured data. To achieve this, a cost function was developed which compares the upper transducer's signal, $y_2(t)$, against an estimate of the signal, $y_{2(\mathrm{est})}(t)$. This was implemented using a similar technique to the ToF simulation. The estimated signal is given by

$$Y_{2(\mathrm{est})}(j\omega, E) = A(z_0, \Delta z) \exp\left(j\omega \Delta z \sqrt{\frac{\rho}{E}}\right) Y_1(j\omega); \tag{4.31}$$

where E is the effective stiffness, parametrised by the values of the viscoelastic model being used; and $Y_1(j\omega)$ is the FFT of the signal measured at the lower transducer. The transfer function and input signal were multiplied in the frequency domain, followed by an inverse FFT to generate $y_{2(\mathrm{est})}(t)$.

The *error function* was then generated using

$$e(t) = y_{2(\mathrm{est})}(t) - y_2(t). \tag{4.32}$$

The error function was then multiplied by a time-delayed Hann function of length $N = 100$ samples, as was done for the gain calculation. The RMS value of the windowed error-function was returned by the cost function. The optimisation algorithm attempts to minimise the cost function. Consequently, it attempts to find the viscoelastic parameters which best match $y_{2(\mathrm{est})}(t)$ to $y_2(t)$.

Scipy is a numerical analysis package, implemented using the Python programming language [Jones et al. 2014]. Scipy's mathematical optimisation routines were used for

Table 4.2 Fitted model parameters. Each of these models were calculated at a fitting distance of $\Delta z = 0.5\,\mathrm{m}$

Model type	Spreading	E_0 (GPa)	E_1 (GPa)	τ (μs)	$\lvert E(30\,\mathrm{kHz})\rvert$	Mean error
Voigt	Spherical	16.23	n/a	1.29	16.70	0.30
Voigt	Cylindrical	11.37	n/a	7.01	18.84	0.33
Zener	Spherical	15.88	5.78	5.47	19.08	0.23
Zener	Cylindrical	11.28	101.40	0.81	20.35	0.32

finding the model parameters. First, a coarse *brute force* search of the parameter space was performed using Scipy's `brute` function. For the Voigt model, the parameter space searched was: $E_0 \in [1, 100]\,\mathrm{GPa}$, $\tau \in [1, 100]\,\mu\mathrm{s}$. For the Zener model, the parameter space searched was: $E_0 \in [1, 100]\,\mathrm{GPa}$, $E_1 \in [1, 100]\,\mathrm{GPa}$, $\tau \in [1, 100]\,\mu\mathrm{s}$. Ten equally spaced points were searched for each range. The output of the brute function was used as the initial condition of Scipy's `fmin` function, which was used to run the Nelder-Mead simplex algorithm [Nelder and Mead 1965].

This technique was applied for both the Voigt and Zener models, with both spherical and cylindrical spreading. The models were determined at a transducer separation of $\Delta z = 0.5\,\mathrm{m}$. The resulting parameters are shown in Table 4.2. A metric was devised for determining the performance of each model. The *relative error* is the ratio of $e(t)$ with the window applied, to $y_2(t)$ with the window applied,

$$\text{relative error} = \frac{\mathrm{RMS}\left\{e(t) \cdot w(t - \tau_{\mathrm{th}})\right\}}{\mathrm{RMS}\left\{y_2(t) \cdot w(t - \tau_{\mathrm{th}})\right\}}, \tag{4.33}$$

where τ_{th} is the threshold time (first arrival) of y_2. A relative error of 0 means that the estimated signal matched perfectly. A relative error of 1 means that the model was a complete mismatch. The "mean error" shown in Table 4.2 is the relative error, averaged over all measurements, from all separation distances.

For the case of spherical spreading, both the Voigt and Zener models determined a static stiffness of about 16 GPa. For the cylindrical spreading case, both models determined a static stiffness close to 11 GPa. Table 4.2 also shows the effective stiffness at a frequency of 30 kHz.

Time domain plots of the measured signals, window function, and the estimated signals (with the window applied) for both models, are shown in Figure 4.8. The time domain plots are shown for separations of $\Delta z = 0.2\,\mathrm{m}$ and $\Delta z = 0.5\,\mathrm{m}$. For both separation distances, the Zener model appears to match the measured signal slightly more effectively than the Voigt model. At $\Delta z = 0.5\,\mathrm{m}$, the Voigt model appears to have filtered much of the high frequency energy, so only the signal's envelope matches the measured signal.

The relative error for all measurements, captured at all transducer separation

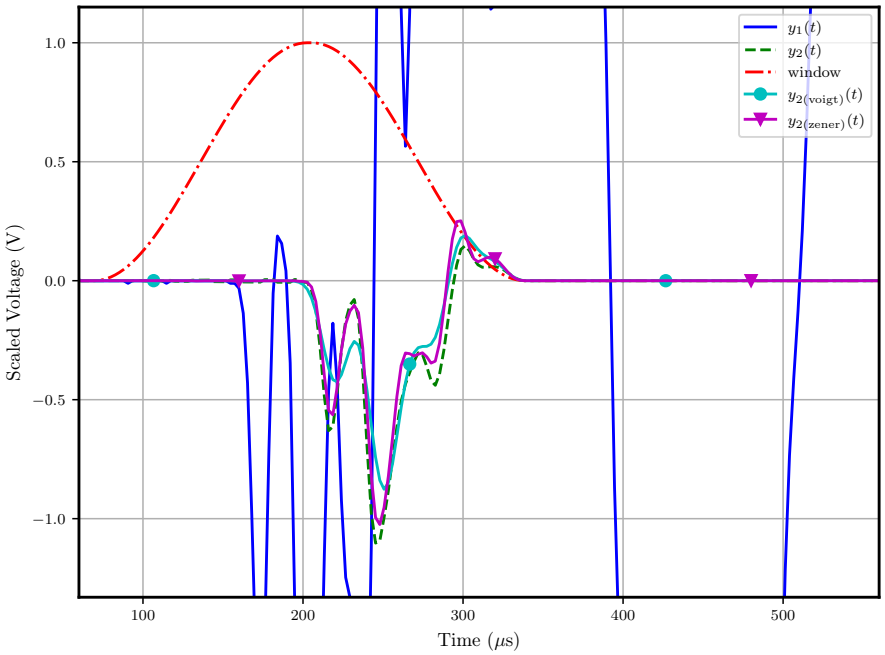

(a)

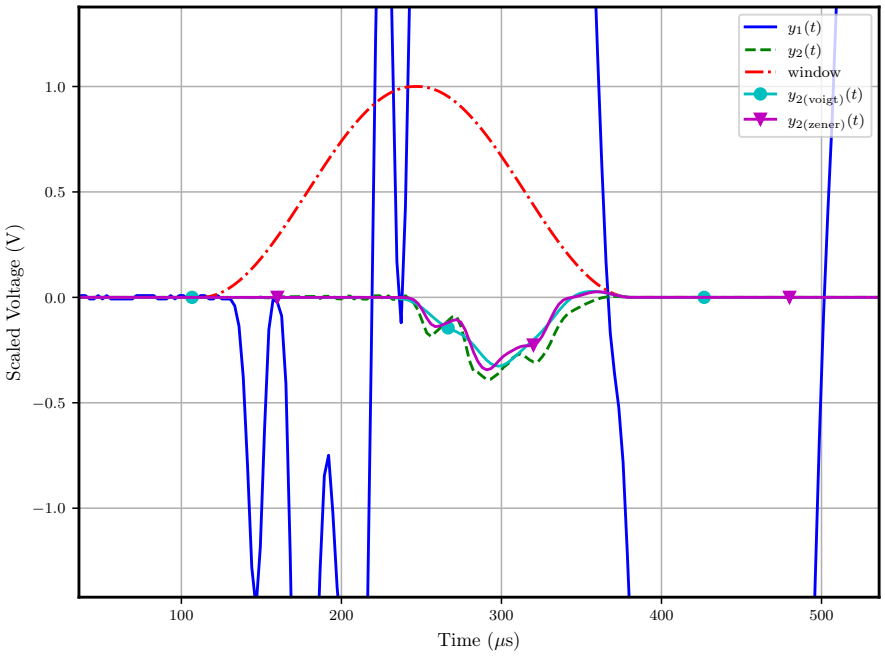

(b)

Figure 4.8 Time domain plots of the measured and estimated signals. Plotted at separations of: (a) $\Delta z = 0.2\,\text{m}$, (b) $\Delta z = 0.5\,\text{m}$. The signals were normalised so that Max $\{|y_2|\} = 1$.

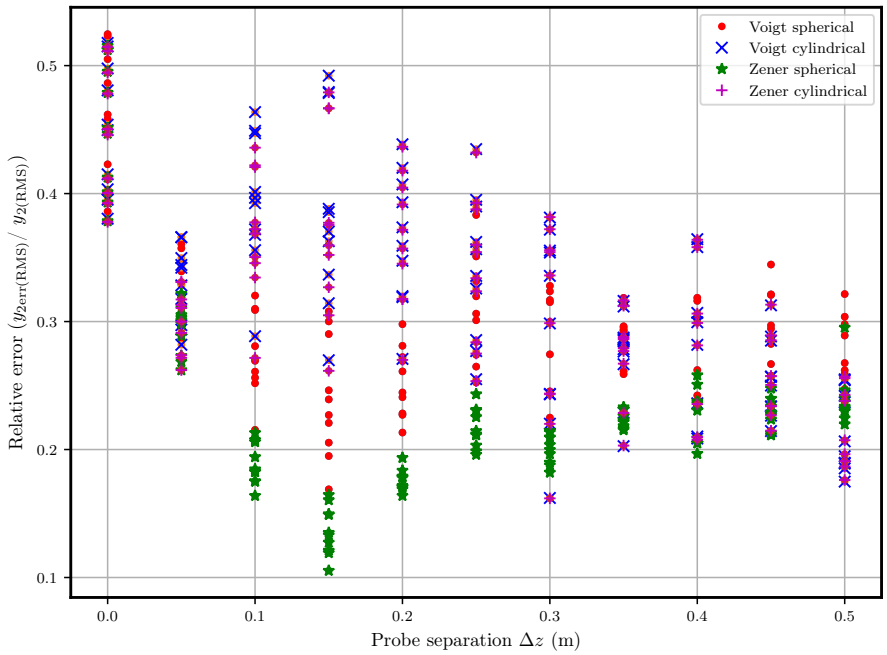

Figure 4.9 The relative error for all captured signals using model parameters of Table 4.2.

distances, is shown in Figure 4.9. It should be noted that the model has no effect at $\Delta z = 0\,\mathrm{m}$, i.e., the estimated signal is always equal to $y_1(t)$. This is because the transfer function is equal to unity when $\Delta z = 0\,\mathrm{m}$. The large error at $\Delta z = 0\,\mathrm{m}$ appears to be caused by a non-zero delay between the two transducers, possibly caused by a local inhomogeneity in the tree or a poor placement of the transducers when conducting those measurements. Overall, the Zener model with spherical spreading appears to have performed the best, with a mean relative error of 0.23. The other models were approximately equal overall, with values for the mean relative error of approximately 0.3.

4.4.3 Effective absorption coefficient

In Section 4.1.1, an overview was provided of previous researcher's efforts to measure acoustic attenuation in wood. In order to compare their findings against the viscoelastic models described in this chapter, the absorption coefficient of each model was calculated.

For each of the models listed in Table 4.2, the absorption, in decibels per centimetre, was calculated using (4.4). It was demonstrated in Figure 4.4(b) that the absorption coefficient of both the Voigt and Zener models increases with frequency. The value of the absorption was calculated at frequencies of 1 kHz and 1 MHz. The resulting values are shown in Table 4.3.

All of the models predict a very low value for the absorption at 1 kHz. This suggests that at low frequencies, the spreading losses account for the majority of the attenuation. The absorption at 1 MHz is much greater. The values predicted by the models with

Table 4.3 Effective absorption coefficients for the models of Table 4.2 expressed in units of decibels per metre.

Model type	Spreading	α at 1 kHz (dB/m)	α at 1 MHz (dB/m)
Voigt	Spherical	-0.05	-3138.42
Voigt	Cylindrical	-0.36	-1704.45
Zener	Spherical	-0.09	-45.53
Zener	Cylindrical	-0.37	-451.42

spherical spreading are much greater than those with cylindrical spreading. This is because cylindrical spreading attenuates more slowly with distance, so the optimisation routine increased the model's absorption to compensate. The absorption values of the Voigt model at 1 MHz are improbably large. Note that an absorption value of -1 dB/cm, i.e., -100 dB/m, corresponds to a 10^5 times reduction in amplitude each metre. Consequently, -5 dB/cm is a very large value, and -20 dB/cm is improbably large.

4.5 DISCUSSION

It is well understood that the time of flight method measures an overestimation of a standing tree's stiffness. In this chapter, it was hypothesised that this overestimation is, in part, due to dispersive wave behaviour in wood. It was explained that the dispersion of an acoustic wave is closely related to the amount of absorption in the medium. To investigate this hypothesis, a study of viscoelastic absorption models was performed. Bucur [2006] explained the there are three main causes of acoustic attenuation in wood. The first is the geometry of the radiation field, which includes spreading in space due to the transducer's radiation pattern, and interference effects due to reflection and refraction. The second cause is absorption due to frictional effects within the wood. The third cause is due to scattering of the wave within the material.

A transfer-function was developed for modelling the behaviour of an acoustic wave in a time of flight system. This study is the only known attempt to model stress-wave behaviour in a standing tree using viscoelastic transmission-line models. The developed transfer-function incorporates two of the aforementioned causes of attenuation: beam spreading, and viscoelastic absorption. Two viscoelastic models: the Voigt model, and the Zener model, were applied to the transfer-function. These models are the simplest possible models of viscoelastic behaviour in a solid. Kolsky [1963] described several other potential solid models, though they were all determined to be inappropriate. The Maxwell model is unsuitable because the effective stiffness is zero for the static case. The auxiliary Voigt model was determined to be functionally equivalent to the Zener model. More complex models are available, such as the generalised Maxwell model [Gutierrez-Lemini 2014]. Future work should consider whether more complex models describe the dynamic stiffness and attenuation of wood more accurately.

The transfer function model did not incorporate a scattering element. Bucur [2006] explained that for wavelengths much longer than the size of the dominant structural feature, i.e., the tracheid length, Rayleigh scattering predominates. For frequencies below the resonant frequency of the dominant feature, Rayleigh scattering predicts that the amount of scattering is inversely proportional to the fourth power of the wavelength. The wavelength's considered in the measurements conducted in this chapter are long compared to the length of a tracheid cell. It is, therefore, unlikely that scattering plays a significant role. However, if future work conducts measurements in the MHz range, scattering may need to be considered.

Both the Voigt model and the Zener model predict that phase velocity, group velocity, effective stiffness, and absorption all increase with frequency. This overall trend is consistent with published data on wood properties. Static stiffness and dynamic stiffness (at 30 kHz) values were provided for each model. The greatest difference in static stiffness between the models was due to the type of spreading used, with approximately 16 GPa for the spherical case, and 11 GPa for the cylindrical case. It

is not known whether the stiffness functions predicted by the models are an accurate reflection of the wood's true stiffness. One method of testing this would be to capture ToF data prior to sawing a tree, and then measure the stiffness of the cut wood, either using resonance or a static-stiffness test. It would be insightful to see whether either of the proposed models was a strong predictor of the outerwood's static stiffness. If this were the case then the model could be integrated into a field ToF measurement device, such as Wireless Treetap (see Chapter 5).

Similarly, it is not known whether the attenuation coefficients predicted by the models are an accurate reflection of the wood's actual attenuation. In the future, this could be measured using one of the methods discussed in Section 4.1.1. It was not possible to perform these measurements in this case because the sample trees could not be chopped down.

It it also unknown whether the dispersion relation is a useful indicator of other mechanical properties. For example, Wang et al. [2002] examined the relationship between acoustic velocity and moisture content, and found that velocity increases as wood is dried. This is not surprising, as stiffness increases (see Section 1.1.3), and density decreases, as wood is dried. Both of these properties contribute towards an increase in acoustic velocity, as given by (1.6). It might be insightful to determine whether a predictable relationship also exists between dispersion and moisture content, or other mechanical parameters.

The metric *relative error* was used to evaluate the performance of the model at various separation distances. This metric suggested that the Zener model with spherical spreading was the best fitting model. The effective absorption coefficient was also calculated for each model. The absorption of the Voigt model at 1 MHz is thought to be improbably high, with values exceeding -1700 dB/m. The absorption of the Zener model at 1 MHz is more similar to the values observed by previous researchers, which are on the order of -2 dB/cm. The absorption coefficient values at 1 kHz were small for all models. It is difficult to know whether these values realistic, as previous researchers did not quote a value for the attenuation coefficient at low frequencies. It is reasonable, however, to expect a much smaller level of absorption at low frequencies. Resonance testing (described in Section 1.2.2) requires that a low-frequency wave propagates many times along the length of a harvested stem. This requires an absorption coefficient on the order of -0.1 dB/m.

The Nelder-Mead simplex algorithm was used to determine the model parameters. A potential problem with optimisation methods is that the procedure may converge on a local minimum, rather than the best global solution. The current approach is to perform a coarse brute-force search of the parameter space prior to model fitting. It is currently unknown whether this step is necessary. Local minima were not found in the parameter space of the models and measurements considered in this chapter, though it

is unknown whether this will remain true when the technique is applied to other trees. To test this, future work should apply the procedure to measurements from more trees.

Some improvements could be made to the experimental procedure. There was a small time-delay between the two transducers at $\Delta z = 0\,\mathrm{m}$. This delay is likely present because it is not physically possible to place the two transducers at the exact same location. The time delay causes a significant relative error value, as the error is particularly sensitive to phase variations. This can be seen in Figure 4.9, where the error at $\Delta z = 0\,\mathrm{m}$ is large, even though the transfer function at this distance has no effect. The relative error is also sensitive to local variations in the wood's properties. The transfer function assumes that the wood's stiffness and density are constant along the entire length, which is untrue in many situations, especially where major defects such as knots are present in the wood.

A key component of the procedure described in this chapter is the bandwidth of the transducers and measurement device. The SD-02 transducers used in this experiment cannot measure frequencies which greatly exceed 30 kHz (see Chapter 3 for a detailed description of these devices). Therefore, they only provide a limited sample of the wood's dispersion relation. If a transducer with increased bandwidth is employed then the sampling frequency of the measurement device must be necessarily increased, as required by the sampling theorem [Ambardar 1999]. Another concern is the spectrum of the excitation. The metal spike employed in the experiment may only produce excitation frequencies within a limited band. Future work could explore additional types of transducers and signal sources.

Chapter 5

THE WIRELESS TREETAP SYSTEM

Treetap the name of a series of ToF measurement systems developed at the University of Canterbury. Wireless Treetap (WTT) is the next iteration of this project. The goal of the project is to create a smartphone-based system for measuring wood stiffness. In previous Treetap versions, two wired transducers were attached to a small box of measurement electronics. In the WTT system, each transducer is coupled to its own electronic instrumentation, forming a standalone unit known as a *probe*. A complete WTT system consists of two probes, which wirelessly connect to a smartphone for controlling the system.

The initial work on this system was conducted as part of a final-year undergraduate engineering project at the University of Canterbury [Harrison et al. 2014]. This chapter describes the continuation of this project, through to a working prototype of the system. Section 5.1 is a review of existing ToF tools. Section 5.2 describes the specifications of the system. Section 5.3 describes the hardware design of the WTT probe, including electronic component selection; the design and performance of the analogue front-end; digital design considerations; power supply design and battery performance; and the design of the probe's external housing. Section 5.4 describes the implementation of the system's software, including the probes firmware, and a smartphone application (app) for coordinating and controlling the system. Section 5.5 outlines the hardware and software algorithm employed for time-synchronising multiple probes, a necessary feature for operation of the system. Section 5.6 provides a brief overview of time-delay estimation techniques, and compares four delay-estimation techniques, for potential integration into WTT. Section 5.7 describes a field test which was conducted of the system, and its comparison to a previous Treetap system. Finally, a discussion of the project's findings are provided in Section 5.8.

5.1 REVIEW OF EXISTING TIME-OF-FLIGHT TOOLS

The ToF method is an established technique for measuring wood stiffness in standing trees. An overview of the method, and a summary of relevant research findings, was

provided in Section 1.2.3. Several commerial and research oriented ToF devices have been developed. While the principle of operation between these devices is fundamentally the same, there are differences in device construction, form-factor, and operating procedure. In this section, an analysis of existing ToF devices is performed, and the differences between these systems is explored in detail.

A range of ToF devices are shown in Figure 5.1. An early developer of ToF tools was Fakopp Bt[1], who released the Microsecond Timer in 1994 [Fakopp Bt 2001]. They also released the TreeSonic–an industrialised version of the Microsecond Timer [Fakopp Bt 2005]; and the Ultrasonic timer–targeted at more sensitive measurements, such as those performed on young seedlings [Divos 2010]. Fibre-Gen developed the ST-300–a commercial ToF tool with a number of innovative features [Carter et al. 2005, Fibre-gen 2017]. Intrumenta Mechanik Labor (IML) developed the Micro Hammer, a device targeted at measuring decay in trees [IML 2017]. Metriguard was another early developer of ToF tools. They developed the Stress Wave Timer–a device used to detect decay in trees and wood structures [Metriguard 2017]. Agricef developed the USLab Ultrasonic timer [Agricef 2017]. CBS-CBT's developed the Sylvatest Trio [CBS-CBT 2017]. A number of ToF devices have been developed at the University of Canterbury. These include Timbersonic [Hayes and Chen 2003], and Treetap [Toulmin 2005, Waugh 2004, Woods 2006].

Most devices use two wired piezoelectric-probes connected to a measurement unit. The probes are usually sharp, rugged, spike-shaped transducers, allowing them to be hit with a hammer through the tree's bark and into the outerwood. The Fakopp Treesonic device is unique in that a hammer apparatus is integrated into the transducer, to assist attachment to the tree. In some systems, the stress-wave is excited by striking one of the transducers with a hammer. This method is used by the Fibre-Gen ST300, Fakopp-Treesonic, and Fakopp-Microsecond. One disadvantage of these systems is that striking the transducer to create the wave can potentially damage the transducer. Also, there is a much larger signal induced at the striking transducer, which can cause the sampling electronics to saturate. For most devices this is not an issue, as they do not analyse the entire waveform, only the initial edge.

The original developers of Treetap recognised that striking the transducer would shorten its life, so they decided to use a separate "hit probe" for exciting the wave. The hit probe is a steel spike, which is hit into the tree, typically 20 cm below the lower receiving probe. A hit probe is also used by the IML Micro Hammer. In the Micro Hammer, the initiating transducer is integrated into the hammer, not embedded in the tree, and the hit probe is just a passive device for the hammer to strike. This arrangement might allow for an accurate measurement of the hammer's excitation signal, though this has not been documented.

[1] `http://fakopp.com`

(a) (b) (c)

(d) (e) (f)

(g) (h) (i)

(j)

Figure 5.1 Existing ToF devices. (a) Fakopp's Microsecond Timer. (b) Fakopp's Treesonic Timer. (c) Fakopp's Ultrasonic Timer. (d) Fibre-Gen's ST300. (e) IML's Micro Hammer. (f) MetriGuard's Stress Wave Timer. (g) Agricef's Ultrasonic Timer. (h) CBS-CBT's Sylatest Trio. (i) University of Canterbury's Timbersonic. (j) University of Canterbury's Treetap.

Another method of producing the stress-wave is to electrically excite a transmitting transducer. A piezoelectric device can operate reciprocally, i.e., generating a stress signal when an electric field is applied [Arnau 2008]. In order to produce a significant force at the transducer, the measurement device must drive a high-voltage pulse across its terminals. This method is used by the Fakopp-Ultrasonic, Agricef-Ultrasonic, CBS-CBT-Sylvatest Trio, and is optionally available on Treetap 7c. This method is less reliable in wet-wood, where the acoustic attenuation is high [Bucur 2006]. It is best used in dry wood or smaller samples, such as increment cores. A problem with this method is that the excitation transducer can add an additional delay, due to the asymmetry of the system, even with no wood material between the transducers. This effect is demonstrated in the Fakopp Ultrasonic Timer's manual[2], which shows that the measured time delay is typically non-zero when the probe separation is zero. This offset should be removed through a correction factor. Another difficulty with these systems is preventing the high-voltage impulse from electrically coupling into the receiving channel. This effect was observed in Treetwist system [Hayes and Pink 2012], which attempted to subtract the coupled signal from the receiver channel.

Most devices only return the ToF in microseconds to the user; the user must calculate the velocity using an independently measured distance. This is conducted either by programming this distance into the device, or manually calculating the velocity afterwards. Some devices store the measurement data in memory, and allow the data to be downloaded to a PC for analysis. Each measurement is usually tagged with a tree-id, which the measurement data is associated with. It appears that none of the commercial ToF devices record the full waveform, only the resulting propagation time or velocity.

Fibre-Gen's ST300 is the only known system to incorporate a distance measurement system in the device. The probes incorporate an ultrasonic range-finder to measure the acoustic propagation time in air, allowing the device to automatically calculate the velocity. The ST300 is also the only known system to use wireless probes. This is achieved by using an infra-red LED on the transmitting probe to indicate that a measurement has begun. When the stress wave is received, the receiving probe compares the start and end times, and returns the difference to a PDA device. This device also allows additional data to be entered and recorded, such as stand location, species, etc.

5.2 SPECIFICATIONS

The Treetap range of ToF systems has been in development at the University of Canterbury for over 10 years [Woods 2006]. The currently used devices, Treetap 4 and Treetap 7c, suffer from several problems. The wired probes are a common point of failure, as the wires are easily twisted or snagged on branches when moving through a forest. The devices use a threshold algorithm to detect the wave start. This is prone to

[2]Available at `http://fakopp.com/docs/products/ultrasonic/UltrasonicGuide.pdf`.

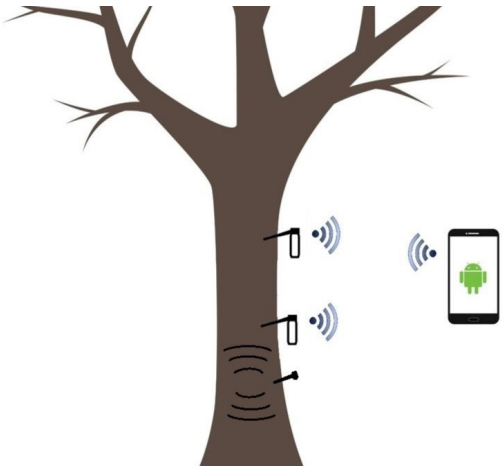

Figure 5.2 Wireless Treetap consists of two independent receiver-probes and a smartphone, which controls the system and provides an interface for the operator.

errors if signal strength is weak. The devices only have a minimal LCD display. An updated system, using smartphone technology, could make use of a number of useful features, including: a high-resolution display, touchscreen input, geo-tagging of data via GPS, time-stamping of data, and networked upload of measured data. The following specifications for the new ToF system were devised:

- The system will use the two receiving-probes topology. The excitation will be provided using a metal-spike embedded in the tree, reducing wear on the probes due to excess hitting. A diagram of the proposed system is shown in Figure 5.2.

- Each probe will function as a standalone measurement device, consisting of: an acoustic transducer, measurement electronics, wireless communication, and a rechargeable lithium polymer (LiPo) battery.

- Each probe unit will be compact enough to be easily held in one hand. Each probe must be rugged enough to sustain repeated insertion in many trees.

- The two probes will connect to a smartphone application via Bluetooth. The data sampled by each probe will be downloaded and saved by the phone application.

- The system should be capable of measuring an acoustic delay between the two probes to an accuracy of $1\,\mu$s.

- Each probe should be capable of running for full working day (8 hours) without being recharged. The probes will enter a low power mode after being idle for some time, maximising battery life.

5.3 HARDWARE DEVELOPMENT

The WTT system's hardware design presented several challenges. The probe units need to be physically compact, rugged, reliable. They also need to provide accurate measurement results. In this section, these challenges are addressed through the design of the probe hardware. Section 5.3.1 provides an overview of the high-level system design and component selection. Section 5.3.2 provides details for the design of the probe's analogue front-end. Section 5.3.3 describes the battery and power supply design of the probe. Section 5.3.4 describes the design of the housing (or enclosure) for the probe's electronics. In Section 5.3.5, the probe's measurement performance is detailed. Section 5.3.6 describes the method used to set the device's *trigger threshold*, a key parameter for identifying an acoustic wave arrival.

5.3.1 System design

Each probe contains a microcontroller for coordinating and controlling the probe's subsystems. An ARM-based microcontroller was selected because of its low cost and popularity for embedded-systems applications. Treetap 7c used an Atmel SAM7S ARM microcontroller, which is now listed as an obsolete device. The SAM4S [Atmel 2013] is a pin-compatible replacement for the SAM7S, though there are many internal differences between the two. This device was selected for use in the WTT probe. This allowed some existing driver code to be reused.

Previous iterations of Treetap used the Fakopp SD-02 transducer [Fakopp Bt 2000]. Operators of Treetap devices reported that the measurement reliability, which is closely related to the transducer performance, was acceptable. For this reason, the SD-02 was again selected for the WTT system. For each probe, the transducer's cable was cut so that it could be directly connected to the probe's input header.

Many commercially available ToF devices only record the time delay between the transducers, not the entire waveform. It was decided that WTT would sample and record the entire waveform. This is because WTT is, in part, a research tool, and one of the potential research goals is to develop a better understanding of wave behaviour in wood. To achieve this, an analogue front-end was designed for the probe, including a programmable gain amplifier, an anti-aliasing low-pass filter, and an analogue to digital converter. Further details regarding the front-end design are provided in Section 5.3.2.

Each probe contains its own independent clock. However, when conducting a measurement, both probe's waveforms must be referenced to a common clock in order to calculate the time delay. Therefore, the probes must periodically synchronise to account for the differences between their individual clocks. Several options were considered for implementing the synchronisation. Initially, a GPS-based solution was considered. This would make use of the highly accurate "pulse per second" output, derived from

atomic clocks inside the satellites [Allan et al. 1997]. However, initial prototyping revealed that the selected GPS receiver, the GP-2106 [ADH 2010], does not reliably obtain a satellite fix under forest canopy, probably because of its small antenna size. Several other synchronisation options were considered by Harrison et al. [2014] while performing the initial background research for the WTT project. Ultimately, a low power radio, the nRF24L01+ [Nordic Semi 2008], was included in the design specifically for time-synchronising devices. A temperature-controlled crystal oscillator (TCXO), the ASTX H11 [Abracon 2015], was selected as the clock source for the probe because of the improved frequency stability when compared against a standard quartz crystal. Further details regarding the implementation of the synchronisation algorithm are provided in Section 5.5.

A low cost Bluetooth transceiver module was selected for communication with the smartphone. LiPo batteries were selected as the best option for powering the devices, as they are rechargeable, and are among the most energy-dense batteries currently available. A micro-USB interface was included on the probe for battery charging and debugging on a PC. An integrated LiPo battery charger was included in the system for charging the device via USB. For simplicity and noise performance, it was decided that all electronic devices in the probe would operate using linear-regulated power supplies. A JTAG interface was included on the probe for uploading firmware to the probe and performing interactive debugging. A block diagram of the subsystems implemented in each probe is shown in Figure 5.3.

5.3.2 Analogue front-end design

The WTT system is designed with two purposes in mind: to be a robust ToF device for measuring tree stiffness in forestry applications, and to capture waveform data for advancing the understanding of acoustic wave behaviour in wood. Consequently, the measurement performance is significantly over-specified, when compared to a device which is only required to measure ToF tree stiffness.

A block diagram of the WTT probe's analogue front-end is shown in Figure 5.4. The front-end consists of several subsystems: a clamping circuit, a programmable gain amplifier, a single-supply biasing network, an anti-aliasing filter, and an analogue to digital converter. This topology was adapted from that used in Treetap 7c, though many of the components were updated to more modern variants.

The probe is designed to operate from a single LiPo battery, thus, the front-end is a single-supply design. In order to allow both positive and negative voltage swings, the inputs of each of the front-end stages were biased to $V_{\text{ref}}/2$. This was achieved using a voltage divider to drive the input of a unity-gain operational amplifier (op-amp). The active bias provides a low impedance source for the rest of the front-end, reducing sag on the bias rail when downstream circuits are activated. A large voltage can be induced

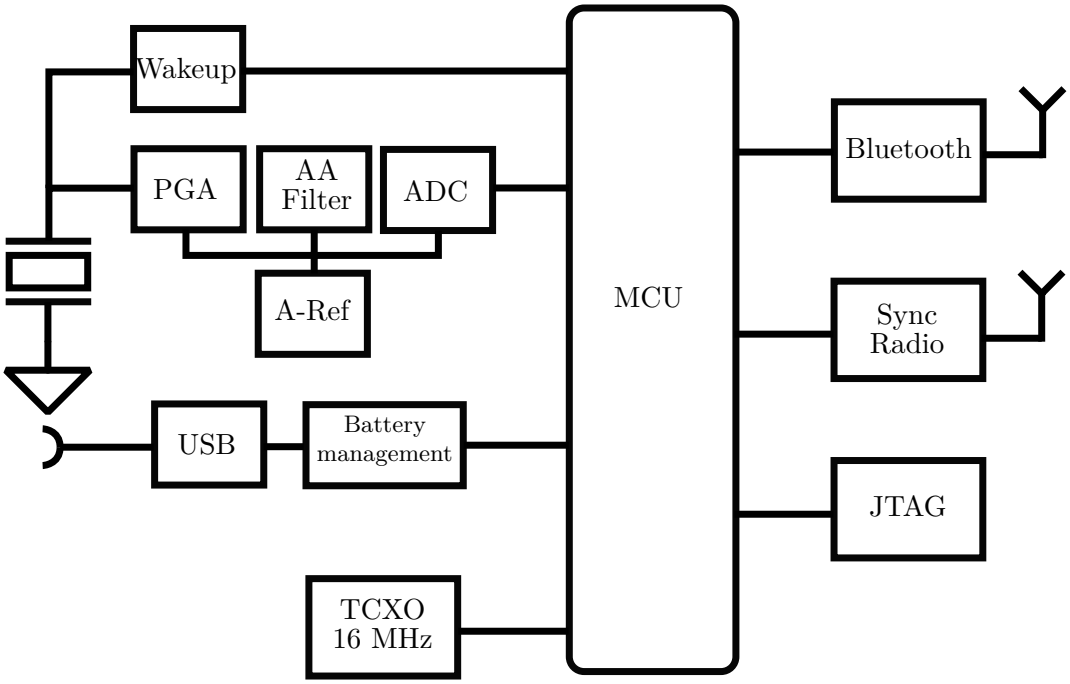

Figure 5.3 Block diagram of the probe's hardware subsystems.

across the transducer when a large stress is applied to it, such as when it is hit into a tree with a hammer. To protect the front-end electronics from a potentially damaging voltage, a clamp circuit was placed at the probe's input. The clamp consists of two BAV99 packages [Fairchild 2014], each containing two series silicon diodes (each with forward-voltage ≈ 0.7 V). So the transducer is limited to voltage swings of approximately ± 1.4 V from the bias point. The front-end also includes a wake-up circuit. This works by connecting the transducer, via a MOSFET, to a microcontroller pin, so that a large input can trigger an interrupt. This allows the probe to be awoken from its low power (sleep) state by striking the transducer.

The front-end does not require a large voltage gain when performing stiffness measurements on standing trees. However, in the future the system may be applied in other scenarios, where smaller amplitude signals are measured. To allow this, a programmable gain amplifier (PGA) was included in the front-end design; the device selected was the MCP6S21 [Microchip 2003]. This device allows voltage gains from $A_{\mathrm{PGA}} = 1$ to $A_{\mathrm{PGA}} = 32$ to be selected. Following the PGA, a combination fixed-gain and low-pass filter stage was included. This stage serves as an anti-aliasing filter prior to sampling. It was implemented using an OPA2365 op-amp [TI 2007] configured as a two-pole, multiple-feedback active filter [Horowitz and Hill 2015], followed by a single-pole passive low-pass RC filter. The cutoff frequency for this filter was set to 125 kHz, and the gain was set to $A_{\mathrm{fixed}} = -8$, i.e., the filter is an inverting stage.

Two different analogue to digital converters (ADCs) were considered for use in the probe. The SAM4S has a built-in ADC peripheral, which is a 12-bit successive approximation device, this is referred to as the *internal* ADC. The second ADC considered was an external package, the AD7274 [Analog 2005], which is also a successive approximation architecture. This device is referred to as the *external* ADC. Either of these devices can be selected during manufacturing by populating a $0\,\Omega$ resistor on the circuit board. The ADC's sampling frequency must be at least twice the highest frequency of interest, as required by the sampling theorem [Ambardar 1999]. Therefore, the sampling frequency must be set to at least 250 kHz to avoid aliasing. The ADCs reference voltage was provided using a precision voltage reference, the REF5030 [TI 2013].

5.3.3 Power supply design

As stated in Section 5.3.1, the probe is powered using LiPo batteries. Two battery connectors were included, one on either side of the circuit board, so that two LiPo cells can be connected in parallel. This arrangement maximises the available space inside the probe's housing.

The probe's circuit board is divided into a number of power-supply regions. These regions are: MCU power, analogue power, Bluetooth power, and clock-sync power. Each

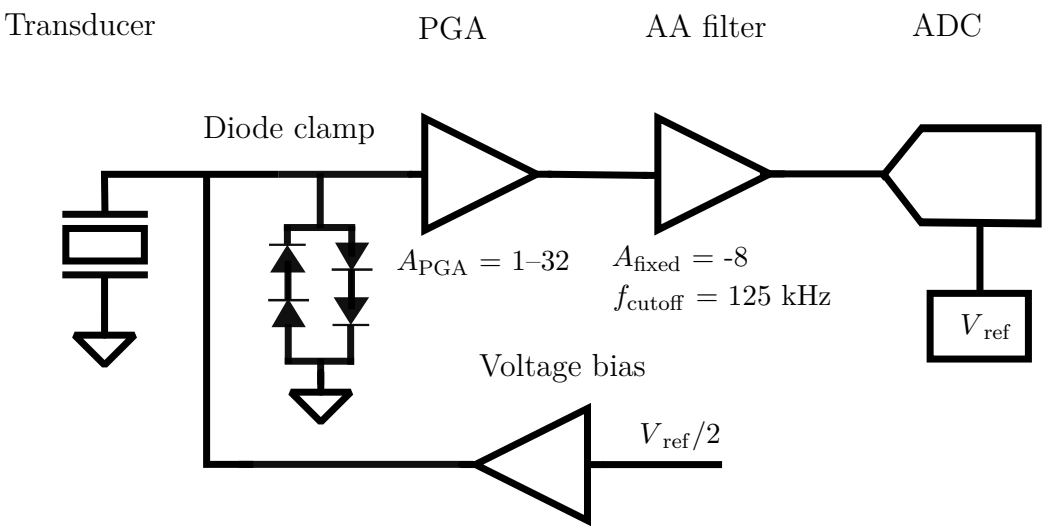

Figure 5.4 Block-diagram of the WTT probe's analogue front-end.

region is powered via its own linear regulator, which is connected to the battery. This configuration reduces noise in the front-end due to digital switching and power-supply loading. It also allows each power-supply to be disabled when the device enters sleep state. When this occurs, only the MCU's power supply remains active.

The device is designed to switch to a low-power sleep mode if it receives no commands for a certain amount of time. In lower power mode all peripheral devices on the printed circuit board (PCB) are disabled and the microcontroller is placed in a low power mode. The current draw of the device in low power mode was measured at approximately 150 μA. The battery capacity of the device, when using two LiPo cells, is approximately 600 mAh. Thus, in sleep mode, the battery is expected to last longer then 150 days before fully discharging.

5.3.4 Manufacturing and housing design

The probe's hardware design; as discussed in Sections 5.3.1, 5.3.2, and 5.3.3; was manufactured into a PCB. Several problems with the design were encountered during this process, including: inadequate or faulty power supply design, incorrect component selection, incorrect component footprints, and manufacturing faults. Four iterations of the PCB were constructed before all of these problems were fixed. The final version of the PCB is shown in Figure 5.5.

An important component of the WTT system is the physical design of the probe housing. The specifications for the housing are as follows. Each probe must be robust enough to withstand being struck many times, as the attached transducer will be hit into

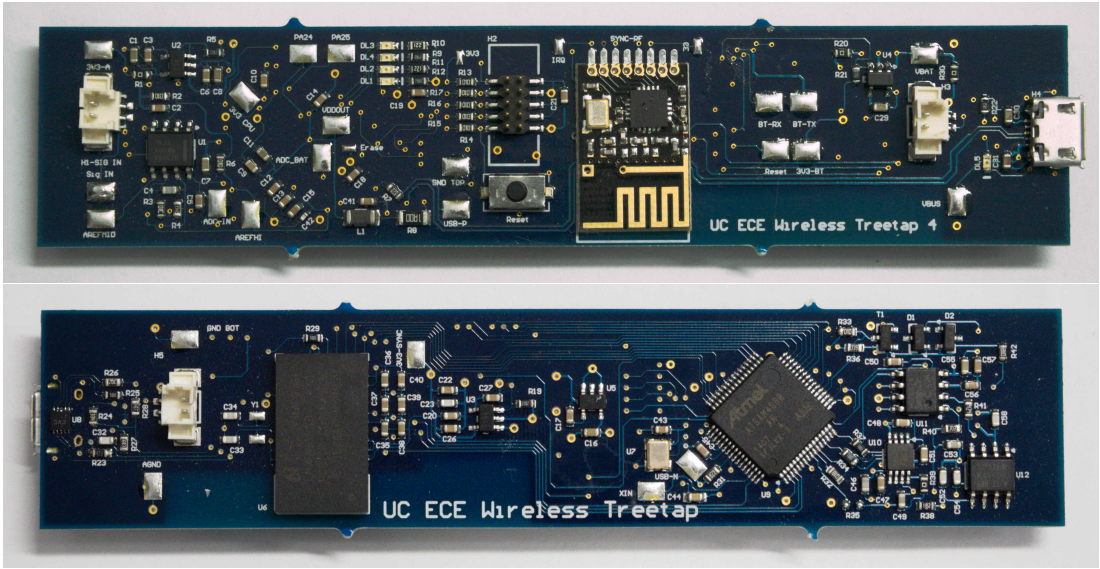

Figure 5.5 The final version of the Wireless Treetap PCB.

many trees. The probe must be water-resistant. It is not expected that the probes will be submerged underwater, or used in very heavy rain, but they should withstand light rain or high levels of humidity. The LiPo batteries are charged via a USB connection, this port needs to be easily accessed. Ideally, the probes should be easy to disassemble, as the batteries will need to be replaced approximately annually. Mr Nigel Pink from the University of Canterbury School of Forestry used these specifications to design and construct the WTT housing. The components of the housing are shown in Figure 5.6.

The outer housing of the probe is built from impact resistant nylon. The outer housing is in two pieces: the transducer housing, and the electronics housing. The two pieces connect using a nylon thread. The electronics housing is a hard perspex tube; the PCB is fixed on its edge using two grub screws. A nylon end-cap with an o-ring seal protects the circuit board from moisture entering. The outer housing and end-cap can be removed without any tools, allowing for easy charging.

5.3.5 Front-end performance

In this section, two experiments are documented which were conducted to measure the performance of the analogue front-end. These experiments are: the measurement of the front-end's frequency response, and the measurement of the front-end's noise performance.

5.3.5.1 Frequency response

An experiment was performed to determine the frequency response of the probe's front-end. An Agilent 3320A Function generator [Keysight 2015b] was connected at the

Figure 5.6 The Wireless Treetap kit.

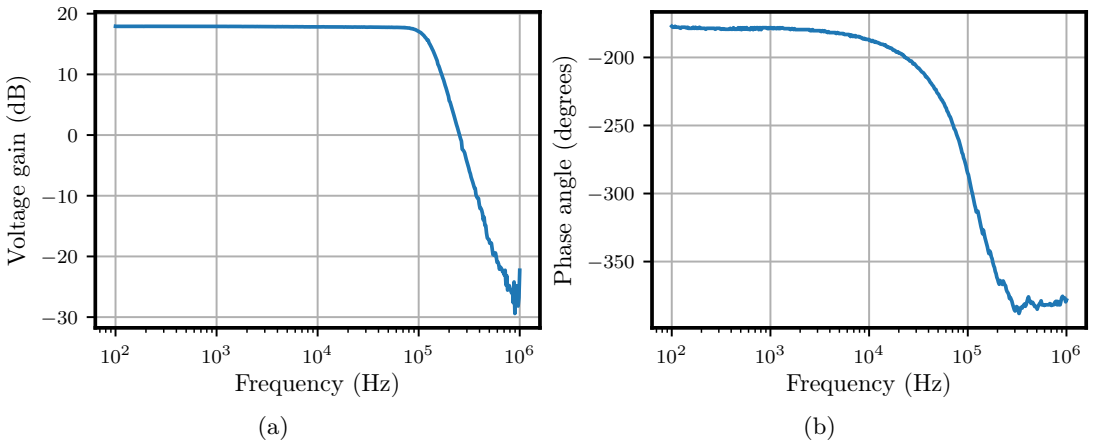

Figure 5.7 The frequency response of the WTT probe's front-end, plotted as (a) magnitude gain, and (b) phase shift.

probe's input, in place of the transducer. An Agilent DSO6014A Oscilloscope [Keysight 2015a] was connected at the probe's ADC-input. A Python script was written to programmatically control the function-generator and oscilloscope. The input frequency was varied incrementally, and the output voltage and phase were recorded using the oscilloscope. The PGA's gain was set to $A_{\text{PGA}} = 1$. The resulting voltage-gain and phase-shift of the front-end are plotted in Figure 5.7.

This analysis revealed that the cutoff frequency of the anti-aliasing filter is approximately 131 kHz, and the gain is approximately $A_{\text{fixed}} = -7.87$. These values are acceptably close to the designed values of 125 kHz, and $A_{\text{fixed}} = -8.0$. The magnitude gain shown in Figure 5.7 is reasonably flat over the pass band. The phase shift is close close to -180°for most of the pass band, though it does increase significantly above 10 kHz.

5.3.5.2 Noise performance measurements

An experiment was performed to evaluate the noise performance of front-end, and compare the internal and external ADCs. A WTT probe was configured to record a series of samples. An SD-02 transducer was connected to its input, and the probe was placed in an acoustically and electrically-quiet location. The WTT app (described in Section 5.4.2) was configured to sequentially capture a number of buffers. The trigger threshold (described in Section 5.3.6) was set to zero ADC-counts so that the device would immediately trigger. Each buffer recorded by the probe was transmitted to the app via Bluetooth. 100 buffers were captured, each of length 1024 samples, at a sampling frequency of $f_{\text{s}} = 1\,\text{MHz}$. The experiment was repeated for each of the available PGA gain levels. It was also repeated using both the internal ADC and the external ADC.

Suppose that the first buffer recorded by the probe always contains some spuri-

Table 5.1 Sample standard deviation, σ_n, of the probe's noise. Measured for both the internal and external ADC. Values have been referred to the device's input.

Gain (A_{PGA})	σ_n Internal ADC (counts)	σ_n External ADC: Std-dev (counts)
1	0.845	0.105
2	0.853	0.155
4	0.872	0.298
8	0.940	0.539
16	1.124	0.868
32	1.610	1.494

ous artefact, then using the noise measurement procedure described in the previous paragraph, this artefact would be present in every captured buffer. For example, the first buffer might always contain a spike due to the front-end powering-up. To avoid this effect, a *noise-test* mode was created. In this mode, the probe ignores the first N buffers it records, and saves the $(N+1)$th buffer. Once this buffer is returned to the app, the probe increments N and the measurement begins again.

The buffers captured by the app were combined into a zip file which was then downloaded to a PC. A Python script was developed to analyse the captured data. This script parses the received data, analyses the results, and presents them as usable plots. The recorded samples, which are formatted in units of ADC counts, were converted to volts using the formula

$$V_{\text{in}} = \frac{C \cdot V_{\text{ref}}}{A_{\text{PGA}} \cdot A_{\text{fixed}} \cdot 2^B - 1}, \tag{5.1}$$

where C is the number of ADC counts, V_{ref} is the ADC's reference, A_{PGA} is the PGA gain, A_{fixed} is the front-end's fixed gain, and B is the number of the bits of the ADC.

The power spectral density (PSD) of the measured data was calculated using Welch's method. This technique averages overlapping FFT-segments, which reduces the variance of the spectral-density estimate when compared to simply squaring the signal's FFT-magnitude [Oppenheim and Schafer 2010]. The implementation which was employed used a Hanning window of length $N = 1024$. Plots showing the noise performance of the external ADC are shown in Figure 5.8. Plots showing the noise performance of the internal ADC are shown in Figure 5.9. Table 5.1 shows the standard deviation, measured in ADC-counts, at each gain level, for both ADCs.

5.3.6 Trigger-threshold determination

The trigger-threshold is used to determine when a sampling WTT probe in the *waiting* state becomes *triggered* (the device states are described in Section 5.4.1). To avoid spurious triggering in the absence of a signal, the threshold-level must be above the device's noise floor. Section 5.3.5.2 described an experiment performed to measure the noise performance of a WTT probe. The data captured in this experiment was also

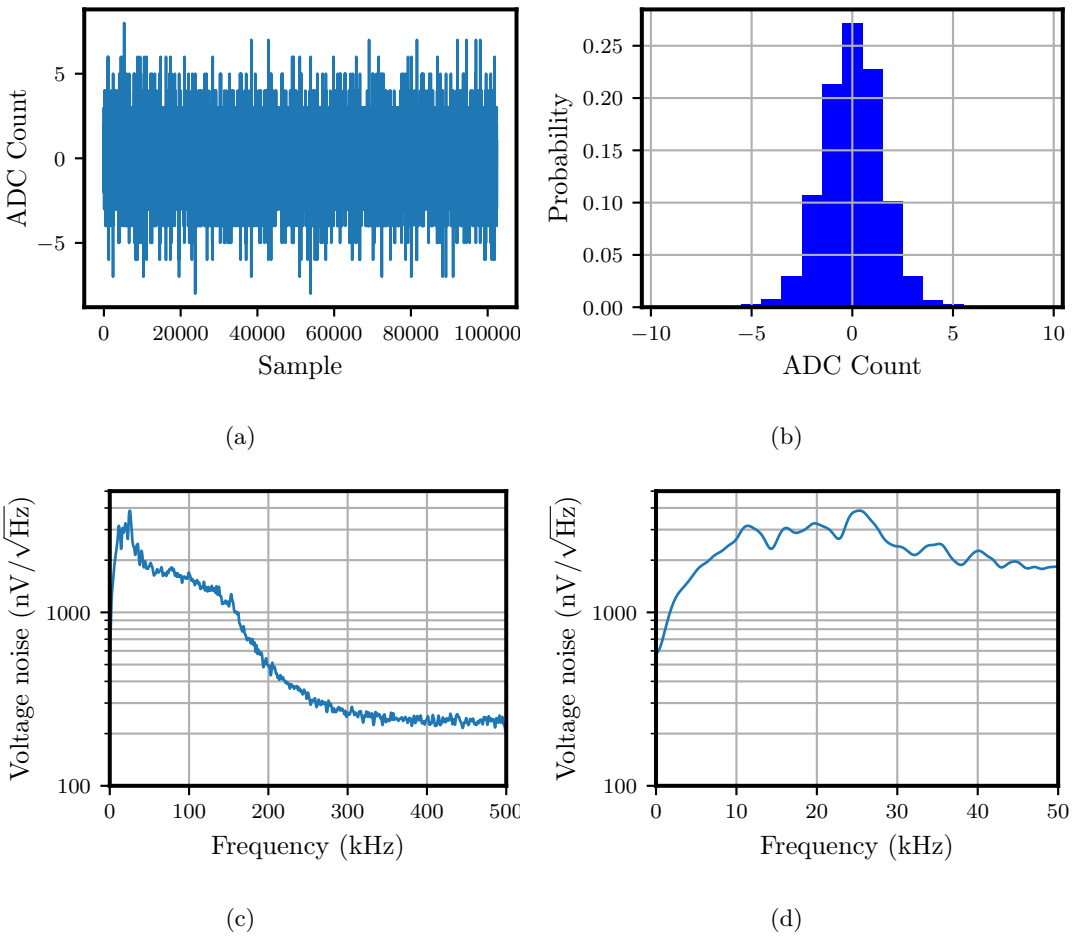

Figure 5.8 Noise performance of WTT probe using the external ADC with $A_{\mathrm{PGA}} = 32$. (a) ADC count versus buffer index. (b) Histogram of captured ADC counts. (c) Voltage spectral density, referred to the ADC's input. (d) Voltage spectral density, zoomed to 0–50 kHz.

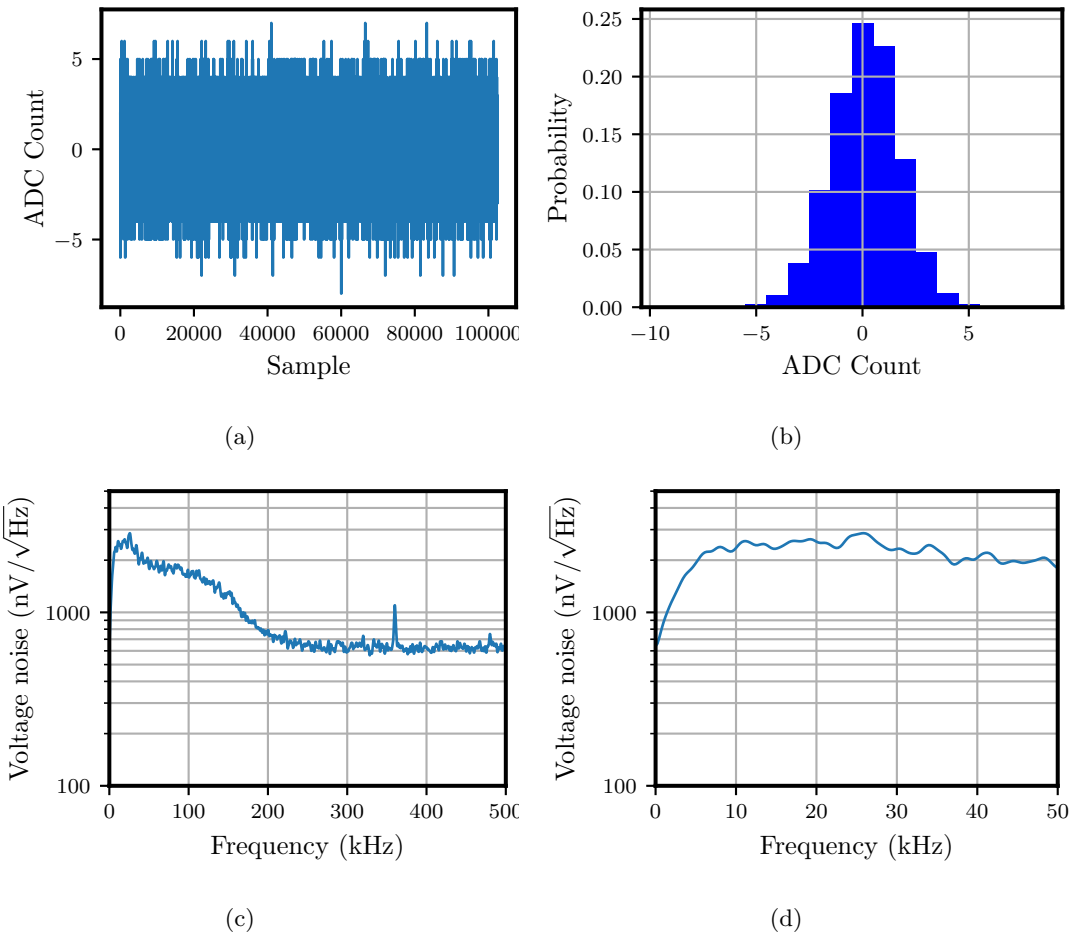

Figure 5.9 Noise performance of WTT probe using the internal ADC with $A_{\mathrm{PGA}} = 32$. (a) ADC count versus buffer index. (b) Histogram of captured ADC counts. (c) Voltage spectral density, referred to the ADC's input. (d) Voltage spectral density, zoomed to 0–50 kHz.

used to determine an appropriate threshold for triggering the probe.

5.3.6.1 Probabilistic noise model

The noise histograms shown in Figure 5.8(b) and Figure 5.9(b) closely resemble a Gaussian distribution. This suggests that a Gaussian distribution may be an appropriate model for the ADC counts in the absence of an applied external signal. The application of this model allows the probability of a false trigger to be determined.

To calculate the probability of a false trigger, it is assumed that the noise is Gaussian. Further, it is assumed that the noise is zero-man. In practice this is not true, due to input offsets in the front-end. However, the mean can easily be estimated and subtracted prior to beginning a measurement. The Gaussian model allows a probability density function to be defined,

$$f_n(x) = \frac{1}{\sigma_n\sqrt{2\pi}} e^{-\frac{1}{2}\left(\frac{x}{\sigma_n}\right)^2}, \tag{5.2}$$

[Krishnamoorthy 2006] where σ_n is the standard deviation. The associated cumulative distribution is,

$$F_n(x) = \frac{1}{2} - \frac{1}{2}\mathrm{erf}\left(\frac{x}{\sigma_n\sqrt{2}}\right), \tag{5.3}$$

where $\mathrm{erf}(z)$ is the error function, given by,

$$\mathrm{erf}(z) = \frac{2}{\sqrt{\pi}} \int_0^z \exp\left(-x^2\right) \mathrm{d}x. \tag{5.4}$$

In this model, the cumulative distribution can be used to predict the probability that a noise value will exceed a certain level. If event **A** is a noise value exceeding the threshold T, and event **B** is a noise value below the threshold. Then,

$$P(\mathbf{A}) = F_n\left(|x| \geq T\right) \tag{5.5}$$

$$= 2F_n\left(T\right) - F_n(0), \tag{5.6}$$

and,

$$P(\mathbf{B}) = 1 - P(\mathbf{A}). \tag{5.7}$$

If a sequence of length N samples is captured, the probability of at least one sample exceeding the threshold is,

$$P\left(\text{at least one above threshold}\right) = 1 - P\left(\mathbf{B}\right)^N. \tag{5.8}$$

This means that for a chosen threshold, T, and a chosen sampling time, $\tau = N/f_\mathrm{s}$, the probability of an erroneous trigger can be determined. In the following section, this approach is used to select the probe's threshold level.

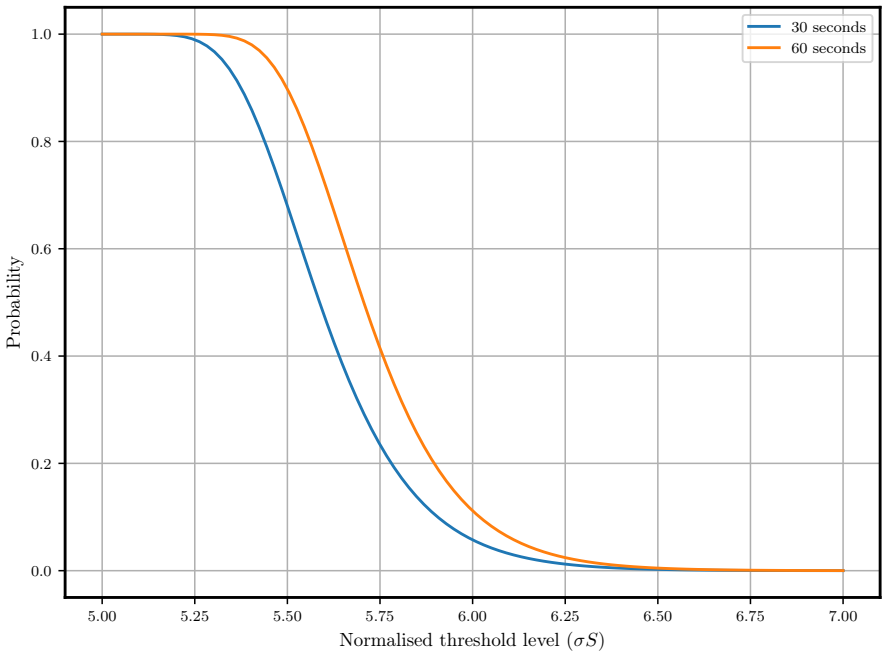

Figure 5.10 Probability of erroneously triggering in an interval vs. threshold level. The probability is plotted for 30 s and 60 s sequences, assuming a sampling rate of $f_s = 1\,\text{MHz}$.

5.3.6.2 Threshold sensitivity level

The probability of erroneous trigger is given by (5.8). This equation can be used to plot the probability of an erroneous trigger, assuming a Gaussian noise model. In Figure 5.10, this probability is plotted against threshold level, which is specified in terms of standard deviations, $T = \sigma_n S$. The erroneous trigger probability is plotted for two sequence lengths, 30 s and 60 s, assuming a sampling frequency of $f_s = 1\,\text{MHz}$.

The probe's threshold level is given by

$$T = \sigma_n S, \tag{5.9}$$

where T is the threshold level (in ADC counts), and S is the sensitivity multiplier.

The app allows the user to select the PGA gain and *sensitivity* in its configuration options. The app then calculates the trigger-level, using the noise levels given by Table 5.1, and sets the level on each probe. The WTT app has four sensitivity levels to select from. The high sensitivity level was chosen to maximise detection of small signals. The trade-off is that there is a reasonable chance of triggering within 60s; $T_{\text{high}} = 6.0\,\sigma$ corresponds to approximately $P = 0.15$ within this time. The normal sensitivity level was selected so that it's very unlikely to trigger the device during normal operation. The low sensitivity level is extremely unlikely to trigger under normal operation, but was added so that the device can still be used in noisy environments. An *Always trigger* mode was also added, this is used when measuring the probe's noise performance. The available sensitivity levels are shown in Table 5.2. Prior to a measurement, the app

Table 5.2 The probe's sensitivity levels.

Sensitivity level	Threshold value
Always-trigger	0
High	6.0 σ_n
Normal	8.0 σ_n
Low	10.0 σ_n

configures each attached probe by setting the probe's trigger-threshold according to its gain and sensitivity settings.

5.4 SOFTWARE DEVELOPMENT

The WTT software consists of two major components: the probe firmware and the smartphone application. The WTT firmware is a program which runs on the probe's SAM4S microcontroller, this program is described in Section 5.4.1. An Android application was developed to run on a smartphone, this application is described in Section 5.4.2.

5.4.1 Probe firmware

The *firmware* is the software that runs on the probe's SAM4S microcontroller. The firmware is written in the C programming language. Each probe contains identical firmware; any unit-specific configuration is done at runtime. The WTT-probe firmware is constructed in a modular architecture, organised into four library-level groups: application code (`wtreetap`), application libraries (`libs`), general purpose libraries (`mmculib`), and peripheral drivers (`mat91lib`). The firmware was implemented as a *baremetal* application, i.e., there is no operating-system running on the microcontroller. A diagram of the program structure is shown in Figure 5.11.

The top-level program, `wtreetap`, contains the main loop, program logic, handling of communication messages, measurement control, and power-state control. It is written in a modular structure so that specific tasks are grouped in separate source files, e.g., power supply control functions are in `psu.c`. Coupling between modules are kept to a minimum. The modules at this level are application-specific in the sense that they are not expected to be reused, should another application be developed.

The application code depends on two groups of modules. The first, `libs`, contains device-specific and application-specific libraries. These are libraries and device drivers which could potentially be ported to another application. This group includes a driver for the Bluetooth device, drivers for the internal and external ADCs a driver for the synchronisation radio and a driver for the PGA. The second group of modules required

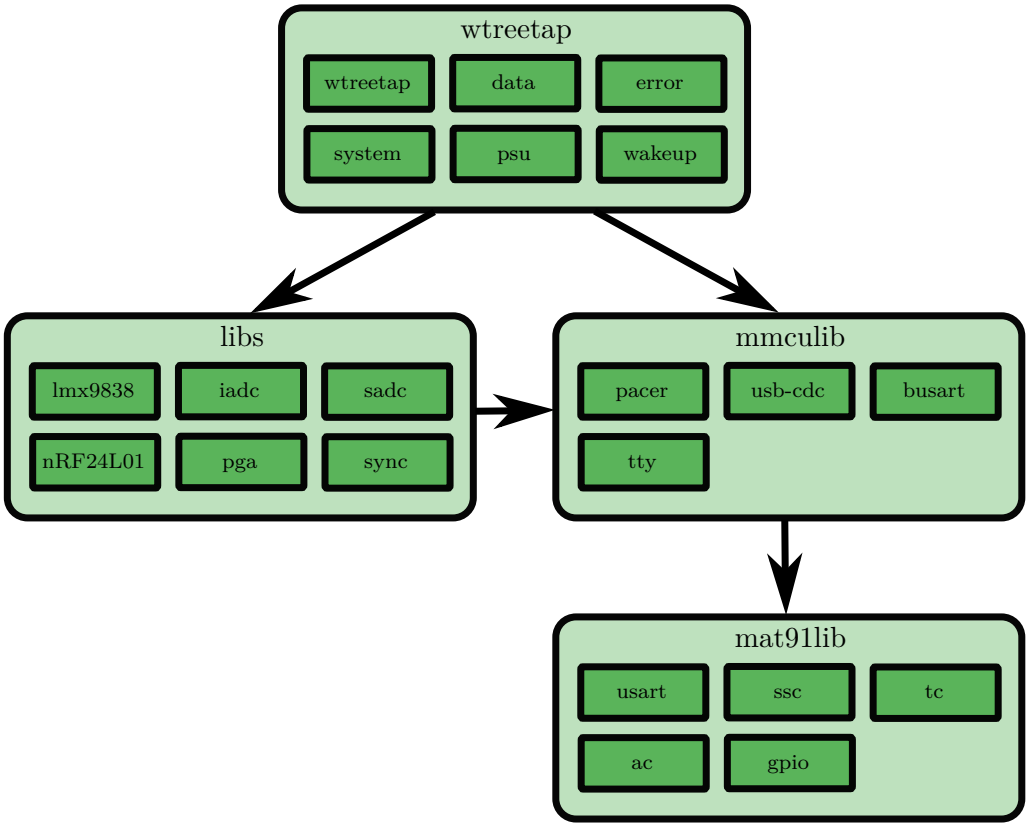

Figure 5.11 The dependency structure of the WTT probe's firmware. The application code, `wtreetap`, is decoupled from its dependent libraries: `libs`, `mmculib`, and `mat91lib`.

by the application belong to the `mmculib` library[3]. This is a library for programming baremetal microcontroller applications. It provides high-level application programming interfaces (APIs) for: timing tasks, communication interfaces, and controlling a wide range of external devices. `mmculib` is designed to be independent of the underlying hardware. It depends on another library, `mat91lib`[4], for providing access to the microcontroller's peripherals. `mat91lib` provides APIs for accessing the MCU's peripherals on the SAM4S device.

Listing 5.1 shows a pseudocode overview of the main operations the probe performs while it is not in low power (sleep) mode. The firmware utilises a `pacer` module, which calls the `pacer_wait()` function in the main loop. This function causes the CPU to wait until the pre-defined period has been exceeded, which is set to 1 ms. The function `command_poll()` accepts a communication interface (either Bluetooth or USB), and handles messages received over this interface. The communication interfaces are implemented as unix-standard streams [Kernighan and Ritchie 1988]. This allows the hardware specific details of those devices to be abstracted. All communication to

[3]Available at `https://github.com/mph-/mmculib`, accessed 24/08/2017.
[4]Available at `https://github.com/mph-/mat91lib`, accessed 24/08/2017.

the probe is initiated synchronously by the USB or Bluetooth device communicating with it, i.e., the PC or smartphone app. Thus, the probe acts as a server, with the client initiating and controlling the device's state. Once a measurement has begun, the `measure_data()` function is periodically called. This function checks the received ADC buffers, which are populated concurrently to the main loop using direct memory access (DMA). The buffers are scanned to find a sample which exceeds the trigger threshold. Once a sample exceeds the threshold, the buffers are saved, sampling ceases, and the device's state changes to `TRIGGERED`. Communication over the Bluetooth and synchronisation radio are ignored during sampling, i.e., in the `WAITING` state. This is done to minimise the effect of RF noise and digital switching from coupling into the front-end. A state machine showing the probe's operational modes is shown in Figure 5.12.

Listing 5.1 Pseudocode listing of the WTT probe's main loop.

```
void main() {

        state = STATE_STOPPED;

        initialise_hardware ();
        initialise_pacer (PACER_PERIOD);

        while (1) {
                pacer_wait ();

                command_poll (dev_usb);
                if (state == STATE_WAITING) {
                        measure_data ();
                } else {
                        command_poll (dev_bt);
                        sync_poll ();
                }
        }
}
```

5.4.2 Smartphone application development

An Android app was developed for controlling and coordinating the probes. Android was selected over its main rival, iOS, because of its high quality development tools, prevalence of Android hardware, and Android's non-restrictive support of Bluetooth serial port profile (SPP)[5]. The core functions of the app are:

- Managing Bluetooth connections to probe devices.

[5]iOS does not support Bluetooth SPP without an approved MFi license `https://support.apple.com/en-nz/HT204387`, accessed 5/7/2018.

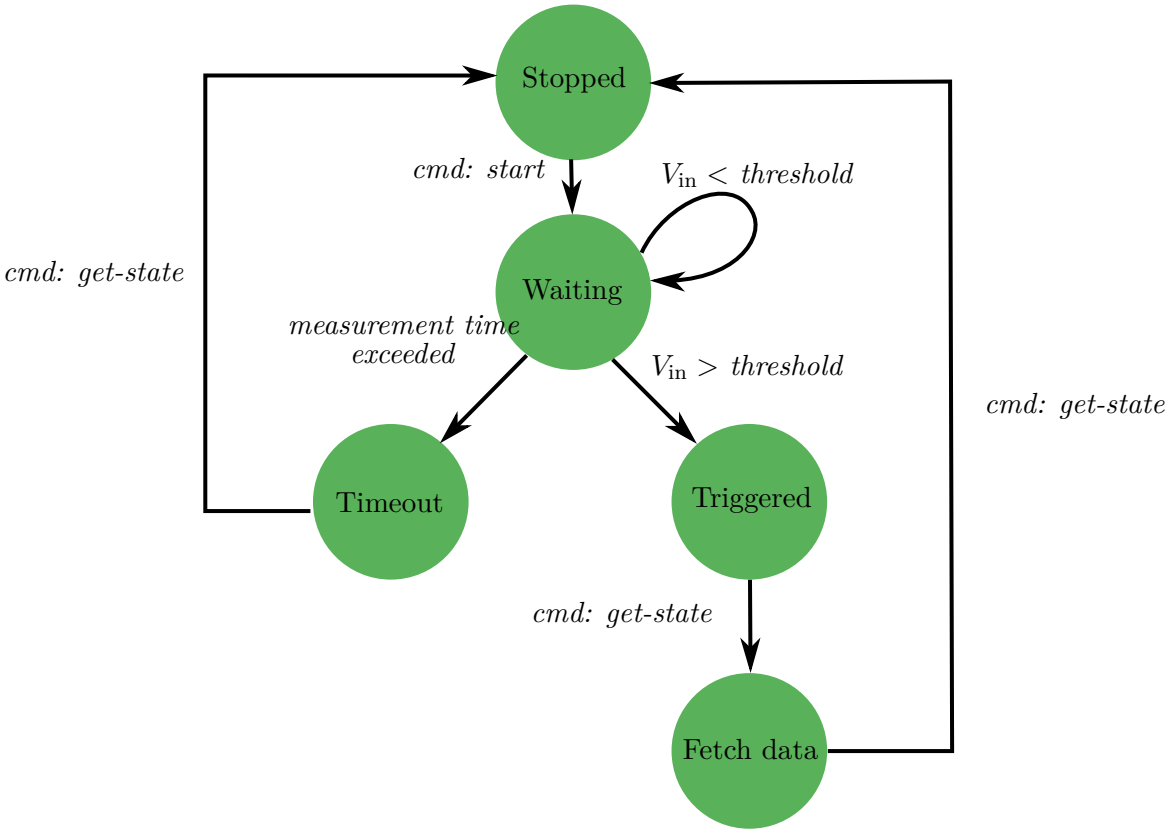

Figure 5.12 State-machine diagram of the WTT probe. The nodes represent the probe's states; the edges represent the condition under which a state-change occurs.

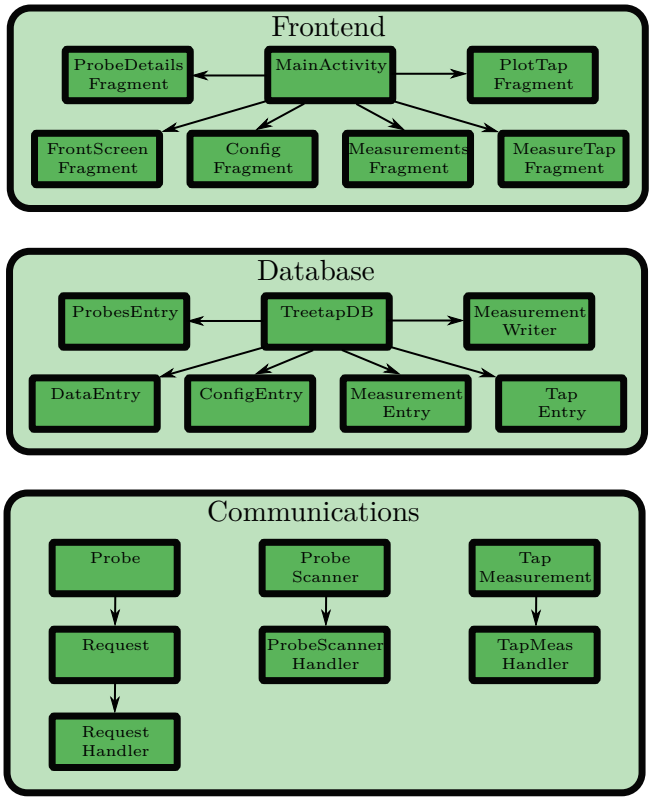

Figure 5.13 An overview of the architecture of the WTT app.

- Controlling the process of initiating, recording and synchronising a ToF measurement.
- Providing an interface for viewing, managing, and exporting recorded ToF data.

An overview of the app's architecture is shown in Figure 5.13. The graphical user interface (GUI) is implemented using the `Activity` and `Fragment` classes [Google 2017]. An `Activity` is an object which allows the app's visible content to be viewed and interacted-with by the user. Usually there is one `Activity` for each single, focused thing that a user can do, i.e., an interface covering one screen. However, `Fragments` allow the content of an `Activity` to be edited in-place, preserving the rest of the `Activity`'s state. The WTT app uses a separate `Fragment` for each screen in the app.

The app uses a SQLite database for storing persistent program state. This includes: captured measurements, configuration options, and a list of known probes.

The components listed under the `communications` section in Figure 5.13 constitute the protocols for handling communication and control of the probes. Each instance of the `Probe` class is responsible for communicating with a single probe. Each `Probe` has an `InputStream` and an `OutputStream` for reading and writing, respectively, to each probe via Bluetooth. Bluetooth communications are conducted on separate threads so

that the GUI is still responsive while communications are in progress. Each probe has a thread-safe message queue. `Request` objects are created on the GUI thread, which are then passed to the `Probe` and sequentially sent to the device over the Bluetooth stream. Once the response has been returned, the `Probe` uses the `Handler` pattern [Google 2017] to return the response to the GUI thread. This enables communication with the probes to be asynchronously handled by the GUI, even though the underlying Bluetooth communication is synchronous.

The `ProbeScanner` is a class for managing connections to probes. Originally this class was used to scan and discover new probes, though in recent versions of the app, discovery is performed using the Android OS's Bluetooth-pairing interface. Exactly two probes must be connected to allow a ToF measurement to take place.

While an instance of the app is running, the Bluetooth streams connecting to the probes remain open. If the probes are put into the sleep mode, as they do after idling for some time, an exception is thrown and the streams are lost. When the user performs an action in the app which requires communication, the connection is automatically re-established by the app, providing the probes have been re-awoken.

The app is responsible for implementing the clock-synchronisation algorithm, as described in Section 5.5.6. Specifically, the app performs the regression component of the algorithm, for converting the slave's time into the master's time base. Once this has been performed, the app converts time delay between the two signals. The app does not calculate the stiffness as in (1.6), only the time delay, τ, is returned to the user, or the velocity, c, if the user has programmed the probe separation in the app's configuration.

5.5 CLOCK SYNCHRONISATION

When performing a measurement, each device independently samples its transducer until a stress-wave is detected. When a signal is detected, the device records the capture-time using its own internal clock. Each device has an independent clock; thus, it is necessary to map each capture time onto a common clock reference. This procedure, referred-to as *clock synchronisation*, is described in this section. In Section 5.5.1, a brief overview of wireless clock synchronisation algorithms is provided. In Section 5.5.2, the algorithm used by WTT, known as the *flooding time synchronisation protocol*, is described. In Sections 5.5.3, 5.5.4, and 5.5.5, three experiments are described, where key parameters of the synchronisation algorithm were measured. In Section 5.5.6, Wireless Treetap's implementation of the algorithm is described.

5.5.1 Wireless clock-synchronisation

Each node in a wireless network has its own oscillator circuit, and thus its own clock. This necessitates periodic synchronisation so that data can be referenced to a common time.

Clock synchronisation has been extensively studied in wireless network applications. Reviews on the topic have been written by Sivrikaya and Yener [2004], Simeone et al. [2008], and Wu et al. [2011].

The clock in a low cost electronic sensor is typically derived from a quartz crystal-oscillator tuned to a particular frequency. The error in the tuned frequency is specified in parts per million (ppm), and is usually 40 ppm or better [Horowitz and Hill 2015]. A node's clock's value is expressed as $C(t)$, where t is the independent (and unknown) reference time, or true time. A simple model for clocks in a wireless network is a linear frequency-offset model. This assumes that each clock has a different rate (frequency), but this rate is assumed to be constant. So the ith node's clock is given by

$$C_i(t) = f_i t + \theta_i, \tag{5.10}$$

where θ_i is the clock's offset and f_i is the clock's rate. In practice, the clock rate is not constant, and is influenced by environmental factors including temperature, humidity, pressure, vibration, and electromagnetic fields [Allan et al. 1997, Walls 1990].

Suppose the goal is to synchronise two nodes: A and B. This requires the two nodes to periodically record their clock values, simultaneously. In practice,this might be achieved as follows: node A records its clock value, then sends a message to B, which then records its clock value. There will be some delay in transmitting the message to the receiving node. The delay can be decomposed into the following categories [Wu et al. 2011]:

- *Send time* - Time spent constructing the radio message in the transmitter.
- *Access time* - Time waiting channel access. This depends on multiple factors including the protocol used, and the congestion of the channel.
- *Transmission time* - The time to transmit the message. This depends on the bit rate and the protocol being used.
- *Propagation time* - Time for the electromagnetic wave to propagate to the receiver.
- *Reception time* - Time for the message to be received. This is equal to the transmission time.
- *Receive time* - Time to process the received message and signal the application processor.

These components can be classified into deterministic and non-deterministic delays [Wu et al. 2011]. The send time, transmission time, propagation time, and receive time are, for the most part, deterministic, though this depends on the specific implementation. The greatest uncertainty arises in the access time, which usually depends on other

devices operating on the channel. The receive time is usually considered partially non-deterministic, due to the unknown bit-alignment of the message. The received message often contains a synchronisation word at the start, which must be aligned to an expected pattern. This can require an unknown number of shift operations. The receive time also includes the time to signal the application processor, which can depend on the processor's state and configuration of interrupts.

5.5.2 The flooding time synchronisation protocol

Tackett et al. [2011] demonstrated an implementation of a wireless network using the Nordic nRF24L01+ radio. Their implementation synchronised a network of clocks running at the relatively low rate of 32.768 kHz. To achieve this, they implemented an algorithm known as the flooding time synchronisation protocol (FTSP). This approach is feasible for use in WTT for several reasons. The nRF24L01+ radio is cheap, well documented, and widely available. The nRF24L01+ does not suffer from the *access time* uncertainty discussed in Section 5.5.1, as it does not implement *data link layer*[6] features [Nordic Semi 2008]. Additionally, the over-the-air baud rate of the radio is up to 2 Mbps, so the jitter of a message due to bit alignment is less than 1 μs, which is the required specification described in Section 5.2.

In the FTSP protocol, an elected master node periodically broadcasts its time to all available slave nodes. Each slave node records its local time at message reception, forming a global-local time pair [Maróti et al. 2004]. This can be considered an example of a one-way message dissemination protocol [Sivrikaya and Yener 2004]. Using the clock model given by (5.10), the clock value of the kth broadcast message received at the ith slave can be modelled as,

$$C_{i,k} = f_i \left(C_{1,k} + \tau_{\text{rf}} + X_k \right) + \theta_i, \tag{5.11}$$

where $C_{1,k}$ denotes the clock value of the master at the kth broadcast time, τ_{rf} is the deterministic component of the radio's send-receive delay, and X_k is the random component of the radio's delay. As discussed in Section 5.5.1, quartz crystal oscillators have a clock rate which is accurate to just a few 10s of ppm, i.e., $f_i \approx 1$. Therefore, according to (5.11), it is difficult to differentiate between the clock offset, θ_i, and the radio delay, $\tau_{\text{rf}} + X_k$. This means that in order to effectively calculate each slave's clock rate and offset, the deterministic radio delay, τ_{rf}, should be known, and the random delay, X_k should be minimised by transmitting many messages. A FTSP-based system uses a collection of synchronisation messages to form a table of global-local timestamp pairs. A linear regression is then calculated on this table to find each slave's rate and offset. The FTSP also allows multi-hop synchronisation. After receiving

[6]The nRF24L01+ does not try to detect collisions with other radios on the same channel. It is up to the user to prevent this from occurring.

a synchronisation message, the slave nodes re-broadcast their received times to any remaining slave nodes.

Tackett et al. use a modified version of the FTSP to calculate each slave node's rate and offset. In their implementation, the master node transmits the previous synchronisation message's time. It does not send the current message's time because the timer is latched[7] immediately after transmission. The nRF24L01+ radio employed has an interrupt request (IRQ) pin which can be configured to assert on certain events. The IRQ pin on the radio was connected to the microcontroller's timer peripheral, and was used to latch the timer value each time the master's transmission completes. On the slave side, the nRF24L01+ was configured to assert its IRQ and latch the timer when a message is received. In this way, the slave constructs a table of master-slave times, with an entry for each received message. The slave performs linear regression on its synchronisation table to calculate its clock rate and offset relative to the master. Prior to calculating the regression, the slave must *normalise* the synchronisation table by moving each transmission time up the table by one place, so that the master time corresponds to the correct slave reception time. Tackett et al.'s implementation of the FTSP did not consider the transmit-receive delay, $\tau_{\text{rf}} + X_k$.

5.5.3 Radio delay experiment

It was stated in Section 5.5.2 that Tackett et al. [2011]'s implementation of the FTSP disregarded the radio's transmit-receive delay. In this section, it will be shown that this delay must be considered in the WTT system.

An experiment was performed to measure the mean transmit-receive delay of the nRF24L01+ radio. Two prototype WTT boards were used, one configured as the master, transmitting; the other as the slave, receiving. The master was configured with two timers modules running synchronously, i.e., each timer has the exact same value at any time. The first timer was configured to latch its value when the IRQ line from the master's radio asserts. This occurs when the transmit is complete. The second timer module was set to latch when the IRQ line on the slave's radio asserts, on reception. The slave's IRQ line was connected to the master board via a short wire. It is assumed that the propagation delay over the wire is much smaller than the transmit-receive delay. By subtracting one latched timer from the other, the transmit-receive delay was measured. The timer values were sent to a PC via a USB serial port. This experiment was performed using radio data rates of 1 Mbps and 2 Mbps.

A histogram of the measured delays is shown in Figure 5.14. At each data rate, the delay appears to be split into two distributions. The separation between these two distributions corresponds to the period of one bit at that rate, i.e., $\Delta\tau_{(1\,\text{Mbps})} = 1\mu s$,

[7] To *latch* a register means to hold its value. In this case the timer's instantaneous value is held in a separate register or memory location.

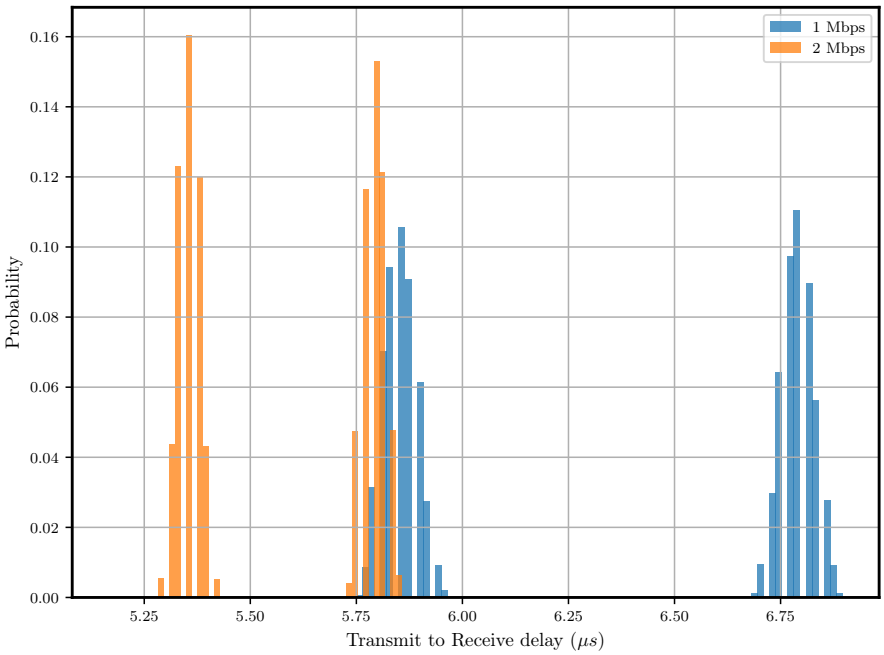

Figure 5.14 Histograms showing the transmit-receive delay of the nRF24L01+ radio. The two WTT boards were placed parallel to each other with a separation of 10 cm. The bin width of the histogram is equal to the period of the timer clock $t = 1/(48\text{ MHz})$.

$\Delta\tau_{(2\,\text{Mbps})} = 0.5\mu s$. This one-period delay may be caused by the preamble bit-alignment delay, described in Section 5.5.1. The mean and standard-deviation of each set of delays is shown in Table 5.3. The mean transmit-receive delay, for either data rate, is significantly greater than the specified measurement accuracy of $1\,\mu$s for the system overall. In order to correct for the synchronisation error caused by the transmit-receive delay, the mean delay must be subtracted from the slave's synchronisation time, prior to performing the synchronisation regression.

Table 5.3 Mean and Standard-deviation of the transmit-receive delays of Figure 5.14, rounded to 2 significant figures.

	Mean (μs)	Std-dev (μs)
1 Mbps	6.32	0.47
2 Mbps	5.57	0.22

5.5.4 Clock rate experiment

The linear clock model, (5.10), assumes that the clock's rate is constant over the period of the experiment. In practice, the rate of quartz-crystal based clocks are known to drift over time as temperature, humidity, and pressure change [Allan et al. 1997]. Rather than use a basic quartz crystal for the WTT probe, a more accurate TCXO module was selected, because of its improved frequency and temperature stability [Horowitz

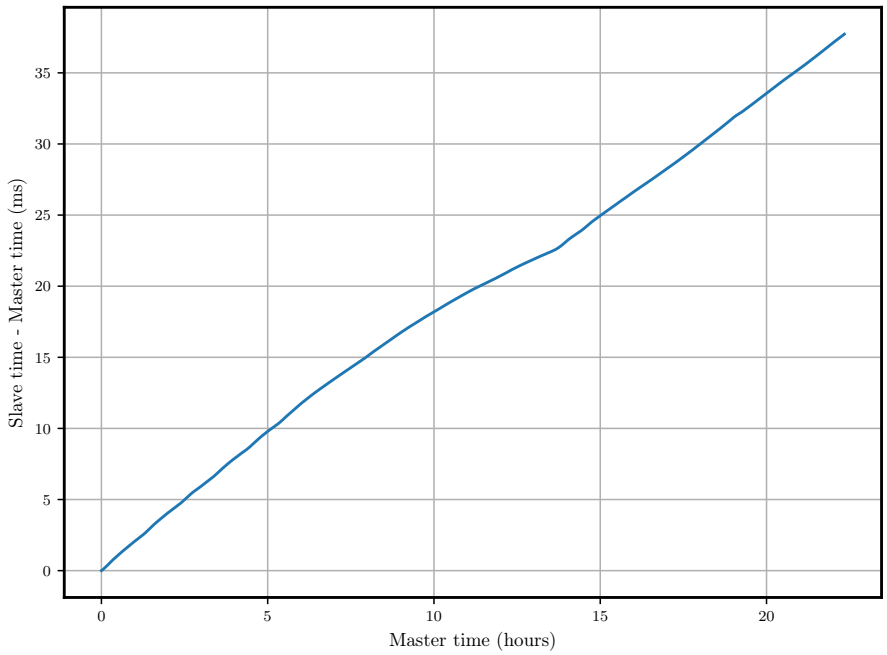

Figure 5.15 The difference between the two device's clocks, plotted over 22 hours. The gradient indicates the relative clock rate, in this case the average relative-rate is $f_{1,2} = 0.469\,\text{ppm}$.

and Hill 2015]. In order to determine the effectiveness of this device, an experiment was performed to measure the relative clock-rate between two prototype WTT probes.

One WTT probe was configured as the master node, and the other was configured as the slave. Both probes were set up with a free running timer, which was set to latch its value when a pin was asserted. The master was configured to periodically assert a pin, which was connected to the timer-input pins on both the master and the slave. When the pin was asserted, both timers were printed to a console on a PC via USB for later analysis.

The TCXO used by WTT has a specified maximum frequency stability of $f_{\text{TCXO(max)}} = 2\,\text{ppm}$ [Abracon 2015]. So the maximum theoretical relative clock rate between the two oscillators is 4 ppm. It should be noted that it is not possible to measure the absolute clock rate using this method. There is no absolute time reference, so only the relative rate can be measured.

The experiment was performed over a period of 22 hours. The timer was captured once per second. The difference between the two clocks is shown in Figure 5.15. The average clock rate between the two devices was determined to be $f_{1,2} = 0.469\,\text{ppm}$. This is significantly lower than that predicted by the TCXO's specifications.

5.5.5 Synchronisation parameters experiment

A test implementation of the FTSP algorithm was built as a Python program. This test-program allowed two important parameters, the table-size and the synchronisation

interval, to be measured. The test implementation was applied to data measured from two prototype probes. In this section, these measurements are described, and values for the synchronisation algorithm's parameters are provided.

One probe was configured as the master, the other as the slave. As in the experiments described in Sections 5.5.3 and 5.5.4, a wire connecting the two devices was used to periodically latch both device's clock values. These values were printed to a PC via a USB console. The synchronisation radio was also used to send the master's timer value to the slave, generating master-slave timer pairs, as in the final algorithm implementation. These values were printed to the PC, and were used to generate the synchronisation table. This approach allowed the actual times to be compared to those derived from the synchronisation algorithm. Thus, a value for the synchronisation error can be determined.

The experiment was performed over a period of 20 hours, with a synchronisation message sent every 2 s, with a radio data rate of 1 Mbps. Figure 5.16 shows a histogram of the synchronisation error, calculated after each received message. Note that the transmit-receive delay (Table 5.3) has not been subtracted from the data in this experiment. If this were conducted, the distribution would have zero-mean.

An analysis was performed to calculate the effect of table size and synchronisation interval. The interval, in seconds, between synchronisation messages is denoted λ. The size of the table is denoted N. Thus, the time required to fully populate the table is given by $T = N\lambda$. T should be minimised because a long synchronisation time causes unnecessary delays for the user. Also, a longer time synchronising will cause a greater drain on the system's battery. Figure 5.17 shows the effect of table size on the synchronisation error. For a table size of $N = 40$, the synchronisation error is unlikely to be greater than $0.1\,\mu$s.

5.5.6 Algorithm implementation

The algorithm implemented by WTT is similar to the FTSP system used by Tackett et al. [2011]. For the typical two probe system, one probe is elected the master and the other is the slave. The master periodically broadcasts messages containing the timer value of the previous message's transmission time. Both the master's transmission time and the slave's reception time are determined using the nRF24L01+ radio's IRQ pin to drive a timer-input pin, which latches the timer when it is asserted. The master also transmits a *message ID* to the slave. This allows the slave to determine whether a message was dropped in transit, since the nRF24L01+ does not implement re-transmissions.

On the slave, the table of timer-pairs is implemented as a circular buffer. This buffer is at maximum 100 entries long, though only the newest 50 entries are used to synchronise the system. It is longer than required because messages with discontinuous message IDs are stored, even though they are not used when calculating the clock

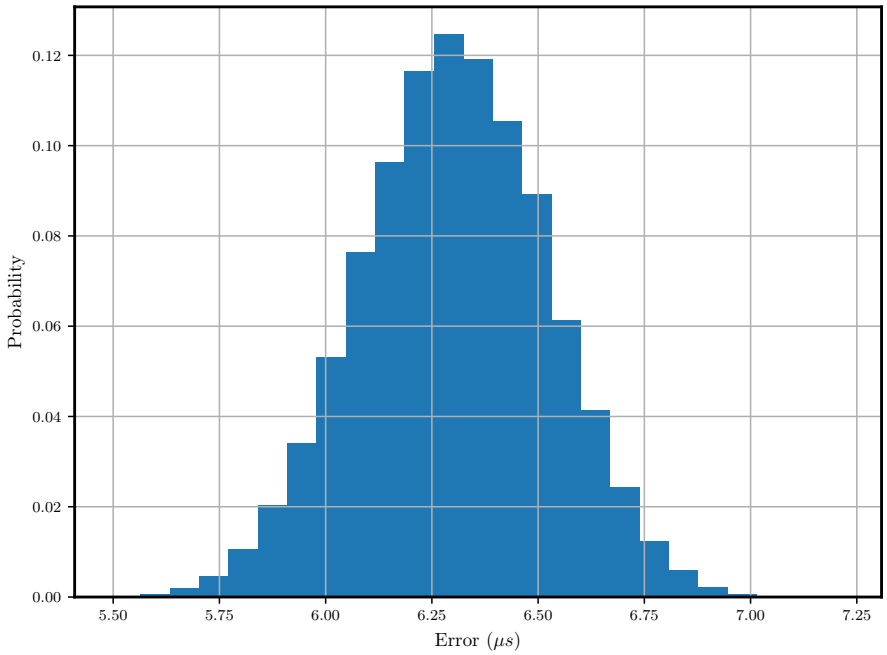

Figure 5.16 The distribution of synchronisation errors. The synchronisation algorithm employed a table size $N = 20$, captured at synchronisation interval $\lambda = 2\,s$. The mean and std-deviation, rounded to two S.F., are 6.30 μs and 0.21 μs, respectively.

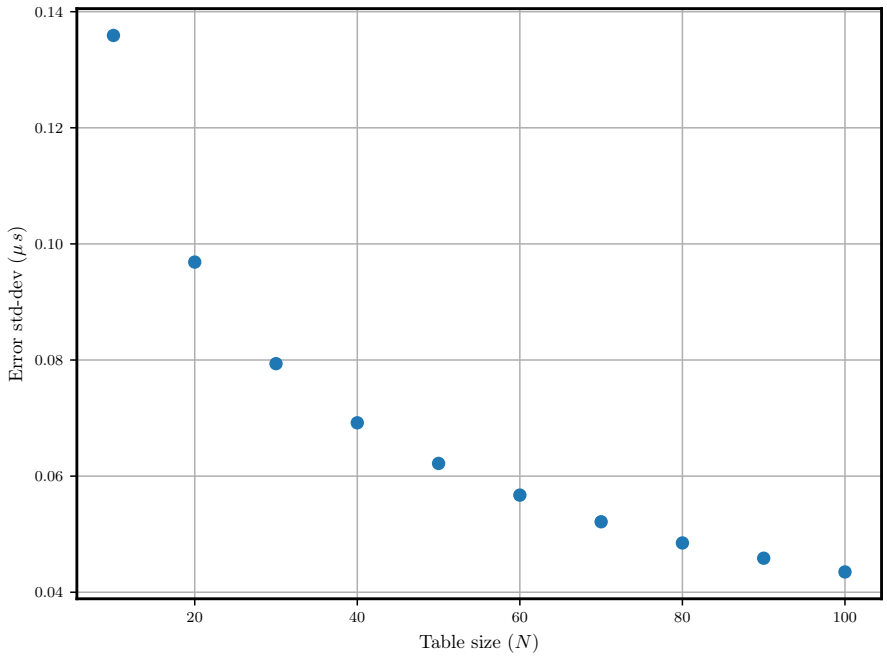

Figure 5.17 The standard deviation of the synchronisation error, plotted against table size, N. The synchronisation was performed with an interval of $\lambda = 100\,\text{ms}$

model. In normal operation the master sends a synchronisation message once every second. This means that the table is very slow to populate. To address this, a *quicksync* function was implemented. When the probes are first connected, the master sends 100 synchronisation messages in quick succession, preloading the table.

The calculation of the slave probe's clock rate and offset is performed by the Android app. After a measurement has completed and the app has downloaded each probe's waveform, it requests the slave's synchronisation table. If the table is insufficiently short (less than 50 entries), the app indicates that synchronisation is incomplete, and the measurement is discarded[8]. If the table is long enough, the slave normalises the table by offsetting the master entries, then returns the table to the app. The app then subtracts the transmit-receive delay (the measurement of which was described in Section 5.5.3) and performs a linear regression on the table to calculate the slave's clock rate and offset. The linear clock model is then used to find the true time difference between both probes at the waveform start. This delay is then returned to the user and saved by the app.

5.6 TIME DELAY ESTIMATION

It was explained in Section 5.3.6 that WTT uses a threshold method to detect when a probe has become *triggered*. The simplest method of determining the time delay, τ, between the two probes is to take the difference between each probe's trigger time, after time synchronisation has been performed. However, this is not the only possible method of calculating the time delay. In this section, several different methods of calculating the time delay are discussed.

A simple model for the signals received by each probe is

$$s_1(t) = x(t) + n_1(t), \tag{5.12}$$

$$s_2(t) = Ax(t-\tau) + n_2(t), \tag{5.13}$$

where x is the ideal (noise-less) signal received by each probe; n_1 and n_2 are noise signals, modelled as additive white gaussian noise (AWGN); A is the (attenuating) gain of the far signal, due to propagation through the wood; and τ is the acoustic delay due to propagation through the wood. In a ToF measurement system, such as WTT, the time delay, τ, is estimated, then (1.11) is used to calculate the velocity.

In practice, there are additional complexities in the velocity calculation. The distance, z, between probes may not be known to a high accuracy, which introduces additional uncertainty in the velocity. Also, the measured signals are not as simple as that suggested by (5.12). For example, a stress wave propagating in a standing tree reflects when it encounters an impedance mismatch, such as the outer edge of the

[8]This error should not occur during normal operation.

xylem. These reflections result in a highly reverberant environment, complicating direct comparison of the two waveforms. Additionally, wood is a dispersive medium, so the resulting velocity depends on the frequency of the input signal. This effect is discussed further in Chapter 4.

Björklund [2003] provided a review of time delay estimation methods, as applied to linear systems. He explained that these methods have been used in a variety of applications including radar, sonar, cellular radio, and speech analysis. The time delay estimation problem can be summarised as follows. The received signal, $s(t)$, is sampled to a sequence $s[n]$. The time delay, τ, is then extracted using an *estimator* function, g,

$$\hat{\tau} = g(s[0], s[1], \ldots, s[N-1]), \tag{5.14}$$

where $\hat{\tau}$ is the estimate of the delay. Kay [1993] explained that the output, $\hat{\tau}$, can be described by a joint probability density function (PDF). A measure of the estimator function's performance is desired so that the estimator can be compared against other potential candidates. A commonly used performance metric is the *variance* of the estimator. The variance is a measure of its expected deviation from the actual parameter, defined as,

$$\mathrm{Var}(\hat{\tau}) = E\left[\left(\hat{\tau} - E[\hat{\tau}]\right)^2\right], \tag{5.15}$$

where E is the expected-value operator. Kay [1993] also explains that the variance of the estimator is always larger than a value known as the Cramér-Rao lower bound (CRLB), which is defined in Kay [1993].

5.6.1 Delay estimation methods

The measured delay is strongly influenced by the method used, i.e., the estimator, used to determine the signal arrival. In this section, several estimators are defined. These methods fall into two categories: threshold based methods, and correlation based methods. Threshold based methods are described in Section 5.6.1.1. Correlation based methods are described in Section 5.6.1.2. In Section 5.6.2, an experiment is described where ToF measurements were recorded using WTT. The proposed delay estimators are then compared.

5.6.1.1 Threshold-based methods

The simplest, and most commonly used, method of estimating the time delay in ToF systems is using a fixed threshold. With this method, the waveform start is defined as the time at which the first sample exceeds the threshold,

$$\tau_{\mathrm{th}} = \min(t) : |s(t)| > T, \tag{5.16}$$

where τ_{th} is the threshold time, and T is the threshold voltage. The total time delay is then given by subtracting each signal's threshold time. When using a fixed threshold with no additional processing, this method is referred to as the *threshold method*.

The measured signal includes additive noise. This noise tends to bias the arrival time of each signal to less than the true value, as the additive noise can prematurely exceed the threshold. To counter this effect, a band-pass filter can be applied to the measured signal to remove out of band noise, and also remove any DC-offset which could also bias the arrival time. The filter cutoff frequencies should be selected so that it removes as much noise as possible without removing the in-band signal. This method is referred to as the *threshold method with filtering*.

It is well understood that wood is a highly attenuating medium (see Chapter 4). This means that the far signal, s_2, tends to have a smaller amplitude, as reflected in the model, (5.12). An effect of this is that the far signal's threshold-time tends to increase, because the rise-time of a sinusoidal signal is inversely proportional to both frequency and amplitude [Ambardar 1999]. To counter this effect, the far signal can be normalised to increase its amplitude. One way to define the normalisation factor, G, is

$$G = \frac{\max|s_1(t)|}{\max|s_2(t)|}, \tag{5.17}$$

which is then multiplied by s_2 before calculating the threshold-time. This method is referred to as the *threshold method with normalisation*.

5.6.1.2 Correlation-based methods

Another method of estimating the time-delay is using the *cross-correlation* function [Knapp and Carter 1976]. This method has been previously applied to ToF acoustics for the purpose of measuring the speed of sound in *Pinus radiata* seedlings [Emms et al. 2012, 2013]. The cross-correlation between signals $s_1(t)$ and $s_2(t)$ is given by

$$R_{s_1 s_2}(\tau) = E\left[s_1(t)s_2(t-\tau)\right]. \tag{5.18}$$

The delay, τ, is then the value which maximises $R_{s_1 s_2}(\tau)$. However, in practice $R_{s_1 s_2}(\tau)$ cannot be determined due to finite-length signals. The correlation may be estimated using the cross-correlation function, which is defined as

$$\hat{R}_{s_1 s_2}(\tau) = \int_{-\infty}^{\infty} s_1(t)s_2(t-\tau)\mathrm{d}t \tag{5.19}$$

[Ambardar 1999]. Again, the time delay is the time at which the cross-correlation function is a maxiumum,

$$\tau_{\text{corr}} = \tau : \max\left[\hat{R}_{s_1 s_2}(\tau)\right]. \tag{5.20}$$

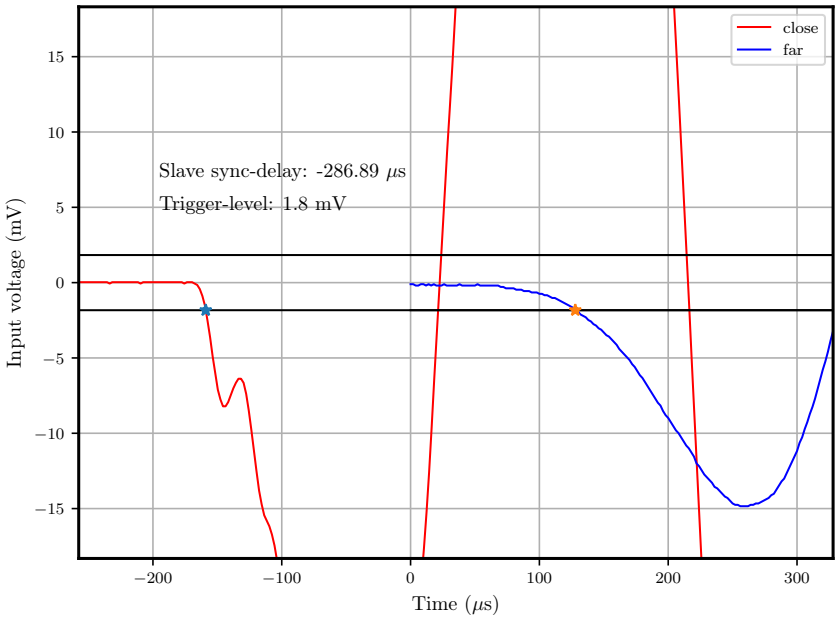

Figure 5.18 A signal captured by WTT devices during the time delay experiment. The signals have been scaled to the probe's input voltage.

The correlation is a measure of the similarity, or the *coherence* of the two signals. Knapp and Carter [1976] explained that a variant of the cross-correlation function, known as *generalised cross-correlation*, can provide an improvement over standard correlation if the noise spectrum is not flat. This approach was not considered further in this analysis.

5.6.2 Time delay experiment

An experiment was performed to capture a series of waveforms in a standing Beech tree. 108 measurements were recorded using two WTT probes, separated longitudinally in the tree by 50 cm. A metal spike was placed 20 cm below the lower probe, as in the experiment described in Chapter 4. The probes were not moved throughout the experiment, therefore, each of the 108 measurements should have approximately the same time delay.

An example of one of the measurements is shown in Figure 5.18. The threshold voltage is marked with a horizontal line. The threshold voltage was selected using the trigger threshold, at the Low sensitivity level, as defined in Section 5.3.6. The threshold method with filtering was also implemented. A finite impulse response (FIR) digital filter was created with a low-frequency cutoff of 100 Hz and a high-frequency cutoff of 75 kHz. The filter was designed using the window method [Oppenheim and Schafer 2010]. The threshold method with normalisation was also implemented, using the normalisation factor given by (5.17). A correlation-based method was also implemented using the discrete cross-correlation function [Oppenheim and Schafer 2010]. It was found that

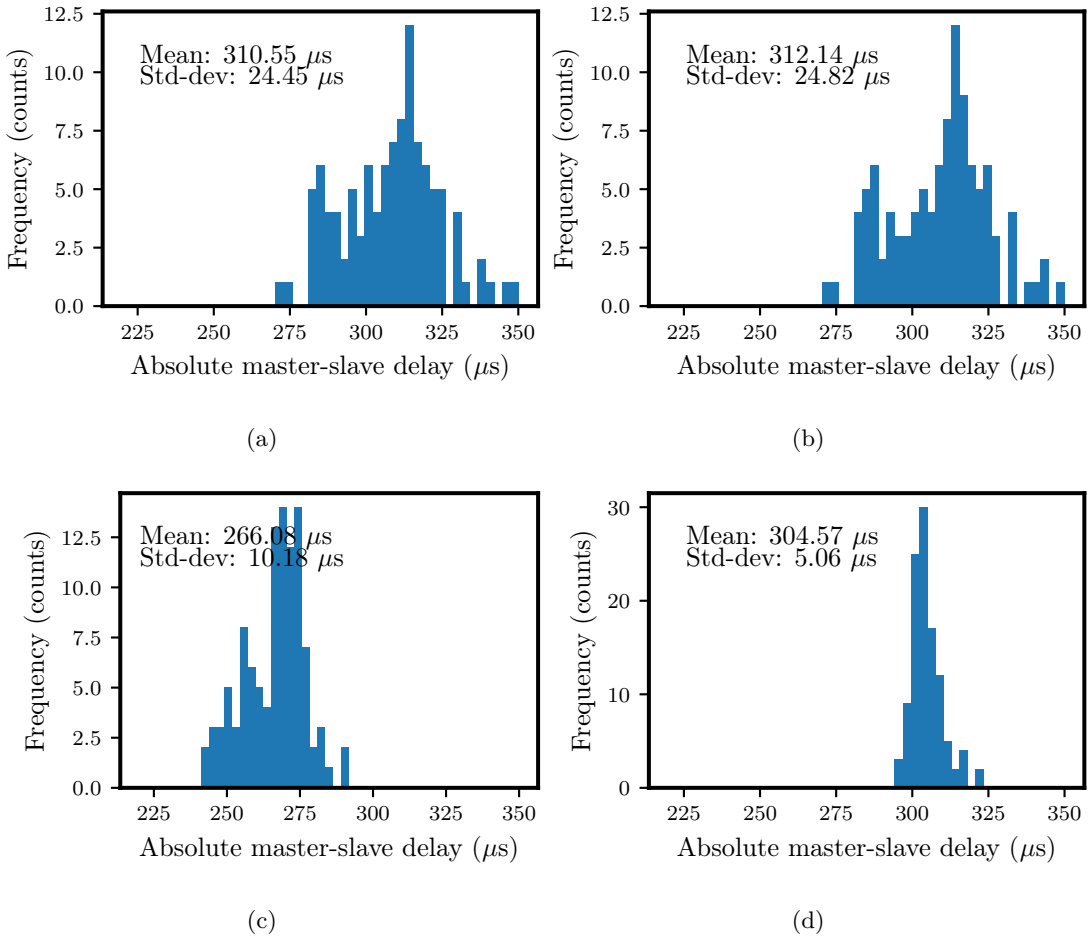

Figure 5.19 Delay histograms for each method of determining the time delay. (a) threshold method, (b) threshold method with filtering, (c) threshold method with normalisation, (d) cross-correlation with Hann window.

it was difficult to select the correct peak from the resulting cross-correlation because the signals are not identical in form. To correct for this effect, a window function was applied to the initial part of the waveform. A Hann window of length $N = 300$ samples was applied, centred around each signal's threshold sample.

Each of the four methods was applied to all 108 measurements. Histograms of the measured delays are shown in Figure 5.19. The simplest method, the threshold method, determined a mean delay of 310.55 μs. The FIR filter did not have a significant effect on the measured delays, as the mean and standard-deviation of these delays is similar to that of the threshold method. The threshold with normalisation method reduced the measured delays significantly, and also reduced the variance of delays. This was expected, as the slower rise time of the attenuated signal has a large effect on the measured delay. The cross-correlation method determined a similar delay to the threshold method, with a mean value of 304.57 μs. The standard-deviation of the correlation method, however, is significantly smaller than the other methods, with a

value of 5.06 μs. This suggests that it might be the best method of the four considered in this study.

As of the time of writing, WTT only implements the threshold method, using the trigger threshold. Future work could integrate other methods into the app, such as the cross-correlation method.

5.7 FIELD TESTING

A field test of the WTT system was conducted in Rotu forest, in the Northland region of New Zealand. This test was conducted as part of a breeding trial, run by The Radiata Pine Breeding Company (RPBC). WTT was used to measure the ToF velocity on 144 5-year old *Pinus radiata* trees. The ToF was measured on two opposite sides of each tree using both WTT and also Treetap 4, which is shown in Figure 5.1(j). The trial was conducted by a subcontractor of RPBC, Wharekura Forestry Services Ltd, who have been using Treetap devices in field trials for over 10 years. An image of a measurement being conducted using the WTT system, taken during the trial, is shown in Figure 5.20.

The objective of this trial was to test several aspects of the WTT system including: the device's strength and robustness, the reliability of the system's software, the ease of use, the speed of conducting measurements, the battery life of the devices, and the reliability of the ToF results produced by the system.

After completing the trial, minor damage was observed on one of the probes. Some cracking had occurred in the perspex around a grub screw. The circuit board also came loose from its fixing grub screws, enabling it to freely move inside the perspex tube. These issues suggest that some work on the probe housing is required before the system is deployed for large scale field use. The software was found to be reasonably reliable. The Android app did crash a few times during the trial, but this did not prevent the trial from continuing. The trial operators stated that they found the app to be beneficial when compared to Treetap 4. In particular, the ability to tag each measurement with a specific tree ID is very useful. Treetap 4 uses an auto-incrementing numerical tree ID, which makes measuring trees out of order difficult. Additionally, if the operator makes a mistake with the tree ID they cannot correct it immediately, as they can with the WTT system. The operators found that the WTT system was slightly slower to use than Treetap 4. Each individual tap takes slightly longer with WTT, due to the delay of downloading the data to the phone. However, the operators noted that fewer errors due to tree ID mistakes may cause the system to be faster overall. The probe batteries lasted for the duration of the trial. The trial took a total time of 4 hours 50 minutes to complete, and the remaining battery charge of the probes were 67% and 46%, respectively.

A comparison of the velocities measured by the two devices was performed. Figure 5.21 shows the distribution of velocities measured during the trial for both devices.

Figure 5.20 Wireless Treetap field trial.

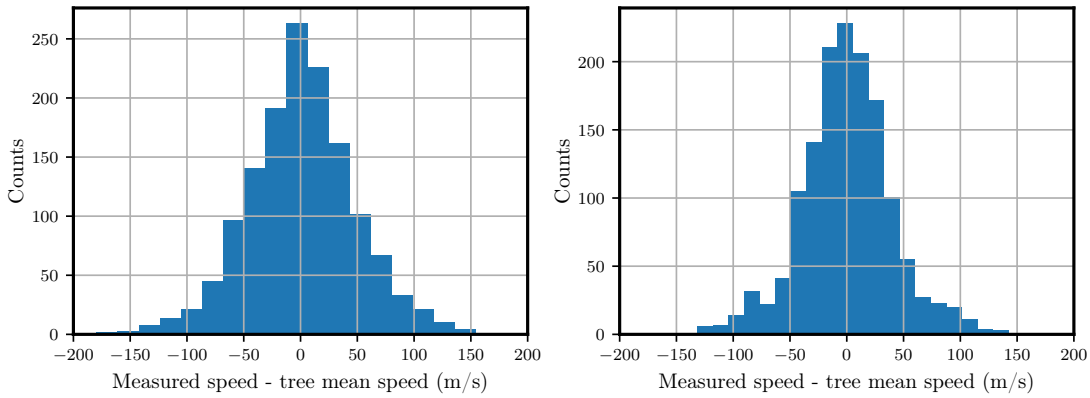

Figure 5.21 Histograms of velocities measured during the field test for (a) Wireless Treetap, and (b) Treetap 4. To allow comparison between trees, the mean velocity of each tree has been subtracted from each measurement. The standard deviation of each distribution is WTT: $\sigma = 73.34\,\mathrm{ms}^{-1}$, TT4: $\sigma = 48.55\,\mathrm{ms}^{-1}$.

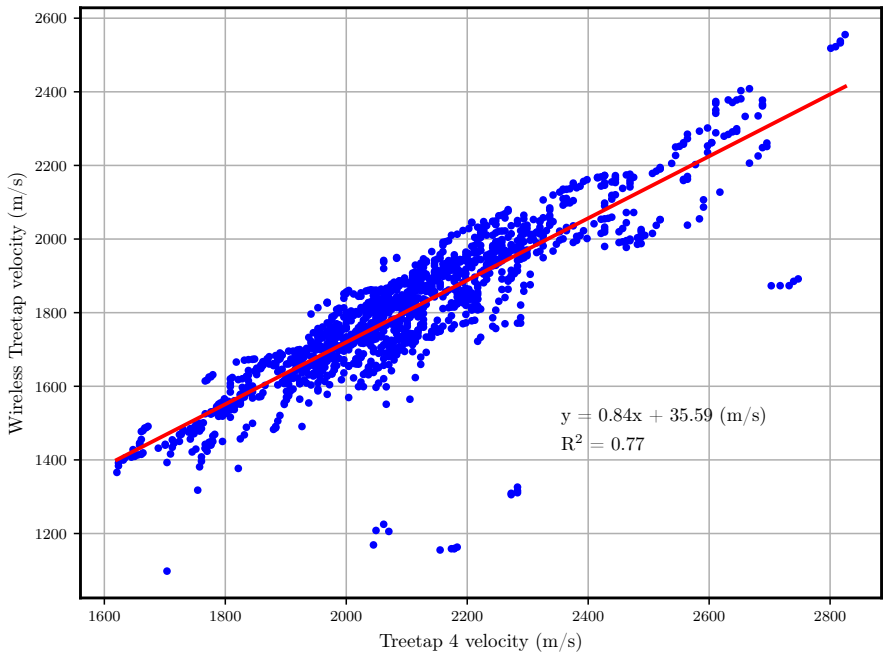

Figure 5.22 Scatter plot of the velocities measured by Wireless Treetap and Treetap 4 during the field trial.

Each measured tree has a considerably different velocity, therefore, the mean velocity of each tree was subtracted so that the variation in velocity measured by the device could be observed. These plots demonstrate that WTT measured a slightly higher variation in velocity across the trial. A scatter plot showing the correlation between the two devices is shown in Figure 5.22. A linear regression line has been indicated on the plot, this demonstrates that WTT has measured a slower overall speed than Treetap 4; the gradient of the fitted line is 0.84. The reason for this finding is unknown, a possible explanation is provided in the following section. Figure 5.22 also contains a number of outlying points, the majority of which fall below the trend line, i.e., indicating that WTT has measured a lower velocity than Treetap 4. It is not possible to tell from this plot which device is in error. However, it is likely that WTT is reporting low velocities, as the measurements taken from the other side of the tree are closer to the velocities reported by Treetap 4. The reason for this error is unknown at the time of writing.

5.8 DISCUSSION

Time of flight systems have been available since the early 1990s. However, the form and implementation of these tools has changed little over time. The Wireless Treetap project is an effort to advance the state of the art, through development of a system utilising modern electronic technologies. WTT is the first known ToF system to use a smartphone as an interface device. This chapter demonstrated the feasibility of building a wireless, smartphone based ToF system. A prototype system was constructed, consisting of two probe units and a smartphone running the Treetap app.

A field trial was conducted to evaluate the robustness and performance of the system. The system functioned reasonably reliably, though the app did crash several times. The errors causing these crashes are probably trivial to fix, though the cause of each error needs to be identified before they can be addressed. A simple way to identify such errors is to automatically save the app's crash log. This should be implemented in future versions of the app. The overall function of the app was well received by the operators. Simple features like allowing tree IDs to be manually input, and erroneous data to be removed, are very useful in the field. Some improvements could be made to the app, such as a simplified means of downloading the measured data. Currently, the data is downloaded from the phone in CSV format using a USB cable. The system may benefit from an automatic data-synchronisation feature, so that data could be automatically sent to a database over the internet. This type of system is more in line with current practices of smartphone software, which rarely uses wired connectivity.

The most concerning outcome of the field trial is the damage observed in one of the probe's housing. The current housing is probably unsuitable for long term use. Each probe should ideally be robust enough to function for a long time, i.e., a year or more of continuous use. There are several possible options of improving the system's physical robustness. Different materials could be used for the probe housing. Currently, clear perspex is used for the inner electronics housing. This material is very hard, but quite brittle, especially in locations where small cracks have developed, e.g., around screw holes. Another method of improving the robustness could be to change the way the transducer attaches to the electronics. Currently, the transducer is rigidly attached to the electronic housing. This means that the housing experiences an impulsive stress when the probe is hit into the tree. The housing could be decoupled from the transducer by separating the two using a short length of cable. When performing a measurement, the electronics housing would dangle from the cable, and would be fixed to the cable using either a crimp or a screwed locking-connector. This arrangement would also have the advantage that the operator must grab the transducer at its head when removing it from the tree. With the current system, they can easily grab at the bottom of the probe, potentially applying a damaging torque where the transducer and housing connect.

Alternatively, the probe's robustness could be addressed by moving back to a

wired solution. Like Treetap 4, this system could use wired transducers and a box of measurement electronics. The measurement box would connect via Bluetooth to the Treetap app. This would significantly reduce the complexity of the system overall, as most of the electronic subsystems, which currently reside in each probe would only need to be implemented once. It would also eliminate the need for the clock synchronisation system, which represents a significant portion of the engineering effort of the WTT system. Using wired probes in a dense forest has been reported to be a nuisance, as they are easily snagged on branches. However, a conscientious operator is not seriously impeded, as extra care can be taken when moving.

The results of the field trial indicated that WTT measured a slightly lower overall velocity than the Treetap 4 system. This is not particularly concerning, as the measured velocity is strongly dependent on the method used for determining the wave start (see Section 5.6). Currently, WTT is using a fixed-threshold algorithm for determining the wave start, and the sensitivity (threshold) used for performing the field trial was the lowest provided setting. It may be that the threshold was set too low in this experiment, which led to a longer delay due to the signal's increased rise-time. The method used by Treetap 4 for determining the wave start is not currently known. Future work could explore alternative wave-start algorithms. One advantage of the smartphone-based system is that it is relatively easy to implement a new algorithm, then deploy a new version of the app. Compared to firmware-only systems, like Treetap 4, where upgrading the software is comparatively difficult.

Chapter 6

MEASURING THE STIFFNESS VARIATION IN HARVESTED TREE-STEMS

Acoustic resonance tools have been used in log grading applications since the early 1990s. These systems are useful for estimating the overall stiffness of a harvested stem, allowing logistical decisions to be made prior to sawing. Resonance-based systems provide a single measurement of a stem's acoustic velocity. However, in practice the stiffness, and thus acoustic velocity, can vary considerably throughout a stem.

In this chapter, a system is proposed for measuring the spatial variation in velocity in a harvested stem. In Section 6.1, an overview of existing log grading techniques are examined, and some of their deficiencies described. A brief overview is provided of known stiffness variation within *Pinus radiata* stems. In Section 6.2, the proposed system for measuring the stiffness variation is described. To test the feasibility of this system, an experiment was performed to capture a series acoustic signals along the length of two *Pinus radiata* stems. This experiment is described in Section 6.3. Two different approaches of processing the captured data are assessed in Section 6.4 and Section 6.5. An analysis of the results of the experiment and processing methods are provided in Section 6.6. Finally, a discussion of these results is provided in Section 6.7.

6.1 INTRODUCTION

Foresters and wood-processors seek to maximise the financial return from their raw wood stock. When a tree is harvested, the sawmill cuts the stem to target a particular market. Therefore, the sawing pattern has a direct impact on the value obtained from a stem. Typically, after a stem is harvested it is sawn into three or four logs of length between 4 to 8 m [Blackwell and Walker 2006]. The log at the base of the stem is termed the *butt* log, and higher logs are typically numbered *second*, *third*, etc. From these logs, a number of finished products can be produced including veneer, timber, pulp, packaging, and roundwood posts. Each of these products has different requirements from the raw wood, and each has a different return value for the seller. For example, the return on structural wood can be double that of lower value products such as pulp/paper and

packaging products [Apiolaza 2009]. Unfortunately, the amount of structural wood being produced in New Zealand can be as low as 10% of the total yield [Cown and van Wyk 2004].

The purpose of grading systems is to match the requisite traits of a particular market to the wood being graded. Traditionally the industry has relied on human visual inspection of stems and logs to determine value, though more recently there has been a movement towards machine grading, which directly measures the stiffness[1] of cut timber within the sawmill. An overview of these grading systems was provided in Section 1.2.1.

Researchers have applied acoustic technology to grading of logs since the early 1990s [Aratake et al. 1992, Ross et al. 1997, Snyder et al. 2000, Wang 1999, Wang et al. 2001a]. This research has led to the development of acoustic tools employed in production lines for log grading [Carter et al. 2007, Divos 2010]. One example of a commercially available grading machine is Fibre-gen's LG640[2]. This device measures the log's acoustic velocity using a resonance technique. Tools like this allow grading to take place prior to sawing of the log. This enables a sawing pattern to be assigned based on wood quality, minimising wastage and improving logistical efficiency. Existing resonant-frequency based grading systems provide a single measure of the overall stiffness of a log. However, stiffness is known to vary spatially within a log. The ideal grading system would measure the longitudinal stiffness of the entire log in three dimensions, i.e., a *heat map* of the log's internal stiffness.

Wood stiffness inside a tree stem varies both directionally (relative to the grain), and spatially throughout the stem. It is stiffest in the direction of the grain, and significantly less stiff in the radial and tangential directions. This variation is an example of orthotropic anisotropy [Bodig and Jayne 1982, Bucur 2006]. A discussion of wood's directional variation was provided in Section 1.1.2. The stiffness within *Pinus radiata* stems is also known to vary spatially [Cown et al. 1980, Searles 2012, Tsehaye et al. 2000b, Xu and Walker 2004]. When quantifying the spatial variation, generally only the longitudinal stiffness is considered, due to its importance in structural applications. The general trend is that the stiffest wood occurs in the mature outerwood, while the least stiff wood occurs in the corewood. This discrepancy is exaggerated at the base of the stem, where juvenile corewood and high-stiffness outerwood both reside [Xu and Walker 2004]. The exaggerated stiffness profile in the butt log means that the area-weighted stiffness within an average stem is more uniform than if only the corewood or outerwood were considered independently [Tsehaye et al. 2000b]. An overview of the spatial stiffness variation in softwood stems was provided in Section 1.1.2.

The area-weighted stiffness of an average stem may be approximately uniform, however, this does not mean that all trees are uniform throughout. Environmental,

[1] In this chapter, when the generic term *stiffness* is used it refers to Young's modulus in the longitudinal direction of a log or stem.

[2] Fibre-gen LG640–`http://www.fibre-gen.com`.

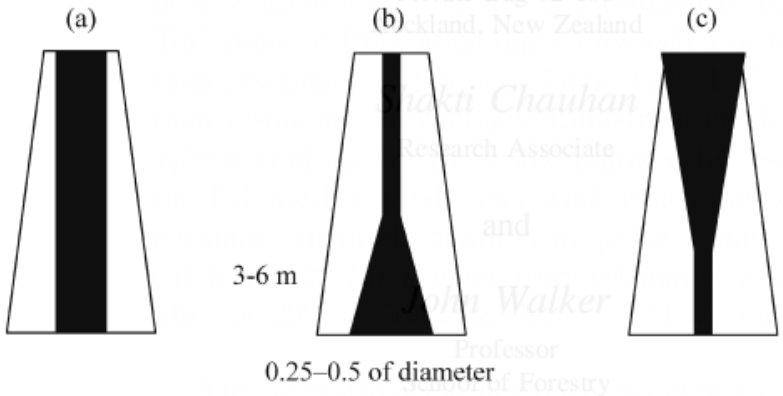

Figure 6.1 Wood quality profiles in radiata pine. (a) where a cylinder of low density wood extends up the entire stem. (b) for stiffness and crook or bow where a variable-sized cone of high microfibril angle is located within the butt log. (c) for twist represented by an inverted cone in the upper logs where spiral grain can be significant ($> 6°$). Taken from Walker [2006b].

genetic, and silvicultural techniques all influence a tree's stiffness [Chauhan et al. 2006b]. Localised effects can cause a portion of a tree stem to exhibit a lower or higher stiffness than might be expected from observing a "normal" region. Some examples of this variation were provided by Xu and Walker [2004]. They described the density variation within a stem due several anomalous growth patterns. For example, in a tree with significant sweep in the butt log, low density cylindrical corewood extends further from the pith than would otherwise be expected. This reduces the overall stiffness of the butt log, and consequently the amount of merchantable wood produced. Some of the possible corewood profiles are shown in Figure 6.1 [Walker 2006b].

One possible approach to this problem is to measure the stiffness variation along the stem prior to sawing. This could allow the low quality logs to be assigned to production lines requiring lower stiffness wood, e.g., pulp or packaging wood, while the higher quality logs are assigned to production lines destined for structural timber. This could potentially allow for an increase in the yield of high-quality wood produced.

6.2 PROPOSED SYSTEM

As discussed in the previous section, stiffness is known to vary considerably within *Pinus radiata* stems. Wood processors would like to gain an indication of this variation, potentially enabling them to more effectively designate raw wood to a particular product prior to sawing.

The proposed system is an extension of the single-transducer resonance system, described in Section 1.2.2. Instead of a single transducer at the end of the stem, multiple transducers are placed along its length, at fixed intervals. As in the resonance method, the stem is struck at the base to induce a stress wave. A sampling device is used to capture the signal at each transducer. By measuring the time taken for the wave to

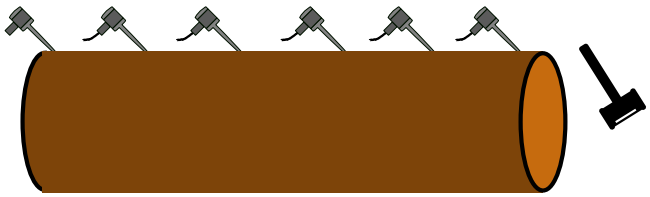

Figure 6.2 The proposed system utilises multiple transducers placed at intervals along the stem.

propagate between the transducers of each segment, the *incremental velocity* can be determined. This should provide an indication of the longitudinal variation in stiffness. It does not measure the radial variation in stiffness. The method assumes that the incremental velocity provides an indication of the average stiffness through a segment, as has been observed for the resonance method [Carter et al. 2007]. If this assumption is correct, the incremental velocity in a segment which has a low overall stiffness, e.g., a bowed butt log, should also be low.

6.3 EXPERIMENTAL METHOD

An experiment was performed to estimate the variation in stiffness along the length of two 8 metre stems. Each stem is the lower (Butt) log taken from two 25 year old *Pinus radiata* trees. This experiment was performed on each stem in two separate stages. First, a series of acoustic waveforms was captured from the complete stem; this stage is referred to as the *stem* experiment. Second, the stem was sawn into 1 m segments on which additional waveforms were captured; this stage is referred to as the *segment* experiment. A more detailed explanation of each of these stages follows. A photo of the *Pinus radiata* stems is shown in Figure 6.3.

Four Fakopp SD-02 acoustic transducers were employed for the stem experiment. The following procedure was performed on each stem. One transducer, labelled *start*, was placed on the bottom face of the stem (closest to the butt of the stem). Another transducer, labelled *end*, was placed at the top face of the stem. Another two transducers, labelled *forward* and *reverse* were each placed at an angle of 45° to the stem, located a distance z from the bottom face. The stems were supported by pieces of timber placed approximately at the nodal points of the second harmonic (see Figure 6.6) to minimise the loss through the supports. A diagram of the experimental setup is shown in Figure 6.4a.

The forward and reverse transducers allow the *inplane* (longitudinal) and *out-of-plane* (transverse) signals to be measured. This is achieved by taking the vector sum and difference of the two signals, respectively. This method was inspired by the stereophonic playback method used in vinyl records [Blumlein 1931]. Thus, the inplane signal is

Figure 6.3 The 8m *Pinus radiata* stems.

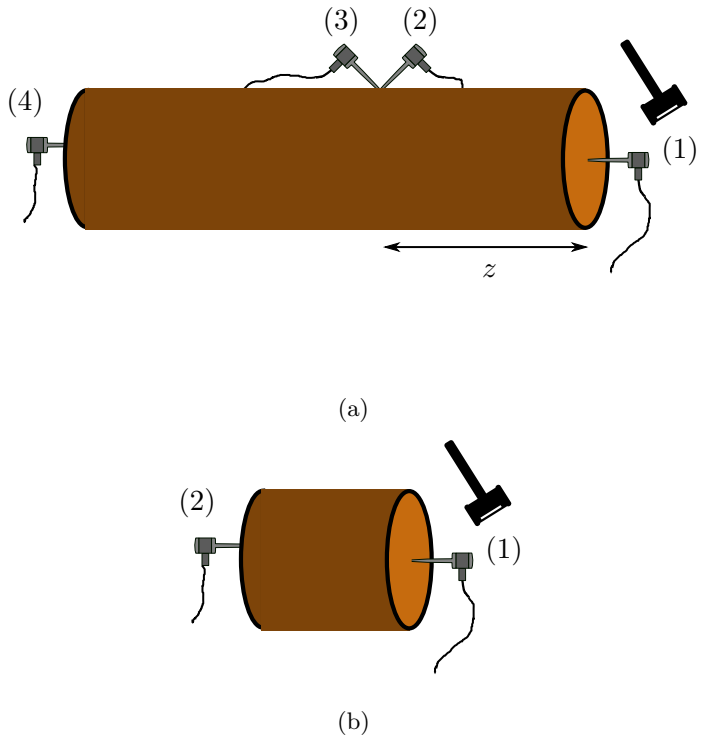

Figure 6.4 The experimental setup for the two phases. In the stem experiment (a), the transducers are labelled (from the right): *start* (1), *forward* (2), *reverse* (3), *end* (4). In the segment experiment (b), the transducers are labelled (from the right): *start* (1), and *end* (2).

given by

$$y_{\text{inp}} = \frac{y_{\text{fwd}} - y_{\text{rev}}}{2}. \tag{6.1}$$

The out of plane signal is given by

$$y_{\text{out}} = \frac{y_{\text{fwd}} + y_{\text{rev}}}{2}. \tag{6.2}$$

The stress waves were induced by striking the base of the stem with a hammer.

For stem 1, the forward and reverse transducers were moved up the stem in 0.25 m increments. At each increment the stem was struck 5 times. For stem 2, the experiment was performed at 0.1 m increments. For each strike, the set of signals was captured on a four channel Tektronix DPO3014 oscilloscope[3]. Note that the Wireless Treetap system, described in Chapter 5, would have been a viable alternative for performing these measurements. However, the Wireless Treetap system was not yet functionally complete at the time that these experiments were conducted. The oscilloscope was configured to capture $N = 100$ k points at a sampling rate of $f_{\text{s}} = 2.5$ MHz, for a total sampling time of 40 ms. The oscilloscope was configured to trigger on the transducer at the butt of the stem, at a voltage of -5 mV. The oscilloscope was configured to capture 1 ms of data prior to triggering. The oscilloscope has an 8-bit analogue to digital converter (ADC), but averaging was enabled on the device, which increases the effective resolution to 12-bits.

Preliminary testing revealed that repeated striking of the hammer on the base of the stem caused permanent damage to the wood. The damaged region has a very low stiffness, likely due to the hammer damaging the wood fibres. This damage caused an additional time delay and increased damping of the received signal. To counter this effect, a metal plate was fixed to the end of the stem. This allows the total force of the hammer to be spread over a larger area, reducing the stress across the bottom face of the stem.

In the second phase of the experiment, referred to as the segment experiment, each stem was sawn into segments of approximately 1 m. The start and end transducers were inserted into each face of the sawn segment at the pith. The forward and reverse transducers were not utilised for this phase of the experiment. The oscilloscope was configured in the same manner as in the stem experiment: $N = 100$ k samples, $f_{\text{s}} = 2.5$ MHz. The segment was struck with the hammer at the end closest to the base. For each strike, the start and end signals were captured and recorded on the oscilloscope. This was repeated 5 times for each segment. The metal plate was not required for this phase of the experiment, as each segment was struck a total of only 5 times. A diagram of the setup for the segment experiment is shown in Figure 6.4b.

[3]Technical documentation available at `https://www.tek.com/oscilloscope/mso3000-dpo3000`.

6.4 THE TIME OF FLIGHT METHOD

The time of flight (ToF) method was evaluated as a potential means for finding the incremental velocity. As discussed in Section 1.2.3, ToF systems measure the stress-wave velocity by determining the elapsed time, τ, between two transducers separated by a known distance, z. The remainder of this section describes the signal processing operations which were performed on the received signals to extract the variation in acoustic velocity.

One difficulty with this method is in determining the precise time at which the waveform arrives. The simplest method is to define a threshold voltage. This method was defined in Section 5.6.1.1.

It is well known that green wood is highly attenuating (see Chapter 4). This fact, in combination with the spreading of the wave's energy, means that as the distance, z, increases, the received amplitude is significantly reduced relative to the start transducer. For this reason, each received signal was normalised prior to determining the threshold time. Each signal was normalised by its RMS value,

$$y_{\text{norm}}(t) = \frac{y(t)}{y_{\text{RMS}}}, \tag{6.3}$$

where y_{RMS} is given by,

$$y_{\text{RMS}} = \text{RMS}\left\{y\right\} = \sqrt{\frac{1}{N}\sum_{n=0}^{N-1} y^2\left(n\right)}, \tag{6.4}$$

where N is the total length of the signal in samples. For brevity, y_{norm} will be referred to simply as y in subsequent signal processing operations.

A fixed value threshold, as given by (5.16), relies on the received signal having a zero mean value. If this is not the case, an additional delay will be present in the propagation time, due to the finite rise-time of the received signal. This additional delay could either add or subtract from the true delay, depending on the sign of the mean and the polarity of the received signal. To counter this effect, the mean, μ, was estimated and then subtracted from each signal. The mean was estimated using the samples captured prior to the oscilloscope's trigger time,

$$\mu = \frac{1}{M}\sum_{n=0}^{M-1} y\left(n\right), \tag{6.5}$$

where M is the sample at which the oscilloscope was triggered[4].

[4]The oscilloscope's *trigger* is implemented using a threshold approach. The oscilloscope defines its time origin as the sample at which the trigger voltage is exceeded. The oscilloscope will continuously sample and record data, but only displays the waveform once the trigger has been exceeded.

The threshold, T, was selected by taking the RMS value of the recorded signal prior to triggering, i.e., the noise, and then multiplying it by a fixed factor,

$$T = \alpha \cdot \mathrm{RMS}\left\{y\left(n\right)\right\} : 0 \leq n \leq M, \tag{6.6}$$

where α is the *threshold factor*. Since the mean has been removed, the RMS value is equivalent to the sample standard deviation[5]. The threshold factor was selected using trial and error, choosing α to be small, while also avoiding spurious triggering due to noise. The value selected was $\alpha = 6.0$.

If the noise is a Gaussian process, then the probability of a sample exceeding a certain value can be calculated. The probability of a single sample to exceed the selected threshold is very small ($P(y\left(n\right) > 6\sigma) \approx 1.973 \times 10^{-9}$). It was found that choosing a value of α less than 6.0 caused the algorithm to prematurely trigger. Therefore, it is unlikely that the noise is a purely Gaussian process.

Another method of identifying the wave's arrival time is to search for the first peak. In this method, a waveform is incrementally searched for the first maximum which exceeds a certain threshold. This method is susceptible to finding a peak on erroneous maxima because of noise present in the signal. Therefore, it is necessary to first reduce the noise using a low-pass filter. In this case, a Gaussian filter with a cutoff frequency of 50 kHz was used to smooth the signal. This type of filter is commonly used for signal smoothing applications, and also has the benefit that it has the minimum possible group delay [O'Haver 2018].

The velocity between the base of the stem and the inplane probes was calculated for each incremental probe position. This is referred to as the *cumulative* velocity, given by

$$c_i = \frac{z_i}{\tau_i}, \tag{6.7}$$

where i is the measurement number, z_i is the distance from the butt to the transducers at position i, and τ_i is the ToF from the base to that distance. The measurement number is an index which indicates a measurement taken at a particular distance, z. For example, $i = 0$ corresponds to the measurement at $z = 0.25\,\mathrm{m}$, $i = 1$ corresponds to $z = 0.5\,\mathrm{m}$ etc.

The objective of this experiment is to measure the incremental velocity between sensor positions. To determine the variation in velocity along the length of the stem, the difference between adjacent ToF measurements was taken. This is referred to as the *differential* velocity, given by

$$c_{ij} = \frac{z_i - z_j}{\tau_i - \tau_j}. \tag{6.8}$$

The measurement index, j, can be set to $i - 1$ to compare the ToF between adjacent

[5]Weisstein, Eric W "Root-Mean-Square." From MathWorld `http://mathworld.wolfram.com/Root-Mean-Square.html`

measurements, or set to a greater value, such as $i-4$ to compare the ToF between 1 m increments. The results of applying the ToF method to the captured data is provided in Section 6.6.

The cumulative velocity, (6.7), was also used to calculate the ToF velocities for each of the cut segments. The same approach was used for the segments, except only the start and end transducers were placed in the segment.

6.5 THE RESONANCE METHOD

The *resonance method* uses the longitudinal oscillation frequency of a harvested tree stem to determine the wood's stress-wave velocity. A measurement is typically conducted by placing an acoustic transducer against one end-face of the stem. The operator then strikes the face with a hammer, which causes a stress wave to propagate. The signal reflects back and forth along the stem, establishing a standing wave. The frequencies of which are given by

$$f_{\text{res}} = \frac{nc}{2L}, \tag{6.9}$$

where $n = 1, 2, ...$ These frequencies are known as the *resonant harmonics* of the system, or simply the *harmonics*. The transducer receives the signal, which is transformed to the frequency domain by performing an FFT. The frequency of either the fundamental or the second-harmonic is extracted from the FFT data. The wave velocity is then calculated using (6.9). For more information about the resonance method, and its application to wood grading, see Section 1.2.2.

The resonance method provides an indication of the overall stiffness of a log, it does not measure the spatial stiffness variation. In this section, the resonance method is examined to see if it can be adapted determine the spatial stiffness variation. In Section 6.5.1, a transfer function model of the resonance method in an ideal stem is derived. In Section 6.5.2, the transfer function is generalised to allow a stem with variable acoustic velocity. A modification of the transfer function, referred to in this chapter as *reflected-wave cancellation*, is proposed in Section 6.5.3. The signal processing methods which were applied to the data captured in the stem and segment experiments are described in Section 6.5.4.

6.5.1 Transfer function derivation

In this section, a transfer function is derived for the amplitude and phase of a stress-wave propagating in a tree stem. The stem is assumed to be of known length, L. The stress wave is assumed to propagate longitudinally as a plane wave with no radial component. This means that width of the stem is not considered, and no bar-wave effects are observed (see Appendix B). The wood material constituting the stem is assumed to be

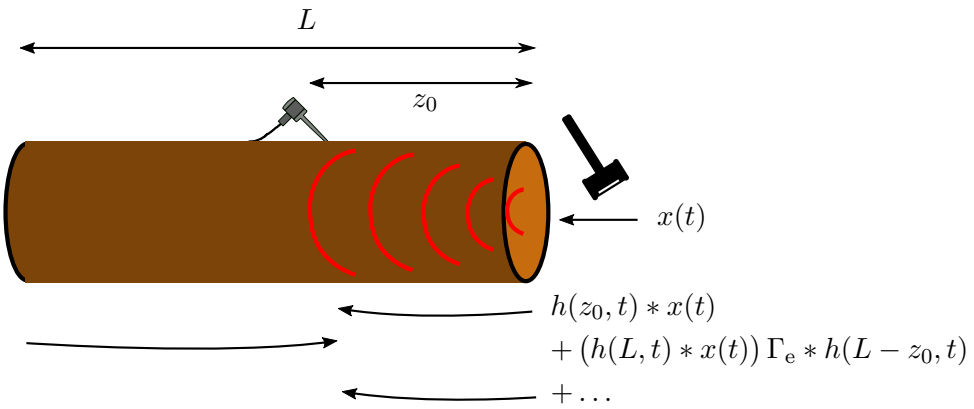

Figure 6.5 The stem's transfer function at a distance z can be described by summing the infinite series of forward and backward travelling-wave components.

isotropic and homogeneous. The wood material is assumed to be adequately modelled as a LTI system, with an impulse response $h(z,t)$.

Consider a signal $x(t)$ generated at one end of the stem. The signal propagates to the far end of the stem, where a portion of the wave is reflected back. The back-propagating signal then reflects off the initial face and the cycle continues. This behaviour can be described as an infinite series of waves. This series can be summed to produce a resultant waveform at a point along the stem. Rather than considering this sum at one end of the stem, the series is generalised by considering the resultant wave at an arbitrary distance, z, along the stem. In the time domain this series is of the form

$$\begin{aligned} y(z,t) = {} & h(z_0,t) * x(t) \\ & + \left(h(L,t) * x(t)\right) \Gamma_e * h(L - z_0, t) \\ & + \Big[\left(h(L,t) * x(t)\right) \Gamma_e * h(L,t)\Big] \Gamma_s * h(z_0,t) \\ & + \Big(\Big[\left(h(L,t) * x(t)\right) \Gamma_e * h(L,t)\Big] \Gamma_s * h(L,t)\Big) \\ & \qquad \Gamma_s * h(L - z_0, t) \\ & + \ldots, \end{aligned} \tag{6.10}$$

where $h(z,t)$ is the impulse response of the wood, $x(t)$ is the applied input signal, L is the length of the stem, Γ_s and Γ_e are the start and end reflection coefficients, respectively, and $*$ denotes the convolution operator. A diagram of this system is shown in Figure 6.5. It was assumed in (6.10) that Γ_s and Γ_e are constant and independent of frequency, allowing them to be multiplied by the time-domain signal. The first term of (6.10) is the first *incident* wave (forward travelling), the next is the *reflected* wave (backward travelling), followed by incident, reflected, *ad infinitum*.

Taking Fourier transforms of both sides gives

$$\begin{aligned} Y(z,j\omega) &= H(z_0,j\omega)X(j\omega) && \text{(incident)} \\ &+ H(L-z_0,j\omega)H(L,j\omega)\Gamma_\mathrm{e}X(j\omega) && \text{(reflected)} \\ &+ H(z_0,j\omega)H^2(L,j\omega)\Gamma_\mathrm{e}\Gamma_\mathrm{s}X(j\omega) && \text{(incident)} \\ &+ H(L-z_0,j\omega)H^3(L,j\omega)\Gamma_\mathrm{e}\Gamma_\mathrm{s}^2X(j\omega) && \text{(reflected)} \\ &+ \dots . \end{aligned} \tag{6.11}$$

(6.11) is then divided by $X(j\omega)$ to obtain a transfer function for the system, $T(z_0,j\omega)$. This can be expressed as the sum of two series,

$$\begin{aligned} T(z_0,j\omega) &= H(z_0,j\omega)\sum_{n=1}^{\infty} H^{2(n-1)}(L,j\omega)\left(\Gamma_\mathrm{e}\Gamma_\mathrm{s}\right)^{n-1} && \text{(incident)} \\ &+ H(L-z_0,j\omega)\sum_{n=1}^{\infty} H^{2n-1}(L,j\omega)\Gamma_\mathrm{e}^n\Gamma_\mathrm{s}^{n-1}. && \text{(reflected)} \end{aligned} \tag{6.12}$$

The first term in (6.12) is the sum of the forward travelling waves, and the second term is the sum of the backward travelling waves. The characteristic acoustic impedance of wood (as defined by (3.5)) is much greater than that of air. Therefore, the reflection coefficients will closely approximate unity, $\Gamma_\mathrm{e},\Gamma_\mathrm{s} \approx 1$. Thus, these terms can be discarded from the transfer function. Each term of (6.12) is a geometric series [Anton et al. 2012]; by substituting the value of the series, the transfer function reduces to

$$T(z_0,j\omega) = \frac{H(z_0,j\omega)H(L,j\omega)}{1-H^2(L,j\omega)} + \frac{H(L-z_0,j\omega)H(L,j\omega)}{1-H^2(L,j\omega)}, \tag{6.13}$$

provided that $\left|H^2(L,j\omega)\right| < 1$.

(6.13) can be further simplified by making an assumption about the wood's (one-way) transfer function. It is assumed that the wood's transfer function is modelled by that of a lossy transmission line, which is of the form

$$H(z,j\omega) = \exp\left(-\gamma z\right), \tag{6.14}$$

[Pozar 2012], where exp is the exponential function, γ is the *propagation coefficient* of the wood, which in general is a complex, frequency dependent function, i.e., $\gamma = \gamma(j\omega)$. Making these substitutions, the transfer function becomes

$$T(z_0,j\omega) = \frac{\exp\left(\gamma(L-z_0)\right) + \exp\left(-\gamma(L-z_0)\right)}{\exp\left(\gamma L\right) - \exp\left(-\gamma L\right)} \tag{6.15}$$

$$= \frac{\cosh\gamma(L-z_0)}{\sinh\gamma L}, \tag{6.16}$$

where cosh and sinh are the hyperbolic trigonometric functions [Abramowitz and Stegun

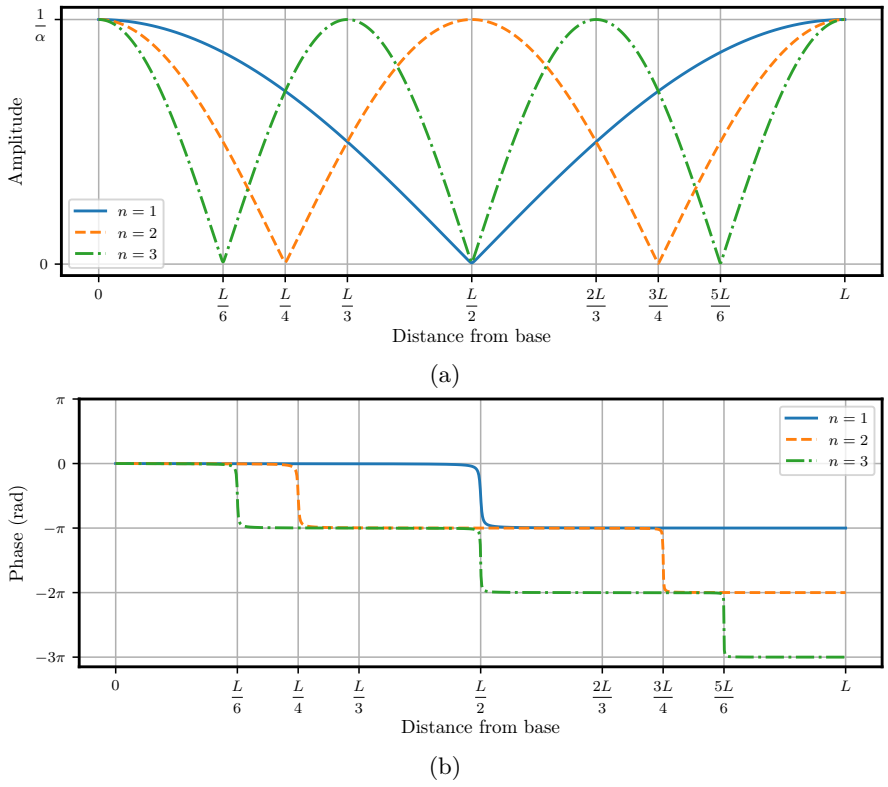

Figure 6.6 The magnitude (a) and phase (b) of the stem's transfer function, $T(z_0, j\omega)$, are plotted against distance along the stem, evaluated at the frequencies of the first 3 harmonics. The regions in the magnitude response where the amplitude is minimal are referred to as *nodes*, and the regions where the amplitude is maximal are referred to as *anti-nodes* [Feynman et al. 1963].

1965]. The propagation coefficient can be expanded into real and imaginary components $\gamma = \alpha + jk$ (described in Section 2.6).

If the attenuation, α, is assumed to be small, the transfer function (6.16) reduces to

$$T(z_0, j\omega) = \frac{\cos\left(\frac{\omega}{c}\left(L - z_0\right)\right)}{j\sin\left(\frac{\omega}{c}L\right)}. \tag{6.17}$$

The poles of this transfer function occur at the frequencies given by (6.9). The transfer function's magnitude and phase for the first three harmonics are plotted in Figure 6.6. A small, non-zero attenuation coefficient was used when plotting, as otherwise the transfer function tends towards infinity at the anti-nodes. For the fundamental resonance, the magnitude response is maximum at the ends of the stem and diminishes to zero in the middle of the stem. The phase response of the fundamental resonance is constant, except for a shift of $-\pi$ radians at the midpoint of the stem. In practice, $\Gamma_s, \Gamma_e \neq 1$ and $\alpha \neq 0$, so the backward travelling wave is smaller than the forward travelling wave, and a small amount of energy will be radiated from the ends of the stem.

6.5.2 Spatial variation in velocity

The transfer function, $T(z_0, j\omega)$, derived in Section 6.5.1, assumed that the wood's propagation coefficient, γ, is independent of distance along the stem, z. In other words, the acoustic velocity and attenuation was assumed to be constant along the stem. This model is clearly insufficient, as determining the spatial variation in the velocity is the objective of this study.

Suppose that instead of a constant velocity, it is a function of distance, $c(z)$. The wood's transfer function from the base of the stem to a point z is given by

$$H(z, j\omega) = \exp(-\gamma z), \tag{6.18}$$

where γ is generalised into a function of z, $\gamma = \gamma(z)$. Let the exponent of (6.18) be denoted as $\Phi = -\gamma z$. This can be expanded and evaluated for a variable velocity from the base of the stem to a point z,

$$\begin{aligned}\Phi(z) &= -(\alpha + jk)z \\ &= -\alpha z - j\omega \int_0^z \frac{1}{c(\zeta)} \mathrm{d}\zeta.\end{aligned} \tag{6.19}$$

The imaginary component of the propagation coefficient is now a function of distance along the stem, where previously it was only a function of distance interval.

The exponent, Φ, can also be evaluated between two arbitrary points (z_0, z_1) on the stem,

$$\Phi(z_0, z_1) = -\alpha|z_1 - z_0| + j\omega \int_{\min(z_0,z_1)}^{\max(z_0,z_1)} \frac{1}{c(\zeta)} \mathrm{d}\zeta. \tag{6.20}$$

In the above analysis, the attenuation coefficient, α, is assumed to be constant.

The distance-dependent transfer function, (6.18), and its exponent, (6.20), can be substituted into the series, (6.12), which can be numerically evaluated (to a sufficiently high number of terms) to plot the transfer function of the stem. Figure 6.7 shows the magnitude and phase plots where this has been performed, for the case that $c(z)$ is a linear function, increasing with z. The stem's transfer function for both the constant-velocity case (Figure 6.6) and the variable velocity case (Figure 6.7) are of similar form. The magnitude response of both transfer functions exhibit a node near the centre of the stem for the fundamental resonant frequency. Figure 6.7(a) demonstrates that the lower velocity at the base moves the node in the amplitude response closer towards the base. The shift of $-\pi$ radians in the phase response has moved closer towards the base, but the phase response is still constant for distances above and below this point.

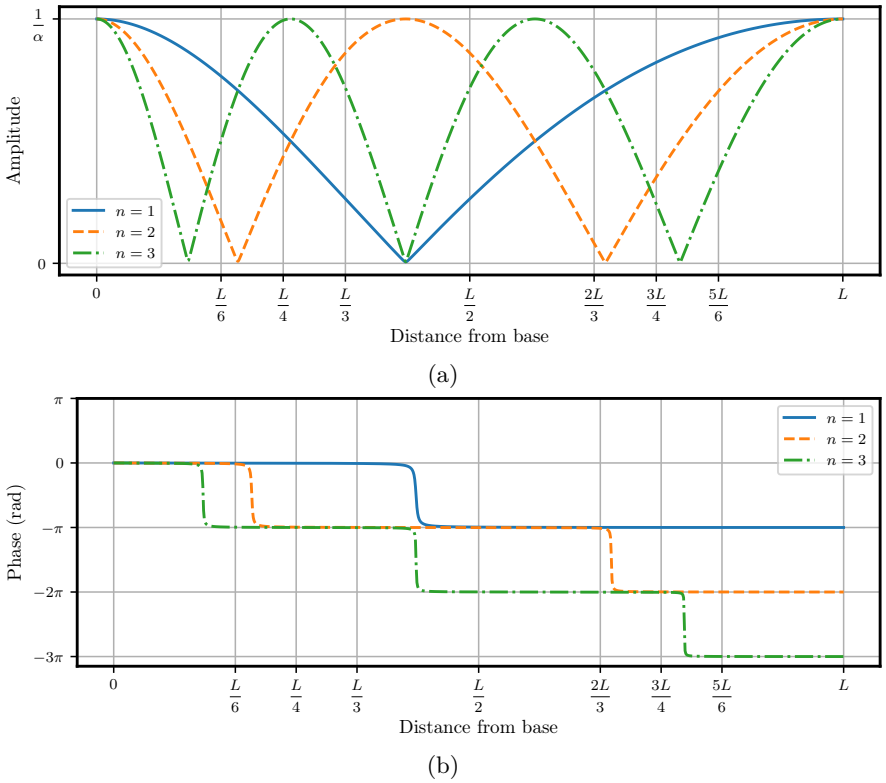

Figure 6.7 The magnitude (a) and phase (b) of the stem's transfer function, $T(z_0, j\omega)$, for a varying velocity along the stem. The transfer function is plotted for the first three harmonics. The velocity function selected was c_0 at the base of the stem and $2c_0$ at the top of the stem, increasing linearly, i.e., $c(z) = \frac{c_0}{L} z + c_0$. The comparatively lower velocity at the base of the stem has shifted the nodal points further towards the base.

6.5.3 Reflected-wave cancellation

The transfer functions for the stem, for both the constant-velocity and non-constant velocity cases, show that the phase response of the fundamental resonance is constant with respect to distance, except for a phase shift of $-\pi$ near the centre. A small modification can be made to the transfer function to convert it from constant phase to *linear phase*. If the reflected (backward travelling) terms of (6.11) are removed, then the sum of the series reduces to,

$$T_{\mathrm{RC}}(z, j\omega) = \frac{H(z_0, j\omega)H(L, j\omega)}{1 - H^2(L, j\omega)}. \tag{6.21}$$

The one-way transfer function of the wood (6.14) can then be substituted. The stem's transfer function becomes

$$T_{\mathrm{RC}}(z, j\omega) = \frac{\exp(-\gamma z)}{\sinh \gamma L}, \tag{6.22}$$

which has a linear phase with respect to distance. This *reflected-wave cancellation* has linear phase and constant magnitude. The phase for the first three harmonics, for both the constant velocity and non-constant velocity cases, is plotted in Figure 6.8.

This transfer function can be used to calculate the velocity over a distance interval. The average velocity over an interval is given by

$$\widehat{c} = -2\pi f_{\mathrm{res}} \frac{\Delta z}{\Delta \phi}, \tag{6.23}$$

where $\Delta\phi$ is the phase difference over the interval, and Δz is the interval distance. Clearly, this method is dependent on the implementation of a signal processing method capable of removing the backward travelling wave components.

6.5.4 Resonance method signal processing

The resonance method was applied to the data captured in the stem and segment experiments. In this section, a description is provided of the signal processing techniques which were applied to implement the resonance method.

The preliminary operations applied to the raw signals were the same as for the ToF processing. The mean was subtracted from each signal using the same procedure described in Section 6.4. Additionally, each signal was normalised by its RMS value.

The fundamental resonant frequency of the inplane signal at each distance was calculated. This was achieved by taking the FFT of each signal and finding the frequency at which the maximum magnitude in the FFT occurred. Prior to calculating the FFT, the signal was zero-padded by a factor of 8. This has the effect of increasing the apparent frequency resolution (though no more information is added to the signal) [Ambardar

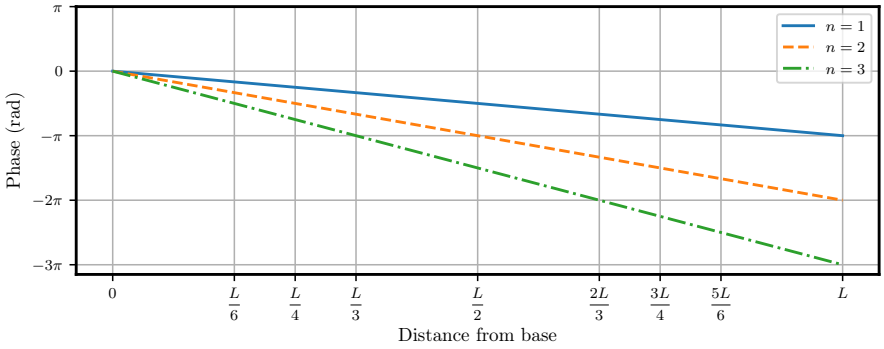

(a)

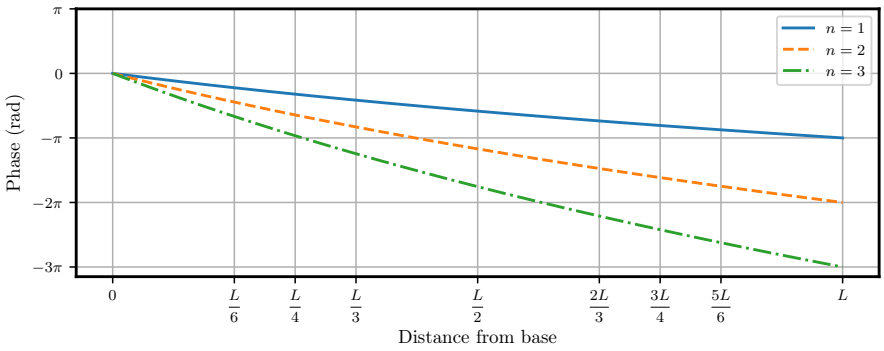

(b)

Figure 6.8 The phase of the reflected-wave cancelled model (6.22) for the first three harmonics. The phase is plotted for the constant velocity case (a), and the linear velocity case when the velocity function is $c(z) = \frac{c_0}{L} z + c_0$ (b).

1999]. The zero-padding operation makes it simpler to visually determine the location of the resonant peak, and also makes the implementation of the peak-finding algorithm simpler, as a sinc interpolation step has already been applied.

The FFT was only calculated within the bounds

$$100\,\text{Hz} \leq f_{\text{res}} \leq 300\,\text{Hz}. \tag{6.24}$$

This simplified the process of selecting the fundamental resonance, as in some cases the second or third harmonic is more prominent than the fundamental. The bounds listed in (6.24) are reasonably large, as the measured resonance did not vary significantly as the transducer position was varied. In a real system, where the frequency range of the fundamental resonance is not known, a better method of identifying the frequency would be required. Once the location of the resonance was identified, quadratic interpolation was performed around the peak's samples to improve the estimate of the peak position [Süli and Mayers 2003].

The phase of the FFT at the fundamental resonance was calculated for each signal. This calculation applied a similar approach to that of the resonant frequency, except the angle of the FFT at the resonant frequency was extracted. Prior to calculating the phase, the FFT response of the inplane signal was normalised by the start signal's FFT response,

$$Y_{\text{norm}}(j\omega) = \frac{Y_{\text{inp}}(j\omega)}{Y_{\text{start}}(j\omega)}, \tag{6.25}$$

where $Y_{\text{norm}}(j\omega)$, $Y_{\text{inp}}(j\omega)$, and $Y_{\text{start}}(j\omega)$ are the FFT-response sequences of the normalised, inplane, and start signals, respectively. This step is necessary to remove the non-zero constant phase shift present in the inplane signal. The normalisation step establishes the start signal as the *reference* signal, thus the phase is determined relative to the start signal. A *phase-unwrapping* step was also applied to the phase data. In this step, phase discontinuities greater than π were removed by adding or subtracting 2π.

The resonance method was also used for calculating the velocity of the segments. For the segments, the FFT bounds, (6.24), were changed to

$$1000\,\text{Hz} \leq f_{\text{res}} \leq 1800\,\text{Hz}, \tag{6.26}$$

to allow for the shorter length of the segments.

6.5.5 Approximation to cancellation of reflected waves

It was explained in Section 6.5.3 that the variation in velocity along a stem can be calculated from the phase response, providing that the backward-travelling wave components can be estimated and removed from the signal.

In general it is difficult to completely remove the backward travelling waves, as they

overlap, and are are superimposed, with the forward travelling components. Therefore, rather than attempt to extract the backward travelling components, a simplified approach was used. Suppose that the wave velocity, c is known, then the transit time for a wave's round trip propagation is also known, given by

$$\tau_{2\mathrm{L}} = \frac{2L}{c}. \tag{6.27}$$

Consider a wave measured at a location $z = z_0$ along the stem. If the stem's wave velocity is assumed constant then the first incident wave arrives at $\tau_{\mathrm{I}0} = z_0/c$. The first reflected wave arrives at $\tau_{\mathrm{R}0} = (2L - z_0)/c$. Subsequent wave arrivals occur at additional intervals of $\tau_{2\mathrm{L}}$. These arrival times can be generalised as

$$\tau_{\mathrm{In}} = \frac{2Ln + z_0}{c} \quad n = 0, 1 \ldots \tag{6.28}$$

$$\tau_{\mathrm{Rn}} = \frac{2L(n+1) - z_0}{c} \quad n = 0, 1 \ldots, \tag{6.29}$$

where τ_{In} is the arrival time of the nth incident wave, and τ_{Rn} is the arrival time of the nth reflected wave.

The method proposed here is to nullify (set to zero) the parts of the waveform which contain a backward travelling wave and do not overlap part of a forward travelling wave, i.e.,

$$y_{\mathrm{inp}}(t) = 0 : \tau_{\mathrm{Rn}}(n) \leq t \leq \tau_{\mathrm{In}}(n+1), n = 0, 1 \ldots. \tag{6.30}$$

Only a portion of the reflected wave is cancelled; the portion where the incident and reflected overlap. The velocity used to calculate the arrival times was determined using the resonant frequency calculated at the start of the stem. Local variations in velocity mean that the arrival times of (6.28) and (6.29) are only an approximation of the actual arrival times.

6.6 ANALYSIS AND RESULTS

As discussed in sections 6.4 and 6.5, two different methods were considered to determine the velocity variation along the stem: the time of flight method, and the resonance method with reflection cancellation. In addition, resonance method was used to measured the acoustic velocity of the cut segments, as a comparison for the other methods. In this section, the results of these methods, as applied to the stem and segment experiments, are discussed.

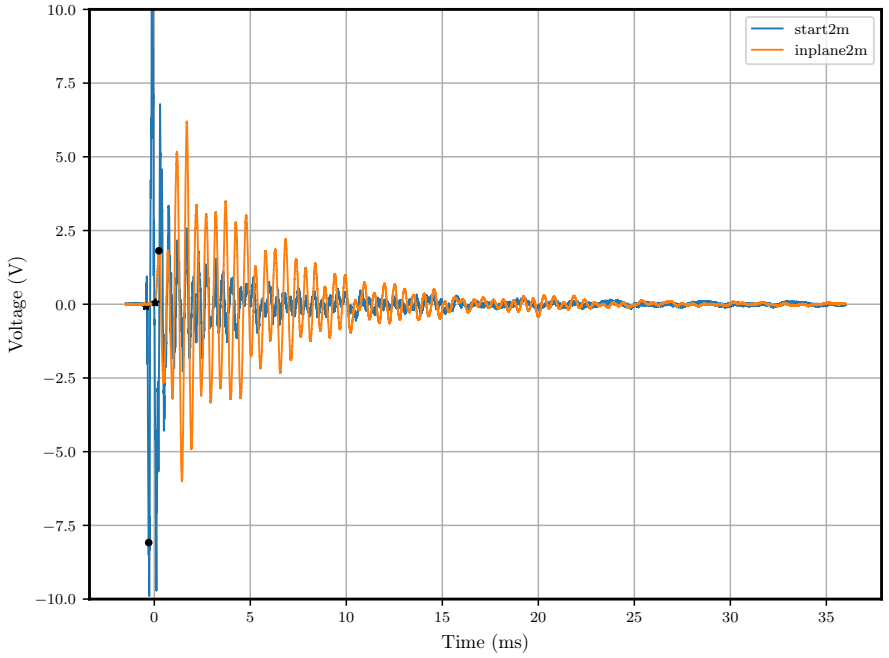

(a)

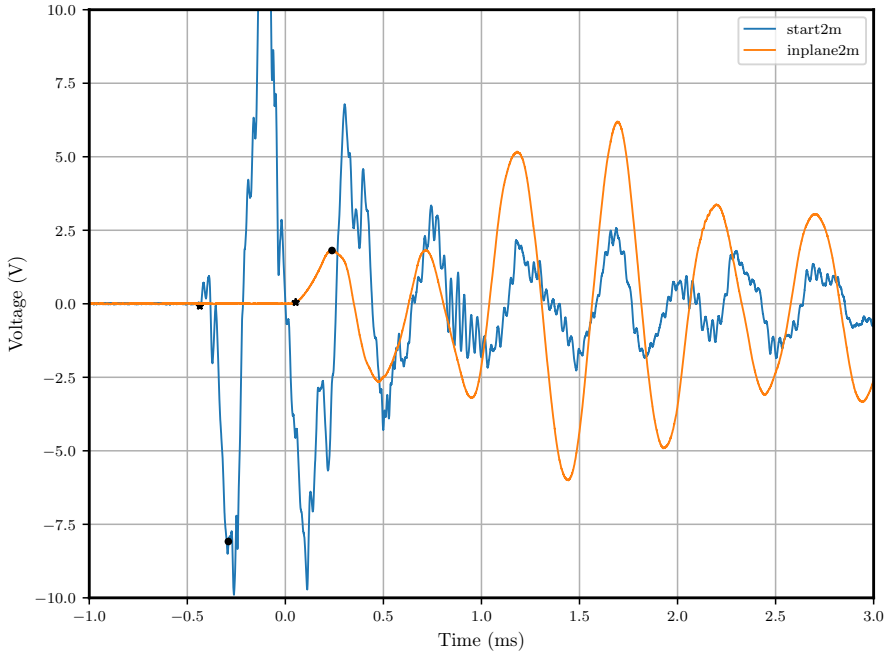

(b)

Figure 6.9 Time-domain plots of the signals captured at $z = 2\,\text{m}$, for stem 1. The start and inplane signals are shown for the entire capture time (a), and then zoomed to the beginning of the signals (b). The detected threshold and peak times are marked on the signals.

6.6.1 Time of flight results

An example of one of the recorded signals, at a distance of $z = 2\,\text{m}$, is shown in Figure 6.9. The wave arrival time, detected using both the threshold and peak methods, are indicated in the plot. The high-frequency energy present in the start signal has been significantly diminished in the inplane signal. This effect adds an additional delay to the measured arrival time.

Figure 6.10(a) shows the ToF delay from the start transducer to the inplane signal using both threshold and peak methods. The ToF measurements have been plotted for all distances, i.e., 0.25 m increments for stem 1 and 0.1 m increments for stem 2. Both stems show an approximately linear trend with distance for both the threshold and peak methods. Stem 2 shows a significantly longer ToF, likely indicating a lower overall stiffness.

The linear trend in Figure 6.10(a) suggests that little variation in velocity has been detected along the length of the stem. Several researchers have hypothesised that the ToF method tends to measure the fastest path through the wood, which is typically the high-stiffness outerwood (see Section 1.2.5). The stems measured in this experiment are mature enough to have developed high-stiffness outerwood along the entire length. Therefore, it is not surprising that the ToF velocity is reasonably constant. The ToF times shown in Figure 6.10(a) are not perfectly linear, however. There is some variation between adjacent measurements. This may be due to genuine detection of the variation along the stem, or it may be due to specious effects. There are several reasons why the detected variation could be erroneous. The ToF method is susceptible to measurement error due to local inhomogeneities, such as knots and defects. Therefore, transducer placement has a large effect on the resultant measurement. Additionally, if the operator fails to hit the wood on an axis directly inline with both transducers, the stress-wave will propagate along an off-axis path (possibly across the grain), adding additional delay.

Stem 2 actually shows a decrease in the ToF from 0–0.5 m. This might be caused by the hit position of the hammer-strike occurring close to the pith, while the transducer placement was on the outside of the stem. This means that even when the transducers were at $z = 0$, the stress wave had to take a cross-grain path to reach the transducers.

For most distances, the peak method measured a longer ToF than the threshold method. This is likely due to the wood's dispersion causing a spreading in time of the waveform's initial pulse (see Chapter 4 for further discussion of dispersion in wood). A correlation-based method of determining the ToF (as described in Section 5.6.1.2) was also applied to the measurements. The correlation ToF results have not been included in Figure 6.10(a) because this method was found to be unreliable. It was found to be difficult to determine the correct peak in the correlation, as the correlation function was sinusoidal in shape as a result of the relatively narowband input signals. For the

measurements on which the correct peak was selected, the correlation method tended to measure a ToF slightly longer than the threshold method, but a shorter ToF than the peak method.

The cumulative and differential velocities, as defined in Section 6.4, are plotted in Figure 6.10(b). In order to directly compare the stem and segment experiments, the differential and cumulative ToF-velocities were evaluated at 1 m increments. The differential velocity is plotted at distances corresponding to the midpoint of each interval, and the cumulative velocity is plotted at the endpoint of each interval. The cumulative velocity converges to a value just below $4000\,\mathrm{ms}^{-1}$ for stem 1, and just above $3000\,\mathrm{ms}^{-1}$ for stem 2. The differential velocity for stem 1 is maximal in the 1–2 m segment, with a value of approximately $4600\,\mathrm{ms}^{-1}$, and trending downwards towards the top of the stem. The differential velocity for stem 2 is comparatively constant along its length, with values of around $3200\,\mathrm{ms}^{-1}$, except at the top of the stem, where the velocity increases to $4000\,\mathrm{ms}^{-1}$.

6.6.2 Resonance results

Figure 6.11(a) shows the fundamental resonant frequency of the inplane signal captured along the length of each stem. The frequency was detected using the procedure described in Section 6.5.4. For stem 1, the resonant frequency is reasonably constant along the stem's length, with a value of approximately 213 Hz. For stem 2, the resonant frequency is less consistent. The detected frequency varies somewhat from $z = 1$–2 m, and then varies greatly from 3.1–3.6 m, and then converges to a stable value at the top of the stem of approximately 187 Hz.

The normalised magnitude of the FFT at each distance's resonant frequency is shown in Figure 6.11(b). The shape of these curves corresponds approximately to the transfer function of the fundamental resonance, shown in Figure 6.6(a). The magnitude is at a minimum near the centre of each stem, where a node occurs. The position of the node coincides with the greatest variation in the detected resonant frequency. This is because the peak-finding algorithm has difficulty selecting the correct peak, because the method employed in this analysis searches for the largest peak within a fixed range. The large uncertainty in the resonant frequency from $z = 1$–2 m appears to coincide with a large variation in the magnitude response over the same interval. The reason for this variation is unknown.

For stem 2, the minimum magnitude is closer to the base of the stem than the top, at $z = 3.3$ m. It was demonstrated in Figure 6.7(a) that this effect would be observed if there was a large proportion of low-stiffness wood in the lower half of the stem.

The phase of the inplane signal at the resonant frequency, for each distance along each stem, is shown in Figure 6.12(a). For stem 1, the phase is relatively constant until $z = 4$ m, where the phase is shifted by approximately -180°. For stem 2, the

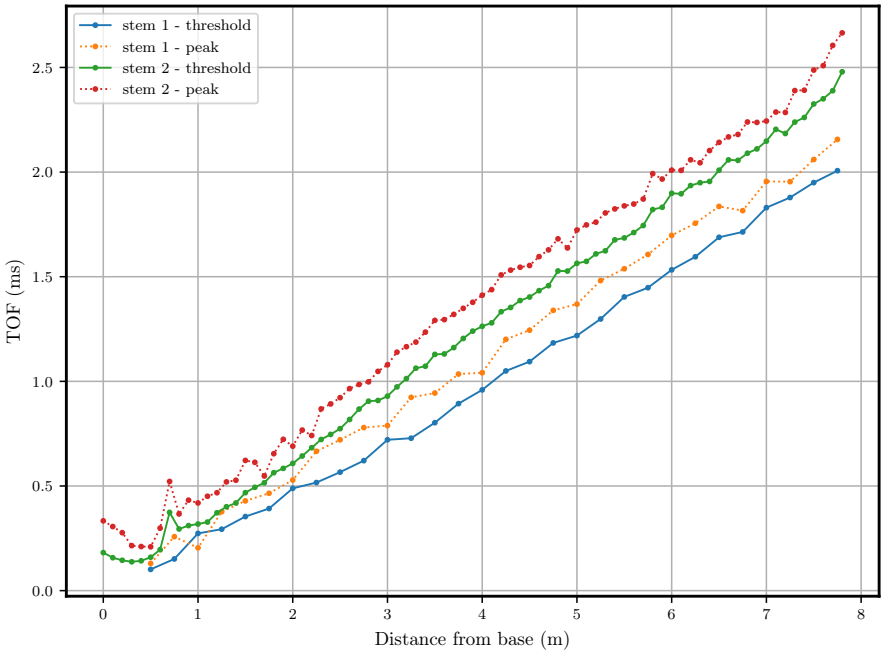

(a)

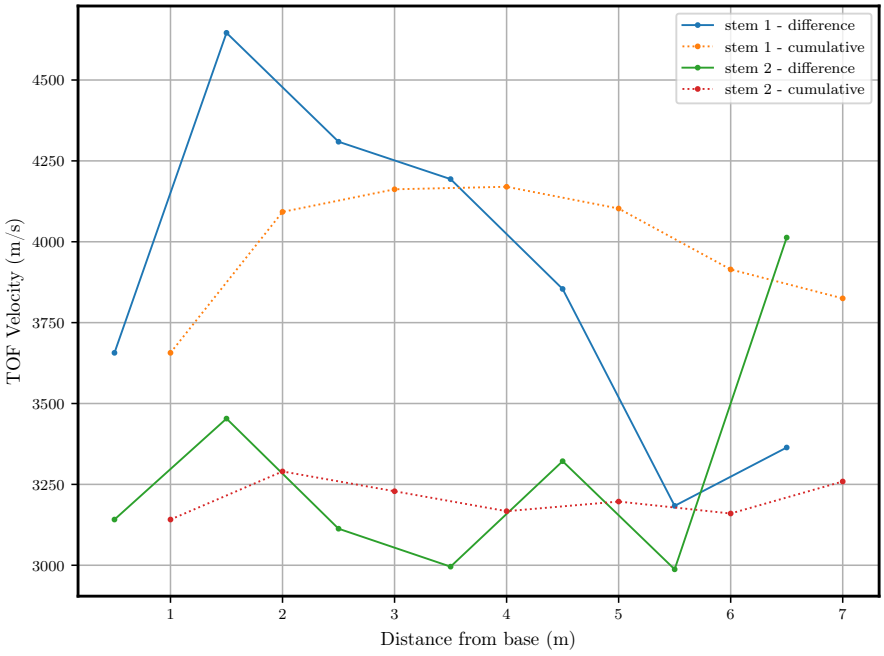

(b)

Figure 6.10 (a) The ToF from the start transducer to the inplane transducers. The ToF delay is shown for threshold and peak methods. (b) Cumulative and differential velocities measured in 1 m increments.

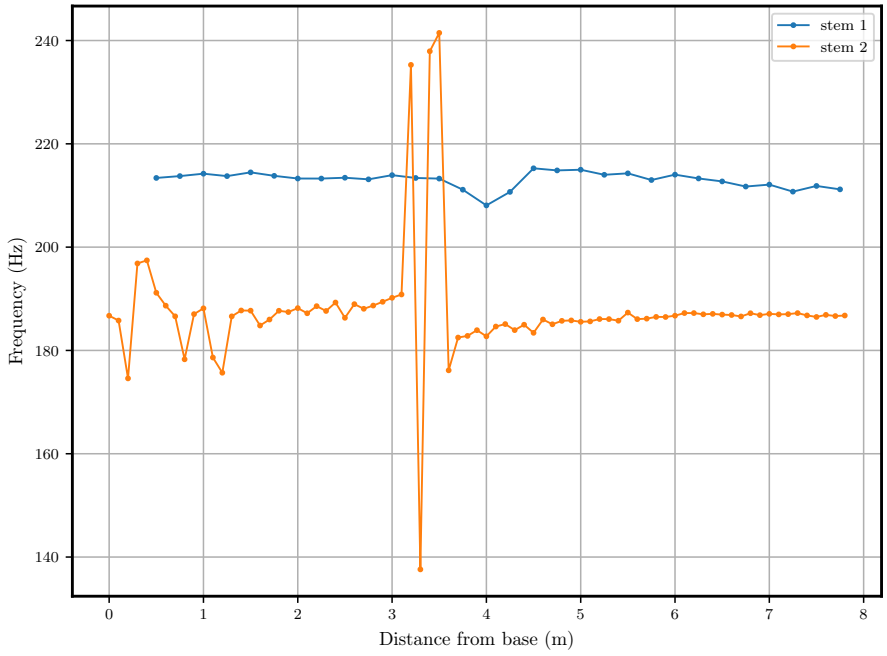

(a)

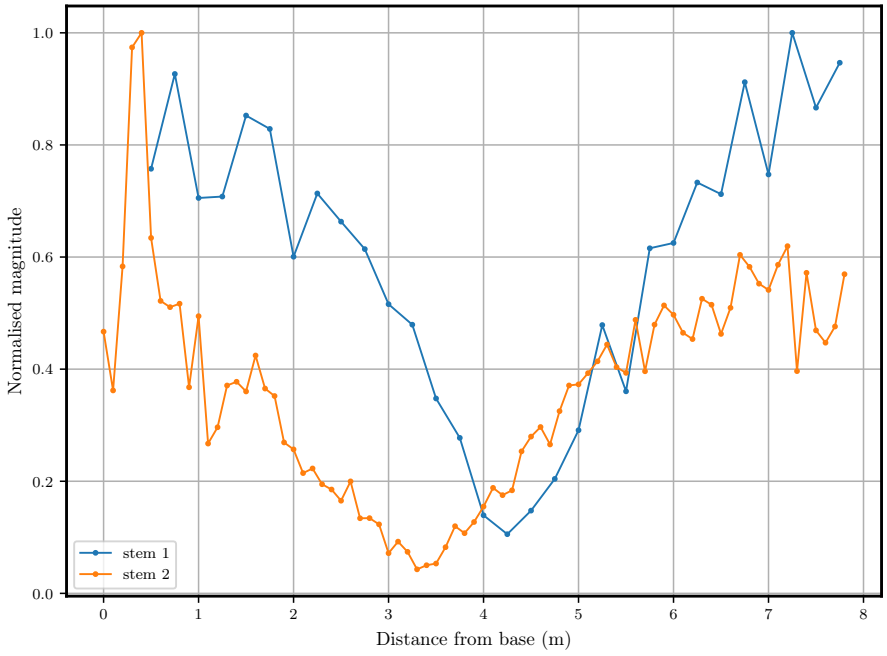

(b)

Figure 6.11 The resonant frequency of the fundamental harmonic of the inplane signal (a), and the corresponding magnitude response at this frequency (b). The node in the centre of the stem results in a reduced signal magnitude which increases the uncertainty in the measured frequency.

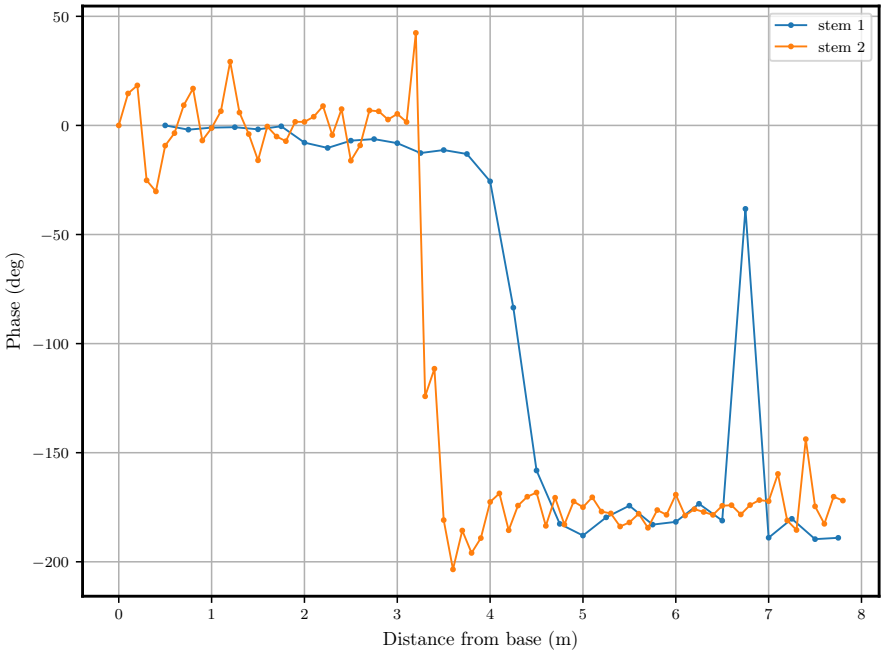

(a)

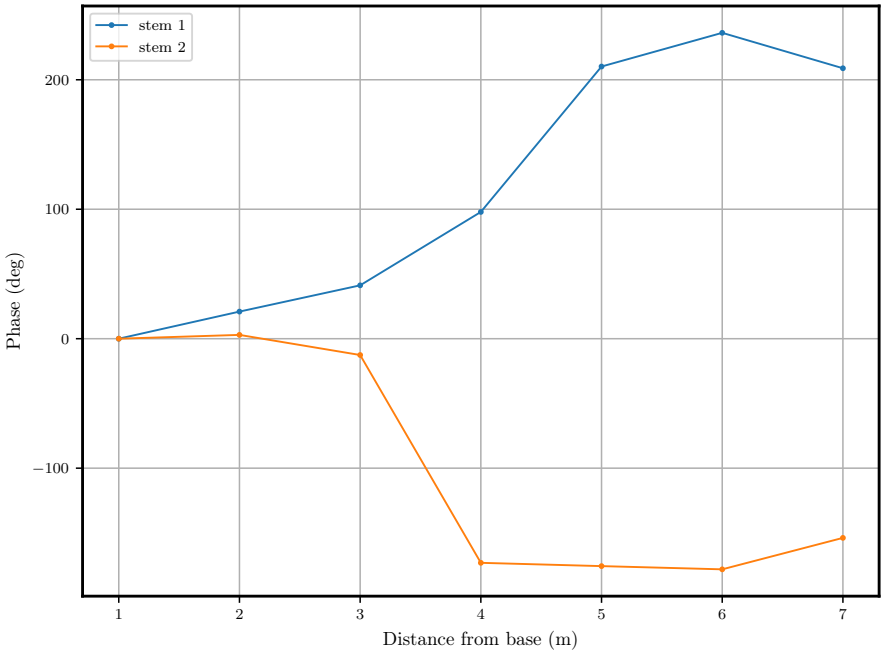

(b)

Figure 6.12 The phase of the fundamental resonant frequency for each measurement along the length of each stem (a), and the corresponding phase when using the method of approximate reflection cancellation, plotted at 1 m increments (b).

measured phase is less consistent. At approximately 3.3 m, the phase shifts by -180°, this shift occurs at the same distance at which a minima was observed in the magnitude response. The phase curves approximately match the phase of the derived transfer function (Figure 6.6(b)), but also contain some outlying points. The phase of stem 1's signal at $z = 6.75$ m is significantly different to its neighbouring points. The reason for this outlier is unknown, as the signal strength of the resonant frequency at this distance is particularly strong.

The phase of the inplane signal with the approximated reflection-cancellation procedure was also calculated, using the implementation described in Section 6.5.5. The relflection-cancelled phase is shown in Figure 6.12(b). It was hypothesised that if this method worked successfully, the phase should decrease approximately linearly, as shown in Figure 6.8(a). A decreasing phase indicates a time delay (lag), while an increasing phase indicates a time advancement (lead). Therefore, causality dictates that the phase should always decrease with distance. Unfortunately, this is not the case; the phase plotted in Figure 6.12(b) for stem 1 leads the reference signal for the majority of the length. The phase of stem 2 decreases somewhat over its length, however, the decrease is not close to linear. The phase difference from 1–3 m is very small, indicating very little time-delay, and thus a very high velocity. This result suggests that the reflection-cancellation method has not worked correctly. A further discussion of this result is provided in Section 6.7.

It is well established that the ToF method measures a considerably higher velocity in wood (see Section 1.2.4). This effect was also observed in this experiment. The overall ToF velocity of each stem was calculated by finding the time delay between the start and end transducers. The overall resonance of each stem was found by taking the resonant frequency at the end transducer and calculating the velocity using (1.9). The ToF velocity for stem 1 was 3825 ms^{-1}, and its resonance velocity was 3388 ms^{-1}. The ToF velocity for stem 2 was 3260 ms^{-1}, and its resonance velocity was 2989 ms^{-1}. These measurements correspond to a discrepancy between ToF and resonance velocities of 12.9% and 9.1% for stem 1 and stem 2, respectively. The studies which were described in Section 1.2.4 reported that the discrepancy between ToF and resonance velocities can vary considerably, as the range of reported mean velocity discrepancies was between 11-41%. The stems examined in this chapter lie at the lower end of this range. Note that the velocity discrepancies reported in Section 1.2.4 are mean values, not individual trees, as was reported in this experiment.

6.6.3 Segment results

The resonance method was used to determine the stress wave velocity of the 1 m segments. The segment velocity is shown in Figure 6.13. Both stems display a trend of increasing resonant-velocity progressing up the stem. The velocity measured in

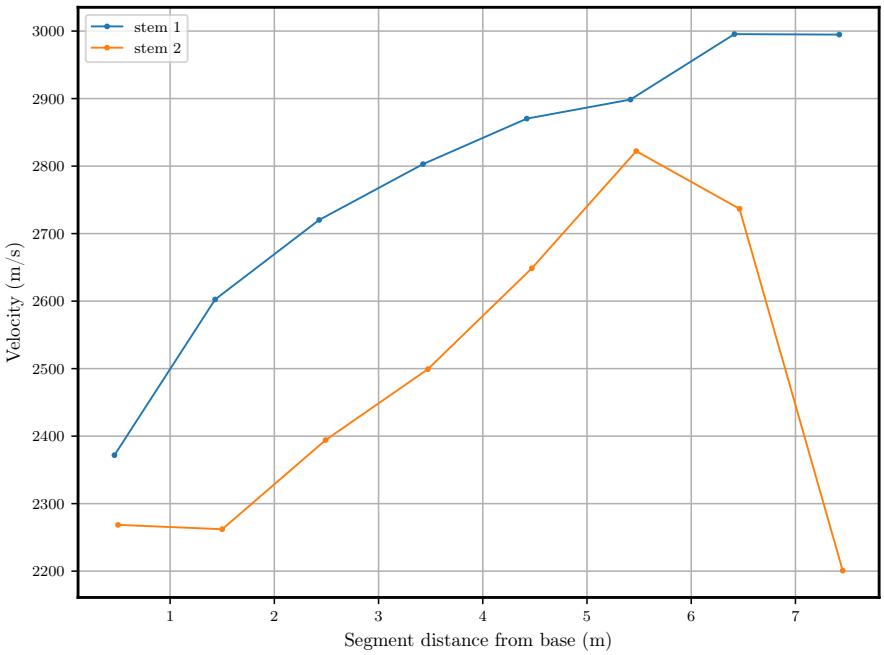

Figure 6.13 The stress-wave velocity of each segment, determined using the resonance method with the end transducer. The velocities are plotted against the midpoint-distance of each segment relative to the base of the stem.

stem 2 is considerably lower than that of stem 1. This finding is consistent with the resonance-magnitude plot of Figure 6.11(b), where the central node was shifted towards the base of the stem. Stem 2 contains an outlying data-point in the top-most segment, where the velocity drops to $2200\,\mathrm{ms}^{-1}$. Direct inspection of the signal's spectrum revealed that this signal does not contain any discernible harmonics. This may have been caused by poor measurement technique, such as loose transducer placement in the wood, or placement in a location where the resonant frequency failed to propagate.

6.7 DISCUSSION

In this chapter, a method was investigated for non-destructively measuring the variation of acoustic velocity within a harvested tree stem. The purpose of this work was to develop acoustic grading systems, which enhance the logistical efficiency of sawmills by allowing raw wood to be assigned to a finished good prior to sawing. Acoustic measurements were performed on two *Pinus radiata* stems by incrementally moving transducers along the length of the stems. The stems were then cut into 1 m lengths so that the velocity along each segment could be measured. Two separate signal processing methods were considered for estimating the velocity variation: the time of flight method and the resonance method.

Several factors limited the effectiveness of the stem experiment. Due to the limited availability of suitable transducers and data acquisition devices, it was not possible to simultaneously capture waveforms along the length of the entire stem. This increased the difficulty of comparing measurements from different distances, as each waveform was produced with a slightly different hit-intensity, and the hammer struck the stem in a slightly different location. Ideally, future experiments should aim to capture measurements simultaneously, or instead use a predictable and repeatable excitation source.

It was found that stem 1 measured a lower ToF delay for the entire stem than that of stem 2, and thus a greater ToF velocity. The ToF is understood to overestimate the overall stiffness (see Section 1.2.5), but has been used to successfully rank stiffness amongst a set of trees, particularly with respect to outerwood stiffness. Therefore, it is likely that the outerwood on stem 1 is of greater stiffness than that of stem 2.

The ToF (delay) was also measured at each incremental distance, from the start transducer to the inplane transducers. It was expected that the ToF should always increase as the transducers were moved along the stems. However, there are numerous points in the ToF data for which the ToF delay decreased when compared to the previous adjacent measurement. This effect is likely due to local inhomogeneities in the wood, such as knots or other deviations in the grain, which can cause an additional delay on the received signal. For this reason, it is thought that the ToF method is particularly sensitive to transducer placement. For stem 2, the ToF delay was observed to decrease initially as the transducers were moved along the stem. It is hypothesised that this effect is a result of the hammer hitting close to the pith. When the receiving transducer is close to the base of the stem, the stress wave has to travel directly across the grain, which typically has a much lower velocity. This effect could potentially be corrected by striking the stem close to the top, where the transducers are placed.

The differential ToF was calculated to find the variation in velocity along the length of each stem. It was expected, possibly optimistically, that the ToF-velocity over the length of each stem would be correlated with the resonance-velocity of each

corresponding segment. This is not the case. The differential ToF-velocity curves are very different to the resonance velocity determined by the segment experiment. There are several factors which contribute to this discrepancy. As previously discussed, the ToF measurements are sensitive to probe placement and local inhomogeneities. It is also difficult to precisely identify the wave arrival time in the presence of noise. It has been observed by several authors (see Section 1.2.5) that the ToF method tends to measure the propagation through the fastest part of the wood, i.e., the high-stiffness outerwood. It is likely that the ToF results are only useful for detecting the presence of outerwood and the stiffness of the outerwood, not the relative proportion of outerwood in the stem.

The resonant frequency was calculated using the inplane signal captured at each distance along each stem. The magnitude at this frequency was also calculated for each distance. For stem 1, the resonant frequency was reasonably constant along its length. For stem 2, there were several measurements close to the start of the stem where the resonant frequency varies by about $\pm 10\,\mathrm{Hz}$. The reason for this variance is unknown. In stem 1, the resonance magnitude is smallest close to the centre of the stem. In stem 2, the minimum in the magnitude is shifted slightly towards the base of the stem. It was shown in Figure 6.7(a) that this effect would be observed if the stem's acoustic velocity is lower at the bottom than at the top. This finding agrees with the segment-resonance results (Figure 6.13), which show that stem 2 contains a larger proportion of low velocity wood in its lower half than stem 1. It is possible that a sensor arrangement could be devised which would allow for either the resonance phase or the magnitude-minimum to be measured near the centre of a stem. While this arrangement would not directly measure the variation in overall velocity along a stem, it would give an indication of whether there is a disproportionate amount of low quality wood in one half of a stem.

The phase of the inplane signal at the fundamental resonant frequency was also calculated at each distance. The measured phase was consistent with that of the derived transfer function, which predicts a shift of $-\pi$ radians near the centre of the stem. This phase shift occurred at approximately the same distance along the stem as the magnitude-minima. For stem 2, both the magnitude-minima and phase-shift are moved slightly towards the base of the stem.

A reflection-cancellation algorithm was applied to the signals in an attempt to use the resonance-phase for calculating the velocity variation along each stem. Unfortunately, this method appears to have been unsuccessful. With the approximate reflection-cancellation algorithm applied, the phase of stem 1 increases with distance along the stem. This indicates a non-causal system. The phase of stem 2 decreases, but not in the approximately linear fashion predicted by the modified transfer function (Figure 6.8). The failure of this method is likely due to the long transient response of the excitation signal used in this experiment. The simplistic method, described in Section 6.5.5, nullified the signal between the backward travelling wave's arrival and the next forward

travelling wave. However, the long time-constant of the signal means that the backward travelling wave overlaps with the previous forward travelling wave. The suggested approach to reflection cancellation could only work if the input signal had a very broad bandwidth, and thus a short transient response, i.e., the wavelength of the input signal should be considerably shorter than the length of the stem. If this were true, the overlap between the forward and backward travelling waves would be negligible, allowing the backward travelling pulses to be effectively removed. An input excitation of this form would likely require a high-power ultrasonic transducer with a wide bandwidth.

Chapter 7

CONCLUSIONS AND RECOMMENDATIONS FOR FUTURE RESEARCH

This thesis reviews the techniques of non-destructive testing of wood using acoustics, with an emphasis on plantation forestry applications. The work was categorised into four separate studies:

- The development of mathematical models of an acoustic accelerometer operating in a wood medium.
- A study of dispersive wave behaviour, as applied to time of flight acoustics.
- The development and construction of a new time of flight measurement device– Wireless Treetap.
- The development of an experimental technique, and associated processing algorithms, for measuring the variation in acoustic velocity along the length of a harvested tree stem.

In this chapter, conclusions from these studies are presented in Section 7.1, and recommendations for future research are presented in Section 7.2.

7.1 CONCLUSIONS

A number of conclusions can be drawn from the work in this thesis:

(i) A lumped-element model for an acoustic accelerometer was 'loaded' using various radiation impedance models. It was found that the radiation impedance of a spherical source in a solid medium caused a low-frequency resonance in the accelerometer's frequency response, this is referred to as the *contact resonance*. This resonance defines the lower cutoff frequency of the device. This effect occurs for a variety of radiation impedance models including the Blake impedance, and the Oestreicher impedance. However, the best model for the SD-02 transducer in a standing tree is not yet known.

(ii) The peaks observed in the measured response of the SD-02 transducer are not due to the contact resonance resulting from the radiation impedance. It may be that the actual frequency response does not have an under-damped resonance, as shown in Figure 3.8. Or the excitation might not be producing sufficient energy at the contact resonance frequency in order to be visible in the response.

(iii) Several viscoelastic transmission-line models were used to estimate of the attenuation and dispersion of the initial portion of an acoustic wave over a short distance in a standing tree. A three-parameter model, the Zener model with spherical spreading, was found to provide the best fit to the measured data. Of the four models considered in this study, this model was also considered the most likely, because the attenuation of other models was unrealistically high ($|\alpha| > 400\,\mathrm{dB/cm}$). It is not known, however, whether the stiffness and damping parameters selected by the model are the 'true' values of the wood.

(iv) The viscoelastic transmission-line models were applied to a simulation of a ToF system. This simulation predicts that the measured ToF velocity in a viscoelastic system is greater than that of a lossless system, because the group velocity in the lossy system increases with frequency. It is not known whether this effect is a significant contributor to the well documented overestimation of velocity by ToF measurement devices.

(v) A new ToF measurement system, Wireless Treetap, was designed, and a prototype of the system was constructed. This project demonstrated that a wireless ToF measurement system using a smartphone is feasible. It was also demonstrated, however, that the system is not yet sufficiently robust for field use. The probe housing sustained some minor damage after performing measurements on 144 trees. Additionally, there were some minor software problems.

(vi) It was found that WTT determined a slightly lower mean-ToF velocity than the Treetap 4 system. It is understood, though, that the selected threshold-level strongly affects the measured delay. This is likely the reason for the discrepancy between devices.

(vii) A series of acoustic waveforms were captured from two *Pinus radiata* stems. Signal processing techniques were applied to these measurements with the goal of determining the variation in acoustic velocity along the length of each stem. It was found that a ToF approach did not give a useful indication of the velocity variation, probably because the first arrival is propagated through the outerwood, not the entire cross-section of the stem.

(viii) The magnitude response of the fundamental resonant frequency of each stem was found to give an indication of the acoustic velocity variation. The nodal position, or magnitude minima, indicates the proportion of low quality wood in one half of the stem.

(ix) A technique was developed to use the phase response to find the velocity variation, using an algorithm referred to as *reflection cancellation*. It was determined that this algorithm has failed to adequately determine the variation in velocity. The procedure resulted in a non-causal phase response. This likely occurred because the excitation signal was too narrowband, and thus too protracted in time, which prevented backward-travelling pulses from being sufficiently excluded from the waveform.

7.2 SUGGESTIONS FOR FUTURE RESEARCH

(i) Of the radiation impedance models proposed in Chapter 3, the most appropriate model has not yet been determined. Future researchers could directly measure the response of the transducer in wood, e.g., using a variable-frequency source.

(ii) The overestimation of the ToF method compared to the resonance method is still not well understood. It is unknown, for instance, what portion of the overestimation is due to propagation through outerwood versus viscoelastic effects, which increase the group velocity with frequency. One possible method of resolving this question is to apply the transmission-line models to pieces of wood cut at various distances from the pith, i.e., using cutting patterns similar to that previously used by Xu and Walker [2004], Tsehaye et al. [2000b], and Grabianowski et al. [2006].

(iii) The viscoelastic transmission-line models should be applied to measurements from more trees. Currently the method has only been applied to a single Beech tree, so it is unknown if the wave behaviour will be significantly different in other species.

(iv) The physical robustness of the Wireless Treetap system could be greatly improved by returning to a wired system. This is a difficult recommendation to make, as a lot of engineering effort went into the construction of the wireless probes. The author suggests that the best solution would be to use wired probes connected to a small measurement unit, which wirelessly communicates with a smartphone running the Treetap app. This solution would negate the need for the clock synchronisation circuitry and algorithm. It would also reduce the cost of the system overall, as the total number of components would be lower, and it would be easier to build. Future ToF systems should learn from Treetap 4, a system which has been used in the field for over 10 years, and is still in active use. The success of this device can be largely attributed to its simple design and construction.

(v) Future ToF systems should explore alternate algorithms for determining the wave arrival time. It is known that the threshold method is strongly influenced by the wave amplitude and threshold level. The windowed cross-correlation method

(Section 5.6.1.2) appears to produce a time-delay estimate with a significantly smaller variance.

(vi) The best method of measuring the velocity variation along a harvested stem appears to be that of identifying the location of resonant nodes. Future researchers should investigate this method more closely. It may be possible to estimate the spatial magnitude response (Figure 6.6) using a small number of sensors, and applying a curve fitting algorithm. Additionally, it may be useful to indentify the nodal positions of higher harmonics, to give a higher resolution estimate of the spatial variation in velocity.

Appendix A

DEFINITIONS OF MECHANICAL PARAMETERS

In this appendix, several mechanical parameters are defined which are used in the thesis. In Section A.1, the *Voigt* notational form of representing the strain, stress, and stiffness tensors, is defined. In Section A.2, some tensor operators are defined, which are used in the derivation of the wave equation, in Section 2.5. In Section A.3, several *engineering parameters* are defined. These parameters are, in certain circumstances, more convenient than a complete description of a solid using the stiffness or compliance tensors.

A.1 VOIGT NOTATION

Voigt notation is a convenient way of representing a symmetric tensor. In this section, the strain, stress, and stiffness tensors are each defined in Voigt notation.

A.1.1 Strain

Strain is a measure of the particle deformation within a solid. In Section 2.2.1, strain was defined for three-dimensional continuous media. It was shown that strain can be quantified as a 3×3 tensor. The strain is defined by (2.3), which is symmetric, i.e., $\epsilon_{ij} = \epsilon_{ji}$, thus, there are only 6 unique components in the tensor. Auld [1973] explains that the tensor components ϵ_{ij} can be expressed using numerical subscripts as

$$\boldsymbol{\epsilon} = \begin{bmatrix} \epsilon_{xx} & \epsilon_{xy} & \epsilon_{xz} \\ \epsilon_{yx} & \epsilon_{yy} & \epsilon_{yz} \\ \epsilon_{zx} & \epsilon_{zy} & \epsilon_{zz} \end{bmatrix} = \begin{bmatrix} \epsilon_1 & \frac{1}{2}\epsilon_6 & \frac{1}{2}\epsilon_5 \\ \frac{1}{2}\epsilon_6 & \epsilon_2 & \frac{1}{2}\epsilon_4 \\ \frac{1}{2}\epsilon_5 & \frac{1}{2}\epsilon_4 & \epsilon_3 \end{bmatrix}, \tag{A.1}$$

where the original tensor terms, ϵ_{xx} etc, are defined by (2.3). These components can then be redefined as a six-element column vector

$$\boldsymbol{\epsilon} = \begin{bmatrix} \epsilon_1 \\ \epsilon_2 \\ \epsilon_3 \\ \epsilon_4 \\ \epsilon_5 \\ \epsilon_6 \end{bmatrix}. \tag{A.2}$$

This is the definition of the strain vector in Voigt notation.

A.1.2 Stress

Similarly, the stress tensor can also be redefined as a column vector in Voigt notation,

$$\boldsymbol{\sigma} = \begin{bmatrix} \sigma_{xx} & \sigma_{xy} & \sigma_{xz} \\ \sigma_{yx} & \sigma_{yy} & \sigma_{yz} \\ \sigma_{zx} & \sigma_{zy} & \sigma_{zz} \end{bmatrix} = \begin{bmatrix} \sigma_1 & \frac{1}{2}\sigma_6 & \frac{1}{2}\sigma_5 \\ \frac{1}{2}\sigma_6 & \sigma_2 & \frac{1}{2}\sigma_4 \\ \frac{1}{2}\sigma_5 & \frac{1}{2}\sigma_4 & \sigma_3 \end{bmatrix}, \tag{A.3}$$

$$\boldsymbol{\sigma} = \begin{bmatrix} \sigma_1 \\ \sigma_2 \\ \sigma_3 \\ \sigma_4 \\ \sigma_5 \\ \sigma_6 \end{bmatrix}, \tag{A.4}$$

where the stress terms, σ_{xx} etc, are given by (2.7).

A.1.3 Stiffness

It was explained in Section 2.3 that the stiffness tensor, which relates stress to strain in an elastic solid, is a fourth-order tensor, with a total of 81 components. Lai et al. [1974] explains that the symmetry of the stress and strain tensors means that the stiffness tensor has at most 21 independent terms. The independent terms can be compiled into

a reduced form of the stiffness tensor, which is given by

$$\begin{bmatrix}\sigma_1\\ \sigma_2\\ \sigma_3\\ \sigma_4\\ \sigma_5\\ \sigma_6\end{bmatrix} = \begin{bmatrix} C_{xxxx} & C_{xxyy} & C_{xxzz} & C_{xxyz} & C_{xxxz} & C_{xxxy} \\ C_{xxyy} & C_{yyyy} & C_{yyzz} & C_{yyyz} & C_{xzyy} & C_{xyyy} \\ C_{xxzz} & C_{yyzz} & C_{zzzz} & C_{yzzz} & C_{xzzz} & C_{xyzz} \\ C_{xxyz} & C_{yyyz} & C_{yzzz} & C_{yzyz} & C_{xzyz} & C_{xyyz} \\ C_{xxxz} & C_{xzyy} & C_{xzzz} & C_{xzyz} & C_{xzxz} & C_{xyxz} \\ C_{xxxy} & C_{xyyy} & C_{xyzz} & C_{xyyz} & C_{xyxz} & C_{xyxy}, \end{bmatrix} \begin{bmatrix}\epsilon_1\\ \epsilon_2\\ \epsilon_3\\ \epsilon_4\\ \epsilon_5\\ \epsilon_6\end{bmatrix} \tag{A.5}$$

where C_{ijkl} are the terms of the original stiffness tensor. This subscript notation, however, is unwieldy. Therefore, the stiffness tensor is more commonly represented as

$$\begin{bmatrix}\sigma_1\\ \sigma_2\\ \sigma_3\\ \sigma_4\\ \sigma_5\\ \sigma_6\end{bmatrix} = \begin{bmatrix} C_{11} & C_{12} & C_{13} & C_{14} & C_{15} & C_{16} \\ C_{12} & C_{22} & C_{23} & C_{24} & C_{25} & C_{26} \\ C_{13} & C_{23} & C_{33} & C_{34} & C_{35} & C_{36} \\ C_{14} & C_{24} & C_{34} & C_{44} & C_{45} & C_{46} \\ C_{15} & C_{25} & C_{35} & C_{45} & C_{55} & C_{56} \\ C_{16} & C_{26} & C_{36} & C_{46} & C_{56} & C_{66} \end{bmatrix} \begin{bmatrix}\epsilon_1\\ \epsilon_2\\ \epsilon_3\\ \epsilon_4\\ \epsilon_5\\ \epsilon_6\end{bmatrix}, \tag{A.6}$$

where C_{IJ} are the terms of the stiffness tensor, in Voigt notation. Note that the convention adopted here (adopted from Auld [1973]) is to use lower-case subscripts for terms from the full tensor, and upper-case subscripts for terms from the reduced form tensors.

A.2 TENSOR OPERATORS

In this section, two tensor operators are defined: the divergence, and the symmetric gradient. These operators were used in Section 2.5 as part of the derivation of the wave equation.

A.2.1 Divergence

In Section 2.5, the three-dimensional wave equation was given for an anisotropic solid. This equation, (2.30), makes use of the *divergence operator*. Lai et al. [1974] explained that the divergence of a tensor quantity is a vector. This differs from the more familiar vector-divergence, which produces a scalar quantity. Auld [1973] explained that the divergence operator, when expressed in Voigt notation, can be represented as a matrix.

The divergence operator is defined as

$$\nabla \cdot \boldsymbol{\sigma} \equiv \nabla_{iJ}\sigma_J, \tag{A.7}$$

$$= \begin{bmatrix} \frac{\partial}{\partial x} & 0 & 0 & 0 & \frac{\partial}{\partial z} & \frac{\partial}{\partial y} \\ 0 & \frac{\partial}{\partial y} & 0 & \frac{\partial}{\partial z} & 0 & \frac{\partial}{\partial x} \\ 0 & 0 & \frac{\partial}{\partial z} & \frac{\partial}{\partial y} & \frac{\partial}{\partial x} & 0 \end{bmatrix} \begin{bmatrix} \sigma_1 \\ \sigma_2 \\ \sigma_3 \\ \sigma_4 \\ \sigma_5 \\ \sigma_6 \end{bmatrix}, \tag{A.8}$$

and the resulting product is a 3×1 vector. Note that the capital subscripts in (A.7) indicate that the quantity is in Voigt notation.

A.2.2 Symmetric gradient operator

The three-dimensional wave equation for an anisotropic solid also made use of the *symmetric gradient operator*. Auld [1973] explained that this operator takes the symmetric part of the gradient of a tensor field. It is defined, in tensor notation, as

$$\nabla_{\mathrm{s}}\boldsymbol{u} = \frac{1}{2}\left(\nabla\boldsymbol{u} + \nabla\boldsymbol{u}^{\mathbf{T}}\right), \tag{A.9}$$

where $\nabla\boldsymbol{u}$ is the gradient of the tensor, and $\nabla\boldsymbol{u}^{\mathbf{T}}$ is the associated tensor's transpose. Auld [1973] explained that the symmetric operator can be represented by a matrix. When using Voigt notation, the symmetric gradient operator is defined as

$$\nabla_{\mathrm{s}}\boldsymbol{u} \equiv \nabla_{Ij}u_j, \tag{A.10}$$

$$= \begin{bmatrix} \frac{\partial}{\partial x} & 0 & 0 \\ 0 & \frac{\partial}{\partial y} & 0 \\ 0 & 0 & \frac{\partial}{\partial z} \\ 0 & \frac{\partial}{\partial z} & \frac{\partial}{\partial y} \\ \frac{\partial}{\partial z} & 0 & \frac{\partial}{\partial x} \\ \frac{\partial}{\partial y} & \frac{\partial}{\partial x} & 0 \end{bmatrix} \begin{bmatrix} u_x \\ u_y \\ u_z \end{bmatrix}. \tag{A.11}$$

Note that the order of the capital subscripts serves to differentiate the two tensor operators.

A.3 ENGINEERING PARAMETERS

The stiffness tensor, $\boldsymbol{C}$, defines a material's elasticity in any orientation. However, in many cases it is not necessary to define the entire tensor, for example, when only the stiffness in one or two directions is of interest. Additionally, it is difficult to define the

entire tensor, as multiple measurements are required, including axial and shear modes, in multiple orientations. For these reasons the *engineering parameters*, defined in the following sections, are commonly used.

A.3.1 Poisson's ratio

An object which is subjected to a tensional stress along a particular axis typically also experiences a contraction in the transverse direction. Conversely, if the object is compressed, it tends to expand transversely. This effect is known as the *Poisson effect*. The ratio between the transverse and axial strains is known as *Poisson's ratio*, and is given by

$$\nu = \frac{\epsilon_{\text{trans}}}{\epsilon_{\text{axial}}}. \tag{A.12}$$

A Poisson's value of 0.0 means that no transverse strain occurs when axial strain is applied. This is typical of materials which compress volumetrically, such as cork or foam. A Poisson's value of 0.5 means that the object's volume is conserved under strain, as is typical of some types of rubber. The Poisson's ratio of wood is directionally dependent, and typically ranges from 0.3 to 0.45 [Kretschmann 2010].

A.3.2 Young's modulus

Young's modulus is an example of a *modulus of elasticity* (MoE). It is a measure of stiffness along a particular axis, typically the axis with highest stiffness [Askeland and Phulé 2003]. Young's modulus can be measured by applying a tensional or compressional strain along one axis, and measuring the resulting stress. Young's modulus, E, is then given by

$$E = \frac{\sigma_1}{\epsilon_1} = \frac{1}{s_{11}}. \tag{A.13}$$

Young's modulus is measured in Pascals. Values of Young's modulus for wood across all species range between 0.5 and 20 GPa ($1\,\text{GPa} \equiv 1 \times 10^9\,\text{Pa}$) [Chauhan et al. 2006b].

A.3.3 Lamé parameters

Another commonly used parametrisation for isotropic solids are the Lamé coefficients. Lai et al. [1974] define the parameters as

$$\boldsymbol{\sigma} = \lambda \,\text{Tr}\,(\boldsymbol{\epsilon})\, \boldsymbol{I} + 2\mu\boldsymbol{\epsilon}, \tag{A.14}$$

[1] where λ is Lamé's *first parameter*, μ is Lamé's *second parameter*, also known as the *shear modulus*. $\text{Tr}\,(\boldsymbol{\epsilon})$ indicates the trace function, equal to the diagonal sum of the matrix terms, and $\boldsymbol{I}$ is the identity matrix.

[1] The lowercase λ is commonly used to denote Lamé's first parameter, the capitalised equivalent, Λ, has been used to avoid confusion with wavelength.

The Lamé coefficients can be defined in terms of Young's modulus E and Poisson's ratio ν [Boresi et al. 1993],

$$\lambda = \frac{\nu E}{(1+\nu)(1-2\nu)}, \tag{A.15}$$

$$\mu = \frac{E}{2(1+\nu)}. \tag{A.16}$$

Comparison of (A.15) and (A.16) with the isotropic stiffness tensor, (2.20), shows that the tensor can also be expressed in terms of Lamé parameters,

$$C_{11} = C_{22} = C_{33} = \lambda + 2\mu \tag{A.17}$$

$$C_{44} = C_{55} = C_{66} = \mu \tag{A.18}$$

$$C_{12} = C_{13} = C_{21} = C_{23} = C_{31} = C_{32} = \lambda, \tag{A.19}$$

[Kolsky 1963].

Appendix B

BAR WAVES AND DILATATIONAL WAVES

As explained in Section 2.5, a particular solution to a wave problem consists of three components. These are: the differential equation known as the wave equation, boundary conditions which constrain the wave's propagation, and the initial conditions. A wave propagating in an infinite medium has no boundary conditions. This type of wave is known as a *bulk* wave. In a bounded medium, reflections occur. When a wave strikes a boundary, the reflected wave adds to the incident wave, altering the response at each location in space. In this section, the wave behaviour due to a particular boundary condition is explored–that of a wave propagating longitudinally in a cylindrical bar.

A one-dimensional wave equation was derived in Section 2.5. This derivation assumed a one-dimensional medium, i.e., that there is no displacement or propagation perpendicular to the wave's direction of travel. Most solid objects have a Poisson's ratio, ν, greater than zero[1]. Therefore, a wave propagating longitudinally in a cylinder excites a wave transversely to the propagation direction. Due to the symmetry of the cylinder, this transverse wave is directed radially outwards from the cylinder's axis. This radially-directed wave can interfere with the incident longitudinal wave. This gives rise to a frequency-dependent phase speed for the longitudinal wave.

Wave behaviour in a cylinder has been studied by several authors. It was first investigated by Pochhammer [1876], and also independently by Chree [1889], thus is known as the *Pochhammer-Chree* theory. An account of the Pochhammer-Chree theory was given by Love [1927]. Love explains that by solving the wave equation, with the boundary conditions of an infinitely long cylinder, and an isotropic medium described

[1]It is possible to have a Poisson's ratio equal to zero. Cork is an example of a material with a very low value of ν [Greaves et al. 2011].

by the Lamé parameters, the following equations are obtained,

$$A\left[2\mu\frac{\partial^2 J_0(h'r)}{\partial r^2} - \frac{\lambda}{\lambda+2\mu}\omega^2\rho J_0\left(h'r\right)\right] + 2B\mu k\frac{\partial J_1(\kappa'r)}{\partial r} = 0, \tag{B.1}$$

and,

$$2Ak\frac{\partial J_0(h'r)}{\partial r} + B\left(2k^2 - \frac{\omega^2\rho}{\mu}\right)J_1\left(\kappa'r\right) = 0. \tag{B.2}$$

Here λ and μ are the Lamé parameters, r is the cylinder's radius, J_0, J_1 are the cylindrical Bessel functions of the first kind, of order zero and one, respectively, ω, ρ, and k are the angular frequency, density, and wavenumber, respectively, A and B are the wave-solution amplitudes which were substituted into the wave equation. h' and κ' are given by

$$h'^2 = \frac{\rho\omega^2}{\lambda+2\mu} - k^2 \tag{B.3}$$

$$\kappa'^2 = \frac{\rho\omega^2}{\mu} - k^2. \tag{B.4}$$

The constants A and B may be eliminated by simultaneously solving (B.1) and (B.2). This results in an equation in terms of the angular frequency, ω, the wavenumber, k, the radius of the cylinder, r, the elastic constants, λ and μ, and the density, ρ. This is known as the *frequency equation*.

Kolsky [1963] explains that these solutions are not exact for a bar of finite length since the "condition that the ends are free from traction cannot be obeyed by solutions of this type". However, if the length of the cylinder is long in comparison to the radius, "the residual stresses become very small" [Kolsky 1963].

The Bessel functions may be approximated by a Taylor series [Anton et al. 2012]. Kolsky showed that the Taylor expansion is given by

$$J_0\left(h'r\right) = 1 - \frac{1}{4}(h'r)^2 + \frac{1}{64}(h'r)^4 - \ldots \tag{B.5}$$

$$J_1\left(\kappa'r\right) = \frac{1}{2}(\kappa'r) - \frac{1}{16}(\kappa'r)^3 + \ldots. \tag{B.6}$$

If the radius of the cylinder is small in comparison to the wavelength, then the first term in the Taylor series will dominate. In this case the frequency equation will be

significantly simplified. The resulting longitudinal phase speed is given by

$$\begin{aligned} c_{\text{bar}} &= \frac{\omega}{k} \\ &= \sqrt{\frac{\mu\left(3\lambda+2\mu\right)}{\rho\left(\lambda+\mu\right)}} \\ &= \sqrt{\frac{E}{\rho}}. \end{aligned} \tag{B.7}$$

This shows that for waves which are long in comparison to the radius of the cylinder, the Pochhammer-Chree theory predicts that the wave will propagate with a phase speed defined by Young's modulus. This may be referred to as the *bar speed*.

Kolsky explains that the speed of a longitudinal wave in an infinite, isotropic medium is higher than that given by (B.7). This type of wave, which Kolsky refers to as a *dilatational wave* has a speed given by (2.39). Recall that the dilatational speed is given by

$$c_{\text{dil}} = \sqrt{\frac{C_{11}}{\rho}}. \tag{B.8}$$

The ratio between the dilatational speed and the *bar speed* is given by

$$\begin{aligned} \frac{c_{\text{dil}}}{c_{\text{bar}}} &= \sqrt{\frac{\lambda+2\mu}{E}} \\ &= \sqrt{\frac{1-\nu}{(1+\nu)(1-2\nu)}} \\ &= \sqrt{\frac{C_{11}}{E}}. \end{aligned} \tag{B.9}$$

For the case of steel, which has a Poisson's ratio of approximately $\nu = 0.29$, this ratio is approximately $c_{\text{dil}}/c_{\text{bar}} \approx 1.14$.

Kolsky [1963] explains that for waves which are short in comparison to the cylinder's radius, i.e., high in frequency, the wave's speed approaches that of a Rayleigh surface wave in a semi-infinite medium. This speed is slower than the bar wave velocity. In order to determine the phase velocity for all wavelengths, (B.1) and (B.2) must be solved for the wavenumber, k, which can then be converted to a phase speed using

$$c_{\text{cyl}} = \frac{\omega}{k}, \tag{B.10}$$

where k is a function of frequency. This is difficult to do directly using (B.1), however, Bancroft [1941] claimed that (B.1) can be expressed in a simplified form,

$$\left(\chi-1\right)^2\phi\left(h'r\right) - \left(\beta\chi-1\right)\left[\chi-\phi\left(\kappa'r\right)\right] = 0, \tag{B.11}$$

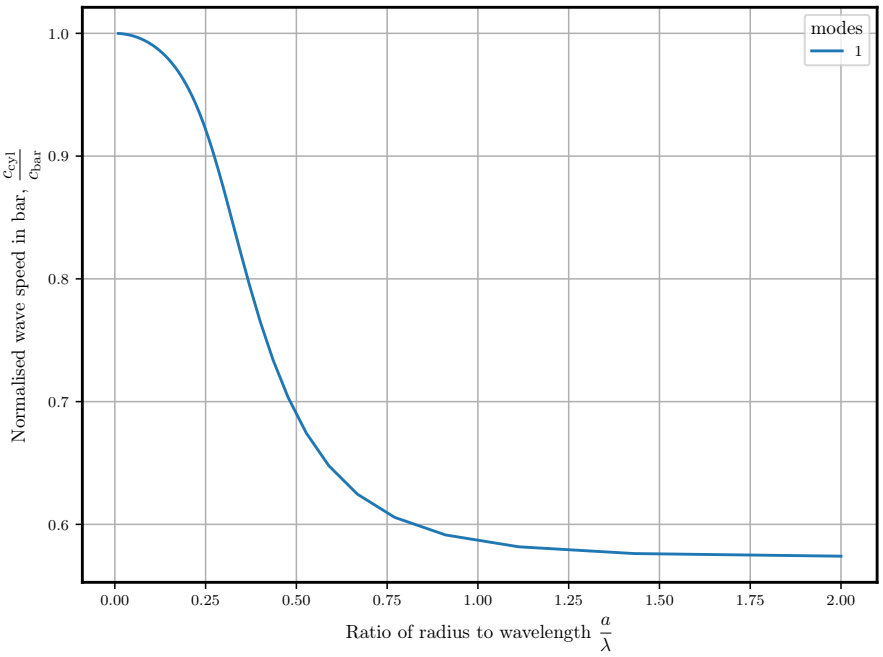

Figure B.1 Phase velocity of longitudinal waves in an isotropic cylindrical bar, with Poisson's ratio, $\nu = 0.29$ (steel).

where,

$$\chi = \left(\frac{c_{\text{cyl}}}{c_{\text{bar}}}\right)^2 (1+\nu)\,, \tag{B.12}$$

$$\phi(y) = y\frac{J_0(y)}{J_1(y)}, \tag{B.13}$$

$$\beta = \frac{1-2\nu}{1-\nu}, \tag{B.14}$$

and h', κ' are as previously defined. (B.11) may be solved numerically for χ, and subsequently c_{cyl} may be found.

(B.11) was evaluated numerically and then plotted; Figure B.1 shows the longitudinal phase speed as the wavelength relative to the cylinder's radius is varied. When the wavelength is long, the phase speed tends towards the bar speed, given by (B.7). As the wavelength is shortened, the speed tends towards that of the Rayleigh surface wave. The value of this lower asymptote is outside the scope of this work but may be found in Kolsky [1963].

Appendix C

MECHANICAL EQUIVALENT CIRCUITS

Each component in an electrical network is described using an *impedance* or *admittance* relationship. These relationships define the ratio between each component's voltage and current. At a fundamental level there is no requirement that the components are electrical in nature, they need only adhere to the required *across* and *through* variable relationships. In an electrical circuit, the across and through variables are voltage and current, respectively. It is equally valid to choose variables which correspond to mechanical quantities, for example: *force* acting across a device and *velocity* acting through it [Ogata 1998].

The choice of these quantities as network variables leads directly to the definition of the mechanical linear circuit elements, as listed in Table C.1. In order to develop an equivalent circuit theory for mechanical components, a means of interconnecting the components is required. In electrical theory the component interconnections are a result of Kirchoff's current law (KCL) and Kirchoff's voltage law (KVL). KCL is understood as–*the sum of the currents into a junction equals the sum of the currents out of the junction.* Applied to the mechanical analogy of Table C.1, this means that the sum of velocities around a junction are conserved, or stated another way, elements in series have equal velocity, i.e, their physical terminals are moving in unison. This is true when elements are mechanically connected in parallel. KVL states that–*the sum of voltages around a closed loop must equal zero.* In the mechanical analogy, an equivalent to KVL can be found in Newton's third law, stated simply–*action equals reaction* [Feynman et al. 1963]. This means that two components which are mechanically in series will

Table C.1 Each electrical element can be shown to have an analogous mechanical component.

	Electrical	Mechanical
Through variable	i (current)	u (velocity)
Across variable	v (voltage)	f (force)
Dissipative element	$R = \frac{v}{i}$ (resistance)	$\eta = \frac{f}{u}$ (viscous damper)
Through variable derivative	$v = L\frac{\mathrm{d}i}{\mathrm{d}t}$ (inductance)	$f = m\frac{\mathrm{d}u}{\mathrm{d}t}$ (mass)
Across variable derivative	$i = C\frac{\mathrm{d}v}{\mathrm{d}t}$ (capacitance)	$u = s\frac{\mathrm{d}f}{\mathrm{d}t}$ (compliance)

exert equal force upon one another. This is true of circuit elements, according to KVL, when they are in parallel.

This means that the component analogies listed in Table C.1 can be used to form equivalent circuits. In doing so, components which are mechanically in parallel become series connections in the equivalent circuit, and vice versa. It should be noted that the analogies described in Table C.1 are not the only possible choice. Equally validly, velocity could have been selected as the across variable, and force as the through variable. This selection changes the equivalent components, and also the interconnections between components.

REFERENCES

Abracon (2015), *ASTX H11 TCXO Datasheet*, Abracon LLC.

Abramowitz, M. and Stegun, I.A. (1965), *Handbook of mathematical functions: with formulas, graphs, and mathematical tables*, Dover Publications, New York.

ADH (2010), *GP-2106 Datasheet*, ADH Technology Co. Ltd, revision 0.2.

Agricef (2017), 'USLab Ultrasonic', `http://www.agricef.com.br`, accessed: 29/08/2017.

Allan, D.W., Ashby, N. and Hodge, C.C. (1997), 'The science of timekeeping', Tech. rep., Hewlett Packard Corporation.

Ambardar, A. (1999), *Analog and digital signal processing*, Brooks-Cole, Pacific Grove, CA, 2nd ed.

Analog (2005), *AD7264 Datasheet*, Analog Devices.

Andrews, M. (2000), 'Where are we with sonics?', In *Proceedings of the Wood Technology Research Centre Workshop: Capturing the Benefits of Forestry Research*, University of Canterbury, pp. 57–61.

Andrews, M. (2002), 'Which acoustic speed?', In *Proceedings of the 13th International Symposium on Nondestructive Testing of Wood*, University of California, Berkeley, California, pp. 159–165.

Anton, H., Bivens, I. and Davis, S. (2012), *Calculus: early transcendentals*, John Wiley and Sons, Hoboken, NJ, 10th ed.

Apiolaza, L. (2009), 'Very early selection for solid wood quality: screening for early winners', *Annals of Forest Science*, Vol. 66, No. 6, p. 601.

Apiolaza, L., Chauhan, S., Hayes, M., Nakada, R., Sharma, M. and Walker, J. (2013), 'Selection and breeding for wood quality. A new approach', *NZ Journal of Forestry*, Vol. 58, No. 1, pp. 32–37.

Aratake, S., Arima, T., Sakoda, T. and Nakamura, Y. (1992), 'Estimation of modulus of rupture (MoR) and modulus of elasticity (MoE) of lumber using higher natural frequency of log in pile of logs–possibility of application for sugi scaffolding board', *Mokuzai Gakkaishi*, Vol. 38, No. 11, pp. 995–1001.

Arima, T., Nakamura, N., Maruyama, S. and Hayamura, S. (1990), 'Natural frequency of log and lumber hit with hammer and applications for production processing', In *Proceedings of the 1990 International Timber Engineering Conference*, pp. 23–25.

Arnau, A. (editor) (2008), *Piezoelectric Transducers and Applications*, Springer-Verlag, Berlin, Heidelberg.

Askeland, D.R. and Phulé, P.P. (2003), *The science and engineering of materials*, Springer, Dordrecht.

ASTM (2014), 'D143: Standard test methods for small clear specimens of timber', *ASTM International*.

Atmel (2013), *SAM4S–Cortex M4 microcontroller datasheet*, Atmel Corporation.

Auld, B.A. (1973), *Acoustic fields and waves in solids*, John Wiley and Sons, New York, NY.

Baar, J., Tippner, J. and Gryc, V. (2012), 'The influence of wood density on longitudinal wave velocity determined by the ultrasound method in comparison to the resonance longitudinal method', *European Journal of Wood and Wood Products*, Vol. 70, No. 5, pp. 767–769.

Bancroft, D. (1941), 'The velocity of longitudinal waves in cylindrical bars', *Physical Review*, Vol. 59, No. 7, p. 588.

Barnett, J.R. and Bonham, V.A. (2004), 'Cellulose microfibril angle in the cell wall of wood fibres', *Biological Reviews*, Vol. 79, No. 2, pp. 461–472.

Bauchau, O.A. and Craig, J.I. (2009), *Structural analysis: with applications to aerospace structures*, Springer Science & Business Media.

Beall, F.C. (2002), 'Overview of the use of ultrasonic technologies in research on wood properties', *Wood Science and Technology*, Vol. 36, No. 3, pp. 197–212.

Beall, F.C., Reis, H., Senalik, A. and McGovern, M. (2013), 'Ultrasonic nondestructive evaluation of wood and wood products-past, present and future.', *Pro Ligno*, Vol. 9, No. 4.

Beer, F.P., Johnston, E.R. and DeWolf, J.T. (2006), *Mechanics of materials*, McGraw-Hill Higher Education, Boston, 4th ed.

Bell, E.R., Peck, E.C., Krueger, N. et al. (1954), *Modulus of elasticity of wood determined by dynamic methods*, Forest Products Laboratory, US Dept. of Agriculture, Madison, Wisconsin.

Björklund, S. (2003), *A Survey and Comparison of Time-Delay Estimation Methods in Linear Systems*, PhD thesis, Department of Electrical Engineering, Linköping University, Linköping, Sweden.

Blackwell, P. and Walker, J. (2006), 'Sawmilling', In J.C.F. Walker (editor), *Primary Wood Processing*, chap. 7, pp. 203–250, Springer-Verlag, Dordrecht, The Netherlands, 2nd ed.

Blake, F.G. (1952), 'Spherical wave propagation in solid media', *The Journal of the Acoustical Society of America*, Vol. 24, No. 2, pp. 211–215.

Blumlein, A. (1931), 'Improvements in and relating to sound-transmission, sound-recording and sound reproducing systems', British Patent GB394325A.

Bodig, J. and Jayne, B.A. (1982), *Mechanics of wood and wood composites*, Van Nostrand Reinhold, New York.

Bonnett, B. (2010), *A multi-channel front-end for synthetic aperture sonar*, Master's thesis, Electrical and Computer Engineering, University of Canterbury.

Boresi, A.P., Schmidt, R.J. and Sidebottom, O.M. (1993), *Advanced mechanics of materials*, Wiley, New York.

Bose, A. (1995), 'MIT 6.312 - Acoustics', Video lectures.

BSI (2011), 'EN 408: Timber structures. structural timber and glued laminated timber. determination of some physical and mechanical properties', *BSI Standard*.

BSI (2017), 'BS 4978: Visual strength grading of softwood–specification', *BSI Standard*.

Buchanan, A. (2007), *Timber Design Guide*, New Zealand Timber Industry Federation Inc, Wellington, New Zealand, 3rd ed.

Bucur, V. (1983), 'An ultrasonic method for measuring the elastic constants of wood increment cores bored from living trees', *Ultrasonics*, Vol. 21, No. 3, pp. 116–126.

Bucur, V. (2006), *Acoustics of Wood*, Springer-Verlag, Berlin, Heidelberg.

Bucur, V. and Feeney, F. (1992), 'Attenuation of ultrasound in solid wood', *Ultrasonics*, Vol. 30, No. 2, pp. 76–81.

Busch-Vishniac, I.J. (2012), *Electromechanical sensors and actuators*, Springer Science & Business Media.

Butterfield, B.G. and Meylan, B.A. (1980), *Three-dimensional structure of wood: an ultrastructural approach*, Chapman and Hall, London, 2nd ed.

Butterfield, B. (2006), 'The structure of wood : Form and function', In J.C.F. Walker (editor), *Primary Wood Processing*, chap. 1, pp. 1–22, Springer-Verlag, Dordrecht, The Netherlands, 2nd ed.

Carson, S.D., Cown, D.J., McKinley, R.B. and Moore, J.R. (2014), 'Effects of site, silviculture and seedlot on wood density and estimated wood stiffness in radiata pine at mid-rotation', *New Zealand Journal of Forestry Science*, Vol. 44, No. 1, p. 26.

Carter, P., Briggs, D., Ross, R.J. and Wang, X. (2005), 'Acoustic testing to enhance western forest values and meet customer wood quality needs', Tech. rep., USDA Forest service.

Carter, P., Chauhan, S. and Walker, J. (2007), 'Sorting logs and lumber for stiffness using director HM200', *Wood and Fiber Science*, Vol. 38, No. 1, pp. 49–54.

Cave, I.D. (1968), 'The anisotropic elasticity of the plant cell wall', *Wood science and technology*, Vol. 2, No. 4, pp. 268–278.

Cave, I.D. (1969), 'The longitudinal young's modulus of pinus radiata', *Wood science and technology*, Vol. 3, No. 1, pp. 40–48.

Cave, I.D. (1997), 'Theory of X-ray measurement of microfibril angle in wood', *Wood Science and Technology*, Vol. 31, No. 4, pp. 225–234.

Cave, I.D. and Walker, J.C.F. (1994), 'Stiffness of wood in fast-grown plantation softwoods: The influence of microfibril angle', *Forest Products Journal*, Vol. 44, No. 5, p. 43.

CBS-CBT (2017), 'Sylvatest Trio specifications', `http://www.cbs-cbt.com/fr/technologie/technologie-sylvatest-5-112-5`, accessed: 29/08/2017.

Chapman, C. (2004), *Fundamentals of seismic wave propagation*, Cambridge university press, Cambridge, UK.

Chauhan, S., Donnelly, R., Huang, C.L., Nakada, R., Yafang, Y. and Walker, J. (2006a), 'Wood quality: In context', In J.C.F. Walker (editor), *Primary Wood Processing*, chap. 5, pp. 121–158, Springer-Verlag, Dordrecht, The Netherlands, 2nd ed.

Chauhan, S., Donnelly, R., Huang, C.L., Nakada, R., Yafang, Y. and Walker, J. (2006b), 'Wood quality: Multifaceted opportunities', In J.C.F. Walker (editor), *Primary Wood Processing*, chap. 6, pp. 159–202, Springer-Verlag, Dordrecht, The Netherlands, 2nd ed.

Chauhan, S. and Walker, J. (2006), 'Variations in acoustic velocity and density with age, and their interrelationships in radiata pine', *Forest Ecology and Management*, Vol. 229, No. 1, pp. 388–394.

Chauhan, S., Entwistle, K. and Walker, J. (2005), 'Differences in acoustic velocity by resonance and transit-time methods in an anisotropic laminated wood medium', *Holzforschung*, Vol. 59, No. 4, pp. 428–434.

Chiu, C.M., Lin, C.H. and Yang, T.H. (2013), 'Application of nondestructive methods to evaluate mechanical properties of 32-year-old taiwan incense cedar (*Calocedrus formosana*) wood', *BioResources*, Vol. 8, No. 1, pp. 688–700.

Chree, C. (1889), 'The equations of an isotropic elastic solid in polar and cylindrical coordinates their solution and application', *Transactions of the Cambridge Philosophical Society*, Vol. 14, p. 250.

Cote, W.A. (1967), *Wood ultrastructure: an atlas of electron micrographs*, University of Washington Press, Seattle.

Cown, D. and van Wyk, L. (2004), 'Profitable wood processing-what does it require? Good wood!', *New Zealand Journal of Forestry*, Vol. 49, pp. 10–15.

Cown, D. (1992), 'Corewood (juvenile wood) in pinus radiata–should we be concerned', *New Zealand Journal of Forestry Science*, Vol. 22, No. 1, pp. 87–95.

Cown, D., McConchie, D. et al. (1980), 'Wood property variations in an old-crop stand of radiata pine', *New Zealand Journal of forestry science*, Vol. 10, No. 3, pp. 508–520.

Crawford, F.S. (1968), *Waves (Berkeley Physics Course, Vol. 3)*, Vol. 3, McGraw-Hill, New York.

Cremer, L., Heckl, M. and Petersson, B.A.T. (2005), *Structure-borne sound: structural vibrations and sound radiation at audio frequencies*, Springer-Verlag, Berlin Heidelberg, 3rd ed.

Dellinger, J.A. (1991), *Anisotropic seismic wave propagation*, PhD thesis, Stanford University.

Dickson, R.L., Raymond, C.A., Joe, W. and Wilkinson, C.A. (2003), 'Segregation of eucalyptus dunnii logs using acoustics', *Forest Ecology and Management*, Vol. 179, No. 1, pp. 243–251.

Dickson, R.L., Matheson, A.C., Joe, B., Ilic, J. and Owen, J.V. (2004), 'Acoustic segregation of pinus radiata logs for sawmilling', *New Zealand Journal of Forestry Science*, Vol. 34, No. 2, pp. 175–189.

Divos, F. (2010), 'Acoustic tools for seedling, tree and log selection', In *The Future of Quality Control for Wood & Wood Products*, .

Divos, F., Martitegui, F.A., Cabo, J.L.F., Herrero, M.E. and González, G.I. (2005), *Course in non-destructive testing of wood*, ETS Ingenieros de Montes.

Donaldson, L., Evans, R., Cown, D. and Lausberg, M. (1995), 'Clonal variation of wood density variables in pinus radiata', *New Zealand Journal of Forestry Science*, Vol. 25, No. 2, pp. 175–188.

Dunlop, J.I. (1983), 'Testing of poles by acoustic resonance', *Wood Science and Technology*, Vol. 17, No. 1, pp. 31–38.

Dyck, B. (2003), 'Precision forestry–the path to increased profitability', In *Proceedings of the 2nd International Precision Forestry Symposium*, University of Washington, Seattle, Washington, pp. 3–8.

Emms, G., Nanayakkara, B. and Harrington, J. (2012), 'A novel technique for non-damaging measurement of sound speed in seedlings', *European Journal of Forest Research*, Vol. 131, No. 5, pp. 1449–1459.

Emms, G.W., Nanayakkara, B. and Harrington, J.J. (2013), 'Application of longitudinal-wave time-of-flight sound speed measurement to pinus radiata seedlings', *Canadian journal of forest research*, Vol. 43, No. 8, pp. 750–756.

Evans, R. and Ilic, J. (2001), 'Rapid prediction of wood stiffness from microfibril angle and density', *Forest Products Journal*, Vol. 51, No. 3, pp. 53–57.

Evans, R. and Kibblewhite, R. (2002), 'Controlling wood stiffness in plantation softwoods', In *Proceedings of 13th International Symposium on Nondestructive Testing of Wood*, University of California, Berkeley, California, pp. 19–21.

Evans, R., Ilic, J., Matheson, C. et al. (2000a), 'Rapid estimation of solid wood stiffness using silviscan.', In *Proceedings of 26th Forest Products Research Conference: Research developments and industrial applications and Wood Waste Forum*, CSIRO Forestry and Forest Products, Clayton, Victoria, pp. 49–50.

Evans, R., Stringer, S. and Kibblewhite, R.P. (2000b), 'Variation of microfibril angle, density and fibre orientation in twenty-nine eucalyptus nitens trees', *Appita Journal*, Vol. 53, No. 6, pp. 450–457.

Fairchild (2014), *BAV99 Datasheet*, Fairchild Semiconductor, revision 1.1.

Fakopp Bt (2000), *SD-02 Datasheet*, Fakopp Enterprise Bt, Hungary.

Fakopp Bt (2001), 'Fakopp microsecond timer user's guide', `http://fakopp.com/docs/products/mstimer/Fakopp_MT_Guide.pdf`, accessed: 28/08/2017.

Fakopp Bt (2005), 'Treesonic microsecond timer user's guide', `http://fakopp.com/docs/products/treesonic/TreeSonicGuide.pdf`, accessed: 28/08/2017.

Falk, R.H., Patton-Mallory, M. and McDonald, K. (1990), 'Nondestructive testing of wood products and structures: state-of-the-art and research needs', In *Proceedings of: Non-Destructive Testing and Evaluation for Manufacturing and Construction*, Boca Raton, Florida, pp. 137–147.

Fengel, D. and Wegener, G. (1983), *Wood: chemistry, ultrastructure, reactions*, De Gruyter, Berlin.

Feynman, R.P., Leighton, R.B. and Sands, M. (1963), *The Feynman lectures on physics: The new millennium edition*, Addison-Wesley, Boston.

Fibre-gen (2017), `http://www.fibre-gen.com`, Accessed: 29/08/2017.

Firestone, F.A. (1933), 'A new analogy between mechanical and electrical systems', *The Journal of the Acoustical Society of America*, Vol. 4, No. 3, pp. 249–267.

Frampton, M.J. and Hayes, M.P. (2014), 'Electromechanical modelling of a time-of-flight transducer for wood applications', In *Proceedings of Electronics New Zealand Conference (ENZCon)*, University of Waikato, Hamilton, pp. 51–56.

Frampton, M.J. and Hayes, M.P. (2016a), 'A system for non-destructively determining variation in acoustic velocity within a harvested tree stem.', In *Proceedings of Electronics New Zealand Conference (ENZCon)*, University of Victoria, Wellington, pp. 152–157.

Frampton, M.J. and Hayes, M.P. (2016b), 'Wireless treetap: a new electronic device for time-of-flight tree-stiffness measurement', In *Proceedings of Electronics New Zealand Conference (ENZCon)*, University of Victoria, Wellington, pp. 32–37.

Frampton, M.J. and Hayes, M.P. (2017), 'Estimating the frequency response of green wood using time of flight measurements', In *Proceedings of Electronics New Zealand Conference (ENZCon)*, University of Canterbury.

Fujisawa, Y., Ohta, S., Nishimura, K., Toda, T. and Tajima, M. (1994), 'Wood characteristics and genetic variations in sugi (cryptomeria-japonica): Clonal differences and correlations between locations of dynamic mooduli of elasticity and diameter growths in plus-tree clones', *Mokuzai Gakkaishi*, Vol. 40, No. 5, pp. 457–464.

Galligan, W. and Courteau, R. (1965), 'Measurement of elasticity of lumber with longitudinal stress waves and the piezoelectric effect of wood', In *Proceedings of the Second Symposium on the Nondestructive Testing of Wood*, Washington State University, Pullman, Washington.

Gibson, L.J. (2005), 'Biomechanics of cellular solids', *Journal of biomechanics*, Vol. 38, No. 3, pp. 377–399.

Gladwell, G. (1968), 'The calculation of mechanical impedances relating to an indenter vibrating on the surface of a semi-infinite elastic body', *Journal of Sound and Vibration*, Vol. 8, No. 2, pp. 215–228.

Glass, S.V. and Zelinka, S.L. (2010), 'Moisture relations and physical properties of wood', In *Wood Handbook–Wood as an Engineering Material*, chap. 4, Forest products laboratory: U.S. Department of Agriculture, Madison, Wisconsin.

Gonçalves, R., Pedroso, C.B., Massak, M.V., Batista, F. and Secco, C.B. (2011), 'Technical note: Velocity of ultrasonic waves in live trees and in freshly-felled logs', *Wood and Fiber Science*, Vol. 43, No. 2, pp. 232–235.

Google (2017), 'Android developers', `https://developer.android.com` Accessed 27/08/2017.

Grabianowski, M., Manley, B. and Walker, J. (2006), 'Acoustic measurements on standing trees, logs and green lumber', *Wood Science and Technology*, Vol. 40, No. 3, pp. 205–216.

Grabianowski, M., Manley, B. and Walker, J. (2004), 'Impact of stocking and exposure on outerwood acoustic properties of pinus radiata in eyrewell forest', *New Zealand Journal of Forestry*, Vol. 49, No. 2, pp. 13–17.

Graff, K.F. (1991), *Wave motion in elastic solids*, Dover Publications, New York.

Greaves, G.N., Greer, A., Lakes, R. and Rouxel, T. (2011), 'Poisson's ratio and modern materials', *Nature materials*, Vol. 10, No. 11, pp. 823–837.

Grundelius, R. (1990), 'Determining the basic density of wood chips', *Tappi Journal*, Vol. 73, No. 4, pp. 183–189.

Gutierrez-Lemini, D. (2014), *Engineering viscoelasticity*, Springer-Verlag, New York.

Haines, D.W., Leban, J.M. and Herbé, C. (1996), 'Determination of Young's modulus for spruce, fir and isotropic materials by the resonance flexure method with comparisons to static flexure and other dynamic methods', *Wood science and technology*, Vol. 30, No. 4, pp. 253–263.

Halabe, U.B., Bidigalu, G.M., Gangarao, H.V.S. and Ross, R.J. (1997), 'Nondestructive evaluation of green wood using stress wave and transverse vibration techniques', *Materials Evaluation*, Vol. 55, No. 9, pp. 1013–1018.

Han, G., Wu, Q. and Wang, X. (2006), 'Stress-wave velocity of wood-based panels: Effect of moisture, product type, and material direction', *Forest Products Journal*, Vol. 56, No. 1, p. 28.

Hankinson, R. (1921), 'Investigation of crushing strength of spruce at varying angles of grain', *Air service information circular*, Vol. 3, No. 259, p. 130.

Harrington, J.J. (2002), *Hierarchical modelling of softwood hygro-elastic properties*, PhD thesis, University of Canterbury. Mechanical Engineering.

Harris, P. and Andrews, M. (1999), 'Tools and acoustic techniques for measuring wood stiffness', In *Proceedings of the 3rd wood quality symposium: emerging technologies for evaluating wood quality for wood processing*, Rotorua, New Zealand.

Harris, P., Petherick, R. and Andrews, M. (2002), 'Acoustic resonance tools', In *Proceedings of the 13th international symposium on nondestructive testing of wood*, University of California, Berkeley, California, pp. 195–201.

Harrison, T., Lower, D. and Potter, T. (2014), 'Android based tree stiffness measurement system: Wireless Treetap', Tech. rep., University of Canterbury.

Hasegawa, M., Takata, M., Matsumura, J. and Oda, K. (2011), 'Effect of wood properties on within-tree variation in ultrasonic wave velocity in softwood', *Ultrasonics*, Vol. 51, No. 3, pp. 296–302.

Hayes, M.P. (2014), 'Lcapy: Linear circuit analysis with Python', In *Proceedings of the 21st electronics New Zealand conference (ENZCon)*, Hamilton, pp. 89–94.

Hayes, M.P. and Pink, N. (2012), 'Treetwist: a spiral grain scanner for increment cores', In *Proceedings of the 21st electronics New Zealand conference (ENZCon)*, University of Otago, pp. 85–90.

Hayes, M. and Chen, J. (2003), 'A portable stress wave measurement system for timber inspection', In *Proceedings of the Electronics New Zealand Conference (ENZCon)*, Hamilton, New Zealand, pp. 1–6.

Hayt, W.H., Kemmerly, J.E. and Durbin, S.M. (2002), *Engineering Circuit Analysis*, McGraw-Hill Higher Education, New York, NY, sixth ed.

Hearmon, R.F.S. (1948), 'The elasticity of wood and plywood', *Forest Products Research*.

Hodousek, M., Dias, A., Martins, C., Marques, A. and Bohm, M. (2017), 'Comparison of non-destructive methods based on natural frequency for determining the modulus of elasticity of cupressus lusitanica and populus x canadensis', *Bioresources*, Vol. 12, No. 1, pp. 270–282.

Horowitz, P. and Hill, W. (2015), *The Art of Electronics*, Cambridge University Press, New York, NY, 3rd ed.

Hsu, C.Y. (2003), *Radiata pine wood anatomy structure and biophysical properties*, PhD thesis, School of Forestry, University of Canterbury.

Huang, C., Lindström, H., Nakada, R. and Ralston, J. (2003), 'Cell wall structure and wood properties determined by acoustics: a selective review', *Holz als Roh- und Werkstoff*, Vol. 61, No. 5, pp. 321–335.

Huang, C. (2000), 'Predicting lumber stiffness of standing trees', In *Proceedings of the 12th International symposium on nondestructive testing of wood*, University of Western Hungary, Sopron, pp. 173–179.

Huang, C. (2005), 'System and method for measuring stiffness in standing trees', US Patent 6,871,545.

Ilic, J. (2001), 'Relationship among the dynamic and static elastic properties of air-dry Eucalyptus delegatensis R. Baker', *Holz als Roh- und Werkstoff*, Vol. 59, No. 3, pp. 169–175.

IML (2017), 'Instrumenta mechanik labor', `https://www.iml-service.com`, Accessed: 29/08/2017.

Itskov, M. (2007), *Tensor algebra and tensor analysis for engineers*, Springer-Verlag, Berlin Heidelberg.

Jane, F.W., White, D.J.B. and Wilson, K. (1970), *The structure of wood*, A. & C. Black, London, 2nd ed.

Jayne, B.A. (1959), 'Vibrational properties of wood as indices of quality', *Forest products journal*, Vol. 9, No. 11, pp. 413–416.

Johnson, K.L. (1985), *Contact mechanics*, Cambridge University Press, Cambridge, UK.

Jones, E., Oliphant, T. and Peterson, P. (2014), 'Scipy: Open source scientific tools for Python', *Published online*.

Kamioka, H. (1988), 'Effects of ultrasonic bonding materials on velocity and attenuation of sound in red lauan wood', *Japanese journal of applied physics*, Vol. 27, No. 2.

Kang, H. and Booker, R. (2002), 'Variation of stress wave velocity with MC and temperature', *Wood Science and Technology*, Vol. 36, No. 1, pp. 41–54.

Kawamoto, S. and Williams, R.S. (2002), 'Acoustic emission and acousto-ultrasonic techniques for wood and wood-based composites: a review', Tech. rep., Forest Products Laboratory: US Department of Agriculture.

Kay, S.M. (1993), *Fundamentals of statistical signal processing*, Prentice-Hall, Englewood Cliffs, New Jersey.

Kelly, P. (2015), 'Mechanics lecture notes part III: Foundations of continuum mechanics', `http://homepages.engineering.auckland.ac.nz/~pkel015/SolidMechanicsBooks/Part_III/index.html`, accessed: 2017-03-09.

Kernighan, B.W. and Ritchie, D.M. (1988), *The C programming language*, Prentice Hall, Englewood Cliffs., New Jersey, 2nd ed.

Keysight (2015a), *6000 Series Oscilloscopes Datasheet*, Keysight Technologies.

Keysight (2015b), *Agilent 33220A: 20 MHz Function/Arbitrary Waveform Generator Datasheet*, Keysight Technologies.

Kim, K.Y. (1994), 'Analytic relations between the elastic constants and the group velocity in an arbitrary direction of symmetry planes of media with orthorhombic or higher symmetry', *Physical Review B*, Vol. 49, No. 6, pp. 3713–3724.

Kinsler, L.E., Frey, A.R., Coppens, A.B. and Sanders, J.V. (2000), *Fundamentals of Acoustics*, John Wiley and Sons, New York, NY, 4th ed.

Knapp, C. and Carter, G. (1976), 'The generalized correlation method for estimation of time delay', *IEEE Transactions on Acoustics, Speech, and Signal Processing*, Vol. 24, No. 4, pp. 320–327.

Kollmann, F.F.P. and Côté, W.A. (1968), *Solid Wood*, Vol. 1 of *Principles of Wood Science and Technology*, Springer-Verlag, Berlin.

Kolsky, H. (1963), *Stress waves in solids*, Dover publications, New York, NY.

Kretschmann, D. and Hernandez, R. (2006), 'Grading timber and glued structural members', In J.C.F. Walker (editor), *Primary Wood Processing*, chap. 1, pp. 1–22, Springer-Verlag, Dordrecht, The Netherlands, 2nd ed.

Kretschmann, D.E. (2010), 'Mechanical properties of wood', In *Wood Handbook–Wood as an Engineering Material*, chap. 5, Forest products laboratory: U.S. Department of Agriculture, Madison, Wisconsin.

Krishnamoorthy, K. (2006), *Handbook of statistical distributions with applications*, Chapman & Hall/CRC, New York, NY.

Lai, W.M., Rubin, D.H., Rubin, D. and Krempl, E. (1974), *Introduction to continuum mechanics*, Pergamon Press, Oxford, UK.

Landau, L.D. and Lifshitz, E.M. (1970), *Theory of elasticity*, Vol. 7, Pergamon Press, Oxford, UK, 2nd ed.

Lasserre, J.P., Mason, E. and Watt, M. (2004), 'The influence of initial stocking on corewood stiffness in a clonal experiment of 11-year-old Pinus radiata D.Don', *New Zealand Journal of Forestry*, Vol. 49, No. 2, pp. 18–23.

Lasserre, J.P., Mason, E.G. and Watt, M.S. (2005), 'The effects of genotype and spacing on Pinus radiata D. Don corewood stiffness in an 11-year old experiment', *Forest Ecology and Management*, Vol. 205, No. 1, pp. 375–383.

Lasserre, J.P., Mason, E.G. and Watt, M.S. (2007), 'Assessing corewood acoustic velocity and modulus of elasticity with two impact based instruments in 11-year-old trees from a clonal-spacing experiment of Pinus radiata D. Don', *Forest Ecology and Management*, Vol. 239, No. 1, pp. 217–221.

Lasserre, J.P., Mason, E.G. and Watt, M.S. (2008), 'Influence of the main and interactive effects of site, stand stocking and clone on Pinus radiata D. Don corewood modulus of elasticity', *Forest Ecology and Management*, Vol. 255, No. 8, pp. 3455–3459.

Lasserre, J.P., Mason, E.G., Watt, M.S. and Moore, J.R. (2009), 'Influence of initial planting spacing and genotype on microfibril angle, wood density, fibre properties and modulus of elasticity in Pinus radiata D. Don corewood', *Forest Ecology and Management*, Vol. 258, No. 9, pp. 1924–1931.

Legg, M. and Bradley, S. (2016), 'Measurement of stiffness of standing trees and felled logs using acoustics: A review', *The Journal of the Acoustical Society of America*, Vol. 139, No. 2, pp. 588–604.

Lemaitre, G., Letinturier, B. and Gazengel, B. (2008), 'Model and estimation method for predicting the sound radiated by a horn loudspeaker–with application to a car horn', *Applied acoustics*, Vol. 69, No. 1, pp. 47–59.

Lindström, H., Harris, P. and Nakada, R. (2002), 'Methods for measuring stiffness of young trees', *Holz als Roh- und Werkstoff*, Vol. 60, No. 3, pp. 165–174.

Lindström, H., Harris, P., Sorensson, C.T. and Evans, R. (2004), 'Stiffness and wood variation of 3-year old pinus radiata clones', *Wood Science and Technology*, Vol. 38, No. 8, pp. 579–597.

Lindström, H., Reale, M. and Grekin, M. (2009), 'Using non-destructive testing to assess modulus of elasticity of pinus sylvestris trees', *Scandinavian Journal of Forest Research*, Vol. 24, No. 3, pp. 247–257.

Llana, D.F., Iñiguez-González, G., Arriaga, F. and Wang, X. (2016), 'Time-of-flight adjustment procedure for acoustic measurements in structural timber', *BioResources*, Vol. 11, No. 2, pp. 3303–3317.

Llana, D.F., Íñiguez-González, G., Martínez, R.D. and Arriaga, F. (2018), 'Influence of timber moisture content on wave time-of-flight and longitudinal natural frequency in coniferous species for different instruments', *Holzforschung*, Vol. 72, No. 5, pp. 405–411.

Love, A.E.H. (1927), *A treatise on the mathematical theory of elasticity*, Cambridge University Press, Cambridge, 4th ed.

Mahon, J.M. (2007), *The use of acoustics for the wood quality assessment of standing P. taeda trees*, Master's thesis, University of Georgia.

Mahon, J.M., Jordan, L., Schimleck, L.R., Clark III, A. and Daniels, R.F. (2009), 'A comparison of sampling methods for a standing tree acoustic device', *Southern Journal of Applied Forestry*, Vol. 33, No. 2, pp. 62–68.

Maróti, M., Kusy, B., Simon, G. and Lédeczi, Á. (2004), 'The flooding time synchronization protocol', In *Proceedings of the 2nd international conference on Embedded networked sensor systems*, ACM, pp. 39–49.

Marra, G.G., Pellerin, R.F. and Galligan, W.L. (1966), 'Nondestructive determination of wood strength and elasticity by vibration', *Holz als Roh- und Werkstoff*, Vol. 24, No. 10, pp. 460–466.

Mason, E.G., Hayes, M. and Pink, N. (2017), 'Validation of ultrasonic velocity estimates of wood properties in discs of radiata pine', *New Zealand Journal of Forestry Science*, Vol. 47, No. 1, p. 16.

Mason, W.P. (1964), *Physical acoustics: principles and methods*, Academic Press, New York, NY.

Mason, W.P. (1948), *Electromechanical Transducers and Wave Filters*, D. Van Nostrand Company, New York, NY, 2nd ed.

Mason, W.P. (1958), *Physical acoustics and the properties of solids*, D. Van Nostrand Company, Princeton, New Jersey.

Matheson, A.C., Gapare, W.J., Ilic, J. and Wu, H.X. (2008), 'Inheritance and genetic gain in wood stiffness in radiata pine assessed acoustically in young standing trees', *Silvae Genetica*, Vol. 57, No. 2, pp. 56–64.

Matheson, A.C., Dickson, R.L., Spencer, D.J., Joe, B. and Ilic, J. (2002), 'Acoustic segregation of pinus radiata logs according to stiffness', *Annals of Forest Science*, Vol. 59, No. 5-6, pp. 471–477.

McNaught, A.D. and Wilkinson, A. (1997), *Compendium of chemical terminology*, Blackwell Science, Oxford, UK.

Metriguard (2017), 'Stress wave timer', `https://metriguard.com/product/model-239a-stress-wave-timer` Accessed: 29-08-2017.

Microchip (2003), *MCP6S21 Datasheet*, Microchip Technology.

Miller, G.F. and Pursey, H. (1954), 'The field and radiation impedance of mechanical radiators on the free surface of a semi-infinite isotropic solid', *Proceedings of the Royal Society of London. Series A, Mathematical and Physical Sciences*, Vol. 223, No. 1155, pp. 521–541.

Mishiro, A. (1995), 'Ultrasonic velocity in wood and its moisture content, 1: Effects of moisture gradients on ultrasonic velocity in wood', *Mokuzai Gakkaishi*, Vol. 41, pp. 1086–1092.

Mora, C., Schimleck, L., Isik, F., J.M. Mahon, J., A. Clark, I. and Daniels, R. (2009), 'Relationships between acoustic variables and different measures of stiffness in standing pinus taeda trees', *Canadian Journal of Forest Research*, Vol. 39, No. 8, pp. 1421–1429.

Nelder, J.A. and Mead, R. (1965), 'A simplex method for function minimization', *The Computer Journal*, Vol. 7, No. 4, pp. 308–313.

Nordic Semi (2008), *nRF24L01+ datasheet*, Nordic Semiconductor, 1st ed.

O'Donnell, M., Jaynes, E.T. and Miller, J.G. (1980), 'Kramers-Kronig relationship between ultrasonic attenuation and velocity', *Journal of the Acoustical Society of America*, Vol. 69, No. 3, pp. 696–701.

Oestreicher, H.L. (1951), 'Field and impedance of an oscillating sphere in a viscoelastic medium with an application to biophysics', *The Journal of the Acoustical Society of America*, Vol. 23, No. 6, pp. 707–714.

Ogata, K. (1998), *System Dynamics*, Prentice Hall, Upper Saddle River, New Jersey.

O'Haver, T. (2018), *A Pragmatic introduction to signal processing*, published online, https://terpconnect.umd.edu/%7Etoh/spectrum.

Okyere, J. and Cousin, A. (1980), 'On flaw detection in live wood', *Materials Evaluation*, Vol. 38, No. 3, pp. 43–47.

Olson, H.F. (1957), *Acoustical Engineering*, D. Van Nostrand Company, Princeton, New Jersey.

Oppenheim, A.V. and Schafer, R.W. (2010), *Discrete-time signal processing*, Pearson Higher Education, London, UK.

Ouis, D. (1999), 'Vibrational and acoustical experiments on logs of spruce', *Wood Science and Technology*, Vol. 33, No. 2, pp. 151–184.

Ouis, D. (2000), 'Detection of decay in logs through measuring the dampening of bending vibrations by means of a room acoustical technique', *Wood Science and Technology*, Vol. 34, No. 3, pp. 221–236.

Ouis, D. (2002), 'On the frequency dependence of the modulus of elasticity of wood', *Wood Science and Technology*, Vol. 36, No. 4, pp. 335–346.

Ozyhar, T., Hering, S., Sanabria, S.J. and Niemz, P. (2013), 'Determining moisture-dependent elastic characteristics of beech wood by means of ultrasonic waves', *Wood science and technology*, Vol. 47, No. 2, pp. 329–341.

Pellerin, R.F. and Ross, R.J. (2002), *Nondestructive evaluation of wood*, Forest Products Society, Madison, Wisconsin.

Pellerin, R. (1965), 'A vibrational approach to nondestructive testing of structural timber', *Forest Products Journal*, Vol. 14, No. 3, pp. 39–43.

Pellerin, R. and Galligan, W. (1973), 'Nondestructive method of grading wood materials', Canadian Patent No: 918286.

Pellerin, R.F. and Ross, R.J. (1991), 'Non-destructive evaluation of structural members', US Patent No: 5,024,091.

Ping, X. (2000), *The mechanical properties and stability of radiata pine structural timber*, PhD thesis, School of Forestry, University of Canterbury.

Pochhammer, L. (1876), 'Ueber die fortpflanzungsgeschwindigkeiten kleiner schwingungen in einem unbegrenzten isotropen kreiscylinder.', *Journal für die reine und angewandte Mathematik*, Vol. 81, pp. 324–336.

Polge, H. (1978), 'Fifteen years of wood radiation densitometry', *Wood Science and Technology*, Vol. 12, No. 3, pp. 187–196.

Porter, A.W., Kusec, D. and Olson, S. (1972), 'Digital computer for determining modulus of elasticity of structural lumber', Tech. rep., Forest products laboratory: U.S. Department of Agriculture.

Pozar, D.M. (2012), *Microwave engineering*, Wiley, Hoboken, New Jersey, 4th ed.

Pritz, T. (1996), 'Analysis of four-parameter fractional derivative model of real solid materials', *Journal of Sound and Vibration*, Vol. 195, No. 1, pp. 103–115.

Radcliffe, B. (1965), 'A theoretical evaluation of Hankinson's formula for modulus of elasticity of wood at an angle to the grain', *Quarterly Bulletin-Michigan State Agricultural Experiment Station*, Vol. 48, No. 1, pp. 286–295.

Reiterer, A., Lichtenegger, H., Tschegg, S. and Fratzl, P. (1999), 'Experimental evidence for a mechanical function of the cellulose microfibril angle in wood cell walls', *Philosophical Magazine A*, Vol. 79, No. 9, pp. 2173–2184.

Richter, B., Twiefel, J. and Wallaschek, J. (2009), 'Piezoelectric equivalent circuit models', In S. Priya and D.J. Inman (editors), *Energy Harvesting Technologies*, pp. 107–128, Springer US, Boston, Massachusetts.

Riddick, J.A., Bunger, W.B. and Sakano, T.K. (1986), *Organic solvents: physical properties and methods of purification*, John Wiley and Sons, New York, NY.

Riley, W.F., Sturges, L.D. and Morris, D.H. (2007), *Mechanics of materials*, John Wiley and Sons, New York, NY, sixth ed.

Robertson, I.A. (1966), 'Forced vertical vibration of a rigid circular disc on a semi-infinite elastic solid', In *Mathematical Proceedings of the Cambridge Philosophical Society*, Vol. 62, Cambridge University Press, pp. 547–553.

Ross, R., DeGroot, R. and Nelson, W. (1994), 'Technique for nondestructive evaluation of biologically degraded wood', *Experimental Techniques*, Vol. 18, No. 5, pp. 29–32.

Ross, R.J. (1984), *Stress-wave speed and attenuation as predictors of the tensile and flexural properties of wood-based particle composites*, PhD thesis, Washington State University, Pullman, Washington.

Ross, R.J. (1992), 'Nondestructive testing of wood', In *Proceedings: Non-destructive evaluation of civil structures and materials*, University of Colorado, pp. 43–47.

Ross, R.J. and Wang, X. (2005), 'A review of the use of acoustic speed to assess standing timber quality', In *Proceedings of the 14th international symposium on nondestructive testing of wood*, .

Ross, R.J., McDonald, K.A., Green, D.W. and Schad, K.C. (1997), 'Relationship between log and lumber modulus of elasticity', *Forest Products Journal*, Vol. 47, No. 2, p. 89.

Ross, R.J. and Pellerin, R.F. (1994), 'Nondestructive testing for assessing wood members in structures: a review', Tech. rep., Forest Products Laboratory, United States Department of Agriculture.

RPBC (2003), 'Radiata pine wood density', Tech. rep., Radiata Pine Breeding Company (RPBC), information Bulletin No. 2.

Sachse, W. and Pao, T.H. (1978), 'On the determination of phase and group velocities of dispersive waves in solids', *Journal of Applied Physics*, Vol. 49, No. 8, pp. 4320–4327.

Sakai, H., Minamisawa, A. and Takagi, K. (1990), 'Effect of moisture content on ultrasonic velocity and attenuation in woods', *Ultrasonics*, Vol. 28, No. 6, pp. 382–385.

Salmi, A., Karppinen, T., Montonen, R., Saranpää, P. and Haeggström, E. (2013), 'Ultrasonic estimate of the modulus of rupture and quantification of the frequency dependent dynamic modulus in Norway Spruce', *Journal of Applied Physics*, Vol. 113, No. 2, p. 24904.

Sandoz, J.L. and Benoit, Y. (2007), 'Timber grading machine using ultrasonic and density measurements: Triomatic', In *Proceedings: 15th international symposium on nondestructive testing of wood*, Duluth, Michigan.

Sandoz, J.L., Benoit, Y. and Demay, L. (2000), 'Wood testing using acousto-ultrasonic', In *Proceedings: 12th International Symposium on Nondestructive Testing of Wood*, University of Western Hungary, Sopron, Hungary, pp. 97–104.

Sandoz, J.L. (1991), 'Form and treatment effects on conical roundwood tested in bending', *Wood Science and Technology*, Vol. 25, No. 3, pp. 203–214.

Sandoz, J. (1993), 'Moisture content and temperature effect on ultrasound timber grading', *Wood Science and Technology*, Vol. 27, No. 5, pp. 373–380.

Schinker, M.G., Hansen, N. and Spiecker, H. (2003), 'High-frequency densitometry: A new method for the rapid evaluation of wood density variations', *International Association of Wood Anatomists (IAWA) Journal*, Vol. 24, No. 6, pp. 231–239.

Schniewind, A.P. (1989), *Concise encyclopedia of wood & wood-based materials*, Pergamon Press, Oxford, England, 1st ed.

Searles, G.J. (2012), *Acoustic segregation and structural timber production*, PhD thesis, Edinburgh Napier University, Edinburgh, Scotland.

Simeone, O., Spagnolini, U., Bar-Ness, Y. and Strogatz, S.H. (2008), 'Distributed synchronization in wireless networks', *IEEE Signal Processing Magazine*, Vol. 25, No. 5.

Sivrikaya, F. and Yener, B. (2004), 'Time synchronization in sensor networks: a survey', *IEEE Network*, Vol. 18, No. 4, pp. 45–50.

Skilling, H.H. (1948), *Fundamentals of electric waves*, Wiley, New York, NY, 2nd ed.

Smith, D.M. et al. (1954), 'Maximum moisture content method for determining specific gravity of small wood samples', Tech. rep., Forest Products Laboratory, US Dept. of Agriculture, Madison, Wisconsin.

Snyder, W.D., Christensen, E., Floyd, S.L., Jones, L.H., Kendall, C.K., Pearce, B.B., Shaw, E. and Yancey, M.J. (2000), 'Log cutting optimization system', US Patent No: 6,026,689.

Stamm, A.J. (1964), *Wood and cellulose science*, Ronald Press Co, New York, NY.

Strang, G. (1993), *Introduction to linear algebra*, Vol. 3, Wellesley-Cambridge Press, Wellesley, Massachusetts.

Stuart, S.A. and Evans, R. (1995), 'X-ray-diffraction estimation of the microfibril angle variation in eucalypt wood', *Appita Journal*, Vol. 48, pp. 197–200.

Subhani, M., Li, J. and Samali, B. (2013), 'A comparative study of guided wave propagation in timber poles with isotropic and transversely isotropic material models', *Journal of Civil Structural Health Monitoring*, Vol. 3, No. 2, pp. 65–79.

Süli, E. and Mayers, D.F. (2003), *An introduction to numerical analysis*, Cambridge University Press, Cambridge, UK.

Tackett, N., Jovanov, E. and Milenković, A. (2011), 'An implementation of time synchronization in low-power wireless sensor networks', In *Proceedings: 43rd Southeastern Symposium on System Theory*, IEEE, pp. 61–66.

TI (2007), *OPA2365 Datasheet*, Texas Instruments.

TI (2013), *REF5030 Datasheet*, Texas Instruments, revision f.

Tilmans, H.A. (1996), 'Equivalent circuit representation of electromechanical transducers: I. lumped-parameter systems', *Journal of Micromechanics and Microengineering*, Vol. 6, No. 1, p. 157.

Timoshenko, S. (1955), *Vibration problems in engineering*, D. Van Nostrand Company, New York, NY, 3rd ed.

Toulmin, M.J. (2005), *The development of a sampling strategy for measuring acoustic velocity in standing radiata pine using the TreeTap time of flight tool*, Bachelor's thesis, School of Forestry, University of Canterbury.

Toulmin, M.J. and Raymond, C. (2007), 'Developing a sampling strategy for measuring acoustic velocity in standing Pinus radiata using the Treetap time of flight tool', *New Zealand Journal of Forestry Science*, Vol. 37, No. 1, p. 96.

Tsehaye, A., Buchanan, A.H. and Walker, J.C.F. (2000a), 'Sorting of logs using acoustics', *Wood Science and Technology*, Vol. 34, No. 4, pp. 337–344.

Tsehaye, A., Buchanan, A. and Walker, J. (2000b), 'Selecting trees for structural timber', *Holz als Roh-und Werkstoff*, Vol. 58, No. 3, pp. 162–167.

Vázquez, C., Gonçalves, R., Bertoldo, C., Baño, V., Vega, A., Crespo, J. and Guaita, M. (2015), 'Determination of the mechanical properties of castanea sativa mill. using ultrasonic wave propagation and comparison with static compression and bending methods', *Wood Science and Technology*, Vol. 49, No. 3, pp. 607–622.

von Gierke, H.E., Oestreicher, H.L., Franke, E.K., Parrack, H.O. and von Wittern, W.W. (1952), 'Physics of vibrations in living tissues', *Journal of applied physiology*, Vol. 4, No. 12, pp. 886–900.

Walker, J. (2006a), 'Basic wood chemistry and cell wall ultrastructure', In J.C.F. Walker (editor), *Primary Wood Processing*, chap. 2, pp. 23–67, Springer-Verlag, Dordrecht, The Netherlands, 2nd ed.

Walker, J. and Nakada, R. (1999), 'Understanding corewood in some softwoods: a selective review on stiffness and acoustics', *The International Forestry Review*, Vol. 1, No. 4, pp. 251–259.

Walker, J.C.F. (editor) (2006b), *Primary Wood Processing*, Springer-Verlag, Dordrecht, The Netherlands, 2nd ed.

Walker, J.C.F. (2006c), 'Water in wood', In J.C.F. Walker (editor), *Primary Wood Processing*, chap. 3, pp. 69–94, Springer-Verlag, Dordrecht, The Netherlands, 2nd ed.

Walls, F.L. (1990), 'Environmental sensitivities of quartz crystal oscillators', In *Proceedings: 22nd Annual Precise Time and Time Interval (PTTI) Applications and Planning Meeting*, pp. 465–477.

Wang, S.Y. and Ko, C.Y. (1998), 'Dynamic modulus of elasticity and bending properties of large beams of Taiwan-grown Japanese cedar from different plantation spacing sites', *Journal of Wood Science*, Vol. 44, No. 1, pp. 62–68.

Wang, S.Y., Chiu, C.M. and Lin, C.J. (2002), 'Variations in ultrasonic wave velocity and dynamic young's modulus with moisture content for taiwania plantation lumber', *Wood and Fiber Science*, Vol. 34, No. 3, pp. 370–381.

Wang, X., Sharplin, N., Carter, P. and Ross, R. (2008), 'Method and apparatus for evaluation of standing timber', US Patent No: 7,418,866.

Wang, X. (1999), *Stress wave-based nondestructive evaluation (NDE) methods for wood quality of standing trees*, PhD thesis, Michigan Technological University, Houghton, Michigan.

Wang, X. (2013), 'Acoustic measurements on trees and logs: a review and analysis', *Wood Science and Technology*, Vol. 47, No. 5, pp. 965–975.

Wang, X., Ross, R., McClellan, M., Barbour, J.R., Erickson, J.R., Forsman, J.W. and McGinnis, G.D. (2000), 'Strength and stiffness assessment of standing trees using a nondestructive stress wave technique', Tech. rep., Forest Products Laboratory, US Department of Agriculture.

Wang, X., Ross, R., A. Mattson, J., R. Erickson, J., W. Forsman, J., A. Geske, E. and A. Wehr, M. (2001a), 'Several nondestructive evaluation techniques for assessing stiffness and moe of small diameter logs', *Forest Products Laboratory Research Paper*.

Wang, X., Ross, R.J., McClellan, M., Barbour, R.J., Erickson, J.R., Forsman, J.W. and McGinnis, G.D. (2001b), 'Nondestructive evaluation of standing trees with a stress wave method', *Wood and fiber science*, Vol. 33, No. 4, pp. 522–533.

Wang, X., Ross, R.J., Brashaw, B.K., Punches, J., Erickson, J.R., Forsman, J.W. and Pellerin, R.F. (2004a), 'Diameter effect on stress-wave evaluation of modulus of elasticity of logs', *Wood and fiber science*, Vol. 36, No. 3, pp. 368–377.

Wang, X., Ross, R.J., Green, D.W., Brashaw, B., Englund, K. and Wolcott, M. (2004b), 'Stress wave sorting of red maple logs for structural quality', *Wood Science and Technology*, Vol. 37, No. 6, pp. 531–537.

Wang, X., Ross, R.J. and Carter, P. (2005), 'Acoustic evaluation of standing trees: recent research development', In *Proceedings of the 14th International Symposium on Nondestructive Testing of Wood*, pp. 455–465.

Wang, X., Carter, P., Ross, R.J. and Brashaw, B.K. (2007a), 'Acoustic assessment of wood quality of raw materials: a path to increased of profitability', *Forest Products Journal*, Vol. 57, No. 5, pp. 6–15.

Wang, X., Ross, R.J. and Carter, P. (2007b), 'Acoustic evaluation of wood quality in standing trees. Part I. Acoustic wave behavior', *Wood and Fiber Science*, Vol. 39, No. 1, pp. 28–38.

Waugh, G. (2004), *The effect of wind on outerwood stiffness using TreeTap acoustic tool*, Bachelor's thesis, School of Forestry, University of Canterbury.

Weisstein, E.W. (2002), *CRC concise encyclopedia of mathematics*, CRC press, Boca Raton, Florida.

Wessels, C., Malan, F. and Rypstra, T. (2011), 'A review of measurement methods used on standing trees for the prediction of some mechanical properties of timber.', *European Journal of Forestry Research*, Vol. 130, No. 6, pp. 881–893.

Wheeler, G.F. and Crummett, W.P. (1987), 'The vibrating string controversy', *American Journal of Physics*, Vol. 55, No. 1, pp. 33–37.

Whitham, G.B. (1974), *Linear and Nonlinear Waves*, John Wiley and Sons, New York, NY.

Woods, S. (2006), *Acoustic Inspection of Timber*, Master's thesis, Electrical and Computer Engineering, University of Canterbury.

Wu, Y.C., Chaudhari, Q. and Serpedin, E. (2011), 'Clock synchronization of wireless sensor networks', *Signal Processing Magazine, IEEE*, Vol. 28, No. 1, pp. 124–138.

Xu, P. and Walker, J.C.F. (2004), 'Stiffness gradients in radiata pine trees', *Wood Science and Technology*, Vol. 38, No. 1, pp. 1–9.

Yaitskova, N. and van de Kuilen, J.W. (2014), 'Time-of-flight modeling of transversal ultrasonic scan of wood', *The Journal of the Acoustical Society of America*, Vol. 135, No. 6, pp. 3409–3415.

Yang, J.L. and Fortin, Y. (2001), 'Evaluating strength properties of Pinus radiata from ultrasonic measurements on increment cores', *Holzforschung*, Vol. 55, No. 6, pp. 606–610.

Yin, Y., Nagao, H., Liu, X. and Nakai, T. (2010), 'Mechanical properties assessment of Cunninghamia lanceolata plantation wood with three acoustic-based nondestructive methods', *Journal of Wood Science*, Vol. 56, No. 1, pp. 33–40.

Zener, C. (1948), *Elasticity and Anelasticity of Metals*, University of Chicago Press, Chicago, Illinois.

Zhang, S. (1995), 'Effect of growth rate on wood specific gravity and selected mechanical properties in individual species from distinct wood categories', *Wood Science and Technology*, Vol. 29, No. 6, pp. 451–465.

Zhang, X., Royston, T.J., Mansy, H.A. and Sandler, R.H. (2001), 'Radiation impedance of a finite circular piston on a viscoelastic half-space with application to medical diagnosis', *The Journal of the Acoustical Society of America*, Vol. 109, No. 2, pp. 795–802.

INDEX